



HAL
open science

Development of highly resolved and photo-modulated Kelvin probe microscopy techniques for the study of photovoltaic systems

Pablo Arturo Fernandez Garrillo

► **To cite this version:**

Pablo Arturo Fernandez Garrillo. Development of highly resolved and photo-modulated Kelvin probe microscopy techniques for the study of photovoltaic systems. Materials Science [cond-mat.mtrl-sci]. Université Grenoble Alpes, 2018. English. NNT : 2018GREAY031 . tel-01970171

HAL Id: tel-01970171

<https://theses.hal.science/tel-01970171>

Submitted on 31 Jan 2019

HAL is a multi-disciplinary open access archive for the deposit and dissemination of scientific research documents, whether they are published or not. The documents may come from teaching and research institutions in France or abroad, or from public or private research centers.

L'archive ouverte pluridisciplinaire **HAL**, est destinée au dépôt et à la diffusion de documents scientifiques de niveau recherche, publiés ou non, émanant des établissements d'enseignement et de recherche français ou étrangers, des laboratoires publics ou privés.

THÈSE

Pour obtenir le grade de

**DOCTEUR DE LA COMMUNAUTE UNIVERSITE
GRENOBLE ALPES**

Spécialité : **Nanophysique**

Arrêté ministériel : 25 mai 2016

Présentée par

Pablo Arturo FERNÁNDEZ GARRILLO

Thèse dirigée par **Dr. Benjamin GRÉVIN**,
et encadrée par **Dr. Łukasz BOROWIK**

Préparée au sein du **Laboratoire d'Électronique et de
Technologie de l'Information** et de l'**Institut Nanosciences et
Cryogénie – CEA Grenoble**
dans l'**École Doctorale de Physique**

Développement de techniques de microscopie Kelvin hautement résolues et photo- modulées pour l'étude de systèmes photovoltaïques

Thèse soutenue publiquement le **25 Septembre 2018**,
devant le jury composé de :

Dr. Sascha SADEWASSER

INL (Praga, Portugal), Examineur

Pr. Pere ROCA i CABARROCAS

LPICM, CNRS, Ecole Polytechnique, (Paris, France), Président

Dr. Guillaume SCHULL

IPCMS DSI (Strasbourg, France), Rapporteur

Pr. Christian LOPPACHER VOIROL

IM2NP, Faculté des Sciences et Techniques, (Marseille, France) Rapporteur

Dr. Benjamin GRÉVIN

UGA, CNRS, CEA, INAC, UMR-5819 (Grenoble, France), Directeur de thèse

Dr. Łukasz BOROWIK

UGA, CEA, LETI (Grenoble, France), Encadrant



THESIS

To obtain the degree of

DOCTOR OF THE UNIVERSITY OF GRENOBLE

Speciality: **Nanophysics**

Ministerial decree: May 25, 2016

Presented by

Pablo Arturo FERNÁNDEZ GARRILLO

Thesis directed by **Dr. Benjamin GRÉVIN**,
and supervised by **Dr. Łukasz BOROWIK**

Prepared at the **Laboratory of Electronics and Information
Technology** and the **Nanoscience and Cryogenics Institute –
CEA Grenoble**
at the **Doctoral School of Physics**

Development of highly resolved and photo-modulated Kelvin probe microscopy techniques for the study of photovoltaic systems

Thesis defended publicly on **September 25, 2018**,
in front of the Ph.D. thesis committee composed by:

Dr. Sascha SADEWASSER

INL (Praga, Portugal), Member

Pr. Pere ROCA i CABARROCAS

LPICM, CNRS, Ecole Polytechnique, (Paris, France), President

Dr. Guillaume SCHULL

IPCMS DSI (Strasbourg, France), Referee

Pr. Christian LOPPACHER VOIROL

IM2NP, Faculté des Sciences et Techniques, (Marseille, France) Referee

Dr. Benjamin GRÉVIN

UGA, CNRS, CEA, INAC, UMR-5819 (Grenoble, France), Ph.D. Director

Dr. Łukasz BOROWIK

UGA, CEA, LETI (Grenoble, France), Supervisor



“Look deep into nature, and then you will understand everything better.”

Albert Einstein

To my family, and especially to Susana, Luis David, Beatriz and Wintila.

Abstract

This thesis is directed towards the proposition and demonstration of a set of novel advanced atomic force microscopy based techniques under ultra-high vacuum conditions, enabling to map simultaneously the surface topography and the photo-carrier dynamics at the nanometre scale. In fact, by monitoring the dependence of the average surface photo-voltage measured with Kelvin probe force microscopy, as a function of the repetition frequency of a modulated excitation source, we will access the built-up and decay dynamics of the surface photo-voltage response which in turn will allow us to study the photo-carrier dynamics over a wide range of samples. In order to enable the 2-dimensional nano-imaging process, Kelvin probe force microscopy under modulated illumination measurements are acquired repeatedly over each point of a predefined grid area over the sample acquiring a set of spectroscopy curves. Then, using an automatic mathematical fit procedure, spectroscopy curves are translated into pixels of the photo-carrier dynamic time-constant images.

Moreover, these set of novel techniques will be used to investigate the surface photo-voltage dynamics in several kinds of photovoltaic samples from different technological branches such as small grain polycrystalline silicon thin films, silicon nanocrystal-based third generation cells, bulk heterojunction donor-acceptor organic photovoltaics and organic-inorganic hybrid perovskite single crystal cells, discussing in each case the photo-carrier recombination process and its relation with the material's structuration/morphology. Finally, technical aspects of these novel techniques will be discussed as well as their limitations and remaining open questions regarding results interpretation.

Résumé

Cette thèse propose, décrit et utilise un ensemble de techniques basées sur la microscopie à force atomique sous ultravide pour la cartographie simultanée, à l'échelle nanométrique, de la topographie de surface et des dynamiques temporelles des photo-porteurs. Ainsi, en contrôlant la dépendance du photo-potential de surface moyen mesuré par microscopie à force de sonde Kelvin en fonction de la fréquence de répétition d'une source lumineuse externe d'excitation, le dispositif expérimental permet d'accéder aux dynamiques temporelles du photo-potential de surface qui, à leur tour, permettent d'étudier les dynamiques des photo-porteurs sur une large gamme d'échantillons. Afin de permettre le processus de nano-imagerie bidimensionnelle, ces mesures sont acquises de manière répétée en enregistrant des courbes spectroscopiques en chaque point d'une grille prédéfinie. En utilisant une procédure d'ajustement mathématique automatique, les dynamiques temporelles des photo-porteurs sont extraites à partir des données expérimentales.

Cet ensemble de nouvelles méthodes est utilisé pour l'étude de plusieurs types d'échantillons issus de différentes technologies photovoltaïques telles que des couches minces en silicium poly-cristallin à petits grains, des cellules de troisième génération à nano cristaux de silicium, des cellules photovoltaïques organiques et des cellules à base de matériaux de structure pérovskite. Dans chaque cas, on décrit les processus de recombinaison des photo-porteurs ainsi que leur lien avec la morphologie et la structuration du matériau. Enfin, les aspects techniques de ces nouvelles méthodes d'analyse sont présentés, ainsi que leurs limites, notamment celles concernant l'interprétation des résultats.

Contents

Abstract.....	ix
Résumé.....	xi
Contents	xiii
List of Figures	xvii
Notations.....	xxi
1 Introduction.....	1
1.1 Thesis Outline	8
References.....	10
2 Photovoltaics.....	13
2.1 Context.....	13
2.2 Physics of classic solar cells: The case of silicon and other inorganic photovoltaics technologies	16
2.3 Organic photovoltaics	26
2.4 Perovskite photovoltaics	32
2.5 Characterization methods.....	35
Conclusion	37
References.....	39
3 Scanning probe microscopy techniques	45
3.1 Context.....	46
3.2 Nanotechnology	46
3.3 Atomic force microscopy.....	47
3.3.1 Contact mode	50

3.3.2 Amplitude modulation atomic force microscopy mode.....	52
3.3.3 Frequency modulation atomic force microscopy mode.....	54
3.3.4 Tip-sample interaction forces	58
3.4 Kelvin probe force microscopy.....	64
3.4.1 Amplitude modulation Kelvin probe force microscopy	68
3.4.2 Frequency modulation Kelvin probe force microscopy.....	69
3.4.3 Kelvin probe force spectroscopy	70
3.5 Calibrated work function mapping by Kelvin probe force microscopy.....	71
3.5.1 Highly oriented pyrolytic graphite: A work function reference sample?	73
3.5.2 An alternative work function calibration protocol.....	75
3.5.3 Absolute work function measurements: Comparison against theoretical values and achievable lateral resolution	81
3.6 Employed scanning probe microscopy setups	84
Conclusion	90
References.....	91
4 Frequency modulated illumination Kelvin probe force microscopy.....	99
4.1 Context.....	99
4.2 Frequency modulated illumination Kelvin probe force microscopy investigations	103
4.2.1 Silicon based photovoltaics	107
4.2.2 Bulk heterojunction donor-acceptor organic photovoltaics	115
4.2.3 Spectroscopic and time-resolved measurements over perovskite photovoltaics ..	131
Conclusion	142
References.....	143
5 Plausible sources of artefacts in frequency modulated illumination Kelvin probe force microscopy and how to avoid them	147
5.1 Context.....	147
5.2 Capacitance artefacts	149
5.3 Comparing amplitude modulation and frequency modulation Kelvin probe force microscopy modes	156
5.4 Frequency mixing	157
5.5 Other sources of artefacts.....	159
5.6 An improved protocol for photo-carriers dynamics investigation.....	160
5.7 On the presence of surface photovoltage contributions displaying inverted polarities	169

Conclusion	179
References	180
6 Towards the numerical analysis of spectroscopy curves	181
6.1 Context	181
6.2 The need for numerical simulations	183
6.2.1 SPECTY	184
6.3 Numerical simulations on a silicon nanocrystal solar cell	187
6.4 Organic photovoltaics: Mathematical fit versus numerical analysis.	192
Conclusion	196
References	197
7 Conclusion	199
8 Appendix	203
8.1 Additional photo-carrier dynamic results over the cross section of epitaxial silicon solar cell	203
8.2 Correcting the fitting functions from the capacitance effects	207
References	213
Publications	215
Patent Application	217
Conferences & Seminars	219
Acknowledgement	221

List of Figures

Figure 1.1– Yearly temperature anomalies from 1880 to 2014.....	2
Figure 1.2– Global PV modules price trend 2009-2016.....	3
Figure 1.3– Research solar cell efficiency records.....	4
Figure 1.4– Textile-based organic photovoltaic integrated with clothing.....	5
Figure 2.1– Band gap schematic.....	18
Figure 2.2– Recombination mechanisms in inorganic semiconductors.....	19
Figure 2.3– Photon absorption in direct and indirect bandgap semiconductors.....	20
Figure 2.4– p-n junction schematic.....	22
Figure 2.5– Hybridization for the case of ethene (C ₂ H ₄).....	27
Figure 2.6– Structure of organic photovoltaic devices.....	29
Figure 2.7– Major steps of charge generation and recombination.....	30
Figure 2.8– Structure of perovskites photovoltaic devices.....	33
Figure 3.1– AFM cantilever.....	49
Figure 3.2– Schematics of an optical-beam AFM cantilever deflection system.....	49
Figure 3.3– Contact AFM operation mode depiction.....	50
Figure 3.4– Approach-retract curve (force curve).....	51
Figure 3.5– AFM amplitude modulation operation mode depiction.....	53
Figure 3.6– AFM frequency modulation operation mode depiction.....	54
Figure 3.7– FM-AFM simplified functioning system scheme.....	58
Figure 3.8– Total tip-sample interaction force over tip-sample distance z.....	59
Figure 3.9– CPD measuring principle with KPFM.....	67
Figure 3.10– Schematic of KPFM and its feedback system.....	70
Figure 3.11– Kelvin parabola of the frequency-shift as a function of a static bias.....	71
Figure 3.12– Topography and CPD images on HOPG by FM-KPFM.....	74
Figure 3.13– Topography images and corresponding cross section profiles of samples.....	78
Figure 3.14– Topography and CPD measurements on Ag (111) sample.....	79

Figure 3.15– Results over BAM-L200 sample	82
Figure 3.16– WF cross-section acquired by FM-KPFM using a SSS probe over the BAM-L200 sample	83
Figure 3.17– LETI’s Omicron UHV VT AFM system.....	85
Figure 3.18– VT-AFM system from Scienta Omicron	86
Figure 3.19– INAC’s Omicron UHV VT AFM system	87
Figure 3.20– Multiple wavelengths laser source	88
Figure 3.21– Backside illumination sample holder	89
Figure 3.22– Arbitrary waveform generator Keysight 33622A.....	89
Figure 4.1– Illustration of the evolution of the surface photovoltage under modulated illumination as a function of time	102
Figure 4.2– Schematic illustration of FMI-KPFM.	104
Figure 4.3– 2-dimensional spectroscopy data acquisition.	106
Figure 4.4– Spectroscopic approach depiction	108
Figure 4.5– Schematic illustrations of the energy band diagrams for the n-doped silicon substrate (n-Si) and the poly-crystalline silicon thin film (poly-Si)	110
Figure 4.6– Results over the poly-Si film sample.....	111
Figure 4.7–Description of the SiNC embedded in 30 nm of SiO ₂ sample	112
Figure 4.8– Results over the SiNC embedded in 30 nm of SiO ₂ sample.....	114
Figure 4.9– FMI-KPFM investigations on back side geometry configuration over an organic photovoltaic sample	117
Figure 4.10– FMI-KPFM investigations on back side geometry configuration over an organic photovoltaic sample (zoomed in).....	119
Figure 4.11– FMI-KPFM at different illumination intensities.	121
Figure 4.12– Average potential as a function of the modulation illumination frequency acquired over the nanophase segregated PDBS-TQx/PC ₇₁ BM blend	123
Figure 4.13– Case of a single SPV component characterized by a built up and a decay time	125
Figure 4.14– Case of two different SPV component characterized by different built up and a decay times.....	126
Figure 4.15– Average potential as a function of the modulation illumination frequency acquired over the nanophase segregated PDBS-TQx/PC ₇₁ BM blend (fitted).....	127
Figure 4.16– Results over the nanophase segregated PDBS-TQx/PC ₇₁ BM blend.....	129
Figure 4.17– Spectroscopic curves acquired for different illumination conditions on the nanophase segregated PDBS-TQx/PC ₇₁ BM blend	131

Figure 4.18– Plot of the KPFM surface potential and of the tip height change relative to its initial position as a function of time during a single illumination pulse.....	134
Figure 4.19– Description of the p-type MAPbBr ₃ sample.....	137
Figure 4.20– Results over the MAPbBr ₃ sample	138
Figure 4.21– MAPbBr ₃ sample evolution.....	139
Figure 4.22– Topography and surface potential images of the UHV cleaved sample after several hours under illumination at 2.8 mW/cm ²	140
Figure 4.23– Topography, SPV decay time, dynamic SPV and SP at 990 Hz images of the UHV cleaved sample respectively.....	141
Figure 5.1– Scheme showing how photo-excited charges modify the effective distance between capacitor plates.....	149
Figure 5.2– Schematic illustration of Kelvin probe force spectroscopy under modulated illumination.....	151
Figure 5.3– Results of Kelvin probe force spectroscopy under modulated illumination	152
Figure 5.4– Graphical comparison of both measured and simulated CPD as a function of the illumination modulation frequency.....	154
Figure 5.5– FMI-KPFM in AM-KPFM mode against FM-KPFM mode.....	156
Figure 5.6– Improve FMI-KPFM protocol depiction.....	160
Figure 5.7– Results of the implementation of the improved FMI-KPFM protocol in single-point mode.....	161
Figure 5.8– Improved FMI-KPFM protocol results	164
Figure 5.9– Corrected SPV decay image.....	166
Figure 5.10– Open loop mode against close loop mode.....	167
Figure 5.11– Single-points FMI-KPFM measurements taken at different illumination intensities.....	170
Figure 5.12– SPV under continuous wave illumination as a function of the illumination intensity.....	170
Figure 5.13– Numerical simulation showing a SPV made up of two different components contributions with inverted polarities and different dynamics	171
Figure 5.14– Unveiling the dual polarity SPV behavior.....	173
Figure 5.15– FMI-KPFM self-consistency check up.....	176
Figure 5.16– Image of d^2C/dz^2 under continuous wave illumination and in dark conditions obtained via the FMI-KPFM improved protocol.....	177
Figure 6.1– Physical description of simulation parameters.....	185
Figure 6.2– SPECTY working principle.....	186
Figure 6.3– SPECTY’s algorithm flowchart	188

Figure 6.4– Comparison between spectroscopy curve obtained via the mathematical fit, measured data points and data points obtained by numerical simulations using $\tau b = 1 \mu s$, $\tau b = 10 \mu s$ and $\tau b = 20 \mu s$ respectively	190
Figure 6.5– Simulated-SPV as a function of time for different excitation modulation frequencies	191
Figure 6.6– Simulated-SPVAV as a function of the number of excitation cycles for different excitation modulation frequencies	192
Figure 6.7– CPD data obtained from the implementation of the improved FMI-KPFM protocol	194
Figure 6.8– Comparison between curves: Mathematical fits and simulated SPV_{AV} curve ...	195
Figure 8.1– Cross section of epitaxial silicon solar cell	204
Figure 8.2– Results over the cross section of epitaxial silicon solar cell	205
Figure 8.3– Different calculation scenarios	208
Figure 8.4– Case of a non-instantaneous sample photo-charging under illumination.....	211

Notations

AFM	Atomic Force Microscopy
AM	Amplitude Modulation
BHJ	Bulk Heterojunction
CPD	Contact Potential Difference
CT	Charge Transfer
CTS	Charge Transfer State
DA	Donor-Acceptor
FF-trEFM	Fast Free Time-Resolved Electrostatic Force Microscopy
FM	Frequency Modulation
FMI-KPFM	Frequency-Modulated Illumination Kelvin Probe Force Microscopy
HOMO	Highest Occupied Molecular Orbital
HOPG	Highly Oriented Pyrolytic Graphite
ITO	Indium Tin Oxide
KPFM	Kelvin Probe Force Microscopy
LCAO	Linear Combination of Atomic Orbitals (method)
LR	Long Range
LUMO	Lowest Unoccupied Molecular Orbital
OPV	Organic Photovoltaic (cell)
PLL	Phase-Locked Loop
PSD	Photo Sensitive Diode
PV	Photovoltaic (cell)
P3HT	Poly(3-Hexylthiophene)
PC₇₁BM	[6,6]-Phenyl-C ₇₁ -Butyric Acid Methyl Ester
QSSPC	Quasi-Steady-State Photo-Conductance
SEM	Scanning Electron Microscopy
SPM	Scanning Probe Microscopy

(S)PV	(Surface) Photovoltage
SR	Short Range
SSS	Silicon Super Sharp (cantilever)
STM	Scanning Tunneling Microscopy
TEM	Transmission Electron Microscopy
TiO_x	Titanium Oxide
trEFM	Time-Resolved Electrostatic Force Microscopy
UHV	Ultra High Vacuum
vdW	van der Waals
WF	Work Function
VT	Variable Temperature
Γ	2 nd harmonic signal from the lock-in detection.
A	Cantilever Amplitude
BE_X	Exciton Binding Energy
BE_{CTS}	Charge Transfer State Binding Energy
C	Capacitance
$CIGS$	Copper Indium Gallium (Di)Selenide
Δf	Frequency Shift
Δf_0	Frequency Shift Setpoint
EF	Fermi Energy
E_{gap}	Semiconductor Bandgap Energy
E_{vac}	Vacuum Energy
f_0	(First) Cantilever Resonance Frequency
f_K	Kelvin Modulation Frequency
F_{2w}	Second Harmonic Component of the Electrostatic Force
F_{el}	Electrostatic Force
F_{int}	(Total) Tip-Sample Interaction Force
F_{SR}	Short-Range Force
F_{vdW}	van der Waals Force

f_2	Second Harmonic Cantilever Resonance Frequency
FF	Fill Factor
H	Hamaker Constant
k	Cantilever Spring Constant
Φ	Work Function
Q	Quality Factor
R	Tip Radius
RMS	Root Mean Square (of surface roughness)
τ_d	Surface Photo-Voltage Decay Time Constant
τ_b	Surface Photo-Voltage Built-Up Time Constant
T	Temperature
$\mu W-PCD$	Microwave Photo-Conductivity Decay
V	Voltage
V_{AC}	Alternating Current Modulation Bias
V_{AV}	Average Surface Photo-Voltage
V_I	Surface Photo-Voltage Under Illumination
V_D	Surface Photo-Voltage in Dark
V_{DC}	Kelvin Compensation Bias
V_{OC}	Open Circuit Voltage
z	Tip-Sample Distance

1 | Introduction

Content

1.1 Thesis Outline	8
References.....	10

Most governments around the world, as well as the scientific community have agreed that in order to prevent catastrophic climate change, global warming must remain under 2°C with respect to pre-industrial mean temperatures.[1] However, the mean global temperature has already risen by 0.8°C since 1880, with two-thirds of the warming occurring since 1975, at a rate of roughly 0.15-0.20°C per decade.[2] Figure 1.1 shows yearly temperature anomalies from 1880 to 2014 as recorded by the United States of America (USA) national aeronautics and space administration (NASA), the USA national oceanic and atmospheric administration (NOAA), the Japan meteorological agency, and the British met office Hadley centre.[3] All data sources show an increasingly fast warming in the past few decades, being the last decade the warmest. In December 2015, at the United Nations climate change conference (COP 21) in Paris, governments acknowledged the increasing threat of climate change and agreed to work together towards keeping global warming to 1.5°C at most. However, society is already facing extreme weather conditions. From dangerous storms and floods, to heatwaves and droughts, extreme weather events are increasing in frequency and intensity.[1]

At the same time, world population increases at a rate of approximately 1.1% per year. Currently there are over 7.4 billion humans living on earth, and world population is expected to reach 10 billion by mid-2050.[4] This growth in population translates into an increasing energy demand that cannot be satisfied with fossil fuels in the long term, not only because of its negative impact on climate change but also for it is a limited resource.

Our dependence on fossil energy is polluting air, increasing the spread of disease and making water supplies scarcer and less safe.[1] Urgent action is needed to reduce carbon

emissions if dangerous climate change is to be avoided. The vast majority of fossil fuels, which are the biggest driver of climate change,[5] have to be left in the ground, to have a chance of preventing dangerous global warming. But at the same time, the energy demand of an increasing population has to be attended.

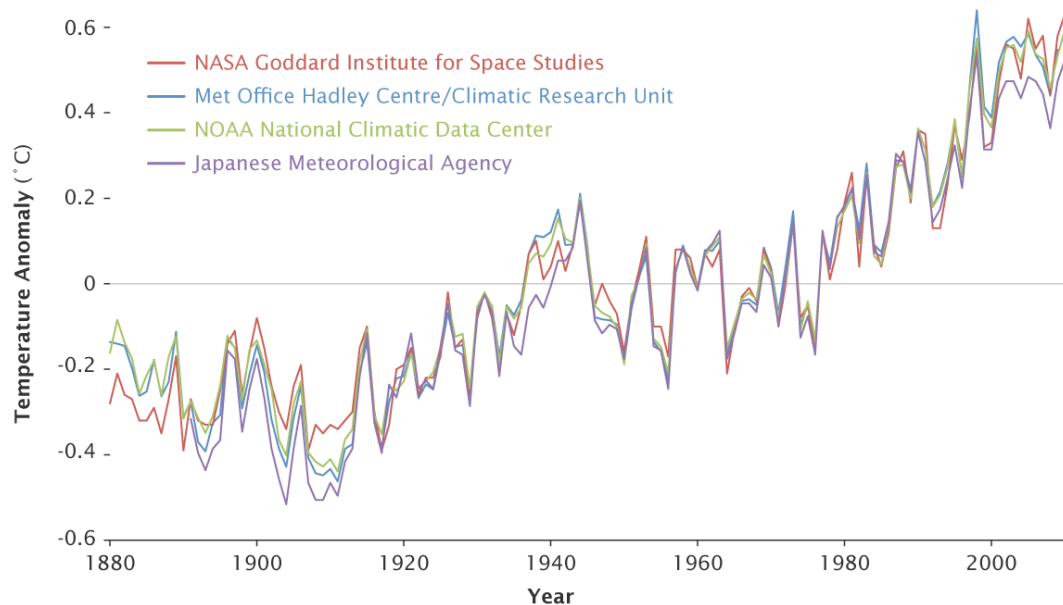


Figure 1.1– The line plot below shows yearly temperature anomalies from 1880 to 2014 as recorded by NASA, NOAA, the Japan Meteorological Agency, and the Met Office Hadley Centre (United Kingdom).

From Ref. [3]

Fortunately, renewable energy alternatives are growing rapidly and are more competitive than ever. Among the different renewable energy sources, the sun is arguably the most abundant clean source of energy that is capable of enabling sustainable economic growth, with minimum detrimental impact on the environment.[6] To emphasize this, it is often alleged that sunlight received by earth in one hour is enough to meet the annual energy needs of the current worldwide population.[7]

Solar power, once so expensive it only made economic sense in spacecraft, is becoming affordable enough that it is anticipated to drive coal and natural-gas plants out of business earlier than previously forecasted. Indeed, solar modules costs have steadily halved every 10

years since 1976 following Swanson's law[8] prediction, currently modules prices for several PV technologies are well below 1\$ per Watt in most Earth locations as shown in Figure 1.2. Moreover, while prices are dropping, solar energy generation is increasing. In 2016, new solar photovoltaic capacity around the world grew by 50% according to the International Energy Agency.[9]

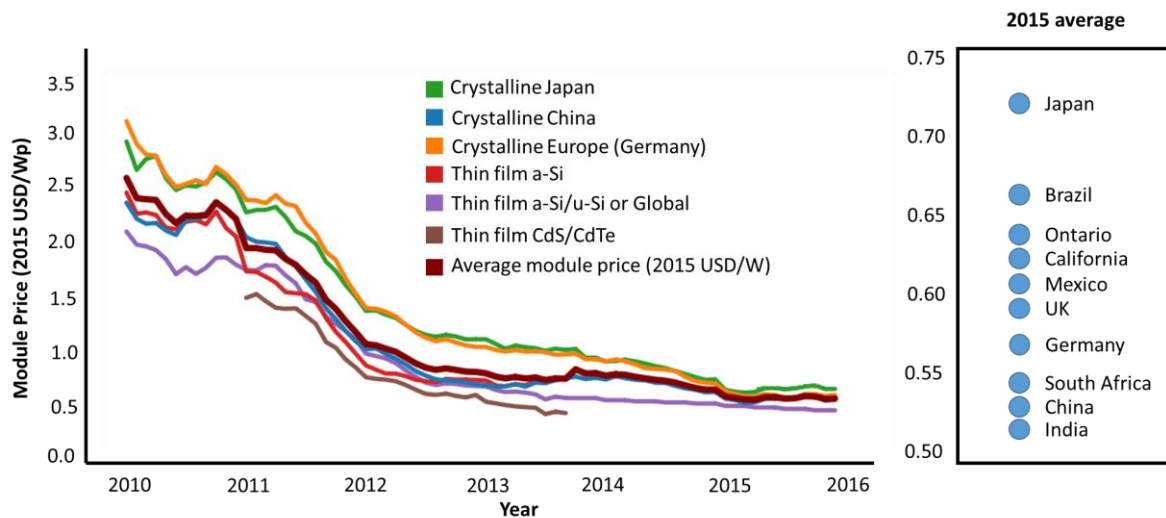


Figure 1.2– Global PV modules price trend 2009-2016. Data from Ref. [10]

To date, photovoltaic (PV) technology stands out as the only renewable energy option that: i) generates electricity without moving parts, ii) is practical for small and large scale applications, iii) is suitable for the urban environment as well as remote applications, iv) is silent, v) is a very low-maintenance technology and vi) has a low 'embodied energy', meaning the amount of energy invested in making PV modules is relatively small, although this can largely vary depending on the technology.

Most of today's installed photovoltaic panels are single junction cells based on monocrystalline silicon.[11] Monocrystalline silicon solar cells have been continuously progressing in efficiency and decreasing fabrication cost over the last half decade.[12, 13] Monocrystalline silicon cells with efficiencies of up to 26.6%[14] have already been attained, which already accounts for more than 70% of the theoretically achievable performance. As

branch in view of silicon technologies[11] and recently efficiencies of 13.1% have been reached.[17] Besides such relatively high performances, OPV cells also offer numerous advantages compared to inorganic solar cells. In contrast to the latter, they can be produced without any energy-intensive manufacturing process. Furthermore, these OPV cells are lightweight and can potentially be constructed on flexible substrates offering possibilities for new applications like the integration in mobile devices, buildings and even in clothes as shown in Figure 1.4.[11, 18]

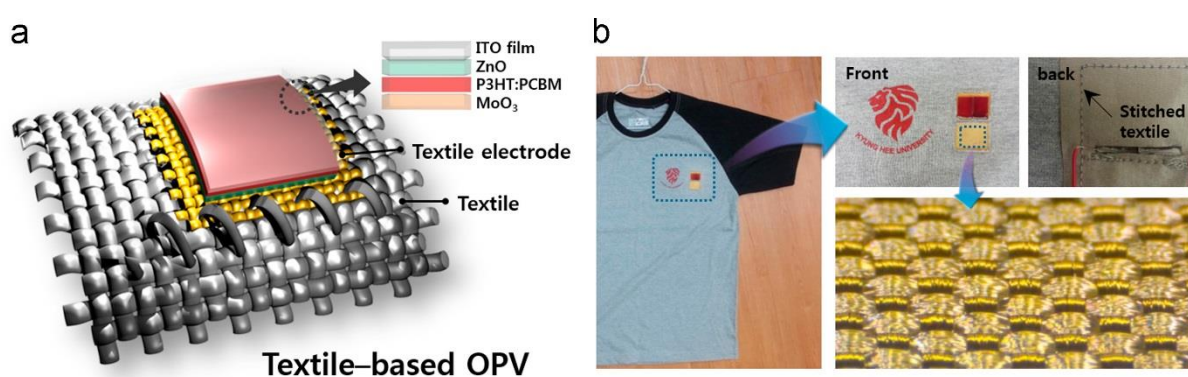


Figure 1.4– (a) Concept of a stitchable OPV on textile electrode. (b) Textile-based organic photovoltaic integrated with clothing. From Ref. [18]

In the emerging field of hybrid perovskites solar cells, efficiencies of up to 22.7%[14] have been reached. These cells can be manufactured with simple wet chemistry techniques in a traditional laboratory environment with the potential to be scaled up with relative feasibility.[6, 19] There is a growing interest in this technology as it promises to break the prevailing PV paradigm by combining both ultimately low cost and high efficiency.[6]

For these emerging PV technologies, it is crucial to fully understand the complex interplay between the nanostructure and photo-transport mechanisms. Indeed, the investigation of PV devices under operation conditions at the nanometer scale can give us valuable information about processes that occur at a scale of the order of tens and hundreds of nanometers, such as exciton dissociation, carrier transport across the material and carrier recombination. Undeniably, fundamental understanding of structure property relations in

energy materials and devices on the mesoscopic and nanoscopic levels is prerequisite to knowledge-driven design and optimization as well as to increase the commercial competitiveness of these technologies.

Indeed, the local investigation of certain PV characterization parameters, plays an important role in the ongoing performance improvement process. For instance, the work function (WF), which is the minimum energy needed to remove an electron to a point in the vacuum immediately outside of the surface (see **Chapter 3**) has a significant importance in the field of photovoltaics as it influence the band line-up at the interface between organic or perovskite materials and the electrodes of the PV device,[20, 21] hence its local study is of utmost importance when it comes to minimize sources of losses and maximize charge collection. [21-23]

Indeed, identifying the mechanisms of loss is at the core of the ongoing quest for increasing PV performances, as well as quantifying the role of heterogeneities on the recombination at the nanoscale. As we well see, photo-carrier lifetime is a parameter of paramount importance in the overall efficiency of a solar cell as it defines the proportion of photo-generated charges collected at the electrodes.

To date, most experimental approaches developed to probe recombination dynamics and hence photo-carrier lifetime, focus on the use of methods such as transient photo-voltage[24], charge extraction[25], microwave photo-conductivity decay (μ W-PCD)[26] and quasi-steady-state photo-conductance (QSSPC).[27] Yet, these techniques average out sample properties over macroscopic scales, rendering them unsuitable for directly assessing the influence of the nanostructure and local defects on photo-carrier dynamics.

In order to overcome this, few teams started to develop time-resolved scanning probe microscopies focused in addressing photo-carrier dynamics at the nanoscale.[28] In this context, Kelvin Probe Force Microscopy (KPFM)[29] under frequency modulated illumination arises as an alternative in photo-carrier dynamics measurements, as it has been used to probe the recombination dynamics in organic[28, 30] and the minority carrier lifetime in inorganic

semiconductors.[31, 32] However, for the most part, time-resolved KPFM-based methods have only been applied to obtain information coming from single points of the sample.

In that context, the focus of this thesis is directed towards the proposition and demonstration of a set of novel advanced atomic force microscopy (AFM)[33] based techniques under ultra-high vacuum (UHV) conditions, enabling to map simultaneously the surface topography at the nanometre scale and the photo-carrier dynamics with a temporal resolution covering 9 decades, from the nanosecond to the second scales (see **Chapter 4**). In particular, the technique covering the nanosecond to the millisecond range consist in monitoring the dependence of the average surface photo-voltage (SPV) measured with KPFM, as a function of the repetition frequency of a modulated excitation source. This process is repeated over each point of a predefined grid area over the sample enabling the 2-dimensional nano-imaging process of the photo-carrier dynamics.

After a brief but concise description of the employed scanning probe microscopy techniques, where special attention is given to describe the basic principle behind KPFM and WF measurements (see **Chapter 3**), in **Chapter 4** KPFM under frequency-modulated illumination (FMI-KPFM) is used to investigate the SPV dynamics in several kinds of PV samples from different technological branches ranging from small grain polycrystalline silicon thin film and silicon nanocrystal-based third generation cells, to bulk heterojunction (BHJ) donor-acceptor (DA) OPV and organic-inorganic hybrid perovskite single crystal cells, giving in each case special attention to the photo-carrier recombination process and its relation with the material's structuration/morphology.

Chapter 5 will be a FMI-KPFM technical chapter devoted to the introduction of plausible artefacts sources and guidelines to diminish their influence on measurements.

Finally, in **Chapter 6** an automatic numerical simulation routine that enables to predict the behaviour of spectroscopy curves of the average surface photovoltage as a function of a frequency-modulated excitation source in photovoltaic materials, is used to compare simulated and FMI-KPFM experimental results. In this chapter it is also shown how this simulation

routine can complement experimental results as additional information about the sample's photo-carriers dynamics can be gained via the numerical analysis.

1.1 Thesis Outline

In the following, a short outline of this thesis will be presented:

In **Chapter 2** the basics of inorganic organic and hybrid photovoltaics will be introduced including all elements needed for the discussion of the experimental results. In this chapter an insightful overview of several emerging photovoltaic technologies will be given, paying special attention to their possible forthcoming role in the PV market. The importance of nano-characterization for the development of different emerging PV technologies will be also highlighted in this chapter.

As mentioned above, **Chapter 3** will give a summarized description of the employed scanning probe microscopy techniques as well as the used UHV AFM systems. Here, special attention is given to describe the basic principle behind KPFM and WF measurements highlighting its importance in the field of photovoltaics. To better illustrate KPFM working principle, in this chapter, an original WF calibration procedure for KPFM probes under UHV using monocrystalline metallic materials with known crystallographic orientation is proposed and demonstrated.

Chapter 4 will introduce the conception and implementation of a novel KPFM-based technique (FMI-KPFM) that allows the acquisition of SPV dynamics images, with a sub-10 nm lateral resolution. Small grain polycrystalline silicon thin films, silicon nanocrystal-based third generation cells, organic donor-acceptor blends and organic-inorganic hybrid perovskite single crystal cells will be used as samples. For each sample, the discussion will be focus on the photo-carrier recombination process and its relation with the material's structuration/morphology.

Chapter 5 will be focused on the discussion of plausible sources of artefacts in FMI-KPFM measurements, such as capacitance and resonant-induced effects. An improved measurement protocol will be introduced, aiming at avoiding or diminishing these effects.

In **Chapter 6** insights on FMI-KPFM data treatment are given. Here, special attention is given to the development of an automatic numerical simulation routine that enables to compare simulated and FMI-KPFM experimental results. It is show how experimental FMI-KPFM results are confirmed by the numerical analysis and how additional information about the photo-carriers dynamics can be found via this simulation routine.

The conclusion in **Chapter 7** will summarize the thesis, discuss current projects and describe future perspectives.

References

1. Nature, W.W.F.F. *Climate & Energy*. 2017; Available from: http://wwf.panda.org/what_we_do/footprint/climate_carbon_energy/.
2. Hansen, J., et al., *Global Surface Temperature Change*. *Reviews of Geophysics*, 2010. **48**(4).
3. Observatory, N.E. *Global Temperatures*. 2014; Available from: <https://earthobservatory.nasa.gov/Features/WorldOfChange/decadaltemp.php>.
4. United Nations, D.o.E.a.S.A., Population Division, *World Population Prospects: The 2017 Revision, Methodology of the United Nations Population Estimates and Projections*. 2017: New York: United Nations.
5. Change, I.P.o.C., *IPCC, 2014: Climate Change 2014: Synthesis Report. Contribution of Working Groups I, II and III to the Fifth Assessment Report of the Intergovernmental Panel on Climate Change 2014*, Intergovernmental Panel on Climate Change: Geneva, Switzerland. p. 151.
6. Snaith, H.J., *Perovskites: The Emergence of a New Era for Low-Cost, High-Efficiency Solar Cells*. *The Journal of Physical Chemistry Letters*, 2013. **4**(21): p. 3623-3630.
7. Morton, O., *A new day dawning?: Silicon Valley sunrise*. *Nature*, 2006. **443**: p. 19.
8. Carr, G., *Sunny uplands*. *The Economist*, 2012.
9. Agency, I.E., *Renewables 2017: Analysis and Forecasts to 2022*. Market Report Series. 2017: International Energy Agency.
10. Agency, I.R.E. *Solar PV Costs 2010-2015*. 2015; Available from: <http://resourceirena.irena.org/gateway/dashboard/?topic=3&subTopic=32>.
11. Fuchs, F., *Model Donor-Acceptor Systems for Organic Photovoltaics Investigated by Scanning Probe Microscopy*, in *Physics*. 2014, Université Grenoble Alpes: Grenoble.
12. Green, M.A., et al., *Solar cell efficiency tables (version 40)*. *Progress in Photovoltaics: Research and Applications*, 2012. **20**(5): p. 606-614.
13. Green, M.A., *Silicon solar cells: evolution, high-efficiency design and efficiency enhancements*. *Semiconductor Science and Technology*, 1993. **8**(1): p. 1.
14. Laboratory, N.R.E. *Best Research-Cell Efficiencies*. 2017; Available from: <https://www.nrel.gov/pv/assets/images/efficiency-chart.png>.
15. Branker, K., M.J.M. Pathak, and J.M. Pearce, *A review of solar photovoltaic levelized cost of electricity*. *Renewable and Sustainable Energy Reviews*, 2011. **15**(9): p. 4470-4482.
16. Brown, R.A., *Theory of transport processes in single crystal growth from the melt*. *AICHE Journal*, 1988. **34**(6): p. 881-911.

17. Zhao, W., et al., *Molecular Optimization Enables over 13% Efficiency in Organic Solar Cells*. Journal of the American Chemical Society, 2017. **139**(21): p. 7148-7151.
18. Lee, S., et al., *Stitchable organic photovoltaic cells with textile electrodes*. Nano Energy, 2014. **9**: p. 88-93.
19. Saidaminov, M.I., et al., *High-quality bulk hybrid perovskite single crystals within minutes by inverse temperature crystallization*. Nature Communications, 2015. **6**: p. 7586.
20. Brabec, C.J., *Organic photovoltaics: technology and market*. Solar Energy Materials and Solar Cells, 2004. **83**(2): p. 273-292.
21. Stratakis, E., et al., *Improving the efficiency of organic photovoltaics by tuning the work function of graphene oxide hole transporting layers*. Nanoscale, 2014. **6**(12): p. 6925-6931.
22. Kim, J.S., et al., *Control of the electrode work function and active layer morphology via surface modification of indium tin oxide for high efficiency organic photovoltaics*. Applied Physics Letters, 2007. **91**(11): p. 112111.
23. Worfolk, B.J., et al., *Work Function Control of Interfacial Buffer Layers for Efficient and Air-Stable Inverted Low-Bandgap Organic Photovoltaics*. Advanced Energy Materials, 2012. **2**(3): p. 361-368.
24. McNeill, C.R., I. Hwang, and N.C. Greenham, *Photocurrent transients in all-polymer solar cells: Trapping and detrapping effects*. Journal of Applied Physics, 2009. **106**(2): p. 024507.
25. Hanfland, R., et al., *The physical meaning of charge extraction by linearly increasing voltage transients from organic solar cells*. Applied Physics Letters, 2013. **103**(6): p. 063904.
26. Ahrenkiel, R.K. and S. Johnston, *Contactless measurement of recombination lifetime in photovoltaic materials*. Solar Energy Materials and Solar Cells, 1998. **55**(1): p. 59-73.
27. Sinton, R.A. and A. Cuevas, *Contactless determination of current-voltage characteristics and minority-carrier lifetimes in semiconductors from quasi-steady-state photoconductance data*. Applied Physics Letters, 1996. **69**(17): p. 2510-2512.
28. Cox, P.A., et al., *Imaging Charge Transfer State Excitations in Polymer/Fullerene Solar Cells with Time-Resolved Electrostatic Force Microscopy*. The Journal of Physical Chemistry Letters, 2015. **6**(15): p. 2852-2858.
29. Nonnenmacher, M., M.P. O'Boyle, and H.K. Wickramasinghe, *Kelvin probe force microscopy*. Applied Physics Letters, 1991. **58**(25): p. 2921-2923.
30. Shao, G., et al., *Intensity-Modulated Scanning Kelvin Probe Microscopy for Probing Recombination in Organic Photovoltaics*. ACS Nano, 2014. **8**(10): p. 10799-10807.

31. Takihara, M., T. Takahashi, and T. Ujihara, *Minority carrier lifetime in polycrystalline silicon solar cells studied by photoassisted Kelvin probe force microscopy*. Applied Physics Letters, 2008. **93**(2): p. 021902.
32. Borowik Ł., L.H., Chevalier N., Mariolle D., Renault O., *Measuring the lifetime of silicon nanocrystal solar cell photo-carriers by using Kelvin probe force microscopy and x-ray photoelectron spectroscopy*. Nanotechnology, 2014. **25**(26): p. 265703.
33. Binnig, G., C.F. Quate, and C. Gerber, *Atomic Force Microscope*. Physical Review Letters, 1986. **56**(9): p. 930-933.

2 | Photovoltaics

Content

2.1 Context.....	13
2.2 Physics of classic solar cells: The case of silicon and other inorganic photovoltaics technologies	16
2.3 Organic photovoltaics	26
2.4 Perovskite photovoltaics	32
2.5 Characterization methods.....	35
Conclusion	37
References.....	39

Ce chapitre a pour objectif d'introduire les bases du composant photovoltaïque en matériau inorganique organique et hybride, tout en incluant tous les éléments nécessaires pour l'analyse des résultats expérimentaux. Notamment, un aperçu approfondi de plusieurs technologies émergentes est présenté, en accordant une attention particulière à leur éventuel rôle dans le développement futur des composants pour le photovoltaïque. L'importance de la nano-caractérisation pour le développement de ces dispositifs est également soulignée dans ce chapitre.

2.1 Context

About 4.5-billion years ago, in the wide vastness of space, gravity, one of the fundamental forces of nature, drew the remnants from the violent death of previous stars along with gas and dust together to create a protostar that would eventually become our Sun.[1] This young protostar was basically a giant ball of hydrogen and helium. Few tens of millions years later, the temperature and pressure inside this protostar increased, jumpstarting the hydrogen's

nuclear fusion process that drives the Sun nowadays (*i.e.*, turning hydrogen into helium). Fast-forward to the future and we will see that in approximately 5-billion years the sun will run out of hydrogen in its core,[2] from that point on, gravity will compress the star which in turn will increase the temperature and pressure until the point where helium is able to fuse into carbon. The energy produced by the helium fusion will cause the Sun to expand outwards many times its current size and become a red giant.[3] While there is still a scientific debate around whether our planet will be engulfed by the Sun's expansion or whether it will orbit dangerously close to the dimmer star, either way, life as we know it on Earth will cease to exist. Fast-forward 1-billion years more into the future and we will witness the Sun's shrinking back down to become a white dwarf, at this point, the life-giving light will slowly dissipate.[2, 4]

However, in the meantime, the Sun has been the source of all of the energy that drives biological and physical processes on Earth. The Sun is responsible for the appearance of life on Earth, as every known life form uses solar energy in some way to sustain itself.

Since the dawn of humankind solar energy has been vital for survival. Aboriginal cultures used the Sun's energy for crucial activities such as heating their dwellings and curing their nourishment.[5] Solar energy played a very important role in these cultures as many of them even worshiped and revered the Sun. As ages passed, more complex ways of capturing the energy irradiated by the sun were developed. Already in 1200 A.D. in the America's, the Anasazi tribe incorporated passive solar design in their cliff dwellings that captured the winter sun to warm their homes.[6] As cultures developed, some even created laws related to accessing solar energy. In the ancient Roman Empire it was forbidden by the law to build a dwelling that blocked the Sun from their neighbour's home. Indeed, the Roman law enforced solar rights as an important source of light and heat.[7]

However, it was not until 1883, when C. E. Fritts, developed the first device which enabled the direct conversion of light into electricity.[8] It consisted of a thin sheet of selenium melted on a metal substrate and covered with a silver film. A few more decades will pass before modern photovoltaic cells based on p-n junctions were invented in 1954 by American researchers at Bell Labs.[9] It was by chance, that they found that silicon p-n junctions

produced current when the light in the room was lit. From that moment on, the solar cells' performance grew quickly. The first performances were of the order of 6% with p-n junction types of Cu₂S/CdS, GaAs and CdTe.

Few years later to this invention, organic electronics emerged. Although currently their performance is lower compared to silicon-based technologies, the use of inexpensive and abundant polymers is a promising alternative for the semiconductor technology. The first steps of this technological branch are to be found in 1970, when Shirakawa, MacDiarmid and Heeger discovered the possibility of turning a polymer conductive by doping it.[10] It turns out that these polymers owe their conductivity to delocalized electrons jumping from site to site between the atoms that form the molecules. In fact, in their ground state, a polymer can be considered as a semiconductor with a wide gap and low conductivity. After doping, for example with oxygen, the conductivity increases significantly. These polymers paved the way for a large number of applications, including organic photovoltaics (OPV). The first organic photovoltaic heterojunction was manufactured in 1986 by Tang et al.[11] Tang developed a bilayer device based on copper phthalocyanine and a perylene tetracarboxylic derivative and achieved a power conversion efficiency of about 1%. Currently, the power conversion efficiency record in the OPV field is held by Zhao et al., with a 13.1% efficiency.[12]

More recently, we have witnessed the extraordinary fast emergence of a novel class of solar cell technology based on mixed organic–inorganic halide perovskites. Perovskites are a crystallographic family with general ABX₃ stoichiometry.[13] Their discovery is credited to Gustav Rose following his report on the oxide perovskite CaTiO₃ in 1839.[14] The advantage of the use of these materials for PV applications relies on the fact that they are relatively inexpensive, can be deposited onto flexible substrates, they possess long electron-hole diffusion lengths, and relatively high carrier mobilities[15] and a high light absorption coefficient which enables ultrathin films of around 500 nm to absorb the black body solar radiation.[16, 17] Miyasaka and co-workers were apparently the first to report photovoltaic results for perovskites.[18] In 2006, they reported cells with an efficiency of 2.2%. Nowadays, laboratory devices have shown efficiencies of more than 22%.[19] This rise in efficiency is what sparked the interest in this promising technology.

Whereas the above mentioned technologies rely on different physical mechanisms to convert light into electricity, they all respond to the same need, find a solution to the world's increasing energy demand while limiting the human impact on the Earth's climate.

In the following, a summarized guide including the basics on classic PV silicon and other inorganic photovoltaic technologies, as well as on other emerging technologies such as OPV, perovskites and technologies including the use of micro/nano-structured materials (also called third generation solar cells) are given. It will provide the reader with the essential elements for the comprehension and discussion of the experimental results shown in subsequent chapters.

In this section the reader will find a description of the physics behind the functioning of these PV technologies, highlighting some key characterization parameters as well as the importance of their local study using different near-field microscopy techniques for their further development. Finally, the expected forthcoming role of each of these technologies in the PV market will be addressed.

2.2 Physics of classic solar cells: The case of silicon and other inorganic photovoltaics technologies

The photoelectric effect is the ability of matter to eject or emit free electrons (also called photo-electrons) when illuminated. It was observed and described for the first time by Heinrich Hertz in 1887.

According to classical Maxwell's wave theory,[20] as the light flux increases, greater the energy with which the electrons should be ejected or emitted from the material. However, experiments prove this prediction to be wrong, instead it was found that the energies of the emitted electrons were independent of the intensity of the light radiation. It was Albert Einstein in 1905 who propose that actually, light itself consisted of individual energy packages which he called quanta, later called photons.[21] It was quanta that interacted with the electrons of

matter behaving like discrete particles instead of a continuous wave. In his model, the energy of each quanta was proportional to its frequency in the following way:

$$E = h\nu \quad (2.1)$$

Where h is the Planck's constant and ν is the frequency of the incident light.

In short, according to Einstein, the photons of a light beam possess an intrinsic energy which is proportional to the frequency of the light. When electrons within some material interact with a photon, the energy of the photon is absorbed by the electrons. If the energy acquired by an electron is greater than its binding energy, this electron will be ejected, otherwise, the electron will not be able to escape the material. A logical conclusion of Einstein's theory is that if the intensity (flux) of a light beam source directed to a material is increased, this will not bring more energetic electrons ejected as result. On the other hand, if the frequency of this light beam source is increased, the energy of the emitted electrons will increase proportionally. This model was later confirmed experimentally and Einstein won the Nobel Prize in physics in 1921 for his discovery.

It turns out, that photoemission can occur in any material, but it is most easily observable in metals or other conductors and semi-conductors.

A particular case of the photoelectric effect is the photovoltaic effect which was actually discovered and described several years prior to Hertz's discovery. Indeed, it was in 1839 when Alexandre Becquerel discovered the photovoltaic effect while studying the effect of light on electrolytic cells.[22] This effect describes the creation of a potential difference in a material upon exposure to light.

While in both the photoelectric and photovoltaic effect, light is absorbed, causing excitation of an electron or other charge carrier to a higher-energy state, the main distinction between them relies in that the photoelectric effect refers to the case when the electron is ejected out of the material. On the other hand the photovoltaic effect, refers to the case when the excited charge carrier is still contained within the material.

Photovoltaic devices, which main function is to directly convert light into electricity are based on the photovoltaic effect. For this energy conversion to take place, a material in which the absorption of light raises an electron to a higher energy state is required.

Like other solids, semiconductor materials have electronic band structure determined by the crystal properties of the material. The actual energy distribution among the electrons is described by the Fermi level[23] and the temperature of the electrons (kinetic energy).[24] In semiconductors without any doping, the Fermi level lies in the middle of a forbidden band or band gap between two allowed bands, called the valence band and the conduction band as shown in Fig. 2.1.

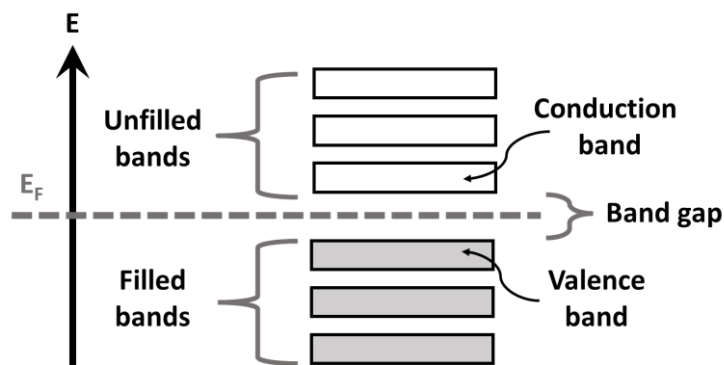


Figure 2.1– Band gap schematic. E_F denotes the Fermi level.

In short, the photovoltaic effect describes photons with energies greater than the energy bandgap of the semiconductor being absorbed, and electrons being promoted from the valence band to conduction band, leaving a corresponding number of holes in the valence band.

This electron-hole pair which is called exciton, remains bound by the Coulomb[25] attraction force. In inorganic semiconductors like silicon, this binding energy is about the same as the thermal energy at room temperature (~ 25 meV)[26], consequently, excitons are naturally dissociated. This process is called photo-generation, as mobile electrons and holes are created due to absorption of electromagnetic radiation. The photo-generation rate is determined by the number of photons, that is, the number of excited electrons, and not the energy of the photons. Though all of the photon energy is absorbed, only a part of it can be used. The energy used is

the one gained over the energy bandgap, the rest of it is lost to phonons, generally called thermalization.[27]

At this point is important to remind the reader that any electron which exists in the conduction band is in a meta-stable state and will eventually stabilize to a lower energy position in the valence band. When this occurs, it will move into an empty valence band state. Consequently, when the electron stabilizes back down into the valence band, it will also effectively remove a hole. The energy difference between the initial and final state of the electron is released in the process. This process is called photo-carrier recombination.[28] In the case of inorganic photovoltaics devices, there are basically three types of photo-carrier recombination: i) radiative, ii) non-radiative, and iii) Auger recombination. As depicted in Figure 2.2a, in the case of non-radiative recombination, this energy is passed on to one or more phonons[29], in the case of radiative recombination, the energy difference between the initial and final state of the electron is emitted in the form of a photon (Figure 2.2b), and in the case of Auger recombination it is given off in the form of kinetic energy to another electron in the conduction band (Figure 2.2c).

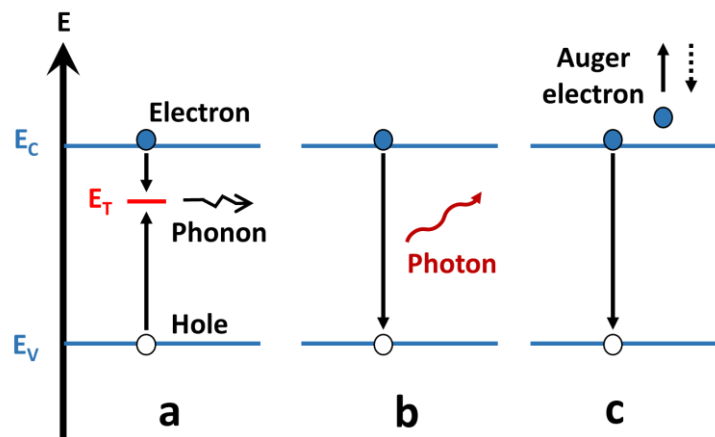


Figure 2.2– Recombination mechanisms in inorganic semiconductors: (a) non-radiative, (b) radiative and (c) Auger. In (a) E_T denotes the energy level of a defect or impurity in the material also called trap.

Depending on the intrinsic characteristics of the material, photo-carrier recombination through one of the recombination mechanisms can be more significant than through the others.

For instance, depending on the band gap type, radiative recombination can be more important than non-radiative. We remind the reader that the band gap of a semiconductor material is always either direct or indirect.[26] As depicted in Figure 2.3, this distinction refers to the alignment of the minimal-energy state in the conduction band with respect to the maximal-energy state in the valence band. Indeed, if these two energy levels are aligned, the band gap is direct, on the contrary, if this energy states are not aligned the band gap is an indirect one. Therefore, radiative photo-carrier recombination is more likely to occur in materials such as gallium arsenide (GaAs) with direct band gaps, while non-radiative Shockley–Read–Hall recombination[30] is usually the predominant recombination type present in Si-based devices favoured by defects and dislocations in the material. Here, is also important to highlight that in highly doped materials, Auger recombination becomes also an important source of energy loss.

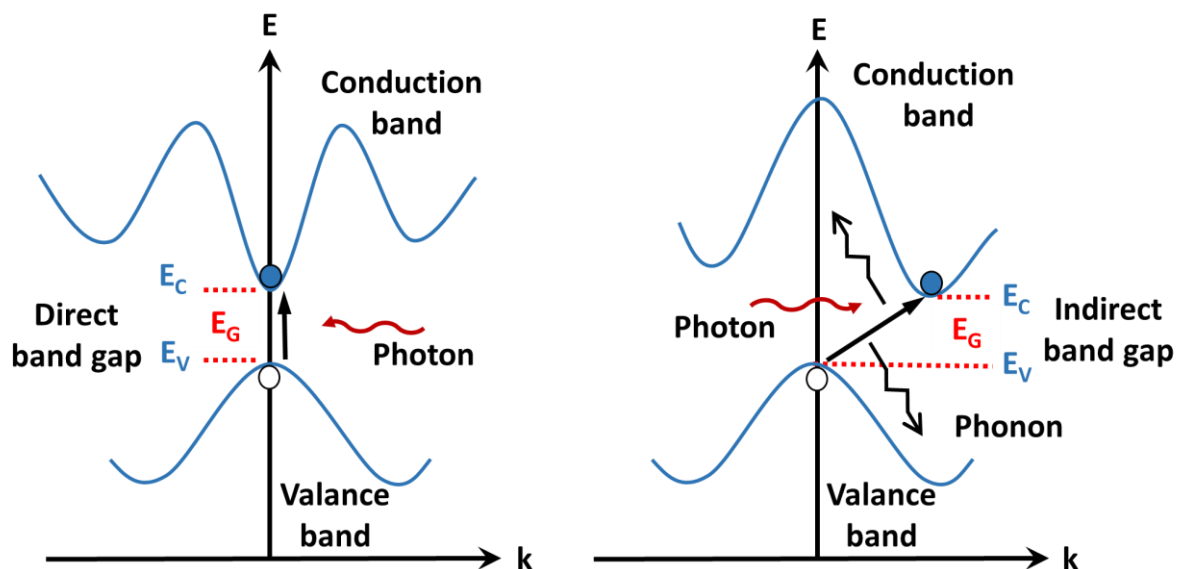


Figure 2.3– Photon absorption in direct (left) and indirect (right) bandgap semiconductor. Here the valence band, conduction band, and band gap are denoted as E_V , E_C and E_G respectively.

Actually there are several sources of losses in a solar cell device, some are intrinsic to the material such as the losses due to poor light absorption, and there are other sources of losses that do not depend on the material but rather the device design such as the losses due to the

shadowing effect of the electrodes bus bars over the active material. In fact, to quantify the total solar conversion efficiency η of solar cell devices, the following expression is often used:

$$\eta = \frac{V_{OC}I_{SC}FF}{P} \quad (2.2)$$

Where V_{OC} is the open circuit voltage and can be defined as the electron-hole quasi Fermi level splitting, I_{SC} is the short circuit current, this is the current generated when the load resistance is zero, FF is the fill-factor which is the ratio of the maximum power generated by the cell divided by $V_{OC}I_{SC}$, and P is the incident light radiation power. On Earth's surface, the solar radiation power is approximately 963 Wm^{-2} . [31]

Among different parameters which can be used to describe processes that occur in solar cell devices that impacts their efficiency, carrier lifetime τ is arguably one of the most important ones. This parameter is defined as the time during which an electron excited by light remains in the conduction band before falling back into the valence band. The carrier lifetime must not be confused with the carrier generation lifetime, which is the duration required to convey an electron in the conduction band. Indeed, carrier lifetime plays a central role in the global effectiveness of solar photovoltaic cells since it limits the proportion of photo-generated charges collected on the electrodes.

We have already described the photo-generation process that take place in PV devices, this is, photon absorption and exciton generation. However, photo-generation is only half of the energy conversion process that takes place in PV devices. Actually, in order to take advantage of the energy of the electrons raised to higher energy states, these electrons must be collected. That is actually the main reason why it is desirable to have substantial carrier lifetimes in solar cells, since this allows to maximize the quantity of collected charges.

Nevertheless, for this charge collection to occur, the electrons and holes need to be driven apart to the cathode and the anode respectively which are usually placed at the top and bottom of the solar cell device. For this, a built-in electric field within the cell is usually required. To create this electric field, two semiconductor layers with different doping types are usually "sandwiched" together, creating a p-n junction. A p-n junction consists in one layer of

negatively-doped material, physically connected to another layer of positively-doped material. A p-type semiconductor possesses abundance of positively charged holes while and an n-type semiconductor has an abundance of negatively charged electrons. When n-type and p-type silicon layers contact, excess electrons move from the n-type side to the p-type side. Because of the flow of electrons (and holes), the p-n junction creates the electric field that drive free electrons and holes towards the electrodes as depicted in Figure 2.4.

Connecting conductive leads to both sides of the solar cell will result in the creation of a side-to-side return path within the cell, allowing the process to continue as long as light is provided to the cell. It is this current of electrons traveling from the n-type side to the p-type side through the circuitry and the potential difference between both layers, what define the electrical power that a solar cell can provide. Maximum power is supplied to the electrical load when its impedance matches that of the illuminated PV cell.[31]

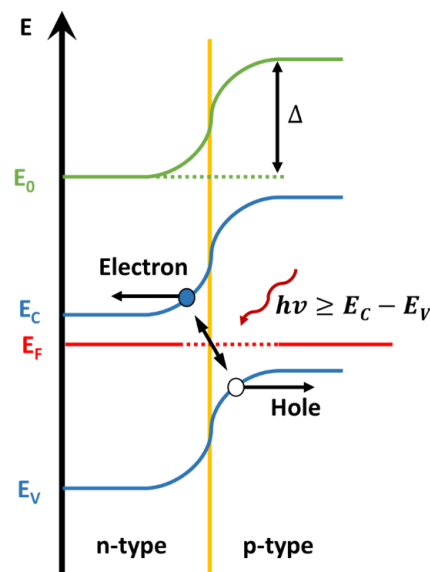


Figure 2.4– p-n junction schematic. An exciton is photo-generated, the charges are then separated and guided to the corresponding electrodes. The valence and conduction bands E_v and E_c are identified, as well as the Fermi level E_f , the local vacuum level E_0 and the potential Δ created by the junction. The photon's energy is defined as $h\nu$, which must be higher than the band gap to promote an electron from the valence band to the conduction band.

After near half a century of industrial production, Si-based solar cells are now easily manufactured at large scales, all over the world and especially in China where currently more than half of the world's photovoltaics are produced.[32] Currently, silicon remains the predominant material used in PV applications, not only because of the mature processing technology, but also for its abundance on earth and well adapted electronic properties. Indeed, silicon has a band gap of 1.12 eV[33] making it suitable for the spectral range[17] of sunlight on earth.

Within silicon based materials, the crystalline quality spans from single crystal to amorphous materials, including materials with different grains size, density and quality of grain boundaries.

In mono-crystalline silicon (c-Si), the wafer material is cut from cylindrical ingots that are typically grown by the Czochralski process.[34] c-Si solar cells display a distinctive pattern of small white diamonds. This material offers the best properties to achieve cell efficiency records. However, the high cost generated by the Czochralski crystal growth is a serious weakness for further increase of the PV cell fabrication.

Unlike mono-crystalline Si-based solar panels, multi-crystalline solar cells, do not require the Czochralski crystal growth process. Instead, for the production of this material, molten silicon is poured into a container and then allowed to cool resulting in silicon ingots with large columnar grains.[31] This means that multi-crystalline solar cells are made from multifaceted silicon crystal, *i.e.*, a crystal that has grown in multiple directions. These materials have the advantage of being less expensive than c-Si however multi-crystalline solar cells are generally 2-3%[31] less efficient than solar cells made of the crystalline material. This reduced efficiency is explained by minority carrier recombination occurring at different defects in the material. Indeed, depending on the crystallization process, the material can have different structural defects, which determine and limit the efficiency of multi-crystalline PV devices. Actually, these defects in the material can act as sinks for photo-excited carriers, negatively impacting the total efficiency. However, in despite of its lower efficiency, multi-crystalline silicon is the most used material at the industrial level[32] because of its reduced manufacturing

cost and the fact that the efficiency gap between c-Si and multi-crystalline solar cells has been reducing over time with the implementation of new design concepts.[19]

On the other side of the spectrum, we find amorphous silicon (a-Si H) which is often used in thin film PV technology applications. Thin films of amorphous silicon are produced using chemical vapour deposition (CVD)[35] of gases containing silane (SiH_4).[36] Layers of this material can be deposited onto rigid or flexible substrates depending on the desired application. Actually, the material which is used in solar cells is hydrogenated amorphous silicon, aSi:H, an alloy of silicon and hydrogen, here the hydrogen plays the important role of passivating the dangling bonds that result from the random arrangement of the silicon atoms. Because of its wide band gap (1.7 eV), only a few microns of material are needed to absorb the most energetic (high frequency) incident light.[31]

Actually, it turns out that the microstructure of the deposit can be tuned by diluting the silane gases in hydrogen. In fact, for highly diluted gases, the deposit consists of regions of crystalline silicon immersed in an amorphous matrix. This two-phase material is known as poly-crystalline silicon with grains sizes on the micro/nano-meter range (sometimes also called micro-crystalline silicon). This material shows several useful advantages over a-Si, one being that if grown properly it can have a higher electron mobility, due to the presence of the silicon crystallites.[31] As a-Si, micro-crystalline silicon is often used in silicon thin film PV technologies.

There is a large variety of new emerging silicon PV technologies, the goal of these technologies being to reduce the thickness of the silicon in the panel to minimise materials usage, to increase the light absorption of the material by advanced light trapping techniques, to tune the band gap by the introduction of embedded nanostructures, to prevent photo-carrier recombination and to reduce the energy required in the fabrication process. In short, to improve the economic competitiveness of PV against fossil and non-renewable energy sources. Among these technologies we find black silicon technology,[37] silicon nanocrystals embedded in a dielectric matrix[38] and all-silicon tandem solar cells.[39]

In most of these emerging technologies, where materials are micro/nano-structured, unveiling the photo-transport mechanisms and identifying the sources of losses by carrier recombination is key for their further development. Indeed, investigating the photo-carrier dynamics in nanostructured and heterogeneous energy materials is of crucial importance from both fundamental and technological points of view.

However, emerging PV technologies are not all silicon-based. In fact, there is a wide variety of materials that have been used in the fabrication of photovoltaic devices. As above mentioned, GaAs has a direct energy bandgap as well as other III-V compounds such as indium phosphide (InP) and gallium antimonide (GaSb). These materials possess high optical absorption coefficients and good values of minority carrier lifetimes (in highly pure, single crystal material) rendering them exceptional materials for making high efficiency solar cells.[31] The main disadvantage of photovoltaic devices based on these compounds is the high cost associated to their production with the high quality required for PV applications. In fact, the use of these materials in solar cells has its beginning in space applications where the cost of production did not constitute a drawback against the high-conversion efficiencies together with the high resistance to extra-terrestrial radiation that these materials possess.

Another interesting compound for PV applications is cadmium telluride (CdTe). Indeed, this II-VI compound, which also possesses a direct band gap, is commonly used in PV thin film technology applications as well as copper indium gallium (di)selenide (CIGS) which has the advantage of being able to be deposited on flexible substrates, producing highly flexible, lightweight solar panels.

In the 80's, multi-junction devices (also called tandem devices) were developed. In fact, by adding several junctions, several band gaps can be defined and more energy can be extracted from each incident photon. In other words, the use of multi-junctions allows to minimize energy losses due to electron (and hole) thermalization. As mentioned before, this technology holds the conversion efficiency record with 46%[19], however, theoretical calculations predict that efficiencies of about 72% could be attained for devices with 32 junctions.[40]

Although inorganic materials dominate the PV market, there is a relatively new technology compared to Si-based PV technologies that arises as a promising approach for the development of alternative PV. Indeed, organic solar cells present many intrinsic advantages, such as their light weight, flexibility, and principally their low material and manufacturing costs. In the following, a brief description introducing the basics of OPVs will be given.

2.3 Organic photovoltaics

Organic photovoltaics are built using thin films of organic semiconductors which includes polymers, oligomers as well as fullerene derivatives.[41-43] Solution processed organic solar cells[44] combine electron donor (polymers or small molecules) and acceptor (usually fullerene derivatives) in π -conjugated systems.

A π -conjugated system simply refers to the way a molecule is structured. In a conjugated system, atoms within the molecule form alternating double and single bonds. Single bonds are known as σ -bonds and are associated with localized electrons, and double bonds contains both σ -bond and a π -bond. In a π -conjugated system, bonds are covalent, *i.e.*, they share their outer shell electrons (valence electron) with their nearest neighbours to obtain a stable energy noble gas configuration (octet rule).[45]. Thanks to the mutual overlap of π orbitals along the conjugation path, the π -electrons are much more mobile than the σ -electrons. Indeed, they can jump from site to site between atoms, which causes the wave functions to delocalize over the conjugated backbone.[46] According to the model of linear combination of atomic orbitals (LCAO)[47], the covalent bonds are created by a linear combination of the orbitals of the isolated atom. Therefore, bound and unbound orbitals with respectively lower and higher energy are obtained. This process is called hybridization. Figure 2.5 depicts hybridization for the case of ethene (C_2H_4). In this case, two orbitals π and π^* are obtained. As π is a lower energy level, it contains the two valence electrons.

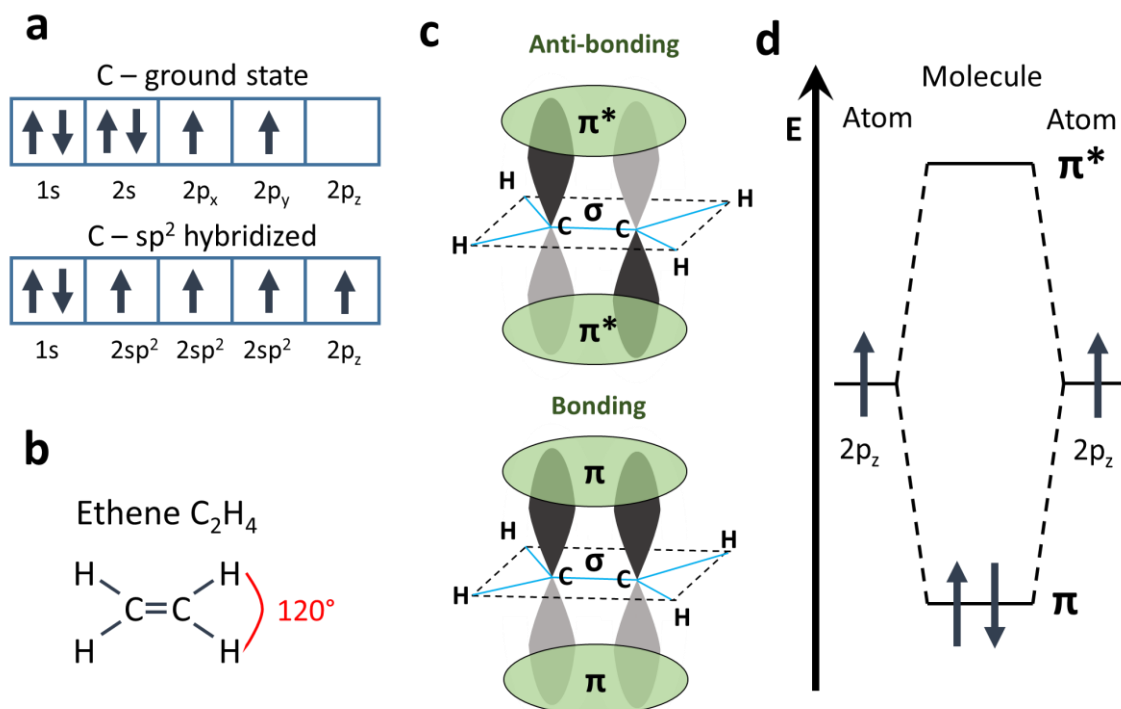


Figure 2.5– (a) Electron occupation of: ground state and sp^2 -hybridized orbitals of a carbon atom. (b) C₂H₄ molecular structure. (c) Illustration of the orbitals of the ethylene molecule. The double bond between the carbon atoms consists of an σ -bond made up of the electrons of the hybrid $2sp$ states, and a π -bond between the electrons of the $2p_z$ state. Two configurations are possible, the π state (bound orbitals) and the π^* state (unbound orbitals). The phase of the p orbitals is indicated by black and grey colour. (d) Energy diagram of the ethylene molecule. When the molecule is not excited, the two electrons are in the π state which is energetically lower. Illustration according to Ref. [48] and adapted from Ref. [49]

In general, the π -bands are either empty (so-called lowest energy unoccupied orbital – LUMO) or filled with electrons (so-called highest energy occupied orbital - HOMO). The gap between the LUMO and HOMO levels has the same properties as the band gap in inorganic semiconductors. In most organic semiconductors this band gap ranges from 1 to 4 eV. In the case of a donor-acceptor interface (described hereafter), these energetic offsets define a type-II heterojunction as depicted in Figure 2.6a.

Under electromagnetic radiation, the energy state of these π electrons increases, and they can be excited from the molecule's HOMO to the LUMO, this is known as a $\pi - \pi^*$

transition. This generates positive and a negative polarons (analogous to an electron-hole pair in inorganics photovoltaics). During this energy transition, the molecule remains stable due to the strong covalent bonds.

OPVs belong to the class of photovoltaic cells known as excitonic solar cells, which are defined by strongly bound electron-hole pairs that are formed after light excitation (typically between 0.1-1 eV). The existence of strongly bound excitons arise as a consequence of the low dielectric constants in the organic components. Indeed, electronic wave functions in organic molecules are more localized, and electrostatic attraction can thus keep the electron and hole together as an exciton. In excitonic solar cells, exciton dissociation occurs almost exclusively at the interface between two materials of differing electron affinities (and/or ionization potentials): in this case, the interface between the electron donor and the electron acceptor.[43] Moreover, OPV devices possess a short exciton diffusion length (10-30 nm), consequently, charge separation can indeed limit the efficiency of these devices.

To overcome this, in the early 1990's the bulk heterojunction (BHJ) architecture was developed. In this type of structure the donor and acceptor materials are processed to form two interpenetrated networks phase-segregated at the 10-30 nm scale to match the exciton diffusion length as depicted in Figure 2.6b. In this architecture, once the photo-generated exciton (typically generated in the donor material) reach the donor-acceptor interface via diffusion, usually a charge transfer to the acceptor material occurs, this transfer at the interface creates a so-called charge transfer state (CTS). At this point, the CTS can either recombine or split up into free charges, which can be later collected by the electrodes as illustrated in Figure 2.6c. Here, we stress that in order to have an efficient charge extraction, it is crucial to establish Ohmic contacts.[50] Adapted interface design[51, 52] is also critical to achieve selective electrical contacts for holes at the anode and electrons at the cathode in BHJ devices. Essentially, this is achieved by using materials with low and high work functions for electrons and holes extraction, respectively.

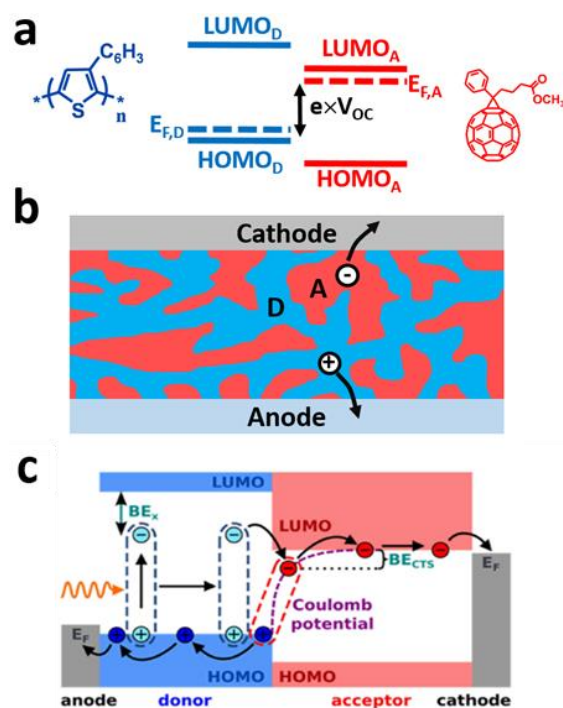


Figure 2.6– (a) Type-II energy level alignment between a π -conjugated electron donor polymer (in this case P3HT) and a π -conjugated electron acceptor molecule (PCBM). Here, the open circuit voltage is defined by the splitting of holes and electrons quasi Fermi levels (represented by dotted lines) under illumination.

(b) Organic bulk heterojunction solar cell. In the figure, D stands for electron donor and A for electron acceptor. (c) Exciton (binding energy BE_x) dissociation into a charge transfer state (coulomb binding energy BE_{CTS}) at a donor-acceptor interface. The free charges resulting from the splitting of the CTS are collected at the cathode (electrons) and anode (holes). Panels (a) and (b) were reproduced from [53]. Panel (c) was adapted and reproduced from [49]

In Figure 2.7 the essential steps of photo-induced charge carrier generation and collection in a complete donor-acceptor BHJ OPV device are depicted. In short: upon photon absorption, excitons are generated, if excitons do not relax and recombine before reaching the donor-acceptor interface, then as mentioned before, the excitons reach the donor-acceptor interface via diffusion. At this point, the exciton is effectively dissociated into a CTS. Once the exciton has been dissociated into a CTS, it can immediately recombine or dissociate into free charges. All recombination events described so far are often referred to as geminate recombination. If the CTS split into free charges, they can either be collected by the electrodes, reach another donor-acceptor interface region and recombine with an opposite charge (non-

geminate recombination) or get trapped in a lower energy state trap in the material (charge trapping). If the charge is released from the trap, it can either recombine with a free counter charge at the donor-acceptor region (trap-delayed recombination) or reach the electrodes and be collected.

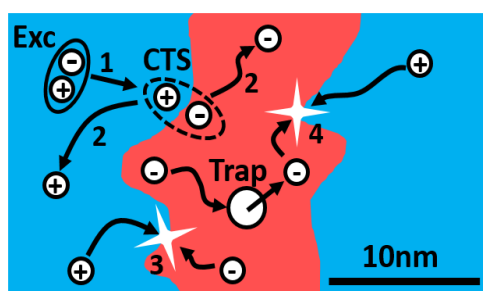


Figure 2.7– Major steps of charge generation and recombination. 1) Exciton diffusion to the donor-acceptor interface and creation of the CTS. 2) Separation of the bound polaron pair into free charges (alternatively, at this point geminate recombination can also occur). 3) Non-geminate recombination of free charge carriers. 4) Charge trapping, release, and trap-delayed recombination with a free counter charge (alternatively, the release charge can get collected by the electrodes). Illustration reproduced from[53].

Based on the aforementioned, the source of losses in BHJ OPV may essentially arise from the relaxation of excitons which fail to reach the donor-acceptor interface, the recombination of CTS states or alternatively, the recombination of geminate polaron pairs, as well as from the electron-hole annihilation of quasi free polarons generated by recombination events on their way towards the electrodes. Additionally, tail states[44, 54] which often display low de-trapping rates, can also be the source of charge trapping. Finally, trapped charges can recombine with a free opposed charge via the so-called trap-assisted recombination process, also denoted as trap-delayed recombination.[55]

Moreover, considering that the charge carrier mobility in solution processed BHJ is low, the performances of functioning devices is significantly limited by the competition between charge extraction to the electrodes and non-geminate recombination processes. Indeed, non-geminate recombination processes has been shown to be a major loss mechanism which limits the performances of operating devices. However, to date, there is still no clear

understanding of all parameters necessary for a full quantitative description of the loss mechanisms in a BHJ OPV cell.[48] Nonetheless, mounting evidence seems to point out that the nanostructure has a critical impact on the photo-carrier dynamics. Indeed, it has been demonstrated, for instance, that in the case of P₃HT:PCBM blends, the relative strength of trap-assisted recombination is strongly sample processing-dependent.[56]

Noteworthy progress has been achieved this past decade in understanding the photo-carrier generation and transport mechanisms in relation with the nanostructure in BHJs. However, many questions are not definitely settled, largely due to the highly complex phase morphology of BHJs.[57] As we will see in **Chapter 4**, there is a growing interest of the scientific community on studying photo-carrier dynamics at the nanoscale in BHJ OPV devices. Indeed, the study of photo-carrier dynamics at the local scale have the potential to yield valuable information about photo-transport mechanisms that could help to unveil the complex interplay between morphology and photo-carrier dynamics.

Although as mentioned before, a comprehensive understanding of the physical processes within an organic solar cell is still missing, organic electronic devices are on the rise and have already entered our day-to-day life.

Currently, the industrial production of OPV devices has already been on the going for several years. Specialized companies develop and synthesize small organic molecules and use the deposition of these molecules in a low temperature, roll-to-roll vacuum process at large scales.

Recently, one of the leading companies in the OPV market signed a development agreement with one of the world's largest producer of flat glass, aiming to develop building integrated photovoltaics by integrating organic solar films in glass to collect solar energy.[58] Actually, a patented technology that enables the generation of clean electricity on see-through glass windows has already been developed, this technology make use of the energy of natural sunlight and artificial sources such as fluorescent and LED lighting. Indeed, as mentioned in **Chapter 1**, considering the advantages that OPV offers, the niche markets it could impact are many, ranging from building integrated photovoltaics to smaller flexible organic solar cells for

the integration in bags or mobile devices.[49] In the future it is expected that OPVs will lead the creation of new markets and novel applications such as therapeutic bandages for monitoring wounds recovery, wearable electronics for monitoring and improving athletic performance as well as highly efficient curved architectural solar power.[58]

However, OPVs are not the only type of solar cell technology that could eventually be used in novel and exciting PV applications for a fraction of the cost of classic Si-solar cells. In fact, a newcomer to the PV field has quickly reached power conversion efficiencies of more than 21% while possessing some of the advantages present in OPVs, such as their light weight, and low material and manufacturing costs. Indeed, organic-inorganic hybrid perovskites, adopting the chemical formula ABX_3 (see Figure 2.8a), where, A and B are cations of dissimilar sizes and X are anions, typically oxygen, halogens or alkali metals have very recently become a new platform for the development of next-generation light harvesting and opto-electronic devices.[59] In the following, the reader will find a brief description introducing the basics of perovskite photovoltaics.

2.4 Perovskite photovoltaics

As mentioned before, perovskite photovoltaics made their debut in 2006 when Miyasaka and colleagues fabricated a perovskite-based solar cell with a power conversion efficiency of 2.2%.[18] Since then, a meteoric rise in power conversion efficiencies has made them the rising star in the PV field and raised a huge interest among the scientific community. Indeed, they show an extraordinary combination of opto-electronic properties that make them excellent materials for the fabrication of PV devices including, high absorption coefficients, direct band gaps, high carrier mobility, high diffusion lengths and long carrier lifetimes.

The structure of a thin-film-like perovskite solar cells (*i.e.*, planar configuration) is depicted in Figure 2.8b. It consist in a perovskite layer sandwiched between an electron transporting/hole blocking layer (ETL) and a hole transporting/electron blocking layer (HTL). In this technology, many of the standard interface layers from the world of OPVs work

relatively well. For example, PEDOT:PSS[60] and the PTAA-class of polymers work well as hole interface layers as well as Spiro-OMeTAD[61], while PCBM, C_{60} [60], ZnO[62] and TiO_2 [63] make effective electron interfaces. Depending of the electrode configuration, the planar cells can be referred to as regular n-i-p or inverted p-i-n devices. In Figure 2.8c the relative position of the energy levels of two electron transporting materials, a perovskite, and a hole transporting material are illustrated.

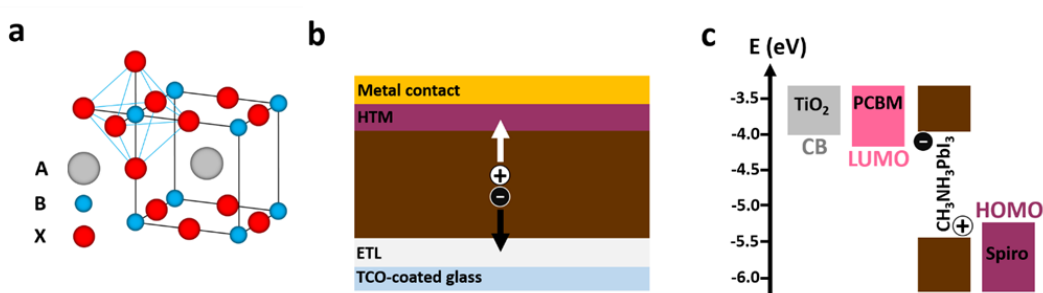


Figure 2.8– (a) ABX_3 perovskite structure; A: methyl ammonium or formalddehyde ammonium, B: Pb or Sn, X: halogen). (b) Planar perovskite solar cell architecture. (c) Relative position of the energy levels of TiO_2 and PCBM, the perovskite $CH_3NH_3PbI_3$ and a hole transporting material (Spiro-OMeTAD). Panel (a) was adapted and reproduced from [53]. Panels (b) and (c) were reproduced from [53] without modifications.

The physics of the charge generation and transport mechanisms in hybrid-perovskites is still the subject of great debate and intensive investigations. Photo-physical studies have shown that in perovskite-structured materials, due to the low exciton binding energy (as opposed to the case of OPVs), free charge carriers can be directly generated at room temperature under optical excitation. In these devices, due to the WF difference between the anode and the cathode, an internal built-in electric field might be generated, responsible of directly driving the charge carriers to the electrodes for collection. But even in the case of a low built-in electric field, selective contacts can still drive the electron and hole flows thanks to their large carrier diffusion lengths in the material.

At this point, the reader might be under the impression that the description of the photo-physical properties of perovskite devices agree with those present in inorganic-based direct band gap photovoltaics such as GaAs. Indeed, it has been suggested through electron beam-

induced current profiling investigations[64] that in fact the perovskite material present in the planar cell configuration can be considered as a high quality low-doped intrinsic semiconductor. Another characteristic that perovskites share with some previous existing PV technologies is the fact that similar to the case of OPV devices, charge collection efficiency relies on the proper alignment between the energy levels of the different interfaces layers depicted in Figure 2.8b. Certainly, interface engineering is essential to achieve highly efficient planar perovskite devices[65], highlighting once more the importance of accurate WF measurements at an adapted scale.[66]

In perovskite devices, structural and chemical defects could potentially affect the solar cell performance. These loss mechanisms remain intensively investigated. However, to date, there is no certainty if structural defects such as grain boundaries are detrimental to the overall device performance as they could be at the source of charge trapping and trap-delayed recombination[60, 67], or if on the contrary their influence is benign.[64] Nonetheless, even in the case where grain boundaries are in fact benign, there are many other types of structural/chemical defects that actually do act as carrier traps, this possibly due to a non-stoichiometric composition and defect sites at the surface of the film.[68-70] However, the correct identification of these defects is still a work in progress.[71, 72]

A particularity of perovskite solar cell devices against their OPV and inorganic counterparts is the presence of ion migration mechanisms. Indeed, the presence of ion migration in perovskite solar cells has received intensive attention from the scientific community, however, so far a comprehensive understating of exactly how it impacts the cell performance is still elusive. Nonetheless, there is some growing evidence that points to photo-induced (and electric-field induced) ion-migration as a mechanism that impact the optoelectronic characteristics of organic-inorganic halide perovskites.[73] Indeed, some models have been developed where the anomalous hysteresis and the defect assisted ion migration in perovskite materials are related.[74] In short, it has been suggested that ion-defect migration is particularly likely to be involved in the slow photoconductivity reaction and solar cell hysteresis phenomena.[75] Moreover, some recent investigation exposed that a complex interplay can exist between the charge carriers, the low energy traps, and mobile halides.[76,

77] As we will see in **Chapter 4**, it is very important to bear in mind this particularity when performing Kelvin probe force microscopy investigations on these materials.

2.5 Characterization methods

As mentioned in **Chapter 1**, identifying the mechanisms of loss is at the core of the ongoing quest for increasing PV performances. Indeed, the comprehensive understanding of the role that heterogeneities play on carrier recombination at the nanoscale is key to improve cell performances. In fact, nowadays, this strongly relies on the development of advanced characterization techniques capable of imaging their opto-electronic properties at the nanoscale. While there exist several experimental approaches which have been developed to probe recombination dynamics such as such as transient photo-voltage[78], charge extraction[79], microwave photo-conductivity decay (μ W-PCD)[80] and quasi-steady-state photo-conductance (QSSPC)[81], most of these techniques average out sample properties over macroscopic scales (few mm^2 at best). Indeed, most of these techniques do not allow to assess the influence of the nanostructure and local defects on photo-carrier dynamics.

Another approach, based on scanning electron microscopy (SEM)[82] allows to map the photo-carriers diffusion length and in some cases the effective photo-carrier lifetime with a submicron spatial resolution (at best). Indeed, electron beam induced current (EBIC)[83], is a technique that allows to measure the diffusion lengths of minority carriers, or to obtain images of the location of defects in the material causing photo-carrier recombination, whether or not they emit light when recombining. While the lateral resolution achievable by EBIC allows the characterization of some polycrystalline materials, it fails in the case of nanostructured materials, impeding to gain a comprehensive understanding of the role of heterogeneities at the nanoscale.

We can also find approaches based on atomic force microscopy (AFM) which allow to obtain information about the photo-carrier recombination dynamics at the local scale. This is the case of techniques relying on a time-resolved analysis of the AFM cantilever dynamics

(transients) after an optical pulse. For instance, time-resolved electrostatic force microscopy (trEFM) [84], is a technique which allow to achieve a temporal resolution of 100 μ s and a lateral resolution of 100 nm. In short, this technique relies on the analysis of the frequency shift decay after optical pulsing. Moreover, in 2012 a trEFM-derived technique called fast free trEFM (FF-trEFM) was introduced by the same group[85], where the temporal resolution was improved by nearly one order of magnitude. However, both trEFM and FF-trEFM were used at the stage of “proof of concept” and where only implemented over OPV devices.

Furthermore, we can also find other AFM-based techniques relying on the recording of a mean signal under modulated excitation (illumination or a voltage bias). In fact, this particular approach has been developed only by few groups [86-89] and is based on Kelvin probe force microscopy (KPFM), an electrostatic mode AFM (see **Chapter 3** for more details). In short, techniques based on this approach measure the evolution of the average surface photo-potential with respect to the repetition frequency of a modulated illumination source. In other words, photo-modulated KPFM can yield an averaged time-integral value of the instantaneous photovoltage. Techniques implementing this approach have been used to evaluate the minority carrier lifetime in micro-crystalline silicon based solar cells[86], third generation solar cells based on silicon nano-crystals[87], the cross section of an epitaxial silicon solar cell [89] and the photo-carrier dynamics in organic BHJ thin films[88]. However, in almost all cases, information about the photo-carrier dynamics can only be obtained at single locations of the sample (without lateral resolution), again limiting the assessment of the influence of the nanostructure and local defects on photo-carrier dynamics.

In that context, this thesis is directed towards the development and implementation of KPFM-based methods enabling the imaging of the photo-carrier dynamics with a lateral resolution which allows to assess the influence of local heterogeneities (few nanometres) on photo-carrier dynamics in a wide range of PV materials. In short, the main challenge that will be addressed in this thesis, consist in the development of photo-carrier dynamics high resolution imaging modes instead of photo-potential dynamics point measurements.

Conclusion

A large path has been covered since the invention of the firsts modern PV devices with efficiencies around 6% and the use of expensive materials, passing through the development of Si-based, thin film technology and tandem PV devices where high energy conversion efficiencies were reached allowing these technologies to compete for the first time with fossil energy sources in terms of price, to the development of PV devices made of abundant, flexible and inexpensive materials which hold the promise of changing the way we produce energy.

Indeed, the development of some emerging PV technologies such as OPVs and perovskites seems to be especially promising due to their low manufacturing costs. Particularly perovskite devices appear to combine this advantage with high energy conversion efficiencies.

However, the lack of a complete and thoughtful understanding of the loss mechanisms and degradation process[90] in these materials, holds back the large scale production and commercialization of solar cell devices.

Having briefly described the leading technologies in the field of PV, it seems rather obvious that the further development of these technologies, including but not limited to emerging third generation PVs, strongly relies on the development of advanced characterization methods capable of investigating their opto-electronic properties at the nanoscale.

Indeed, regardless of the technology, the crucial task in the further development of PVs is to identify the sources of losses, especially those due to photo-carrier recombination. This challenge renders scanning probe microscopy (SPM) techniques as a natural tool to fulfil this task as they allow the local investigation of these materials.

In that sense, this thesis is directed towards the investigation at the nanometre scale of one of the most important parameters in the characterization of PV devices, the photo-carrier lifetime. In the following chapters of this thesis, the more general term of photo-carrier

dynamics will be used to describe the time between photon absorption and photo-carrier recombination in inorganic, organic and hybrid PV materials.

Before introducing a novel characterization method based on the use of scanning probe microscopy techniques under frequency-modulated illumination, which for the first time enable the imaging of the photo-carriers dynamics in a wide range of PV devices with a spatial resolution that can reach a few nanometres, (see **Chapter 4**), **Chapter 3** will review the employed scanning probe microscopy techniques that gave rise to the aforementioned technique. Here, particular attention to the description of Kelvin probe force microscopy and WF measurements will be given as it constitutes a tool that has proven to be useful in the characterization of the energy level alignment at the interfaces of PV devices.

References

1. Cameron, A.G.W., *The formation of the sun and planets*. Icarus, 1962. **1**(1): p. 13-69.
2. Redd, N.T. *Red Giant Stars: Facts, Definition & the Future of the Sun*. 2013; Available from: <https://www.space.com/22471-red-giant-stars.html>.
3. Redd, N.T. *How Was the Sun Formed?* 2017; Available from: <https://www.space.com/19321-sun-formation.html>.
4. Schröder, K.P. and R. Connon Smith, *Distant future of the Sun and Earth revisited*. Monthly Notices of the Royal Astronomical Society, 2008. **386**(1): p. 155-163.
5. Monday, A. *Why Solar Energy is Important?* 2017; Available from: <http://www.techwizard.com.ng/solar-energy-important/>.
6. Tzikopoulos, A.F., M.C. Karatza, and J.A. Paravantis, *Modeling energy efficiency of bioclimatic buildings*. Energy and Buildings, 2005. **37**(5): p. 529-544.
7. Hayes, G.B., *Solar Acces Law: Protecting Access to Sunlight for Solar Energy Systems*. 1979: Ballinger Publishing.
8. Fritts, C.E., *On a new form of selenium cell, and some electrical discoveries made by its use*. American Journal of Science, 1883. **26**(156): p. 465-472.
9. Chapin, D.M., C.S. Fuller, and G.L. Pearson, *A New Silicon p-n Junction Photocell for Converting Solar Radiation into Electrical Power*. Journal of Applied Physics, 1954. **25**(5): p. 676-677.
10. Shirakawa, H., et al., *Synthesis of electrically conducting organic polymers: halogen derivatives of polyacetylene, (CH)*. Journal of the Chemical Society, Chemical Communications, 1977(16): p. 578-580.
11. Tang, C.W., *Two-layer organic photovoltaic cell*. Applied Physics Letters, 1986. **48**(2): p. 183-185.
12. Zhao, W., et al., *Molecular Optimization Enables over 13% Efficiency in Organic Solar Cells*. Journal of the American Chemical Society, 2017. **139**(21): p. 7148-7151.
13. Manser, J.S., J.A. Christians, and P.V. Kamat, *Intriguing Optoelectronic Properties of Metal Halide Perovskites*. Chemical Reviews, 2016. **116**(21): p. 12956-13008.
14. Rose, G.D.P., *Fossili Novo. De Novis Quibusdam Fossilibus Quae In Montibus Uraliis Inveniuntur*. 1839.
15. Xing, G., et al., *Long-Range Balanced Electron- and Hole-Transport Lengths in Organic-Inorganic CH₃NH₃P₃*. Science, 2013. **342**(6156): p. 344-347.
16. Yin, W.-J., T. Shi, and Y. Yan, *Unique Properties of Halide Perovskites as Possible Origins of the Superior Solar Cell Performance*. Advanced Materials, 2014. **26**(27): p. 4653-4658.

17. Iqbal, M., *Chapter 3 - THE SOLAR CONSTANT AND ITS SPECTRAL DISTRIBUTION*, in *An Introduction to Solar Radiation*. 1983, Academic Press. p. 43-58.
18. Kojima, A.T., K.; Miyasaka, T.; Shirai, Y. . *Novel Photoelectrochemical Cell with Mesoscopic Electrodes Sensitized by Lead-halide Compounds (2)*. in *210th ECS Meeting*. 2006. Mexico.
19. Laboratory, N.R.E. *Best Research-Cell Efficiencies*. 2017; Available from: <https://www.nrel.gov/pv/assets/images/efficiency-chart.png>.
20. Maxwell, J.C., *A Dynamical Theory of the Electromagnetic Field*. Philosophical Transactions of the Royal Society of London, 1864. **155**: p. 459-512.
21. Einstein, A., *Über einen die Erzeugung und Verwandlung des Lichtes betreffenden heuristischen Gesichtspunkt*. Annalen der Physik, 1905. **322**(6): p. 132-148.
22. Becquerel, E., *Mémoire sur les effets électriques produits sous l'influence des rayons solaires*. Comptes Rendus, 1839. **9**: p. 561-567.
23. Kittel, *Introduction To Solid State Physics, 7th Ed.*, ed. Wiley India Pvt. Limited. 2007. 688.
24. Holgate, S.A., *Understanding Solid State Physics*. 2009, United States of America: Taylor & Francis Group.
25. Paris, A.r.d.s., *Histoire de l'Academie royale des sciences*. 1788: De l'imprimerie royale.
26. S. M. Sze, K.K.N., *Physics of Semiconductor Devices*. 1981, New York: John Wiley & Sons, Inc.
27. Shah, A., et al., *Photovoltaic Technology: The Case for Thin-Film Solar Cells*. Science, 1999. **285**(5428): p. 692-698.
28. Sah, C.t., R.N. Noyce, and W. Shockley, *Carrier Generation and Recombination in P-N Junctions and P-N Junction Characteristics*. Proceedings of the IRE, 1957. **45**(9): p. 1228-1243.
29. Schwabl, F., *Advanced Quantum Mechanics*. 3th ed. 2005, The Netherlands: Springer.
30. Zimmerman, W., *Experimental verification of the Shockley--Read--Hall recombination theory in silicon*. Electronics Letters, 1973. **9**(16): p. 378-379.
31. Miles, R.W., K.M. Hynes, and I. Forbes, *Photovoltaic solar cells: An overview of state-of-the-art cell development and environmental issues*. Progress in Crystal Growth and Characterization of Materials, 2005. **51**(1): p. 1-42.
32. 2017, R.R.E.P.N.f.t.s.C., *Renewables 2017— Global Status Report*. 2017.
33. Tiedje, T., et al., *Limiting efficiency of silicon solar cells*. IEEE Transactions on Electron Devices, 1984. **31**(5): p. 711-716.
34. Brown, R.A., *Theory of transport processes in single crystal growth from the melt*. AIChE Journal, 1988. **34**(6): p. 881-911.

35. Archer, N.J., *Chemical vapour deposition*. Physics in Technology, 1979. **10**(4): p. 152.
36. Carlson, D.E. and C.R. Wronski, *Amorphous silicon solar cell*. Applied Physics Letters, 1976. **28**(11): p. 671-673.
37. Otto, M., et al., *Black Silicon Photovoltaics*. Advanced Optical Materials, 2015. **3**(2): p. 147-164.
38. Conibeer, G., et al., *Silicon nanostructures for third generation photovoltaic solar cells*. Thin Solid Films, 2006. **511-512**: p. 654-662.
39. Jia, X., et al., *All-silicon tandem solar cells: Practical limits for energy conversion and possible routes for improvement*. Journal of Applied Physics, 2016. **119**(23): p. 233102.
40. Henry, C.H., *Limiting efficiencies of ideal single and multiple energy gap terrestrial solar cells*. Journal of Applied Physics, 1980. **51**(8): p. 4494-4500.
41. *Handbook of Conducting Polymers, Second Edition*. 1998, New York, Basel: Marcel Dekker, Inc.
42. Scherf, U. and K. Müllen, *Design and Synthesis of Extended π -Systems: Monomers, Oligomers, Polymers*. Synthesis, 1992. **1992**(01/02): p. 23-38.
43. Thompson, B.C. and J.M.J. Fréchet, *Polymer–Fullerene Composite Solar Cells*. Angewandte Chemie International Edition, 2008. **47**(1): p. 58-77.
44. Heeger, A.J., *25th Anniversary Article: Bulk Heterojunction Solar Cells: Understanding the Mechanism of Operation*. Advanced Materials, 2014. **26**(1): p. 10-28.
45. Pounds, A.J., *Valency and Bonding: A Natural Bond Orbital Donor–Acceptor Perspective (Frank Weinhold and Clark Landis)*. Journal of Chemical Education, 2007. **84**(1): p. 43.
46. Bagher, A.M., *Introduction to Organic Solar Cells*. Sustainable Energy, 2014. **2**(3): p. 85-90.
47. Huheey, J.E., E.A. Keiter, and R.L. Keiter, *Inorganic Chemistry: Principles of Structure and Reactivity*. 2000: Pearson Education.
48. Zhu, X. and A. Kahn, *Electronic Structure and Dynamics at Organic Donor/Acceptor Interfaces*. MRS Bulletin, 2011. **35**(6): p. 443-448.
49. Fuchs, F., *Model Donor-Acceptor Systems for Organic Photovoltaics Investigated by Scanning Probe Microscopy*, in *Physics*. 2014, Université Grenoble Alpes: Grenoble.
50. He, Z., et al., *Enhanced power-conversion efficiency in polymer solar cells using an inverted device structure*. Nature Photonics, 2012. **6**: p. 591.
51. Chen, L.-M., et al., *Interface investigation and engineering - achieving high performance polymer photovoltaic devices*. Journal of Materials Chemistry, 2010. **20**(13): p. 2575-2598.
52. Lai, T.-H., et al., *Properties of interlayer for organic photovoltaics*. Materials Today, 2013. **16**(11): p. 424-432.

53. B., G., *Kelvin Probe Force Microscopy characterization of organic and hybrid perovskite solar*, in *Kelvin Probe Force Microscopy - From Single Charge Detection to Device Characterization*, S.a.G. Sadewasser, Th. , Editor. 2018, Springer
54. Shuttle, C.G., et al., *Charge-density-based analysis of the current–voltage response of polythiophene/fullerene photovoltaic devices*. Proceedings of the National Academy of Sciences, 2010. **107**(38): p. 16448-16452.
55. Groves, C., J.C. Blakesley, and N.C. Greenham, *Effect of Charge Trapping on Geminate Recombination and Polymer Solar Cell Performance*. Nano Letters, 2010. **10**(3): p. 1063-1069.
56. Nalwa, K.S., et al., *Dependence of recombination mechanisms and strength on processing conditions in polymer solar cells*. Applied Physics Letters, 2011. **99**(26): p. 263301.
57. Banerji, N., *Structure–Property Relations in Polymer:Fullerene Blends for Organic Solar Cells*. CHIMIA International Journal for Chemistry, 2016. **70**(7): p. 512-517.
58. Savastano, D., *OPV Market is Beginning to See Gains*. Printed Electronics Now, 2014.
59. Chen, Q., et al., *Under the spotlight: The organic–inorganic hybrid halide perovskite for optoelectronic applications*. Nano Today, 2015. **10**(3): p. 355-396.
60. Nie, W., et al., *High-efficiency solution-processed perovskite solar cells with millimeter-scale grains*. Science, 2015. **347**(6221): p. 522-525.
61. Nagaoka, H., et al., *Zr Incorporation into TiO₂ Electrodes Reduces Hysteresis and Improves Performance in Hybrid Perovskite Solar Cells while Increasing Carrier Lifetimes*. The Journal of Physical Chemistry Letters, 2015. **6**(4): p. 669-675.
62. Liu, D. and T.L. Kelly, *Perovskite solar cells with a planar heterojunction structure prepared using room-temperature solution processing techniques*. Nature Photonics, 2013. **8**: p. 133.
63. Stranks, S.D., et al., *Electron-Hole Diffusion Lengths Exceeding 1 Micrometer in an Organometal Trihalide Perovskite Absorber*. Science, 2013. **342**(6156): p. 341-344.
64. Edri, E., et al., *Elucidating the charge carrier separation and working mechanism of CH₃NH₃PbI₃–xClx perovskite solar cells*. Nature Communications, 2014. **5**: p. 3461.
65. Yang, G., et al., *Interface engineering in planar perovskite solar cells: energy level alignment, perovskite morphology control and high performance achievement*. Journal of Materials Chemistry A, 2017. **5**(4): p. 1658-1666.
66. Schulz, P., et al., *Electronic Level Alignment in Inverted Organometal Perovskite Solar Cells*. Advanced Materials Interfaces, 2015. **2**(7): p. 1400532-n/a.
67. de Quilettes, D.W., et al., *Impact of microstructure on local carrier lifetime in perovskite solar cells*. Science, 2015. **348**(6235): p. 683-686.
68. Abate, A., et al., *Supramolecular Halogen Bond Passivation of Organic–Inorganic Halide Perovskite Solar Cells*. Nano Letters, 2014. **14**(6): p. 3247-3254.

69. Shao, Y., et al., *Origin and elimination of photocurrent hysteresis by fullerene passivation in CH₃NH₃PbI₃ planar heterojunction solar cells*. Nature Communications, 2014. **5**: p. 5784.
70. deQuilettes, D.W., et al., *Photoluminescence Lifetimes Exceeding 8 μ s and Quantum Yields Exceeding 30% in Hybrid Perovskite Thin Films by Ligand Passivation*. ACS Energy Letters, 2016. **1**(2): p. 438-444.
71. Kiermasch, D., et al., *Improved charge carrier lifetime in planar perovskite solar cells by bromine doping*. Scientific Reports, 2016. **6**: p. 39333.
72. Uratani, H. and K. Yamashita, *Charge Carrier Trapping at Surface Defects of Perovskite Solar Cell Absorbers: A First-Principles Study*. The Journal of Physical Chemistry Letters, 2017. **8**(4): p. 742-746.
73. Gottesman, R. and A. Zaban, *Perovskites for Photovoltaics in the Spotlight: Photoinduced Physical Changes and Their Implications*. Accounts of Chemical Research, 2016. **49**(2): p. 320-329.
74. Zhang, T., et al., *Understanding the relationship between ion migration and the anomalous hysteresis in high-efficiency perovskite solar cells: A fresh perspective from halide substitution*. Nano Energy, 2016. **26**: p. 620-630.
75. Azpiroz, J.M., et al., *Defect migration in methylammonium lead iodide and its role in perovskite solar cell operation*. Energy & Environmental Science, 2015. **8**(7): p. 2118-2127.
76. van Reenen, S., M. Kemerink, and H.J. Snaith, *Modeling Anomalous Hysteresis in Perovskite Solar Cells*. The Journal of Physical Chemistry Letters, 2015. **6**(19): p. 3808-3814.
77. deQuilettes, D.W., et al., *Photo-induced halide redistribution in organic–inorganic perovskite films*. Nature Communications, 2016. **7**: p. 11683.
78. McNeill, C.R., I. Hwang, and N.C. Greenham, *Photocurrent transients in all-polymer solar cells: Trapping and detrapping effects*. Journal of Applied Physics, 2009. **106**(2): p. 024507.
79. Hanfland, R., et al., *The physical meaning of charge extraction by linearly increasing voltage transients from organic solar cells*. Applied Physics Letters, 2013. **103**(6): p. 063904.
80. Ahrenkiel, R.K. and S. Johnston, *Contactless measurement of recombination lifetime in photovoltaic materials*. Solar Energy Materials and Solar Cells, 1998. **55**(1): p. 59-73.
81. Sinton, R.A. and A. Cuevas, *Contactless determination of current–voltage characteristics and minority-carrier lifetimes in semiconductors from quasi-steady-state photoconductance data*. Applied Physics Letters, 1996. **69**(17): p. 2510-2512.
82. McMullan, D., *Scanning electron microscopy 1928–1965*. Scanning, 1995. **17**(3): p. 175-185.

-
83. Chen, J. and T. Sekiguchi, *Electron-Beam-Induced Current*, in *Compendium of Surface and Interface Analysis*, J. The Surface Science Society of, Editor. 2018, Springer Singapore: Singapore. p. 149-154.
 84. Coffey, D.C., et al., *Mapping Local Photocurrents in Polymer/Fullerene Solar Cells with Photoconductive Atomic Force Microscopy*. *Nano Letters*, 2007. **7**(3): p. 738-744.
 85. Giridharagopal, R., et al., *Submicrosecond Time Resolution Atomic Force Microscopy for Probing Nanoscale Dynamics*. *Nano Letters*, 2012. **12**(2): p. 893-898.
 86. Takihara, M., T. Takahashi, and T. Ujihara, *Minority carrier lifetime in polycrystalline silicon solar cells studied by photoassisted Kelvin probe force microscopy*. *Applied Physics Letters*, 2008. **93**(2): p. 021902.
 87. Borowik Ł., L.H., Chevalier N., Mariolle D., Renault O., *Measuring the lifetime of silicon nanocrystal solar cell photo-carriers by using Kelvin probe force microscopy and x-ray photoelectron spectroscopy*. *Nanotechnology*, 2014. **25**(26): p. 265703.
 88. Shao, G., et al., *Intensity-Modulated Scanning Kelvin Probe Microscopy for Probing Recombination in Organic Photovoltaics*. *ACS Nano*, 2014. **8**(10): p. 10799-10807.
 89. Narchi, P., et al., *Nanoscale Investigation of Carrier Lifetime on the Cross Section of Epitaxial Silicon Solar Cells Using Kelvin Probe Force Microscopy*. *IEEE Journal of Photovoltaics*, 2016. **6**(6): p. 1576-1580.
 90. Berhe, T.A., et al., *Organometal halide perovskite solar cells: degradation and stability*. *Energy & Environmental Science*, 2016. **9**(2): p. 323-356.

3 | Scanning probe microscopy techniques

Content

3.1 Context.....	46
3.2 Nanotechnology	46
3.3 Atomic force microscopy.....	47
3.3.1 Contact mode	50
3.3.2 Amplitude modulation atomic force microscopy mode.....	52
3.3.3 Frequency modulation atomic force microscopy mode.....	54
3.3.4 Tip-sample interaction forces	58
3.4 Kelvin probe force microscopy.....	64
3.4.1 Amplitude modulation Kelvin probe force microscopy	68
3.4.2 Frequency modulation Kelvin probe force microscopy.....	69
3.4.3 Kelvin probe force spectroscopy	70
3.5 Calibrated work function mapping by Kelvin probe force microscopy.....	71
3.5.1 Highly oriented pyrolytic graphite: A work function reference sample?	73
3.5.2 An alternative work function calibration protocol.....	75
3.5.3 Absolute work function measurements: Comparison against theoretical values and achievable lateral resolution	81
3.6 Employed scanning probe microscopy setups	84
Conclusion	90
References.....	91

Dans ce chapitre, une description des techniques de microscopie en champ proche utilisées au cours de cette thèse est présentée, ainsi qu'une description des systèmes de microscopie à force atomique sous ultravide. Une attention particulière est accordée à la description du principe de fonctionnement de la microscopie à sonde Kelvin, et de son utilisation dans les mesures de travail de sortie à l'échelle nanométrique. Dans cet objectif, un

protocole pour l'étalonnage de travail de sortie des pointes est proposé et démontré, permettant l'acquisition de mesures du travail de sortie absolues et résolues spatialement sur des échantillons nanostructurés, ouvrant ainsi la voie à son application dans la caractérisation de différentes structures et dispositifs électroniques.

3.1 Context

Scanning probe microscopy (SPM) techniques can probe functional photovoltaic materials and solar cell devices at the nanoscale under operation conditions, therefore they are ideally suited to characterize how the local structure and the electronic heterogeneity can impact performances in these materials and devices.

In this chapter, a summarized description of the scanning probe microscopy techniques employed during the course of this thesis will be given, as well as a description of the used ultra-high vacuum (UHV) atomic force microscopy (AFM) systems. Here, special attention is given to the description of the basics behind the functioning of Kelvin probe force microscopy (KPFM) and its use in work function (WF) investigations at the nanometre scale. In this sense, a protocol for the WF calibration of AFM cantilever tips is proposed and demonstrated, enabling the acquisition of spatially resolved absolute WF measurements over nanostructured samples by KPFM, paving the way for its application in the characterization of different electronic structures and devices.

3.2 Nanotechnology

The study of matter and structures at the nanometre scale has gained an enormous importance over the past decades thanks to the large range of applications that this emerging field of research can offer. In fact, some applications promise to change our daily life. Indeed, from cancer-fighting nano-robots[1] to harvesting solar energy with third-generation nanostructured photovoltaic devices[2], nanotechnology is already modifying the way we live.

Arguably, it can be stated that nanotechnology has its origin back in the late 1950s when Richard Feynman gave his famous lecture "There's Plenty of Room at the Bottom," at an American Physical Society meeting at Caltech in Pasadena, California.[3] In that occasion, Feynman raised the attention on the idea of miniaturization and it is often claimed that his talk provided inspiration for what eventually would become the field of nanotechnology.

However, it was not until 1981 with the invention of the scanning tunnelling microscope (STM)[4] when the door to the nano-world was first opened and the field of scanning probe microscopy was born. Indeed, the invention of the STM represented a major breakthrough in surface and nanoscience as it enabled for the first time, the investigation and manipulation of matter on an atomic scale. In short, STM relies on electrons tunnelling through the vacuum between a conducting tip and the surface to be examined. Since the resulting tunnelling current depends on tip position, applied voltage, and the local density of states of the sample, information about the surface of the sample can be acquired by monitoring the current as the tip scans across the surface.

Nonetheless, a disadvantage of STM is the need for conducting samples as the technique is based on the concept of quantum tunnelling.[5] At the same time, early STM experiments revealed that significant forces can act between tip and sample in addition to the tunnelling current.[6] This finding led Binnig, Quate and Gerber in 1986 to use these forces to map the tip-sample interaction, therefore creating what would later become the atomic force microscope.[7]

3.3 Atomic force microscopy

Atomic force microscopy probes the mechanic interactions that exist between a flexible AFM cantilever with tip and a conducting, semiconducting or insulating surface under investigation.[7] The cantilever tip probes the tip-sample interaction forces and thereby traces the topographic contours. These interaction forces can be of electrostatic, magnetic, chemical, capillary, adhesive and/or of van der Waals type.[8] Indeed, using AFM, it is possible to

distinguish a sample based on its morphological properties. For instance, as it will be described in detail in a further part of this chapter, in its static mode, AFM is a technique where the cantilever tip is in contact with the surface of the sample at a constant force while scanning it. In this case, the topographic information from the sample arises from the deflection of the cantilever due to the sample surface roughness. On the other hand, in its dynamical modes, AFM relies on the oscillation of the cantilever close to the sample surface and in the specific case of intermittent contact mode this includes and intermittent tip-sample contact during the cantilever oscillation. In any case, the interaction of the cantilever tip with the above mentioned forces modifies the cantilever oscillation movement. In fact, this change in the oscillation, carries the information used to image the surface of the sample.

In both static and dynamical modes, the deflection and movement of the cantilever is measured by optical techniques, while the tip-sample distance and the relative horizontal displacement is controlled using piezoelectric ceramics as they are a type of material that expand or contract in the presence of a voltage gradient. Here, we will not discuss the case of Qplus AFM[9], where the force sensor is based on a piezoelectric quartz resonator

AFM can reach a lateral resolution of the order of a fraction of a nanometre[10], (around 1000 times better than the optical diffraction limit) nevertheless, the topographic resolution depends on the tip's characteristics, such as its shape and apex diameter, as well as on the environment (vacuum, liquid or air) and also on the operation mode that as mentioned before can be either static (contact mode) or dynamical (non-contact and intermittent contact).

Usually, in beam-deflection AFM, the cantilever tip is a sharp 3-15 μm tall pyramid with 5-50 nm apexes radius as depicted in Figure 3.1.[11] In most cases, silicon cantilevers are used with their specific spring constant (k), resonance frequency (f_0) and quality factor of the vibrating cantilever (Q), which indicates the rate of energy loss due to dissipation (*i.e.*, relative to the stored energy in the cantilever oscillation).[12] In fact, this last parameter is a very important value in dynamical mode AFM and it will be discussed in a further section of this chapter.

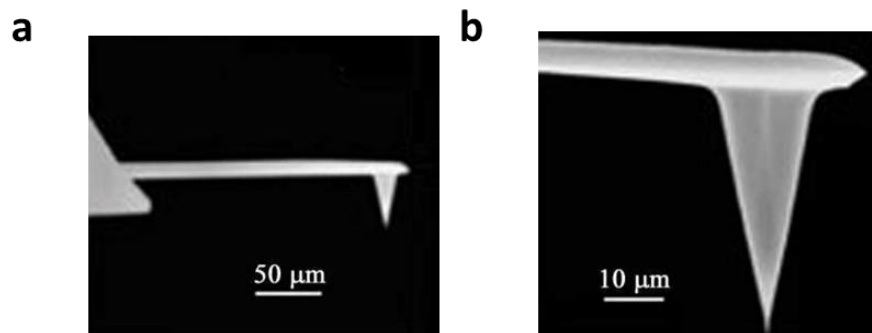


Figure 3.1– (a) Scanning electron microscopy image of an AFM cantilever. (b) Zoomed image of the cantilever tip. Images from both panels were reproduced from Ref. [11]

As mentioned before, the deflection and movement of the cantilever is measured by optical techniques. In fact, nowadays the most common detection system is the beam deflection system introduced by Meyer et al. in 1988.[13] As depicted in Figure 3.2, it consists of the reflection of a laser beam by the cantilever which is collected by a four quadrant photo-sensitive diode (PSD). Both the deflection and the movement of the cantilever can be estimated from the flux of light reaching the quadrants of the photodiode.

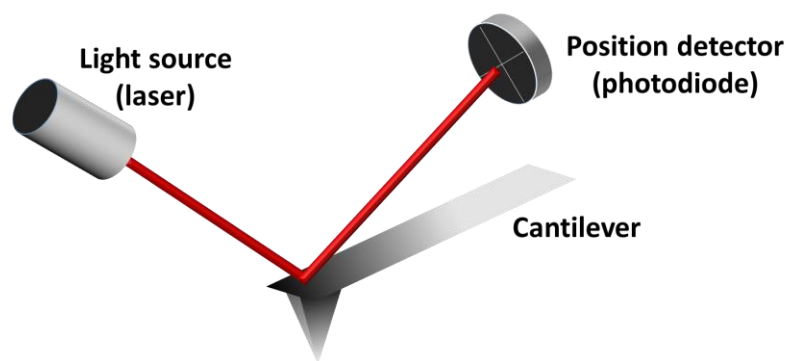


Figure 3.2– Schematics of an optical-beam AFM cantilever deflection system with a four quadrant photo-sensitive diode.

As stated above, AFM imaging can be implemented in different modes. In the following, these modes will be discussed, paying particular attention to dynamical non-contact mode, which was the employed mode for the investigations presented in this thesis.

3.3.1 Contact mode

For non-specialist readers, contact mode AFM can be think of as a vinyl record being played (see Figure 3.3b). In this example, the needle (analogous to the cantilever tip) follows the topographic contour of the record (analogous to the sample surface) which is translated into sound (instead of being translated into an image). Indeed, in contact mode operation, the AFM tip continuously touches the sample surface, and the tip–sample interaction forces deflect the cantilever.[14] The cantilever deflection is monitored and used as a feedback signal as depicted in Figure 3.3a. In other words, topographic information is directly obtained via the static cantilever deflection, which is proportional to the tip-sample interaction forces.

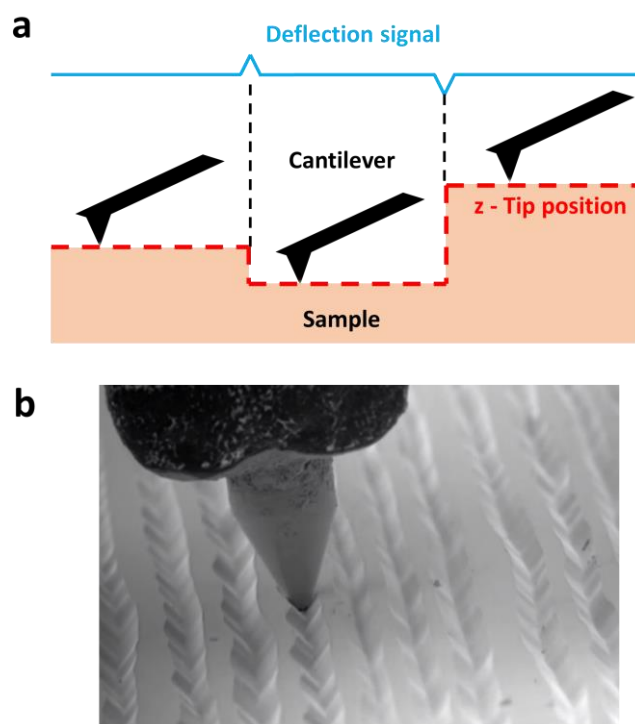


Figure 3.3– (a) Contact AFM operation mode depiction. (b) Phonograph needle running through the grooves of a vinyl record under an electron microscope. Image in panel (b) was taken by Ben Krasnow and extracted from Ref. [15]

In this mode, the contact force between tip and sample is usually around 10^{-10} N, [11] here, this force F is related to the cantilever deflection by Hooke’s law:

$$F = kz \quad (3.1)$$

where k is the cantilever spring constant and z the deflection of the cantilever.

In some cases, low interaction forces are required (*i.e.*, in the case of fragile samples), therefore, soft cantilevers ($k \sim 0.01$ N/m) are often used in order to produce substantial deflections without the need to increase the applied force.[11] At this point we highlight that this deflection can be either negative or positive depending on the attractive or repulsive character of the interaction.

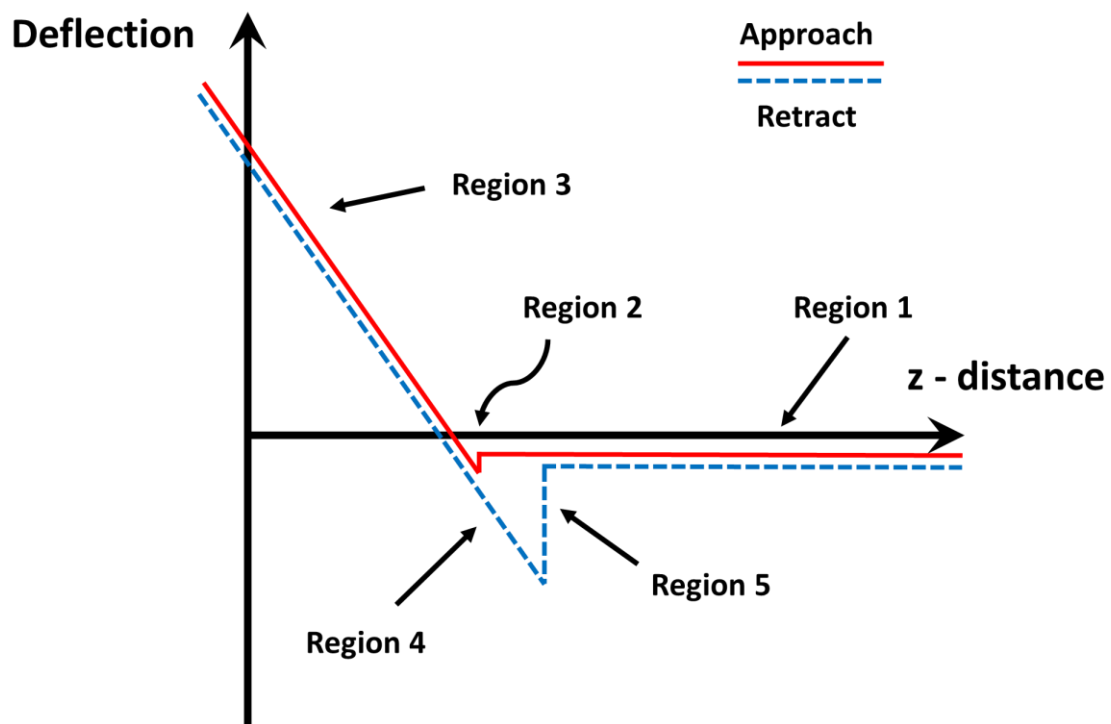


Figure 3.4– Approach-retract curve (force curve). According to Ref. [16]

In Figure 3.4, the so-called force curve depicts five different regions that appear as a function of the cantilever tip vertical displacement (z). First, region 1 illustrates a null interaction between tip and sample when the tip is far from the surface. In region 2 the tip experiences a jump-to-contact with the surface. Region 3 shows the cantilever positive deflection as the tip is repelled by the sample surface. Subsequently, when the tip is retracted

from the surface, attractive forces (adhesion or capillary) cause a region of negative deflection to appear as marked by region 4, followed by a null tip-sample interaction when the tip is finally separated from the surface as shown by region 5.

This mode is used for example, when performing electrical conductivity measurements by conducting AFM (c-AFM) or electrical resistance measurements by scanning spreading resistance microscopy (SSRM) where an intimate tip-sample contact is needed. Moreover, contact mode AFM is also used to electrically charge nanostructures and in nanostructures thermic resistance investigations.[11]

However, in contact mode AFM, the rather large contact area between tip and sample, prevents to easily obtain atomic resolution images.[17] Furthermore, the sample surface can potentially be modified by the tip (just as sometimes occurs to vinyl records).

To overcome these drawbacks, dynamic mode AFM was developed. As mentioned before, in this mode, a mechanical excitation is applied to the cantilever. Due to the interaction forces between tip and sample, this oscillation is modified. In fact, it is this change in the cantilever oscillation what is used to image the surface of the sample under investigation. There are basically two existing dynamic modes: amplitude modulation (AM) and frequency modulation (FM) mode.

3.3.2 Amplitude modulation atomic force microscopy mode

In AM-AFM mode, a mechanical excitation is applied to the cantilever at its resonance frequency f_0 with a typical amplitude of a few tens of nanometres in the case of air conditions.[14] Upon variations in the average tip-sample separation, and therefore changes in the tip-sample interaction forces, the amplitude of the cantilever's oscillation is modified. The amplitude change is measured and used as feedback signal in order to keep the tip-sample average distance at a fixed set-point. In that way, the cantilever follows the sample's topographic contours and the surface can be imaged as depicted in Figure 3.5. This mode is sometimes called tapping mode or intermittent contact mode since usually at the lowest point

of the cantilever oscillation movement, there is a physical contact between the cantilever tip and the sample.

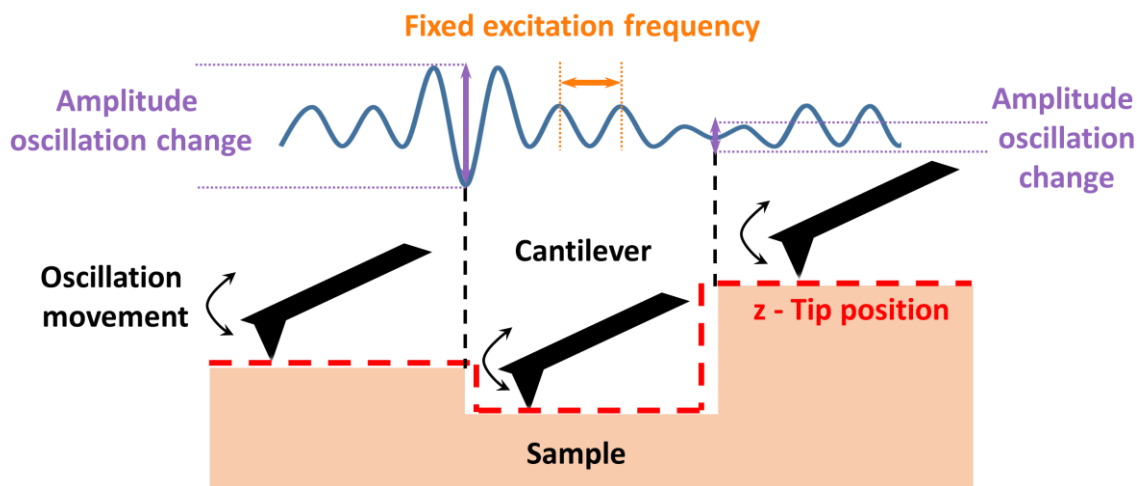


Figure 3.5– AFM amplitude modulation operation mode depiction. In this mode, for most setup conditions, the cantilever tip touches the sample at the lowest point of its oscillation movement (intermittent contact).

Here, the oscillation amplitude is used as feedback signal to maintain an average constant tip-sample distance.

As previously mentioned, a very important parameter in dynamic mode AFM is the quality factor Q of the vibrating cantilever which strongly influences the imaging resolution [12, 18] and defines the bandwidth of the cantilever resonance relative to f_0 :

$$Q = \frac{f_0}{FWHM} \quad (3.2)$$

where, FWHM is the full width at half maxima of the cantilever resonance with respect to f_0 .

Q depends on the environmental conditions of the experiment. Indeed, under air, it can typically reach values of several hundreds, while in UHV conditions it can typically reach values of few ten thousands. If we take this into account, along with the time scale of an amplitude change in AM-mode ($\tau_{AM} \approx 2Q/f_0$) [17] which exhibits a linear dependence with Q , we soon realize that measurements via AM-AFM in UHV conditions are extremely slow. In

fact, this is the reason why AM-mode is an unsuitable technique for UHV conditions. In turn, the majority of the experiments in air or liquid are often performed in AM-mode.[11]

Finally, from an analytical description based on the harmonic oscillator model it can be proved that the tip-sample interaction forces are directly related to the change in the oscillation amplitude of the cantilever. Meaning that in AM-AFM, the force between tip and sample is directly measured.[6, 12]

3.3.3 Frequency modulation atomic force microscopy mode

If in AM-AFM mode, the cantilever oscillation frequency fluctuates around f_0 and the oscillation amplitude changes carry the information about the sample surface, in FM-AFM (also called non-contact mode), the oscillation amplitude is maintained at a fixed set point and the oscillation frequency is used as feedback signal to regulate the average tip-sample distance.[19] Indeed, in FM-AFM upon changes in the tip-sample distance, and thus changes in the tip-sample interaction, the cantilever's resonance frequency is shifted as depicted in Figure 3.6.

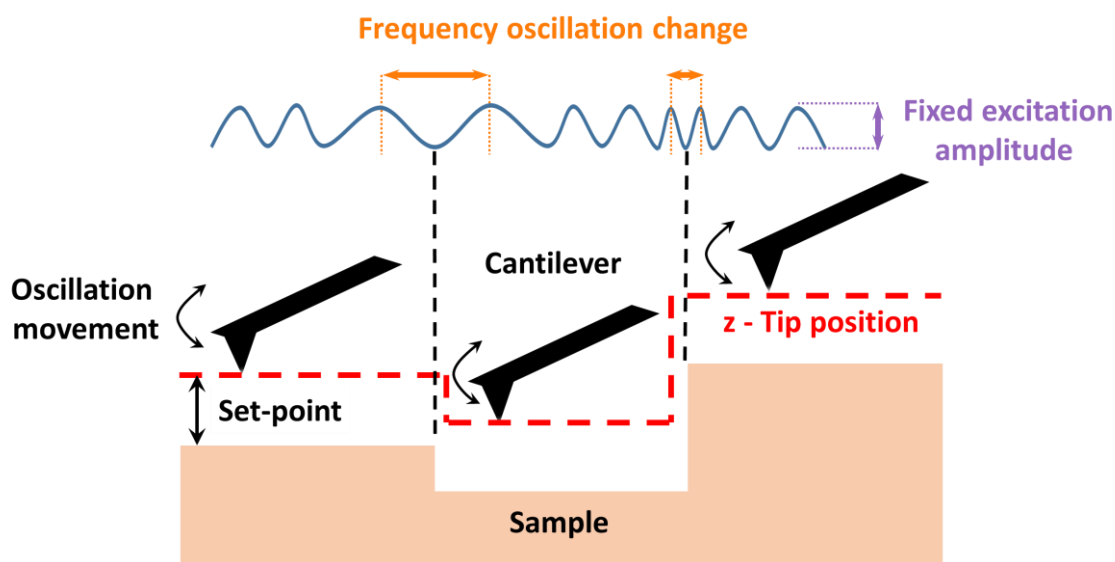


Figure 3.6– AFM frequency modulation operation mode depiction. In this mode, the oscillation frequency is used as feedback signal to maintain an average constant tip-sample distance

As it will be described below, the shift in the oscillation frequency of the cantilever depends on the force gradient between tip and sample. This means that as opposed to AM-AFM mode, in FM-AFM the force gradient between tip and sample is measured, rather than the force itself. As a consequence of this, for most samples the implementation of FM-AFM mode offers an increased spatial resolution compared to AM-AFM mode. [12, 19]

Once more, at this point, we make reference to Q , as in the case of FM-mode, the expression for the minimum detectable frequency shift in FM-mode is given by:

$$\delta(\Delta f)_{min} = \sqrt{\frac{f_0 k_B T B}{4\pi k Q \langle z_{osc}^2 \rangle}} \quad (3.3)$$

where, $k_B T$ denotes de thermal energy, B the measurement bandwidth and $\langle z_{osc}^2 \rangle$ the mean square amplitude of the driven cantilever oscillation.

Indeed, in Eq. 3.3 the impact of Q is directly visualized. [12, 18] Evidently, the measurement sensitivity increases with Q . This renders the FM-mode operation in UHF particularly advantageous. Particularly when we take into account that the time scale of a frequency change in FM-mode is independent of Q ($\tau_{FM} \approx 1/f_0$).[17]

From a theoretical point of view, in dynamic AFM modes, the mechanical excitation applied to the cantilever can be described by the following expression:

$$F = F_0 \cos(\omega t) \quad (3.4)$$

where, ω is angular frequency and t is time.

This excitation applied to the cantilever far away from the surface of the sample results in a motion that can be expressed as:[11, 12, 20, 21]

$$m_c \ddot{z} + \alpha \dot{z} + kz = F_0 \cos(\omega t) \quad (3.5)$$

where, m_c is the mass of the cantilever and both α and k , are constants.

If we divide Eq. 3.5 by m_c and we apply the following variable substitutions $\beta = \alpha/m_c$; $w_0^2 = k/m$ and $B = F_0/m_c$ the following expression is obtained:

$$\ddot{z} + \beta\dot{z} + w_0^2 z = B \cos(\omega t) \quad (3.6)$$

Here, β depends on the fluid damping of the oscillator and w_0 is the cantilever resonance angular frequency.

Solving Eq. 3.6 yields:

$$z(t) = A(\omega) \cos[\omega t - \phi(\omega)] \quad (3.7)$$

where:

$$A(\omega) = \frac{B}{\sqrt{(w_0^2 - \omega^2)^2 + \beta^2 \omega^2}} \quad (3.8)$$

$$\phi(\omega) = \tan^{-1} \frac{\beta \omega}{w_0^2 - \omega^2} \quad (3.9)$$

Here, $A(\omega)$ represents the cantilever oscillation amplitude and $\phi(\omega)$ the phase shift between the cantilever oscillation and its excitation. At this point, Q can now be defined as the ratio between w_0 and β . [11]

If the cantilever is now brought in close approach to the sample surface, different tip-sample interaction forces F_{int} occur and an additional term has to be added to the system's motion equation (Eq. 3.5), yielding:[11, 12, 20]

$$m_c \ddot{z} + \alpha \dot{z} + kz = F_0 \cos(\omega t) + F_{int}(z, t) \quad (3.10)$$

Since the different tip-sample interaction forces are not linearly dependent on the tip-sample separation, F_{int} adds a nonlinear z -dependent component to the differential equation. Therefore, Eq. 3.10 cannot be analytically solved without making some approximations.[20]

Nonetheless, for minor amplitudes and moderated force gradients, the interaction forces can be linearized and it is possible to establish the following relation:[18, 22]

$$\frac{\Delta f}{f_0} = -\frac{1}{2k} \frac{\partial F_{int}}{\partial z} \quad (3.11)$$

This relation applies in the case where the oscillation amplitude lies in the linear force field between tip and sample (oscillation amplitudes of 20-100 pm). However, in the case of most cantilever-based AFM systems, the oscillations amplitudes are normally larger than 1 nm. In other words, the tip probes a significant part of the nonlinear force-field and $\partial F_{int}/\partial z$ is not constant over one cantilever oscillation cycle.

For this reason, F. Giessibl introduced an approach via canonical perturbation theory. This approach results in:[22, 23]

$$\frac{\Delta f}{f_0} kA = \int_0^{2\pi} \frac{d\phi}{2\pi} F_{int}(\bar{z} + A \cos \phi) \cos \phi \quad (3.12)$$

Here, the integral defines the integration over one cantilever oscillation cycle. Quantities on the left side of the expression can be experimentally determined and compared to the integrated force.[23] Inversed versions of Eq. 3.12 ($F_{int}[\Delta f]$) have been developed by others.[24, 25]

Figure 3.7 depicts a simplified scheme of the FM-AFM functioning system. The deflection signal coming from the photodiode is pre-amplified and passed through a bandpass filter. Then, the automatic gain control measures the amplitude and compares it to the previously defined set-point. Subsequently, it adapts the excitation amplitude of the cantilever actuator accordingly. This means that the energy lost via dissipation effects (damping) is restored by the automatic gain control. At the same time, a phase-locked loop (PLL), measures the frequency shift Δf coming out from the bandpass filter and adapts the cantilever z -position to maintain the demanded frequency shift set-point. It also ensures that the cantilever is oscillating at its resonance frequency by means of a phase shifter. Finally, the sample topographic information can be obtained from the z -feedback circuit. Concerning the Δf signal, a topographic map of constant Δf shall be considered an indicative of a correctly parametrized regulation feedback.

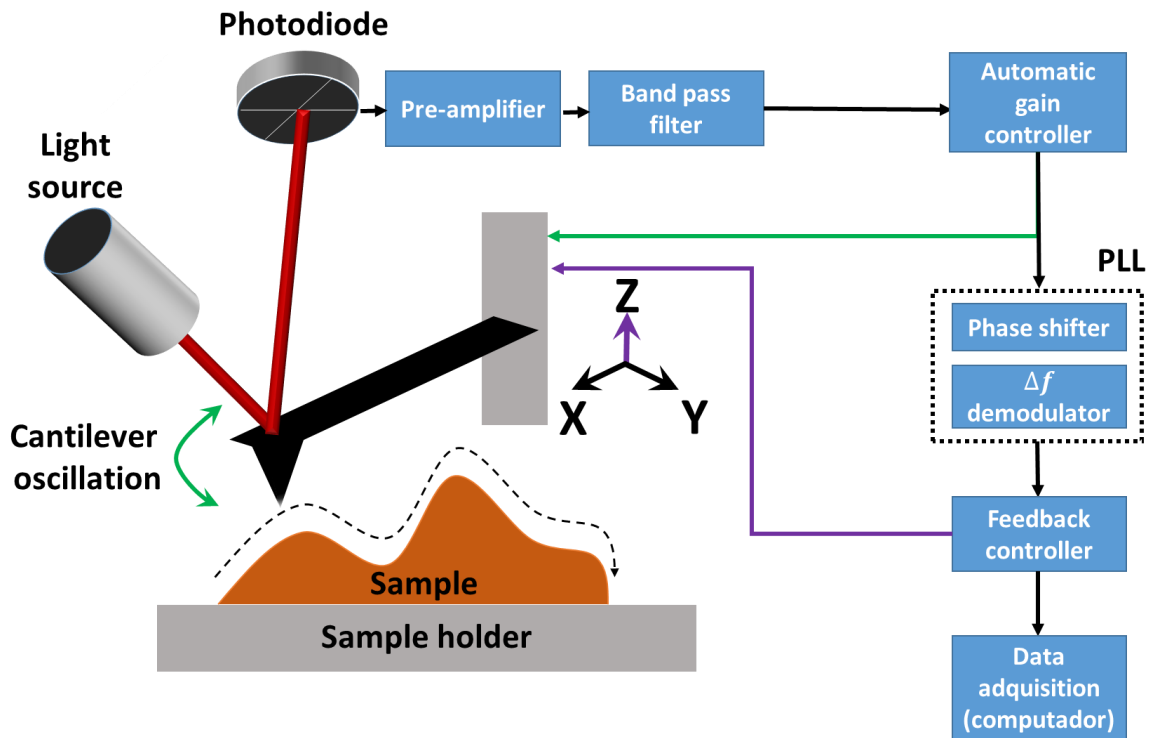


Figure 3.7–FM-AFM simplified functioning system scheme according to Ref. [21].

So far in this chapter, we introduced the existence of different interaction forces between the cantilever tip and the surface of the sample. In fact, the whole AFM operating principle is based on this. We discussed how depending on the AFM operation mode, these forces can either modify the cantilever bending upon tip-sample contact, or modify the oscillation movement of the cantilever in the vicinity of the sample. We also mentioned that these forces can be short range or long range forces. Hereafter, to grasp a better understanding on the nature and origin of these interaction forces, a brief description of the most relevant ones under UHV conditions will be given.

3.3.4 Tip-sample interaction forces

In UHV conditions, the total interaction force F_{int} generally consist in the superposition of long-range electrostatic forces F_{el} and van der Waals forces F_{vdW} as well as the addition of

different short-range forces F_{SR} such as chemical forces and some short-ranges electrostatic forces:[25]

$$F_{int} = F_{el} + F_{vdW} + F_{SR} \quad (3.13)$$

While there exist other interaction forces between tip and sample, such as magnetic forces or capillary forces, they will not be considered as these forces have a stronger influence when measuring in liquid environment and all measurements taken during this thesis were acquired under UHV conditions.

Figure 3.8 depicts F_{int} as a function of z . In this figure, attractive forces have a negative sign and shift downwards the force curve, on the contrary, repulsive force contributions present a positive sign and shift upwards the force curve.

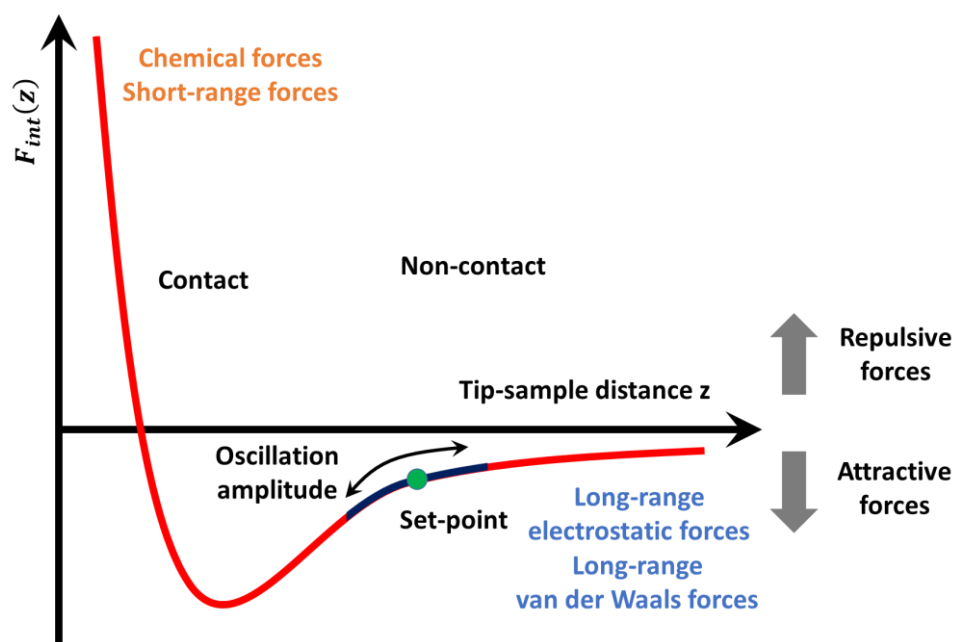


Figure 3.8– Total tip-sample interaction force F_{int} over tip-sample distance z , according to Ref. [17]

As it can be observed from Figure 3.8, the cantilever tip probes a certain part of the force curve around the set-point. The long-range electrostatic and van der Waals forces dominate the tip-sample interactions at increased tip-sample distances, while for small tip-

sample distances, chemical and other short-range forces dominate the interaction. Typically, for tip-sample distances over 1 nm, the long-range forces dominate the interaction while the short-range forces dominate the interaction when tip-sample distance is on the order of several ångströms. In the particular case of FM-mode, the cantilever tip usually passes through both long-range and short-range forces regimes which results in an averaging of the different force contributions.

In the following, the frequency shift Δf experienced by the cantilever oscillation in FM-mode is described in terms of the different components forces that the cantilever tip probes.

Given the superposition of different forces that contribute to the total interaction force between the tip and sample (see Eq. 3.13), one can express the total frequency shift of the cantilever oscillation as following:[23]

$$\Delta f = \Delta f_{el} + \Delta f_{vdW} + \Delta f_{SR} \quad (3.14)$$

where each of the above mentioned forces contribute separately to the total frequency shift experience by the cantilever tip.

An analytical model for each force contribution will be given in the following.

3.3.4.1 Electrostatic forces

If both the tip and sample are conductive or semi-conductive and there exists a non-zero potential difference between them, long-range electrostatic forces will appear. To model this situation we will describe the tip-sample system as a capacitor with a capacitance C which depends on the distance z between tip and sample.[6] Knowing that the electric energy of a capacitor is defined by:

$$W_{el} = \frac{1}{2} C V_{eff}^2 \quad (3.15)$$

where, V_{eff}^2 denotes the effective tip-sample potential difference.

Additionally, knowing that in a capacitor, when the electrodes lie at fixed potential values, the electrostatic force is given by the positive gradient of W_{el} , we can define the electrostatic force $F_{el}(z)$ between the tip and sample in the following way:[20]

$$F_{el}(z) = \frac{\partial W_{el}(z)}{\partial z} \quad (3.16)$$

Additionally, if we consider V_{eff} to be the bias difference V_{DC} applied between tip and sample, minus the contact potential difference (CPD), defined here as the difference between tip Φ_{tip} and sample Φ_{sample} work functions divided by the elementary charge $|e|$, we get:

$$V_{eff}^2 = \left(V_{DC} - \left(\frac{\Phi_{tip} - \Phi_{sample}}{|e|} \right) \right)^2 \quad (3.17)$$

Substituting Eq. 3.17 into Eq. 3.15 and the latter into Eq. 3.16, yields:[20]

$$F_{el}(z) = \frac{1}{2} \frac{\partial C(z)}{\partial z} \left(V_{DC} - \left(\frac{\Phi_{tip} - \Phi_{sample}}{|e|} \right) \right)^2 \quad (3.18)$$

Since the capacitance decreases with the tip-sample distance, the gradient $\partial C(z)/\partial z$ shall always be of negative sign. Therefore, $F_{el}(z)$ is negative and the capacitive force is always attractive. As we will see further in this chapter when discussing Kelvin probe force microscopy in detail, the electrostatic force $F_{el}(z)$ can be nullified by applying a static voltage bias that compensate the CPD as it can be observed from Eq. 3.18.

To quantify the typical electrostatic force magnitude in a common tip-sample system, we can think of the tip as a sphere with radius R being located at a distance z above an infinitely large sample plane.[6] When the tip is brought close to the sample ($z \ll R$) the electrostatic force $F_{el}(z)$ can be described in the following way:[26, 27]

$$F_{el}(z) = -\pi\epsilon_0 \left(\frac{R^2}{z(z-R)} \right) \left(V_{DC} - \left(\frac{\Phi_{tip} - \Phi_{sample}}{|e|} \right) \right)^2 \approx -\pi\epsilon_0 \frac{R}{z} (V_{DC} - CPD)^2 \quad (3.19)$$

where ϵ_0 is the vacuum permittivity.

Assuming typical values of $R = 50 \text{ nm}$, $z = 0.5 \text{ nm}$ and $(V_{DC} - CPD) = 1 \text{ V}$ we get a $F_{el} \sim -1 \text{ nN}$.

Furthermore, from the simplified model presented in Eq. 3.19, an expression for the electrostatic frequency shift contribution Δf_{el} was derived by Guggisberg *et al.*: [23]

$$\frac{\Delta f_{el}}{f_0} kA = -\frac{\pi \epsilon_0 R}{\sqrt{2zA}} (V_{DC} - CPD)^2 \quad (3.20)$$

Eq. 3.20 reveals that Δf_{el} depends on V_{eff}^2 and decays with $1/\sqrt{z}$.

3.3.4.2 Van der Waals forces

Molecules can attract each other at moderate distances (1-10 nm). These attractive forces are collectively called van der Waals forces. These forces are much weaker than chemical bonds, and random thermal motion around room temperature can usually overcome or disrupt them. Van der Waals forces include all intermolecular forces that act between electrically neutral molecules. Van der Waals interactions are caused by variations in the local electric dipole moment of an atom or a molecule and their mutual polarization. [6]

Analogously to the case of the electrostatic forces, the following expression defines the van der Waals tip-sample interaction energy for the same simplified tip-sample system previously described: [28]

$$E_{vdW}(z) = -\frac{HR}{6(z-R)} \quad (3.21)$$

where, R denotes again the cantilever tip radius and corresponds to the material specific Hamaker constant which depends on tip and sample materials type. For most solids, this constant lies around 1 eV. [11]

Knowing that the van der Waals force F_{vdW} corresponds to the gradient of the interaction energy (Eq. 3.21) for tip-sample distances greatly inferior to the cantilever tip radius ($z \ll R$), we obtain:

$$F_{vdW} = -\frac{HR}{6(z-R)^2} \quad (3.22)$$

Using Eq. 3.22 one can determine that for the same typical values used in the precedent example and assuming $H = 1 \text{ eV}$, the van der Waals force lies around -10 nN . This means that F_{vdW} can potentially influence topographic measurements performed in nc-AFM as demonstrated by F. Fuchs.[17]

Finally, as in the case of F_{el} the frequency shift caused by the van der Waals interaction can be defined as:[23]

$$\frac{\Delta f_{vdW}}{f_0} kA = -\frac{HR}{12\sqrt{2}A\bar{z}^{3/2}} \quad (3.23)$$

Eq. 3.23 reveals that Δf_{el} decays with $1/\sqrt{z^3}$.

3.3.4.3 Short-range forces

These interactions occur at small tip-sample distance where the electron wave functions of the tip and sample overlap, they can be both attractive and repulsive forces.[6]

Indeed, when the tip is brought very close to the sample surface (1-2 Ångströms) a strong repulsion force appears, this occurs when occupied electrons orbitals overlap. In fact, this is described by the Pauli exclusion principle which states that two identical fermions cannot occupy the same quantum state. At the same time an attractive force can appear between two atoms that are capable of developing a mutual chemical bond.

These short-range forces can be described via empirical interaction-energy models such as the Morse potential:[23]

$$E_{Morse} = -E_{bond} \left[2e^{\left(-\frac{(z-z_0)}{k}\right)} - e^{\left(-2\frac{(z-z_0)}{k}\right)} \right] \quad (3.24)$$

here, E_{bond} is the bonding energy, k the decay length and z_0 the equilibrium distance two atoms.

This model describes the potential energy of two atoms in close approach. In Eq. 3.24 we find two terms, the first one is an attractive term which represents the result of chemical bond formation. The second one is a repulsive term which describes the Pauli exclusion principle.

There is also another very common model to describe these interaction energies, the Lennard-Jones potential:[29]

$$E_{LJ} = -E_{bond} \left[2 \left(\frac{z_0}{z} \right)^6 - \left(\frac{z_0}{z} \right)^{12} \right] \quad (3.25)$$

This model also describes two terms, a repulsive and an attractive one. Having described the Lennard-Jones potential model, we now go back to the Morse potential model, as it predicts the short-range force F_{SR} to be of the form:

$$F_{SR} = -\frac{2E_{bond}}{k} \left[e^{\left(-\frac{(z-z_0)}{k} \right)} - e^{\left(-2\frac{(z-z_0)}{k} \right)} \right] \quad (3.26)$$

From Eq. 3.26 we can observe that F_{SR} decays exponentially with the tip-sample distance. Moreover, to describe the frequency shift contribution due to short-range forces Δf_{SR} , we can in an approximatively way, ignore the term describing the repulsive energy-interactions, as one mostly chooses a set-point in the attractive short-range regime, always avoiding the Pauli repulsion regime since it can damage the cantilever tip. Therefore, again, in an approximatively way we can describe the frequency shift contribution due to short-range forces Δf_{SR} in the following way:[23]

$$\frac{\Delta f_{SR}}{f_0} kA = -\frac{\sqrt{2}E_{bond}}{\sqrt{\pi Ak}} e^{\left(-\frac{(z-z_0)}{k} \right)} \quad (3.27)$$

3.4 Kelvin probe force microscopy

The concept behind KPFM was first introduced by Lord Kelvin in 1898 to measure the work function difference between two metallic plates.[30] Indeed, Lord Kelvin realized that when two metal plates are brought into electrical contact, a current will flow from one plate to

the other until a certain equilibrium is reached (this equilibrium is defined by the Fermi levels alignment of the plates), and a contact potential difference appears between these two plates. By this mean, the WF of a material can be measured relative to a reference material with known WF. This concept was further refined by W. A. Zisman in 1932, when he introduced an oscillating reference electrode which created an AC voltage directly related to the CPD between the two electrodes.[31] Additionally, Zisman performed measurements under vacuum conditions. Nowadays, this method is still implemented in large-scale systems with the same purposes.

Moreover, in 1991 this technique was adapted for the AFM. This adaptation was made by Nonnenmacher *et al.* when he and his colleagues figured out that the vibrating AFM cantilever could be used as a reference electrode, enabling WF measurements with the highest spatial resolution ever achieved so far. As a result KPFM was invented.[32]

At this point of the discussion it becomes very important to give a proper definition to the WF. In this sense, the definition used in this thesis is the one given by Cahen *et al.* who defined the WF of a material as the minimum energy needed to remove an electron from its electronic ground state within the material to a point in the vacuum immediately outside of the surface. In the case of a metal it is expressed analytically in the following way:[33]

$$\Phi_{metal} = E_{vacuum} - E_f \quad (3.28)$$

where, E_{vacuum} represents the vacuum level and E_f the Fermi level respectively.

Having defined what the WF of a material is, we can now introduce the KPFM working principle. In short, KPFM works by detecting the electrostatic forces between tip and sample. Then by applying a proper static compensation bias V_{DC} , these electrostatic forces are nullified, therefore V_{DC} should equal in magnitude to the CPD between tip and sample. Moreover, we already know from Eq. 3.17 that the $CPD = (\Phi_{tip} - \Phi_{sample})/|e|$. This means that KPFM allows to map the WF of a sample relative to the WF of the tip. As we will see on the following section of this chapter, when using an AFM cantilever with known work function, the sample absolute local WF can be measured.

However, simple as it might appear, we already mentioned that there are several interaction forces between tip and sample, so the question presents itself: How to distinguish F_{el} from the other force contributions? In fact, to do this, a bias modulation V_{AC} is applied additionally to the static compensation bias V_{DC} . This means that the total applied bias between tip and sample can be expressed in the following way:[34]

$$V_{bias} = V_{DC} + V_{AC} \sin(\omega t) \quad (3.29)$$

This bias modulation results in the following oscillating electrostatic force:

$$F_{el}(z) = \frac{1}{2} \frac{\partial C(z)}{\partial z} [(V_{DC} - CPD) + V_{AC} \sin(\omega t)]^2 \quad (3.30)$$

Moreover, this resulting oscillating force can be decomposed into three spectral components:[34]

$$F_{DC} = \frac{1}{2} \frac{\partial C(z)}{\partial z} [(V_{DC} - CPD)^2 + \frac{1}{2} V_{AC}^2] \quad (3.31)$$

$$F_{\omega} = \frac{\partial C(z)}{\partial z} (V_{DC} - CPD) V_{AC} \sin(\omega t) \quad (3.32)$$

$$F_{2\omega} = -\frac{\partial C(z)}{\partial z} \frac{V_{AC}^2}{4} \cos(2\omega t) \quad (3.33)$$

In this set of equations, F_{DC} represents a static component of the electrostatic force that simply adds an offset to the total tip-sample interaction force F_{int} . $F_{2\omega}$ is the second harmonic component, which can be used for the detection of the capacitance gradient.[35] Lastly, the most interesting component of the resulting electrostatic force for us at this point is F_{ω} . As it can be observed from Eq. 3.32, by adjusting V_{DC} , F_{ω} can be nullified completely. In fact, the condition that shall be fulfilled for this to occur is $V_{DC} = CPD = (\Phi_{tip} - \Phi_{sample})/|e|$.

Let us imagine that the WF of the tip is higher than that of the sample, in that case, when the tip and the sample are not electrically connected, there exist an alignment of both tip and sample vacuum levels as depicted in Figure 3.9a. Upon electrical contact, just as in the case of original Lord Kelvin's technique, there is an alignment of the tip and sample Fermi levels, and an electrical current will flow, in this example from the sample to the tip. Consequently,

electrostatic interaction forces between tip and sample will appear, as well as a CPD between tip and sample as a result of the tip induced charging which will additionally offset the vacuum energy level of the sample with respect to that of the tip as depicted in Figure 3.9b. In KPFM, by means of adjusting V_{DC} , the feedback loop tries to compensate the detected electrostatic force component F_w as depicted in Figure 3.9c. As above mentioned, this compensation, as well as the re-alignment of tip and sample's vacuum energy levels is achieved when $V_{DC} = CPD = (\Phi_{tip} - \Phi_{sample})/|e|$.

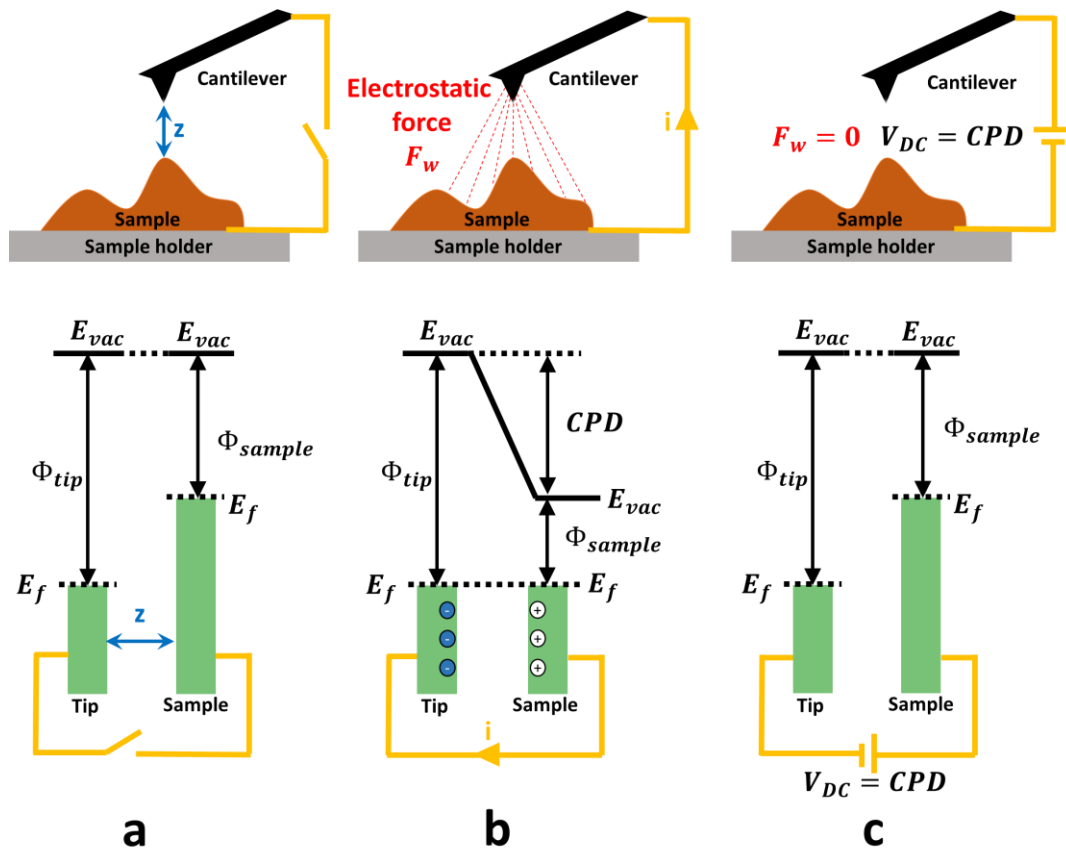


Figure 3.9– CPD measuring principle with KPFM. In the first case (a) tip and sample are depicted with their respective work functions and Fermi levels. In this condition, both sample and tip vacuum energy levels are aligned. In (b) tip and sample are electrically connected. At this point an electric current will flow until both tip and sample Fermi levels are aligned. As a result of this, a CPD will appear between tip and sample, offsetting the vacuum energy levels of the tip-sample system. In (c) the KPFM feedback loop compensated the electrostatic force F_w by making $V_{DC} = CPD$. At this point, the vacuum energy levels of both tip and sample are re-aligned.

As we have seen, the detection of the F_w component of the total electrostatic force lies at the base of the KPFM functioning. In fact, this detection can be made by two different KPFM modes. As in the case of AFM, KPFM can be implemented in AM or FM mode.[34] In the following an overview of both modes will be given.

3.4.1 Amplitude modulation Kelvin probe force microscopy

In AM-KPFM, the dynamic bias excitation V_{AC} which function is to modulate the resulting electrostatic force, is applied at a modulation frequency equal to the first harmonic f_1 of the resonance frequency f_0 of the AFM cantilever.[35] This frequency usually lies around 6.3 times the value of f_0 . Therefore, an electrostatic force F_{el} with a F_w component appears and causes a resonant oscillation at f_1 in addition to the one at f_0 which is used for the topographic AFM regulation.[20] By detecting the amplitude of the second resonance, F_w is directly obtained. Then the KPFM feedback loop adjust V_{DC} in order to suppress F_w . Consequently, the amplitude of the first harmonic resonance of the cantilever is suppressed and the CPD determined.

Although the resonance at f_1 is broader than the one at f_0 , under UHV conditions a quality factor Q_1 associated to the oscillation at f_1 on the order of 6000 can be typically achieved which is still relatively high, allowing a good spatial resolution.[21] Here, is important to mention that, as opposed to the case of AM-AFM where measurements in UHV are extremely slow, AM-KPFM can be performed in UHV without this inconvenient, as the time scale of an amplitude change in AM-KPFM ($\tau_{AM} \approx 2Q_1/f_1$) does not represent an issue due to a lower Q_1 factor in comparison to Q_0 and a frequency $f_1 \approx 6.3f_0$ which results in a characteristic time τ_{AM} of few tens of milliseconds.[21] Let us check this, taking typical values of $f_1 = 472 \text{ kHz}$ and $Q_1 = 6000$, we obtain $\tau_{AM} = 25 \text{ ms}$. Fast but faster than 10 ms, this is the reason why AM-KPFM is considered a relatively slow technique. Moreover, the implementation of this mode demands that the superior bandwidth of the photodiode cantilever oscillation detection shall be higher than f_1 .

3.4.2 Frequency modulation Kelvin probe force microscopy

In the case of FM-KPFM, V_{AC} is applied at an arbitrary low frequency w , usually laying around 1 kHz, thus inducing a modulated electrostatic force F_{el} with a F_w component which is detected by sensing the variation of the frequency shift Δf_0 at the selected frequency w , which can be expressed in the following way:[21]

$$\Delta f_0(w) \propto \frac{\partial F_w}{\partial z} = \frac{\partial^2 C}{\partial z^2} (V_{DC} - CPD) V_{AC} \sin(wt) \quad (3.34)$$

Similar to the case of AM-KPFM, in FM-KPFM a feedback loop adjust V_{DC} in order to suppress Δf_0 , thus nullifying $\partial F_w / \partial z$ and finally obtaining CPD. In this mode, while the frequency w can be chosen arbitrarily, it shall be set high enough to avoid crosstalk with the AFM topography feedback loop and low enough to be within the bandwidth of the Δf demodulator.[36]

At this point, it is important to mention that in practice, a better energy/WF resolution is often achieved using AM-KPFM mode (around 5-7 meV depending on the cantilever, with respect to 10-15 meV in FM-KPFM). This improved energetic resolution arise due to the fact that AM-KPFM measurements achieves a better signal-to-noise ratio thanks to the CPD detection via the first harmonic cantilever.[37-39]

On the other hand, in most experimental cases, a better spatial resolution is obtained via FM-KPFM as in this mode, the electrostatic force gradient of one of the F_{el} component ($\partial F_w / \partial z$) is detected instead of the electrostatic force component F_w itself.[40] Indeed, the detection of the force gradient is made via the tip apex, whereas detecting the force itself involves the whole tip and cantilever.[41] Nevertheless, we highlight the fact that in the literature, atomic CPD resolutions obtained through both techniques can be found.[36, 42]

During this thesis, both modes were implemented depending on the measurement objective. For instance, in experimental investigations where the energetic resolution was a critical matter, the AM-KPFM mode was implemented. On the other hand, when the

measurement objective was focus on achieving a high lateral resolution, FM-KPFM was privileged.

In figure 3.10 a schematic depicting both the AM- and FM-KPFM operation including feedback circuits is given. In this graph, the black circuit along with the blue boxes corresponds to the FM-AFM as introduced in a previous section of this chapter while the red circuit corresponds to the regulation system which is needed in addition for the implementation of KPFM.

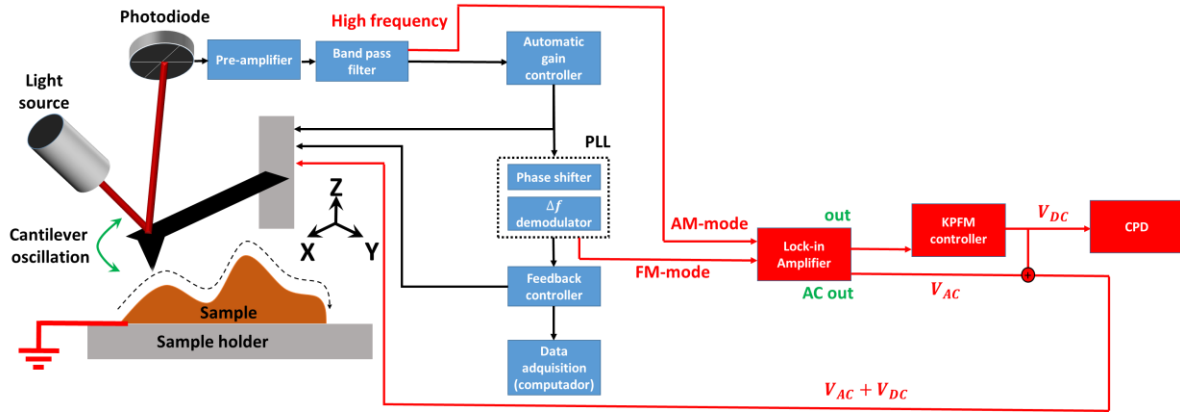


Figure 3.10– Schematic of KPFM and its feedback system. Black circuitry including blue boxes represents the schematic for FM-AFM as depicted in Figure 3.7. The red parts of the scheme represents the additional feedback loops and circuitry needed for the implementation of KPFM in both AM and FM modes. Notice that the sample has been electrically grounded.

3.4.3 Kelvin probe force spectroscopy

Alternatively, CPD measurements can also be made via the acquisition of spectroscopy curves of $\Delta f(V)$, also called frequency-shift bias spectroscopy or Kelvin probe force spectroscopy (KPFs). Indeed, by recording the evolution of the frequency shift in FM-AFM as a function of a static tip-sample bias V_{DC} , a full Kelvin parabola curve is obtained as depicted in Figure 3.11 and according to:[43, 44]

$$\Delta f(V_{dc}) \propto \frac{dF_{el}}{dz} = -\frac{1}{2} \frac{d^2C}{dz^2} (V_{dc} - CPD)^2 + \Delta f_{set-point} \quad (3.35)$$

Fitting Eq. 3.35 to the measured parabola will result in the obtainment of the CPD as well as the second derivative of the capacitance d^2C/dz^2 .

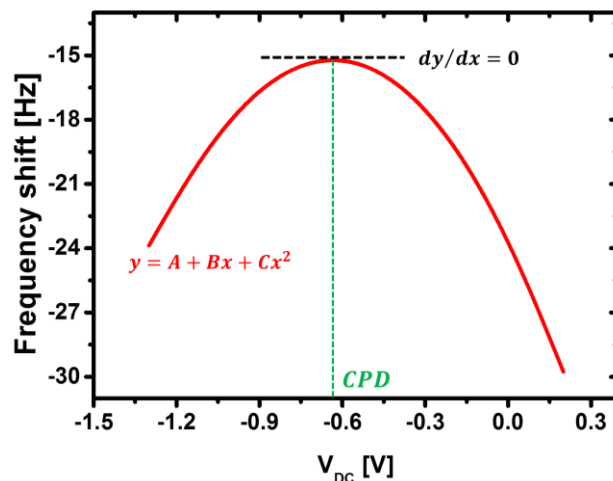


Figure 3.11– Full kelvin parabola $\Delta f(V_{DC})$ of the frequency-shift Δf as a function of a static tip-sample bias V_{DC} . Black dotted line serve as an eye guide to indicate the tangent line at the vertex of the parabola.

Green dotted line indicated the CPD value in the x-axis. This curve was acquired over a nanophase segregated PDBS-TQX/PC₇₁BM organic blend using a Bruker super sharp silicon probe with a resonance frequency of ca. 306.6 kHz and a quality factor Q of ca. 30 k.

This technique allow the acquisition of CPD maps by the repetition of this process over each point of a pre-defined grid area over the surface of the sample.[21, 45]

3.5 Calibrated work function mapping by Kelvin probe force microscopy

One of the main reasons (among several) why is interesting to measure the CPD between an AFM tip and a sample lies in that the CPD is directly linked with the WF of the sample relative to that of the tip. In fact, during this thesis, we employed a setup where the compensation bias is applied to the cantilever tip, therefore, in our case KPFM yields a CPD that can be expressed as:

$$V_{DC} = CPD = \frac{\Phi_{tip} - \Phi_{sample}}{|e|} \quad (3.38)$$

At this point, a curious reader might wonder, why so much interest on studying the WF of materials? As it turns out, the WF is a parameter of utmost importance in the description and control of any electronic device behaviour as well as charge carrier injection and transport. Moreover, due to its sensitivity to chemical variations on surfaces, its measurement can be used as a tool to investigate surfaces conditions.[46] Moreover, as briefly mentioned in **Chapter 1**, the WF has also significant importance in the fields of electroluminescence and photovoltaics, for instance it influence the band line-up at the interface between organic materials and electrodes, which is also noteworthy in the development of organic light-emitting diodes.[47]

There are several procedures used to measure the WF of a material. Among those methods, one can find methods based on thermionic emission, on photoemission and the original Kelvin probe method to name a few.[30, 48, 49] However, the majority of these approaches, lack the spatial resolution required for the nano-characterization of electronics components, not to mention nano-objects or nanostructured surfaces. An exception to this, is precisely KPFM, which as seen before, provides spatially resolved measurements of the CPD between an AFM cantilever tip and the surface of conducting and semi-conducting samples. In fact, the use of an AFM cantilever with known work function allows to measure the local absolute WF of a sample.

Indeed, the WF of an AFM cantilever tip can be calibrated against a reference surface with known WF. Highly oriented pyrolytic graphite (HOPG) is often used as this reference for several reasons such as availability, cost, low resistivity and its hydrophobic properties among others. However, HOPG WF values found in the literature are very much dispersed, ranging from a value below 4.5 eV [50-52] to as high as 5 eV, [53-56] such dispersion of WF values can potentially introduce a high uncertainty level in the cantilever tip WF calibration, compromising the WF value obtained over the surface of interest. We note that large dispersion of HOPG WF values in the literature can be found even for measurements under the same environmental conditions: under air from 4.6 eV to 5 eV [54, 55, 57-59] and in UHV conditions from 4.48 eV to 5 eV.[50, 53, 58-61] For HOPG, theory predicts a value between 4.46 eV and

4.64 eV depending on the number of layers.[62] Thus, attention must be paid when choosing the HOPG reference value. Furthermore, HOPG WF values can be quite laterally dispersed over a measured surface (up to few hundreds mV), even if measurements are acquired over micrometre areas.[63-65]

These reasons led us to propose and demonstrate an alternative AFM tip WF calibration protocol, using different monocrystalline metallic reference samples with known surface orientation as references instead of the most commonly used HOPG sample.[66] In that endeavour, we use FM-AFM combined with FM-KPFM under UHV conditions. Indeed, the use of this configuration offers several advantages. For instance, the implementation of FM-AFM prevents any physical contact between the tip and the sample, as opposed to intermittent contact mode, where the sample's surface can be modified by the tip upon physical contact and vice versa. Moreover, this configuration also allows to maintain a constant effective distance between tip and sample. Additionally, under UHV, both tip and sample can be stored without suffering any substantial surfaces modification for a time period ranging from several days to few weeks depending on sample composition.

3.5.1 Highly oriented pyrolytic graphite: A work function reference sample?

Before introducing the proposed protocol for AFM tip WF calibration, a clean mechanically under air delaminated ZYB grade HOPG sample, provided by the Bruker Company was investigated under UHV conditions by AFM combined with FM-KPFM. The intention of these measurements is to evaluate if indeed HOPG samples can potentially be used as reference samples when performing AFM tip WF calibrations, or if on the contrary the lateral dispersion of WF values even over micrometre areas impedes its use for WF calibration purposes.

For these measurements, we used a Nanosensor platinum/iridium point probe plus electrostatic force microscopy (Pt/Ir-PPP-EFM) cantilever tip, with a resonance frequency of ca. 61.2 kHz. The three-dimensional distribution of the chemical composition of this kind of

tips has already been the subject of study.[67] In addition to the measurements on the as-cleaved sample (Fig 3.12a, b), UHV annealing was performed on the same sample for different temperatures: 300°C, 600°C and 700°C, each time during 30 minutes. The annealing performed at temperatures lower than 700°C did not provide a smoothing of the sample's surface potential, even after the annealing cycles at 300°C and 600°C, the surface potential images (not shown here) displayed multiple dark and white patches and a CPD contrast as high as 60 mV. In contrast, as shown in Figures 3.12c,d the CPD of the 700°C annealed sample was uniform (with the exception of flakes edges) and it reveals a homogeneous $CPD = -260 \pm 15 \text{ mV}$ on the HOPG flakes.

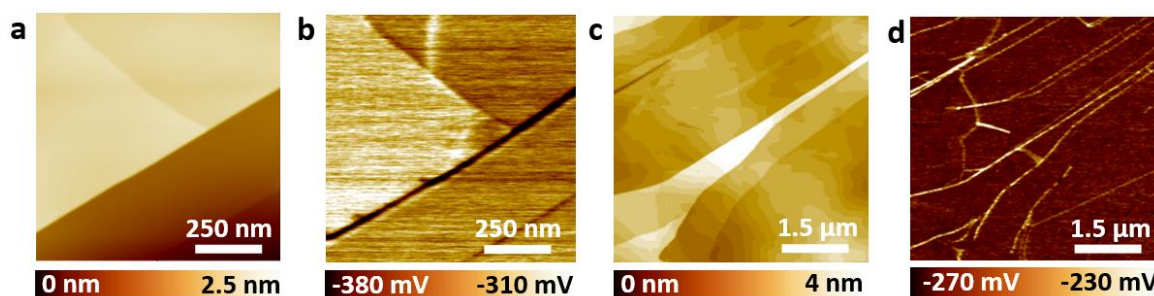


Figure 3.12– Topography (a, c) and CPD (b, d) images on HOPG by FM-KPFM. AFM detuning frequency was $\Delta f = -25 \text{ Hz}$. FM-KPFM was implemented using a modulation frequency $f = 958 \text{ Hz}$ and electrostatically excited with $V_{AC} = 500 \text{ mV}$. Sample presented on panels: (a) and (b) is as-cleaved (without annealing), while panels (c) and (d) present the sample after been annealed in UHV at 700°C during 30 min.

All panels were reproduced from Ref. [66].

This experiment proves that in the case of HOPG, a sample preparation is needed to obtain consistent WF values. Nevertheless, the different values of the HOPG WF found in the literature can lead to confusion. To dispel these doubts, in the following, three monocrystalline metallic samples with known crystallographic orientation are proposed as reference surfaces for AFM tip WF calibration. Then using the proposed protocol, the HOPG WF value will be calculated. Finally, to demonstrate the capability in terms of lateral resolution of WF absolute measurements by KPFM, the local WF variation over a nanostructured semiconductor sample presenting $\text{Al}_{0.7}\text{Ga}_{0.3}\text{As}$ and GaAs layers with variable thickness will be investigated.

3.5.2 An alternative work function calibration protocol

For this calibration protocol, three monocrystalline metallic samples with known crystallographic orientation are proposed as reference surfaces: i) Ag(111), ii) Cu(100) and iii) Al(110). All reference samples, which are commercially available, were provided by the Goodfellow Cambridge Limited Company and stored in UHV conditions during measurements. Prior to this, all samples were stored in ambient conditions. While the proposed samples are not equally adapted for WF calibration (*i.e.*, different oxidation rates, surface roughness, surface contamination, cost, etc.), the purpose of having three different metallic samples is to verify results self-consistency. Additionally, the above mentioned samples were selected following the criteria of having the maximum possible difference between their known WF values as shown in Table I.

Table I. WF values found in literature for proposed samples.

	Ag(111)[68]	Cu(100)[69]	Al(110)[70]
ϕ_{Sample}	4.74 ± 0.02 eV	4.59 eV	4.06 ± 0.03 eV

Note that values presented in Table I can largely vary from one author to another, for Ag(111)[71-78], Cu(100)[79-85] and Al(110)[86, 87]. We note that publications grouping WF values for different materials [88-91] can often be useful. WF values for proposed samples were selected upon critical examination of methods including the use of an UHV system and reduced uncertainty values although this last parameter was not always available.

Following a surface cleaning procedure which shall include both reference samples and the tip, this to ensure clean surfaces, free of contaminants that could potentially modify expected WF values, the tip is calibrated against each one of the reference samples separately. In this step, we assumed that the WF of the reference correspond to the known values presented above in Table I. [68-70, 92] Moreover, it is also assumed that the WF of the tip and the reference samples is constant over time.

With such approach, and if samples are correctly prepared, the cantilever tip absolute WF value obtained over each sample should yield approximately the same result.

To illustrate this, a Pt/Ir-PPP-EFM cantilever tip with a resonance frequency of ca. 65.7 kHz previously in-situ heated at 150°C for 20 minutes, was used to obtain CPD measurements over each reference sample. At this point, we highlight the fact that this heating step is of crucial importance to ensure the tip's WF stability over time. Indeed, by heating the cantilever tip, we removed the adsorbed water from the tip's surface which can induce strong WF variations over time. In fact, we noticed that for some cases of air exposed and non-prepared tips, WF values can change as much as 600 meV over a 24-hours' time period due to water layer modification on the tip cone.

During these measurements, topography and CPD were simultaneously acquired by FM-KPFM and FM-AFM. In all cases AFM detuning frequency was $\Delta f = -10 \text{ Hz}$. FM-KPFM was implemented using a modulation frequency $w = 1 \text{ kHz}$ and electrostatically excited with $V_{AC} = 500 \text{ mV}$. As reported previously, [93] in some cases CPD can vary as a function of tip-surface distance. In our case (metalized tip and homogeneous metal sample surfaces), we did not notice this dependency when changing the detuning frequency from -25 Hz to -5 Hz. However, as a matter of consistency we kept the same detuning frequency during all measurements.

As previously mentioned, prior to the cantilever tip calibration, surface preparation of the reference samples is needed. Generally, surface cleaning means the removal of natural contaminants, such as oxygen, carbon, and hydrogen containing species which form surface layers of only a few nanometres thickness, yet, enough to modify the WF of the sample.

Surface sputtering by ion bombardment is a common choice for in-situ surface cleaning. It offers many advantages, *e.g.* practicability and easy integration into UHV systems, it is a widely used standard procedure for surface cleaning.[94] Nonetheless, ion bombardment has some inherent side effects such as damage creation and particle implantation,[95] therefore annealing of the bombarded surface is necessary for surface reconstruction.

Here, samples were treated with low-energy sputtering to minimize damage creation and particle implantation[94] (500-600 eV, argon positive ions, current flux $\approx 40 \mu\text{A}/\text{cm}^2$) and annealing cycles with temperatures ranging from 470°C to 520°C, following surfaces preparation procedures described elsewhere[96-98], until a ladder-like shape in the sub-nanometre scale consistent with atomic steps appears on the FM-AFM topographic image acquired along with the WF immediately after each cycle. The sputtering and annealing cycles' duration over reference samples are shown in Table II.

Table II. Sputtering and annealing cycles' duration over all samples.

		Al(110)	Cu(100)	Ag(111)
First cycle	Sputtering / Annealing	2 hours / 3.5 hours	0.5 hours / 0.5 hours	2 hours / 1 hour
Second cycle		2 hours / 2 hours	1.5 hours / > 6 hours	1 hour / > 6 hours
Third cycle		5 hours / 2.5 hours	4 hours / 4 hours	3 hours / > 6 hours
Fourth cycle		2 hours / 2 hours		

At this point, we highlight that prior to surface treatment, samples displayed irregular surfaces, in some cases with topographic features of few hundreds of nanometres. After each surface treatment cycle, surfaces began to display more homogeneous surfaces. Topography images of the samples surface at their final state (*i.e.*, after surface preparation was completed) are shown in Figure 3.13. In all cases we see ladder-like shapes in the sub-nanometre scale consistent with atomic steps, indicating that a clean and reconstructed surface was attained. Additionally, the analysis of the damping images, (not shown) recorded simultaneously with the KPFM data suggest a homogenous chemical nature at the surface of each of these samples. Indeed, a homogenous damping signal means that the dissipated energy of the cantilever tip oscillation due to tip-surface interactions remains constant over the imaged area. Lastly,

acquired CPD images were also homogeneous, implying that the surface chemistry[99] of the analysed area is regular.

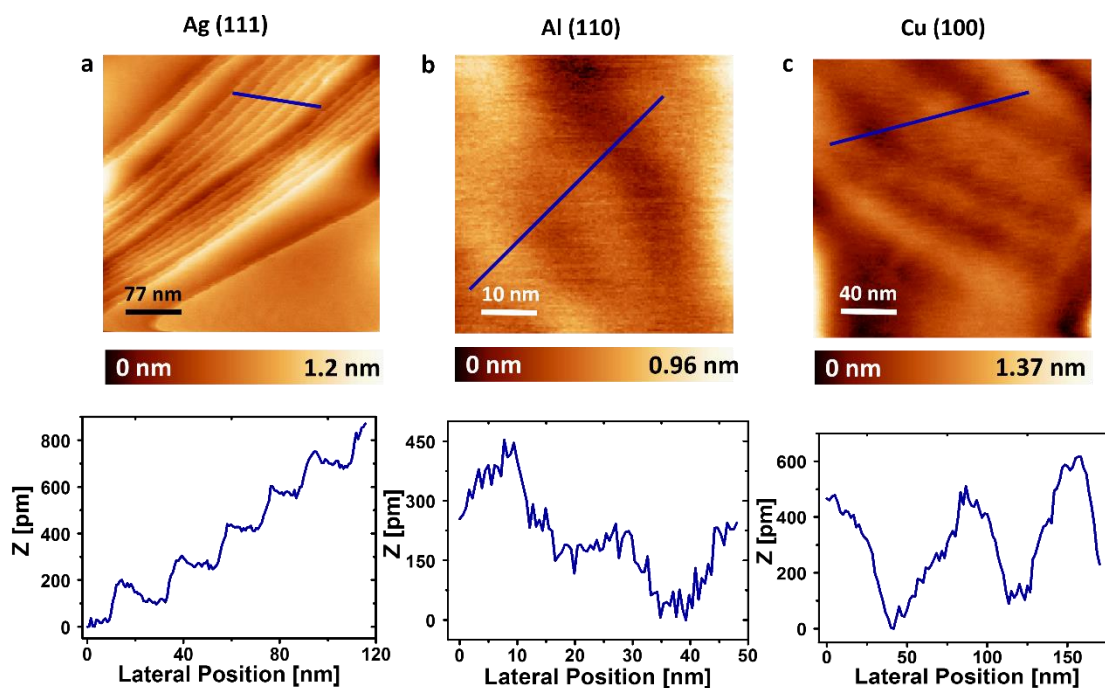


Figure 3.13– Topography images and corresponding cross section profiles (blue line) of (a) Ag (111), (b) Al (110) and (c) Cu (100) samples after surface treatment, showing ladder-like shapes in the sub-nanometre scale. Images were acquired with a Pt/Ir-PPP-EFM cantilever tip. AFM detuning frequency was $\Delta f = -10$ Hz.

All panels were reproduced from Ref. [66].

Measured values of the CPD between the Pt/Ir-PPP-EFM tip and the reference samples are given in Table III. These potential differences corresponds to the mean value of several CPD images acquired over the prepared samples and corroborated by several CPD single-points measurements. The associated uncertainties corresponds to the full width at half maximum value of the images' Gaussian distribution, as represented in Figure 3.14. In all cases CPD values were obtained in FM-KPFM using a modulation frequency of 1 kHz and electrostatically excited with $V_{AC} = 500$ mV. Concerning, the stability of the tip WF, it must be noted that the final measurements of CPD's presented in table III were completed after all samples preparation steps, this to avoid long time delay between CPD measurements.

Table III. Contact potential difference between probe tip and samples.

	Measured CPD
Cu(100)	252 ± 17 mV
Al(110)	773 ± 16 mV
Ag(111)	67 ± 18 mV

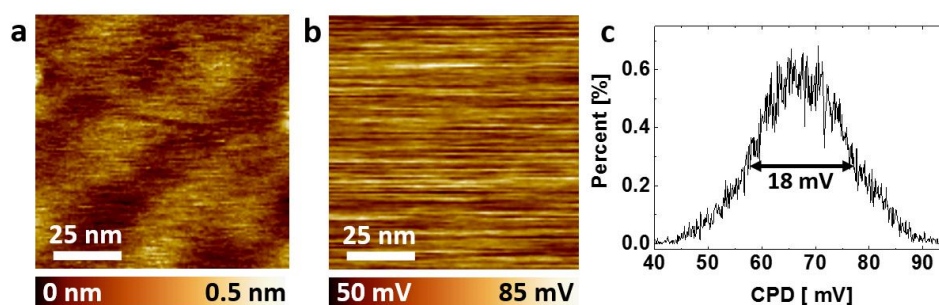


Figure 3.14– (a) Topography and (b) CPD measurements on Ag (111) sample. (c) CPD distribution measured from image (b) with full width at half maximum equal to 18 mV. All panels were reproduced from Ref. [66].

Using Eq. 3.38 and assuming that each sample's WF correspond to values commonly found on the literature [68-70, 92] we can obtain a tip WF value for each sample. The difference between Φ_{tip} values establish the measurement uncertainty. Results are shown in Table IV.

Table IV. Tip WF calculated from CPD measured on reference samples.

	Cu(100)	Al(110)	Ag(111)
Φ_{tip}	4.84 ± 0.017 eV	4.83 ± 0.019 eV	4.81 ± 0.02 eV

As shown in Table IV, tip's WF values calculated over different samples are comparable. It is then reasonable to assume a tip WF weighted value of $\Phi_{tip} = 4.82 \pm 0.03$ eV. Here, it is important to mention that the uncertainty values associated with the calculation of the tip's WF using Ag(111) and Al(110) as references, already include the

original uncertainty value presented for these samples in Table I. On the other hand, the uncertainty of the tip's WF weighted value ($\Phi_{tip} = 4.82 \pm 0.03 \text{ eV}$) was obtained by comparing the results yielded by the calibration against each individual reference sample (Table IV). Indeed, these results differed from each other by 60 meV at the most (taking into account individual uncertainties), which allowed us to establish an uncertainty of $\pm 0.03 \text{ eV}$. Here, we highlight that the determined tip WF value is relatively close to the WF value previously found over a similar cantilever tip ($\Phi_{tip} = 4.28 \pm 0.07 \text{ eV}$) under UHV conditions by Sadewasser et al.[100] However, differences in WF values obtained over similar cantilever tips should not be interpreted as a sign of inconsistency as the WF value of a cantilever tip can be easily impacted by contaminants.

At this stage, the protocol can be applied to determine the WF value of the previously presented ZYB grade HOPG sample. We will use here the sample after the annealing procedure performed at 700°C as at this point the sample revealed a uniform CPD distribution. Here, a previously calibrated Pt/Ir-PPP-EFM tip with $\Phi_{tip} = 4.34 \text{ eV}$ and a resonance frequency of ca. 81.4 kHz is used. The absolute HOPG WF value found was equal to $4.6 \pm 0.03 \text{ eV}$. This value agrees with the HOPG WF theoretical value presented above.[62]

This, strongly suggest that if mechanically under air delaminated ZYB grade HOPG samples are to be used as references for WF calibration procedures, an annealing process should be performed to the sample during 30 minutes at 700°C and a WF value around $4.6 \pm 0.03 \text{ eV}$ should be taken. In fact, it has been reported that graphene (another common reference WF calibration sample) has a WF that varies linearly from ca. 4.3 eV for one monolayer to ca. 4.6 eV for 4 layers and is saturated above.[101] Indeed, in situ annealed HOPG displays a WF similar to thick graphene. Being HOPG more affordable than graphene, this means that when properly prepared, HOPG can replace graphene as a reference WF calibration sample.

3.5.3 Absolute work function measurements: Comparison against theoretical values and achievable lateral resolution

Furthermore, we applied the above described protocol to map the WF over a sample of Al_{0.7}Ga_{0.3}As and GaAs layers with variable thickness (BAM-L200 sample). A full description of the sample can be found elsewhere.[102]

These measurements were made after a surface preparation which consisted in heating the sample under UHV conditions at 150 °C during 30 minutes in order to remove the adsorbed water from the sample's surface. Such preparation is essential to maximize the CPD contrast between materials as reported by Pouch *et al.*[103]

Figure 3.15 depicts the BAM-L200 sample structure as well as the topography and CPD image acquired by FM-AFM combined with FM-KPFM using a previously calibrated Pt/Ir-PPP-EFM tip with a WF value of 4.605 ± 0.03 eV and a resonance frequency of ca. 65.7 kHz previously heated at 150°C for 20 minutes.

In this figure we clearly see the CPD contrast between GaAs and Al_{0.7}Ga_{0.3}As regions, this contrast agrees with previously reported works.[103] Moreover, WF absolute measurements over GaAs and Al_{0.7}Ga_{0.3}As regions yield values of 4.45 ± 0.03 eV and 4.62 ± 0.03 eV respectively.

In order to assess measured WF values we compared them to theoretical WF values of GaAs and Al_{0.7}Ga_{0.3}As as predicted by theoretical models.[104, 105] Given a sample silicon doping level of 5×10^{-7} cm⁻³ (provided by the manufacturer and confirmed by a complementary time-of-flight secondary ion mass spectrometry analysis[106], not shown here) this model predicts a WF of 4.07 eV and 3.62 eV at room temperature for GaAs and Al_{0.7}Ga_{0.3}As respectively.

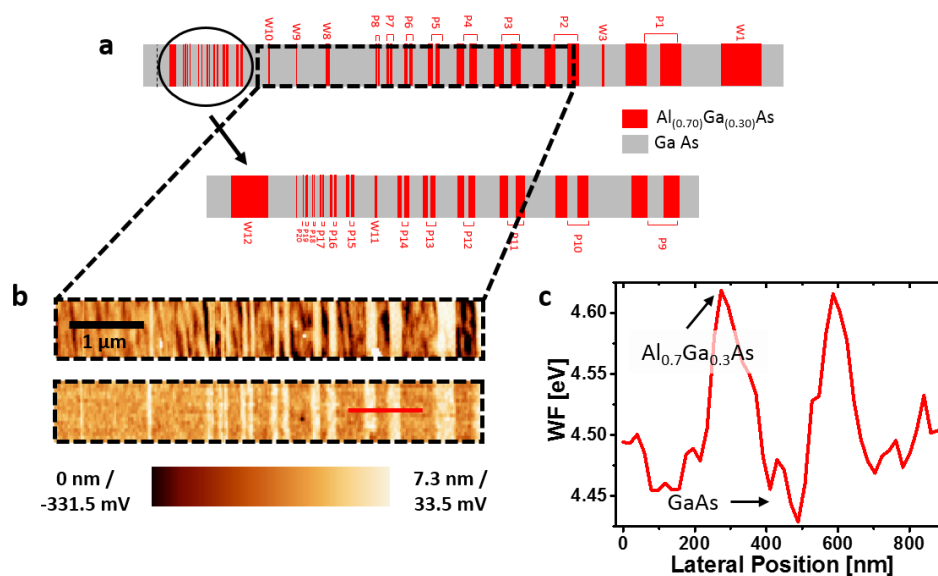


Figure 3.15– (a) BAM-L200 strip pattern scheme. The doublet layers indexed from P₁ to P₈ and from P₉ to P₁₄ have been respectively certified by the fabricant from 587 to 76.5 nm and from 76.5 nm to 17.5 nm. Doublet layers indexed from P₁₅ to P₁₇ have been equally certified from 13.3 nm to 6.9 nm respectively. The separated Al_{0.7}Ga_{0.3}As layers indexed W₈, W₁₀ and W₁₁ are certified to have a thickness of 38 nm, 14.2 nm and 3.5 nm respectively. (b) Topography and CPD measurements acquired over dash-lined box area marked in (a). (c) CPD cross-section acquired over P₃ doublet layers as shown in (b) by the red line. All panels were reproduced from Ref. [66].

However, in our case WF values measured over the sample, both in the case of GaAs and Al_{0.7}Ga_{0.3}As, are influenced by the presence of native oxides. For this reason, measured values are not expected to agree with theoretical ones. Indeed, the native oxide over the sample's surface causes a positive band bending of both GaAs and Al_{0.7}Ga_{0.3}As. In turn, results on GaAs are in good agreement with values previously obtained by others groups over a similar GaAs sample with oxide on its surface.[107, 108] Bastide et al. report a positive band bending of 400 meV in the case of GaAs due to the presence of oxide at the surface, consistent with our measurements and which explain the difference between theoretical and measured values.[107] Additionally, the WF contrast between GaAs and AlGaAs layers is also consistent with contrast values previously reported.[103]

Finally, we proceed to calibrate a Bruker super sharp silicon (SSS) AFM tip with a resonance frequency of ca. 306.6 kHz, previously in-situ prepared by positive argon ion sputtering with an energy of 5 keV during 30 minutes. Upon implementation of the aforementioned AFM cantilever tip WF calibration protocol, the AFM tip revealed a WF value of 4.37 ± 0.03 eV. Thanks to its high aspect ratio this cantilever tip allowed the investigation of the local WF variation over the nanometre-thick layers present in sample's zone 2 as depicted in Figure 3.16. Additionally, the use of this tip serves to demonstrate that the calibration protocol can be implemented regardless of the AFM tip type.

Figure 3.15 shows the WF cross section acquired over the P9-P17 area, we noticed that the WF contrast previously observed, tends to decrease with layers thickness and it disappears when layers thickness drop below few nanometres. As it has been already demonstrated[103] this decreasing tendency is due to an overlay of depletion layers, which causes a band bending overlap.

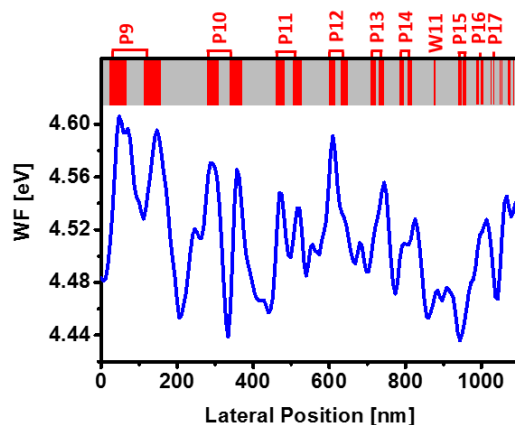


Figure 3.16– WF cross-section acquired by FM-KPFM using a SSS probe over the P₉-P₂₀ area. A scheme of sample's P₉-P₁₇ area was positioned over the cross-section profile to indicate the correspondence between CPD peaks and the different sample's layers. AFM detuning frequency was $\Delta f = -10$ Hz. FM-KPFM was implemented using a modulation frequency $\omega = 1$ kHz and electrostatically excited with $V_{AC} = 500$ mV.

The figure was reproduced from Ref. [66]

3.6 Employed scanning probe microscopy setups

The last section of this chapter will be devoted to give a short overview of the SPM employed setups. Indeed, the research presented in this thesis is the result of the collaboration between two different research units of the French alternative energies and atomic energy commission (CEA), these are: i) the research institute for electronics and information technologies (LETI) and ii) the joint CEA-CNRS-Grenoble Alpes University (UGA) research unit (UMR5819, which is part of the nanoscience and cryogenics institute - INAC), each one possessing a state-of-the-art commercially available Omicron variable temperature UHV SPM for AFM investigations, equipped with dedicated illumination setups, complementary in terms of wavelength and modulation speed. The setup available at the LETI laboratory is shown in Figures 3.17a and 3.17b. As it can be observed from these pictures, the UHV chambers are divided into a preparation chamber and an analysis chamber. The latter is equipped with a heating stage including an optical pyrometer for temperature control and an argon ion sputtering unit among other tools. Figure 3.17a also shows the external Picoquant red (657 nm) laser module used for PV samples and devices illumination.

Figures 3.18a-b shows more in detail the used Omicron unit. Notice that the AFM head placed at the analysis chamber is secured against vibrations via an eddy current damper vibration isolation system. The head of the analysis chamber includes the AFM's piezo tube scanner with tip mount located beneath the sample plate holder. The xyz-scanner has a scan range of 8 μm by 8 μm by 1.5 μm .

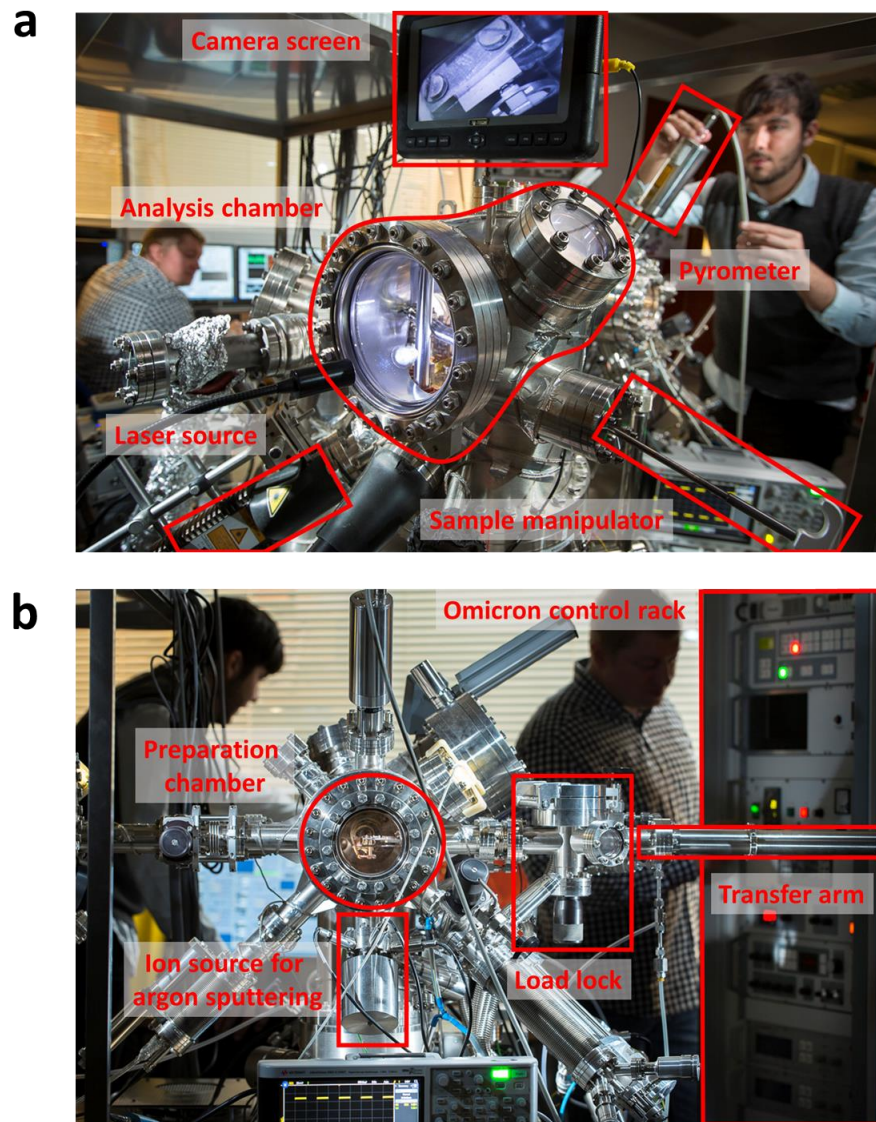


Figure 3.17– LETI's Omicron UHV variable temperature (VT) AFM system. In (a) the analysis chamber including the Picoquant red laser (657 nm) source for PVs illumination, the camera screen, and the sample manipulator can be seen. Additionally, from this picture the optical pyrometer of the preparation chamber can be observed. In (b) the preparation chamber including the ion source for argon sputtering can be seen. In this picture, we can also observe the load lock chamber, where samples are first introduced to the setup, the transfer arm which allows to transfer samples to/from the analysis chamber and the Omicron control rack. ©

CEA-LETI/Chr. Morel.

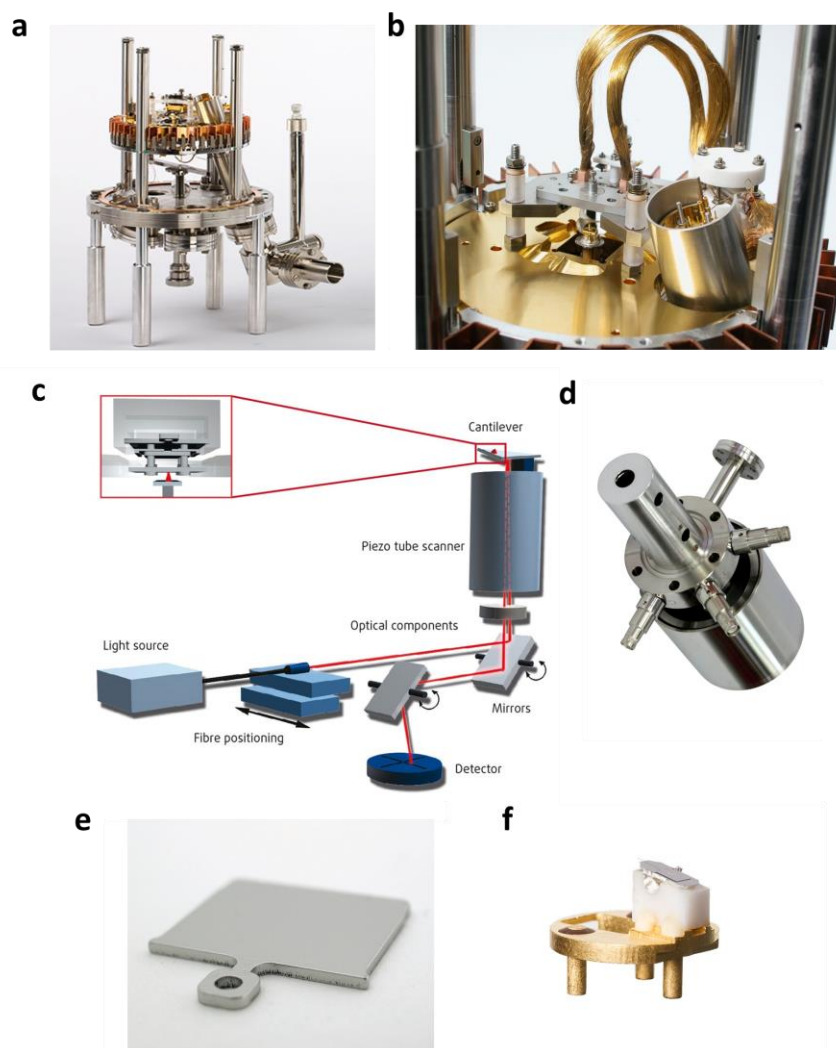


Figure 3.18– VT-AFM system from Scienta Omicron. **(a)** VT-AFM/STM unit with eddy current system and SPM head. **(b)** SPM head with sample plate holder and piezo tube scanner. **(c)** Omicron beam deflection system with laser source, optical components and photo sensitive diode. **(d)** Ion source used for the argon sputtering of tip and samples. **(e)** Standard stainless steel sample plate. **(f)** AFM cantilever mounted on chip carrier. Images taken from <http://www.scientaomicron.com>.

Figure 3.18c, depicts a schema of the integrated beam deflection AFM system. Here, the (infrared) laser beam from the external light source is directed towards the cantilever back. From there, its reflection is guided by mirrors to the four quadrant photo-detector. Figure 3.18d shows a more detailed view of the ion source previously presented in Figure 3.17b. It can be

used for the argon sputtering of cantilever tips or samples with the aim of removing native oxide and possible contaminants from surfaces. Moreover, Figure 3.18e and Figure 3.18f depict a standard UHV compatible sample plate holder and AFM cantilever mounted on a chip carrier respectively.

Finally, the available setup at the INAC laboratory which features an almost identical configuration to the one presented previously is shown in Figure 3.19.

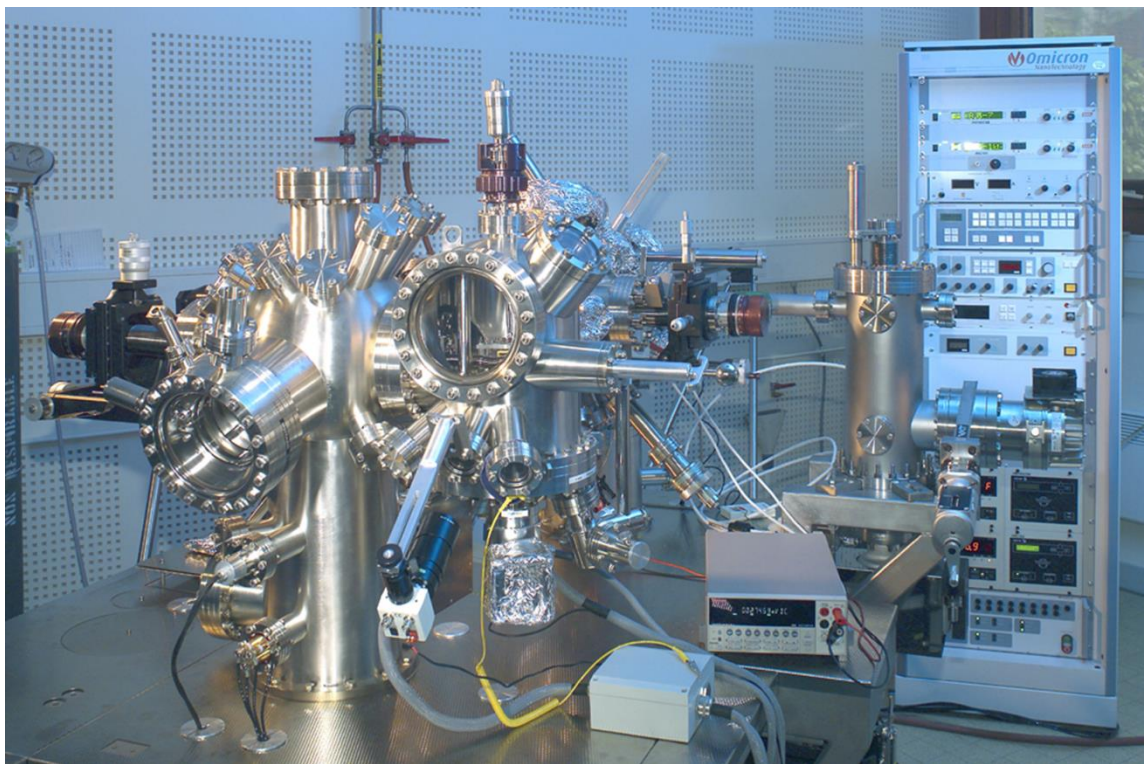


Figure 3.19– INAC's Omicron UHV VT AFM system

The dedicated external illumination setup of the INAC's Omicron UHV VT AFM system, used for the illumination of different PV samples and devices is show in Figure 3.20.

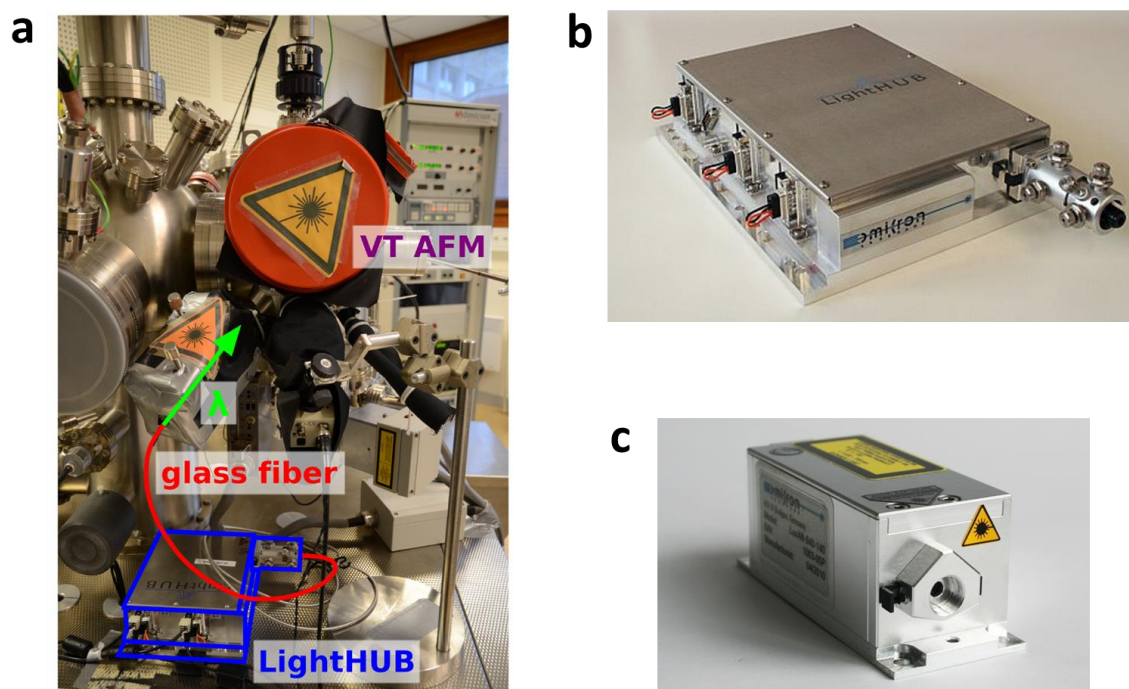


Figure 3.20– In (a) the laser beam is guided via a glass fibre to one of the system's windows. (b) Multiple wavelengths laser source: LightHUB. (c) Standalone PhoxXplus module. Panel (a) was reproduced from Ref. [17], images in panels (c) and (d) were taken from <http://www.scientaomicron.com>.

Figure 3.20b shows the "LightHUB" from Omicron Laserage GmbH, this equipment is connected to the VT-AFM via an optical glass fibre as depicted in Figure 3.20a. The glass fibre guides the laser beam towards one of the setup's windows and illuminates the sample which is placed on the AFM sample stage. Different laser units can be integrated in the LightHUB and the laser beams are guided by the beam combiner unit to the common optical output. In our case, two LuxX laser units from Omicron Laserage GmbH with wavelengths of 515 nm and 685 nm respectively were used. During the last two years of this thesis, a standalone PhoxXplus module from Omicron Laserage GmbH (Figure 3.20c) was used instead, due to its faster (<1.5 ns) rise and fall times in digital modulation mode. In all cases their optical output can be regulated from the sub-mW regime to about 30 mW measured at the exit of the optical fibre. Moreover, in some cases, optical density filters were employed to work in the μW regime.

In the majority of the under illumination investigations, performed using either LETI's or INAC setup, a backside illumination sample holder was used. Indeed, to avoid possible shadowing effects caused by the cantilever chip or tip, as well as to avoid heat-related artefacts, a backside illumination configuration geometry with indirect illumination was used as depicted in Figure 3.21.

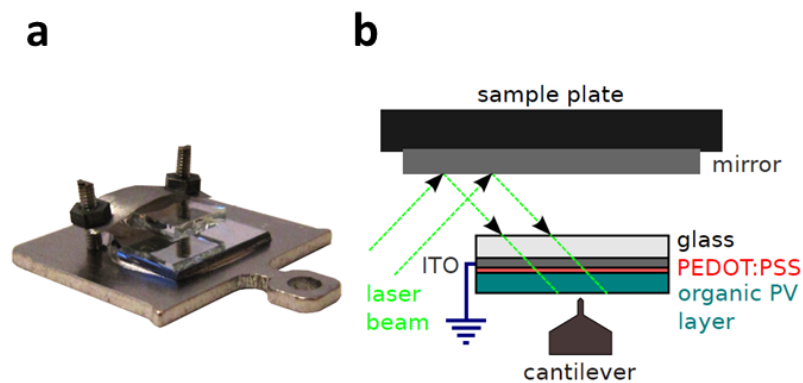


Figure 3.21– (a) Backside illumination sample holder for PV samples on transparent substrates. (b) Backside illumination geometry, featuring an OPV sample. Both panels were reproduced from Ref. [17]

Finally, an important equipment used in all under modulated illumination investigations (**Chapter 4**), is the arbitrary waveform generator (AWG, Keysight 33622A) which was used to operate the laser sources in the modulation mode. This equipment is present at both LETI's and INAC's laboratories and its shown in Figure 3.22.



Figure 3.22– Arbitrary waveform generator Keysight 33622A, present at both LETI and INAC laboratories.

Image taken from <https://www.keysight.com>.

Conclusion

During the first half of this chapter, a summarized description of the scanning probe microscopy techniques employed during the course of this thesis was given. In this section, special attention was granted to the description of KPFM as it represents a tool for the electronic investigation of different materials and devices at the nanoscale, being particularly adapted for the investigation of PV devices under operation conditions. As we saw, KPFM can be implemented in different modes to acquire the CPD between an AFM cantilever tip and the surface of a sample.

In the second half of this chapter, it was demonstrated how KPFM investigations can give access to the absolute WF value of a sample with a lateral resolution of few nanometres. In fact, in order to do this, we saw how the WF calibration of the AFM tip was needed. For this calibration procedure, we proposed the use of three different metallic samples with known crystallographic orientation as references samples, as an alternative to the commonly used HOPG sample, which WF value found in the literature can largely vary from one author to the other.

Furthermore, we demonstrated our proposed calibration protocol over several AFM cantilever tips, which were in turn used to: i) measure the absolute WF value of a clean mechanically under air delaminated ZYB grade HOPG sample after an annealing procedure performed at 700°C during 30 minutes yielding a value of 4.6 ± 0.03 eV and ii) to investigate the local absolute WF variation of a nanostructured semiconductor sample presenting nanometre-thick layers of $\text{Al}_{0.7}\text{Ga}_{0.3}\text{As}$ and GaAs.

Finally, a short overview of the SPM employed setups was given, introducing elements and equipment used in the implementation of frequency-modulated illumination (FMI-KPFM) investigations. A technique based on KPFM under modulated illumination allowing the imaging of the photo-carrier dynamics in different types of PV materials. This technique will be introduced and described in the following chapter.

References

1. Li, S., et al., *A DNA nanorobot functions as a cancer therapeutic in response to a molecular trigger in vivo*. Nature Biotechnology, 2018.
2. Kamat, P.V., *Meeting the Clean Energy Demand: Nanostructure Architectures for Solar Energy Conversion*. The Journal of Physical Chemistry C, 2007. **111**(7): p. 2834-2860.
3. Feynman, R.P., *There's Plenty of Room at the Bottom*. Engineering and Science, 1960. **23**: p. 22-36.
4. Binnig, G., et al., *Surface Studies by Scanning Tunneling Microscopy*. Physical Review Letters, 1982. **49**(1): p. 57-61.
5. Razavy, M., *Quantum Theory of Tunneling*. 2003: World Scientific.
6. Giessibl, F.J., *Advances in atomic force microscopy*. Reviews of Modern Physics, 2003. **75**(3): p. 949-983.
7. Binnig, G., C.F. Quate, and C. Gerber, *Atomic Force Microscope*. Physical Review Letters, 1986. **56**(9): p. 930-933.
8. Meyer, E., *Atomic force microscopy*. Progress in Surface Science, 1992. **41**(1): p. 3-49.
9. Giessibl, F.J., *Principles and Applications of the qPlus Sensor*, in *Noncontact Atomic Force Microscopy: Volume 2*, S. Morita, F.J. Giessibl, and R. Wiesendanger, Editors. 2009, Springer Berlin Heidelberg: Berlin, Heidelberg. p. 121-142.
10. Giessibl, F.J., *AFM's path to atomic resolution*. Materials Today, 2005. **8**(5): p. 32-41.
11. Borowik, Ł., *Etude de propriétés électroniques de nanostructures par microscopie à force atomique sous ultra-vide*. 2009, Université des Sciences et Technologies de Lille: France.
12. García, R. and R. Pérez, *Dynamic atomic force microscopy methods*. Surface Science Reports, 2002. **47**(6): p. 197-301.
13. Meyer, G. and N.M. Amer, *Novel optical approach to atomic force microscopy*. Applied Physics Letters, 1988. **53**(12): p. 1045-1047.
14. Meyer, E., H.J. Hug, and R. Bennewitz, 2004.
15. Krasnow, B., *Electron microscope slow-motion video of vinyl LP*. 2015.
16. Dianoux, R., *Charge injection and detection in semiconducting nanostructures by atomic force microscopy*. 2004, Université Joseph Fourier: France.
17. Fuchs, F., *Model Donor-Acceptor Systems for Organic Photovoltaics Investigated by Scanning Probe Microscopy*, in *Ecole Doctorale de Physique*. 2014, Grenoble Alpes: Grenoble.

18. Albrecht, T.R., et al., *Frequency modulation detection using high- Q cantilevers for enhanced force microscope sensitivity*. Journal of Applied Physics, 1991. **69**(2): p. 668-673.
19. Morita, S., R. Wiesendanger, and E. Meyer, 2002.
20. Nony, L., *Applications de la microscopie de force dynamique en mode non-contact : structures supramoléculaires sur surfaces isolantes et microscopie de sonde de Kelvin*. 2013, Aix-Marseille Université.
21. Biaye, M., *Caractérisation de propriétés électroniques et électromécaniques de nanocristaux colloïdaux par microscopie à force atomique en ultravide*. 2016, Université de Lille 1: France.
22. Giessibl, F.J., *Forces and frequency shifts in atomic-resolution dynamic-force microscopy*. Physical Review B, 1997. **56**(24): p. 16010-16015.
23. Guggisberg, M., et al., *Separation of interactions by noncontact force microscopy*. Physical Review B, 2000. **61**(16): p. 11151-11155.
24. Sader, J.E. and S.P. Jarvis, *Accurate formulas for interaction force and energy in frequency modulation force spectroscopy*. Applied Physics Letters, 2004. **84**(10): p. 1801-1803.
25. John, E.S., et al., *Quantitative force measurements using frequency modulation atomic force microscopy—theoretical foundations*. Nanotechnology, 2005. **16**(3): p. S94.
26. Olsson, L., et al., *A method for in situ characterization of tip shape in ac-mode atomic force microscopy using electrostatic interaction*. Journal of Applied Physics, 1998. **84**(8): p. 4060-4064.
27. Hudlet, S., et al., *Evaluation of the capacitive force between an atomic force microscopy tip and a metallic surface*. The European Physical Journal B - Condensed Matter and Complex Systems, 1998. **2**(1): p. 5-10.
28. Hamaker, H.C., *The London—van der Waals attraction between spherical particles*. Physica, 1937. **4**(10): p. 1058-1072.
29. Israelachvili, J.N. and M. Wilson, *Absorption characteristics of oriented photopigments in microvilli*. Biol Cybern, 1976. **21**(1): p. 9-15.
30. Kelvin, L., *V. Contact electricity of metals*. The London, Edinburgh, and Dublin Philosophical Magazine and Journal of Science, 1898. **46**(278): p. 82-120.
31. Zisman, W.A., *A NEW METHOD OF MEASURING CONTACT POTENTIAL DIFFERENCES IN METALS*. Review of Scientific Instruments, 1932. **3**(7): p. 367-370.
32. Nonnenmacher, M., M.P. O'Boyle, and H.K. Wickramasinghe, *Kelvin probe force microscopy*. Applied Physics Letters, 1991. **58**(25): p. 2921-2923.
33. Cahen, D. and A. Kahn, *Electron Energetics at Surfaces and Interfaces: Concepts and Experiments*. Advanced Materials, 2003. **15**(4): p. 271-277.

34. Melitz, W., et al., *Kelvin probe force microscopy and its application*. Surface Science Reports, 2011. **66**(1): p. 1-27.
35. Sadewasser, S. and T. Glatzel, 2012. **48**.
36. Shigeki, K., et al., *Atomic contact potential variations of Si(111)-7 × 7 analyzed by Kelvin probe force microscopy*. Nanotechnology, 2010. **21**(24): p. 245704.
37. Laurent, N., et al., *On the relevance of the atomic-scale contact potential difference by amplitude-modulation and frequency-modulation Kelvin probe force microscopy*. Nanotechnology, 2009. **20**(26): p. 264014.
38. Sommerhalter, C., et al., *Kelvin probe force microscopy in ultra high vacuum using amplitude modulation detection of the electrostatic forces*. Applied Surface Science, 2000. **157**(4): p. 263-268.
39. Glatzel, T., S. Sadewasser, and M.C. Lux-Steiner, *Amplitude or frequency modulation-detection in Kelvin probe force microscopy*. Applied Surface Science, 2003. **210**(1): p. 84-89.
40. Zerweck, U., et al., *Accuracy and resolution limits of Kelvin probe force microscopy*. Physical Review B, 2005. **71**(12): p. 125424.
41. Borowik, Ł., et al., *Calculating Kelvin force microscopy signals from static force fields*. Applied Physics Letters, 2010. **96**(10): p. 103119.
42. Enevoldsen, G.H., et al., *Atomic Scale Kelvin Probe Force Microscopy Studies of the Surface Potential Variations on the $\text{TiO}_2(110)$ Surface*. Physical Review Letters, 2008. **100**(23): p. 236104.
43. Kitamura, S.i. and M. Iwatsuki, *High-resolution imaging of contact potential difference with ultrahigh vacuum noncontact atomic force microscope*. Applied Physics Letters, 1998. **72**(24): p. 3154-3156.
44. Schumacher, Z., et al., *Measurement of Surface Photovoltage by Atomic Force Microscopy under Pulsed Illumination*. Physical Review Applied, 2016. **5**(4): p. 044018.
45. Mohn, F., et al., *Imaging the charge distribution within a single molecule*. Nature Nanotechnology, 2012. **7**: p. 227.
46. Kahn, A., *Fermi level, work function and vacuum level*. Materials Horizons, 2016. **3**(1): p. 7-10.
47. Schlaf, R., H. Murata, and Z.H. Kafafi, *Work function measurements on indium tin oxide films*. Journal of Electron Spectroscopy and Related Phenomena, 2001. **120**(1-3): p. 149-154.
48. K. Siegbahn, C.N., A. Fahlman, R. Nordberg, K. Hamrin, in *Nova acta regiae societatis scientiarum Upsaliensis*. 1967.
49. Rabalais, J., *Principles of Ultraviolet Photoelectron Spectroscopy*. 1977, New York: John Wiley and Sons.

-
50. Glatzel, T., et al., *Surface photovoltage analysis of thin CdS layers on polycrystalline chalcopyrite absorber layers by Kelvin probe force microscopy*. Nanotechnology, 2008. **19**(14).
 51. Hansen, W.N. and G.J. Hansen, *Standard reference surfaces for work function measurements in air*. Surface Science, 2001. **481**(1-3): p. 172-184.
 52. Liscio, A., et al., *Tip-Sample Interactions in Kelvin Probe Force Microscopy: Quantitative Measurement of the Local Surface Potential*. The Journal of Physical Chemistry C, 2008. **112**(44): p. 17368-17377.
 53. Sommerhalter, C., et al., *High-sensitivity quantitative Kelvin probe microscopy by noncontact ultra-high-vacuum atomic force microscopy*. Applied Physics Letters, 1999. **75**(2): p. 286-288.
 54. Kim, C.H., et al., *Local Work Function Measurements on Various Inorganic Materials Using Kelvin Probe Force Spectroscopy*. Solid State Phenomena, 2007. **124-126**: p. 607-610.
 55. Bohmisch, M., et al., *Atomic force microscope based Kelvin measurements: Application to an electrochemical reaction*. Journal of Physical Chemistry B, 1997. **101**(49): p. 10162-10165.
 56. Kim, C., et al., *Effects of surface treatment on work function of ITO (Indium Tin Oxide) films*. Journal of the Korean Physical Society, 2005. **47**: p. S417-S421.
 57. Palermo, V., et al., *Influence of Molecular Order on the Local Work Function of Nanographene Architectures: A Kelvin-Probe Force Microscopy Study*. ChemPhysChem, 2005. **6**(11): p. 2371-2375.
 58. Sommerhalter, C., *Kelvin probe force microscopy in ultrahigh vacuum for the characterization of semiconductor heterodiodes based on chalcopyrites*, in *Department of Physics*. 2000, Freie Universität Berlin: Germany.
 59. Kawano, H., *Effective work functions for ionic and electronic emissions from mono- and polycrystalline surfaces*. Progress in Surface Science, 2008. **83**(1): p. 1-165.
 60. Schroeder, P.G., et al., *Investigation of band bending and charging phenomena in frontier orbital alignment measurements of para-quaterphenyl thin films grown on highly oriented pyrolytic graphite and SnS₂*. Surface Science, 2000. **459**(3): p. 349-364.
 61. Reihl, B., et al., *Unoccupied electronic states of graphite as probed by inverse-photoemission and tunneling spectroscopy*. Physical Review B, 1986. **33**(8): p. 5770-5773.
 62. Sque, S.J., R. Jones, and P.R. Briddon, *The transfer doping of graphite and graphene*. physica status solidi (a), 2007. **204**(9): p. 3078-3084.
 63. Martinez-Martin, D., et al., *Atmospheric contaminants on graphitic surfaces*. Carbon, 2013. **61**: p. 33-39.

64. Ochedowski, O., et al., *Manipulation of the graphene surface potential by ion irradiation*. Applied Physics Letters, 2013. **102**(15): p. 153103.
65. Lu, Y., et al., *Electrostatic Force Microscopy on Oriented Graphite Surfaces: Coexistence of Insulating and Conducting Behaviors*. Physical Review Letters, 2006. **97**(7): p. 076805.
66. Pablo A. Fernández Garrillo, B.G., Nicolas Chevalier, Łukasz Borowik, *Calibrated work function mapping by Kelvin probe force microscopy*. Review of Scientific Instruments, 2018. **84**(4): p. 043702.
67. Bleuet, P., et al., *A hard x-ray nanoprobe for scanning and projection nanotomography*. Review of Scientific Instruments, 2009. **80**(5): p. 056101.
68. Dweydari, A.W. and C.H.B. Mee, *Oxygen adsorption on the (111) face of silver*. physica status solidi (a), 1973. **17**(1): p. 247-250.
69. Gartland, P.O., Phys. Norv., 1972. **6**: p. 201.
70. Eastment, R.M. and C.H.B. Mee, *Work function measurements on (100), (110) and (111) surfaces of aluminium*. Journal of Physics F: Metal Physics, 1973. **3**(9): p. 1738.
71. Farnsworth, H.E. and R.P. Winch, *Photoelectric Work Functions of (100) and (111) Faces of Silver Single Crystals and Their Contact Potential Difference*. Physical Review, 1940. **58**(9): p. 812-819.
72. Giesen, K., et al., *Two-photon photoemission via image-potential states*. Physical Review Letters, 1985. **55**(3): p. 300-303.
73. Ryu, S., J. Chang, and S.K. Kim, *Interfacial electron dynamics and hot-electron-driven surface photochemistry of carbon tetrachloride on Ag(111)*. The Journal of Chemical Physics, 2005. **123**(11): p. 114710.
74. Chelvayohan, M. and C.H.B. Mee, *Work function measurements on (110), (100) and (111) surfaces of silver*. Journal of Physics C: Solid State Physics, 1982. **15**(10): p. 2305.
75. Giesen, K., et al., *Effective mass of image-potential states*. Physical Review B, 1987. **35**(3): p. 975-978.
76. Li, W.Y., K. Goto, and R. Shimizu, *PEEM is a suitable tool for absolute work function measurements*. Surface and Interface Analysis, 2005. **37**(2): p. 244-247.
77. Li, H.-N., et al., *Electronic state of C60 monolayer on Ag(111) before and after Yb intercalation*. Surface Science, 2005. **586**(1): p. 65-73.
78. Straub, D. and F.J. Himpsel, *Spectroscopy of image-potential states with inverse photoemission*. Physical Review B, 1986. **33**(4): p. 2256-2262.
79. Kim, S.K., et al., *Surface alloying of a Co film on the Cu(001) surface*. Surface Science, 2000. **453**(1): p. 47-58.
80. Haas, G.A. and R.E. Thomas, *Work function and secondary emission studies of various Cu crystal faces*. Journal of Applied Physics, 1977. **48**(1): p. 86-93.

81. Wegehaupt, T., D. Rieger, and W. Steinmann, *Observation of empty bulk states on Cu(100) by two-photon photoemission*. Physical Review B, 1988. **37**(17): p. 10086-10089.
82. Rowe, J.E. and N.V. Smith, *Photoemission spectra and band structures of d -band metals. V. The (100) and (111) faces of single-crystal copper*. Physical Review B, 1974. **10**(8): p. 3207-3212.
83. Tibbetts, G.G., J.M. Burkstrand, and J.C. Tracy, *Electronic properties of adsorbed layers of nitrogen, oxygen, and sulfur on copper (100)*. Physical Review B, 1977. **15**(8): p. 3652-3660.
84. Delchar, T.A., *Oxygen chemisorption on copper single crystals*. Surface Science, 1971. **27**(1): p. 11-20.
85. Strayer, R.W., W. Mackie, and L.W. Swanson, *Work function measurements by the field emission retarding potential method*. Surface Science, 1973. **34**(2): p. 225-248.
86. Grepstad, J.K., P.O. Gartland, and B.J. Slagsvold, *Anisotropic work function of clean and smooth low-index faces of aluminium*. Surface Science, 1976. **57**(1): p. 348-362.
87. Maxwell, A.J., et al., *Electronic and geometric structure of C_{60} on Al(111) and Al(110)*. Physical Review B, 1998. **57**(12): p. 7312-7326.
88. Michaelson, H.B., *The work function of the elements and its periodicity*. Journal of Applied Physics, 1977. **48**(11): p. 4729-4733.
89. Derry, G.N., M.E. Kern, and E.H. Worth, *Recommended values of clean metal surface work functions*. Journal of Vacuum Science & Technology A: Vacuum, Surfaces, and Films, 2015. **33**(6): p. 060801.
90. Riviere, J.C., *Work function: Measurements and results*. Vol. 1. 1969, New York: Dekker.
91. Hölzl, J. and F.K. Schulte, *Work function of metals*. 1979. **85**: p. 1-150.
92. Potter, H.C. and J.M. Blakely, *LEED, Auger spectroscopy, and contact potential studies of copper-gold alloy single crystal surfaces*. Journal of Vacuum Science and Technology, 1975. **12**(2): p. 635-642.
93. Inami, E. and Y. Sugimoto, *Accurate Extraction of Electrostatic Force by a Voltage-Pulse Force Spectroscopy*. Physical Review Letters, 2015. **114**(24): p. 246102.
94. Taglauer, E., *Surface cleaning using sputtering*. Applied Physics A Solids and Surfaces, 1990. **51**(3): p. 238-251.
95. Almadori, Y., et al., *Effect of argon implantation on solid-state dewetting: control of size and surface density of silicon nanocrystals*. Nanotechnology, 2017. **28**(4): p. 045306.
96. Andryushechkin, B.V., et al., *Atomic structure of Ag(111) saturated with chlorine: Formation of Ag_3Cl_7 clusters*. Physical Review B, 2011. **84**(7): p. 075452.

97. A. Czanderna, C.P., T. Madey, *Specimen Handling, Preparation, and Treatments in Surface Characterization*. Methods of Surface Characterization, ed. A.C. C. Powell, D. Hercules, T. Madey, J. Yates. Vol. 4. 1998, New York, Boston, Dordrecht, London, Moscow: Kluwer Academic.
98. Kuk, Y., P.J. Silverman, and F.M. Chua, *Study of Au surfaces by scanning tunnelling microscopy*. Journal of Microscopy, 1988. **152**(2): p. 449-457.
99. Palacios-Lidón, E., C.R. Henry, and C. Barth, *Kelvin Probe Force Microscopy in Surface Chemistry: Reactivity of Pd Nanoparticles on Highly Oriented Pirolytic Graphite*. ACS Catalysis, 2014. **4**(6): p. 1838-1844.
100. Sadewasser, S., et al., *High-resolution work function imaging of single grains of semiconductor surfaces*. Applied Physics Letters, 2002. **80**(16): p. 2979-2981.
101. Hibino, H., et al., *Dependence of electronic properties of epitaxial few-layer graphene on the number of layers investigated by photoelectron emission microscopy*. Physical Review B, 2009. **79**(12): p. 125437.
102. Senoner, M., et al., *BAM-L002—a new type of certified reference material for length calibration and testing of lateral resolution in the nanometre range*. Surface and Interface Analysis, 2004. **36**(10): p. 1423-1426.
103. Pouch, S., et al., *Electronic structure investigation of Al_{0.7}Ga_{0.3}As/GaAs nanometric heterostructures by Kelvin force microscopy*. RSC Advances, 2016. **6**(8): p. 6782-6787.
104. S. M. Sze, K.K.N., *Physics of Semiconductor Devices*. 1981, New York: John Wiley & Sons, Inc.
105. M. Levinshtein, S.R., M. Shur, *Handbook serier on semiconductor parameters* Vol. 2. 1999, London: World Scientific Publishing Co. Pte. Ltd.
106. Sodhi, R.N.S., *Time-of-flight secondary ion mass spectrometry (TOF-SIMS): versatility in chemical and imaging surface analysis*. Analyst, 2004. **129**(6): p. 483-487.
107. Bastide, S., et al., *Controlling the Work Function of GaAs by Chemisorption of Benzoic Acid Derivatives*. The Journal of Physical Chemistry B, 1997. **101**(14): p. 2678-2684.
108. Takashi, M., et al., *Measurement of Contact Potential of GaAs/AlGaAs Heterostructure Using Kelvin Probe Force Microscopy*. Japanese Journal of Applied Physics, 1999. **38**(7A): p. L767.

4 | Frequency modulated illumination Kelvin probe force microscopy

Content

4.1 Context.....	99
4.2 Frequency modulated illumination Kelvin probe force microscopy investigations	103
4.2.1 Silicon based photovoltaics	107
4.2.2 Bulk heterojunction donor-acceptor organic photovoltaics	115
4.2.3 Spectroscopic and time-resolved measurements over perovskite photovoltaics ..	131
Conclusion	142
References.....	143

Dans ce chapitre, nous introduisons une nouvelle méthode de nano-caractérisation pour les composants photovoltaïques basée sur la microscopie à sonde Kelvin sous illumination externe modulée en fréquence. Cette technique permet de cartographier la dynamique des photo-porteurs avec une résolution nanométrique. Nous décrivons son principe de fonctionnement, ainsi que les résultats obtenus sur plusieurs échantillons de composants photovoltaïques de troisième génération. En complément, la physique des différents matériaux pour le photovoltaïque est abordée en soulignant l'apport des méthodes expérimentales décrites précédemment pour les analyser.

4.1 Context

So far in this thesis, we have laid the foundations needed to discuss the development and implementation of a new non-contact atomic force microscopy (AFM) technique based on

the operation of Kelvin probe force microscopy (KPFM) under frequency-modulated illumination which enables to simultaneously image the topography along with the surface photo-potential dynamics over a large range of photovoltaic samples and devices with a sub-10 nm lateral resolution.

As previously discussed in **Chapter 2**, nowadays, the development and further improvement of energy conversion efficiencies in third generation solar cells, strongly relies on the development of advanced characterization techniques capable of imaging their optoelectronic properties at the nanoscale. The interest is to identify the mechanisms of losses which occur mainly through carrier recombination. Indeed, the comprehensive understanding of carrier recombination mechanisms at the nanoscale is crucial to improve solar cell performances.

A non-exhaustive description of several experimental approaches developed to probe recombination dynamics in photovoltaic materials was given in **Chapter 2**. At that point, techniques such as transient photo-voltage[1], charge extraction[2], microwave photo-conductivity decay (μ W-PCD)[3], electron-beam-induced current (EBIC)[4] and quasi-steady-state photo-conductance (QSSPC)[5] were introduced, highlighting however the fact that these techniques do not allow to assess the influence of the nanostructure and local defects on photo-carrier dynamics.

The need for an increased lateral resolution motivated a few research groups to propose approaches based on AFM, which allowed to obtain information about the photo-carrier recombination dynamics at the local scale. A good example of techniques based on this approach is the case of time-resolved electrostatic force microscopy (trEFM)[6, 7], which as previously mentioned is a technique that allows to probe the photo-carrier dynamics with a temporal resolution of around 100 μ s and a lateral resolution of a few tens of nm. Basically, this technique relies on the analysis of the cantilever frequency shift decay after optical pulsing. Both trEFM and fast free trEFM (FF-trEFM), which is an updated version of trEFM where the temporal resolution was improved, have been used to probe photo-charging rates, *i.e.*, the time needed by a system to reach equilibrium after an excitation pulse. However, discussing trEFM

or FF-trEFM in terms of recombination dynamics remains somewhat unclear. In fact, neither trEFM nor FF-trEFM allow a direct access to the carrier lifetime since both the charge generation and recombination impact the time needed to reach an electrostatic charge equilibrium, *i.e.*, the electrostatic equilibrium implies that for a given number of generated charges, the number of recombined charges shall be the same. Moreover, investigations using the above mentioned techniques were only implemented (to the best of our knowledge) over OPV devices.

Furthermore, a few groups[8-11] independently introduced AFM-based techniques relying on the recording of the contact potential difference (CPD) mean signal measured by KPFM under modulated illumination source (see Figure 4.1a). Indeed, comparing the CPD recorded both under illumination and in dark conditions, gives access to the so-called surface photovoltage (SPV) which in turn can be interpreted as a local measurement of the device open circuit voltage. Then, the photo-potential dynamics can be probed by monitoring the dependence of the CPD time average value over time, with respect to the repetition frequency of a modulated illumination source, as shown in Figure 4.1b for the case of a polycrystalline silicon-based solar cell[8] and in Figure 4.1c for the case of a donor-acceptor organic bulk hetero-junction (BHJ) thin film.[10] Alternatively, similar results can be obtained using a modulated bias voltage instead of an illumination source.[11] In other words, techniques based on this approach measure the evolution of the average surface photo-potential with respect to the repetition frequency of an excitation source (illumination or electrical bias). This means that photo-modulated KPFM can yield an averaged time-integral value of the instantaneous photovoltage.

So far, techniques implementing this approach have been limited to single-point spectroscopy measurements. In other words, information about the photo-carrier dynamics can only be obtained at single locations of the sample, again limiting the assessment of the influence of the nanostructure and local defects on photo-carrier dynamics.

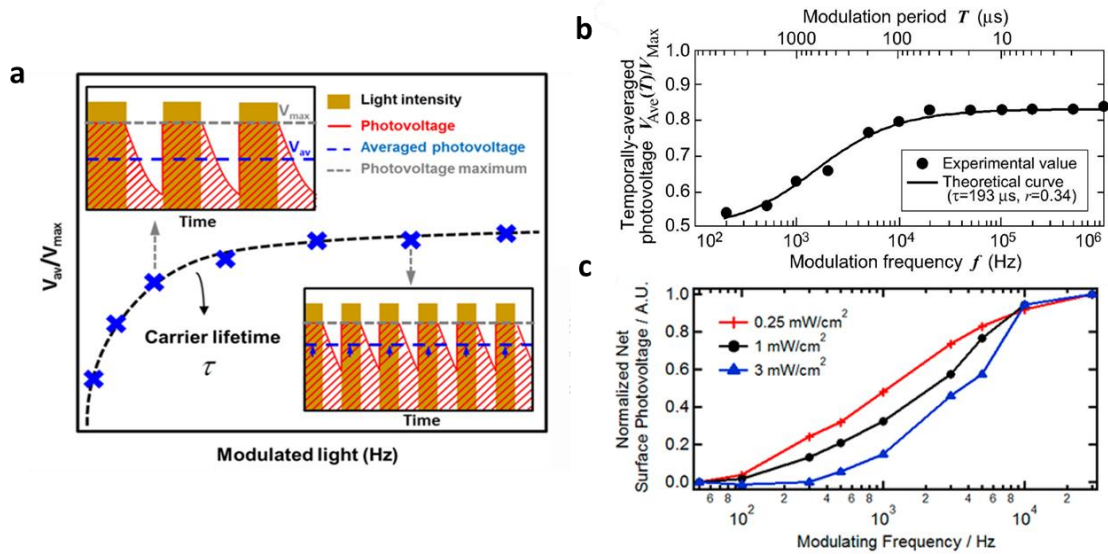


Figure 4.1– In **(a)** a schematic illustration of the evolution of the surface photovoltage under modulated illumination as a function of time: averaged time-integral values of the instantaneous photovoltage are acquired as a function of the excitation modulation frequency. SPV decay time constants are calculated upon a mathematical fit of this curve. **(b,c)** Several examples of the implementation of KPFM-based techniques relying on the recording of the CPD mean signal to gain access to the photo-potential dynamics in photovoltaics: in the case of a polycrystalline silicon-based solar cell **(b)** and in the case of a donor-acceptor BHJ thin film **(c)**. Panels **(a)**, **(b)** and **(c)** were reproduced from Ref. [BJNANO], Ref.[8] and Ref.[10] respectively.

In that context, here, we implement a 2-dimensional time-resolved imaging mode based on frequency-modulated illumination Kelvin probe force microscopy (FMI-KPFM). This new technique constitutes a universal nano-characterization tool for photovoltaics. In the following, a comprehensive description of this technique will be given. We will discuss its operation principle, as well as results of its implementation over several third generation photovoltaic samples. While for the most part, the discussion will be focus on FMI-KPFM technical aspects, in each case the physics of the different materials will be addressed, highlighting how FMI-KPFM allows to unveil different physical processes over different samples.

4.2 Frequency modulated illumination Kelvin probe force microscopy investigations

As discussed in the previous chapter, in photovoltaic materials, KPFM can be used to probe the photo-generated charge carriers by analysing the CPD shift under illumination, *i.e.*, the SPV.[12] Actually, it has been shown that SPV imaging yields a local measurement of the device open circuit voltage at the nanometre scale[13], which in turn can be defined as the electron-hole quasi Fermi levels splitting under illumination.[14] Moreover, the open circuit voltage magnitude is closely related to the carrier recombination mechanisms [15, 16], which themselves depend of the nature of local defect and structural heterogeneities in nanostructured photovoltaic (PV) devices. Thus, the local SPV contrasts detected in KPFM experiments should reflect spatial variations of the photo-carrier recombination rate in relation with the nanostructure. Nonetheless, the SPV contrast cannot be interpreted solely in terms of the photo-carrier dynamics, as there are different contributions to this contrast which are hard to disentangle. For instance, in the case of donor–acceptor (D-A) bulk heterojunction (BHJ) organic photovoltaics, the SPV image owes its contrast to variations of the carrier dynamics at the local scale but also to variations in the D-A gap.[27]

In FMI-KPFM, the SPV is measured as a function of a modulated light source frequency. In this configuration, KPFM measures a temporally averaged surface potential (SP) value for each frequency of the modulated illumination source, as its compensation bias regulation loop cannot follow SPV variations faster than its integration time (typically a few tens of ms for an optimal signal to noise ratio). Figure 4.2 shows a schematic illustration describing the general implementation of FMI-KPFM.

In this configuration, spectroscopic curves of the SP as a function of the illumination modulation frequency f with a constant duty cycle (D) are acquired at each point of a pre-defined grid area over the sample. Here, we underline that generally, the sample illumination is performed in the large perturbation regime. This configuration is similar to the one of conventional macroscopic large perturbation transient photo-voltage (LPTV) experiments.[18]

This, due to the reduced SPV measured using KPFM compared to the open circuit voltage of a full solar cell device with electrodes. Indeed, with SPV of few tens of mV, it becomes challenging to operate FMI-KPFM in a true non-perturbative regime.

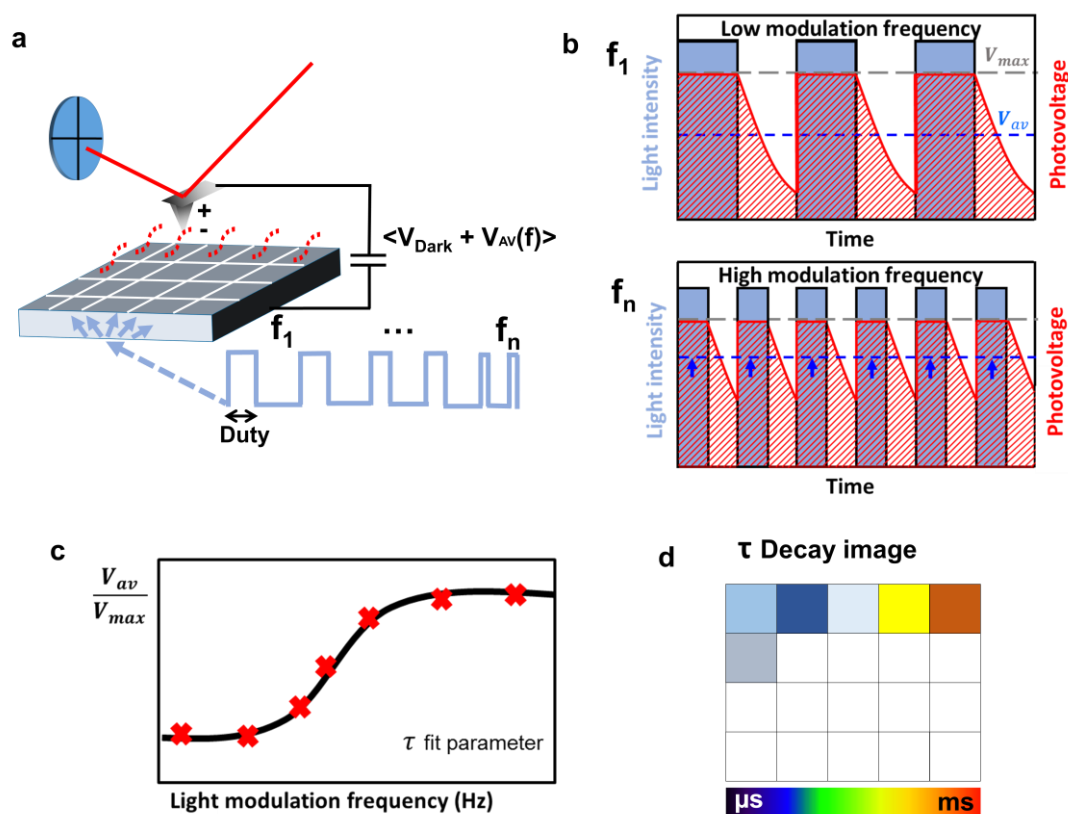


Figure 4.2– (a) Schematic illustration of FMI-KPFM. The KPFM surface potential is measured by applying a compensation bias to the oscillating AFM tip. Spectroscopy curves of the average surface potential (V_{AV}) are acquired at each point of a predefined grid over the sample’s surface, as a function of the illumination’s source modulation frequency (f). (b) Surface potential time-response for increasing modulation frequencies. (c) Spectroscopic curve $V_{\text{AV}}(f)$. The decay time constant is extracted by performing a numerical fit. (d) Automatic curve fit operation is performed on each pixel to recalculate 2-dimensional images of the SPV decay time constant (τ). Panels (a), (c) and (d) were adapted from Ref. [17], panel (b) was adapted from Ref. [9]

Furthermore, the acquisition time of a single spectroscopy curve is typically in the range of 1 to 10 seconds. This time depends on the number of selected frequencies. Typically between five and few tens frequency points are needed. Moreover, for each frequency, the data acquisition time is fixed to overpass the KPFM integration time constant, typically yielding a 100-200 ms data acquisition time.

Taking into account that measurements are carried out over a typical 100x100 square grid area, the total duration of a single experiment can overpass a 24-hours' time period. For this reason, KPFM measurements are performed in single pass mode[19] in combination with beam deflection non-contact (nc-)AFM under ultrahigh vacuum (UHV). Moreover, while all 2-dimensional frequency-spectroscopy data presented in this work have been achieved in closed loop mode, (*i.e.*, uninterrupted z-regulation), in the next chapter we will briefly comment on the advantages and disadvantages of this operation mode against open loop mode.

Furthermore, dynamical surface photo-voltage imaging with KPFM relies on a synchronous acquisition of the 2-dimensional frequency-spectroscopy measurements with regards to the illumination modulation frequency sweep. In fact, as depicted in Figure 4.3, in our setup, we ensure this synchronization by employing logic signals generated by the AFM controller to externally trigger an arbitrary waveform generator (AWG). The latter is used to generate the illumination pulse groups at the selected frequencies by modulating an adjustable output power high frequency (HF) diode-laser device employed to illuminate the sample.

In practice, this has been done using a Keysight 33622 AWG, interfaced with the AFM controller. A list of discrete frequencies can be defined using the 33622 AWG's frequency-sweep option. The generation of each pulse group is triggered during the data acquisition by using a user-configurable analogue output. The data is then acquired by using a multiple-spectroscopy routine, which repeats n times the same process for each image's pixel. Moreover, in the case of the scanning probe microscope (SPM) system controlled using the Nanonis software (LETI's setup), the data is stored as a stack of 2-dimensional images of the average surface photo-potential at a given illumination modulation frequency, instead of series of spectral curves. This, as a result of the SPM controller internal structure. A post data

processing is therefore needed to “re-create” $V_{AV}(f)$ curves at each image’s pixel as depicted in Figure 4.4. Conversely, in the case of the SPM system controlled using the Matrix software (INAC’s setup), a series of spectral curves are directly stored.

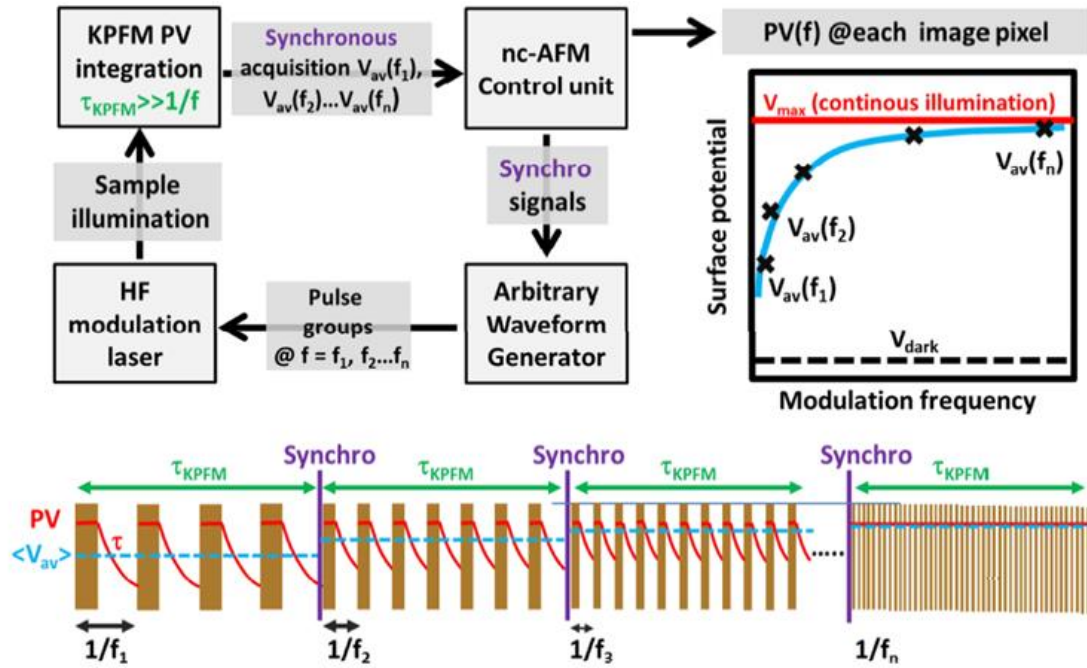


Figure 4.3– 2-dimensional spectroscopy data acquisition: Synchronizing signals are generated by the AFM controller, to trigger the generation of pulse groups at pre-selected frequencies ($f_1, f_2 \dots f_n$) by the AWG.

The KPFM loop integrates the SP (in red) with a time constant of few tens of milliseconds, yielding an average value V_{av} (in blue). $V_{av}(f)$ values are simultaneously recorded by the AFM controller as a stack of images at a given illumination modulation frequency.

In terms of data treatment, the temporally averaged surface potential V_{AV} measured by KPFM can be defined as the time domain integral of the SPV. In fact, if one considers a zero SPV built-up time, which is the time needed for the surface photovoltage to appear in the first place (associated with the exciton generation, charge dissociation and charge transport along the material so that a photo-generated surface potential can be detected using KPFM), the SPV decay time-constant can be extracted by fitting the spectroscopy curves using the following equation[8, 9, 17], (note that the development of the following equation can be found in the appendix section of this thesis).

$$V_{AV}(f) = V_{Dark} + SPV \cdot D + \tau_d \cdot f \cdot SPV \left(1 - e^{-\frac{(1-D)}{\tau_d \cdot f}}\right) \quad (4.1)$$

here V_{Dark} is the in-dark surface potential, SPV the surface photo-voltage measured under continuous wave illumination, τ_d the SPV decay time, f the modulation frequency and D the illumination duty ratio. Note that Eq. 4.1 does not take into account a SPV built-up time, this is justified since in most cases, this time is usually much faster than the SPV decay time.

In order to fit the 2-dimensional matrix of spectroscopy curves, an automatic curve fit operation routine based on the least-square method was developed using the SCILAB software. Furthermore, same results were obtained by using the batch processing options of OriginPro software (OriginLab Corp.). This routine allowed us to import the spectroscopic curves and to recalculate 2-dimensional images of each curve's characteristic time-constants.

4.2.1 Silicon based photovoltaics

Having described the FMI-KPFM operation principle, the first implementation results over silicon based photovoltaic samples will be presented in this section. Here, the discussion will focus on the role of recessed grain boundaries on carrier recombination over a small grain polycrystalline silicon sample. Additionally, the influence of nanocrystal aggregates on the minority carrier lifetime of a silicon nanocrystal-based third generation solar cell will be investigated. In fact, as we will see further on, for this analysis to be performed, statistical fluctuations of the numerical fit procedure shall be ruled out as a possible source of contrast on the obtained SPV decay time image. For this reason, the standard error associated with the mathematical fit procedure performed over each spectroscopy curve will be imaged. This will allow us to confirm that the contrast present on the calculated SPV decay time image has indeed a physical origin.

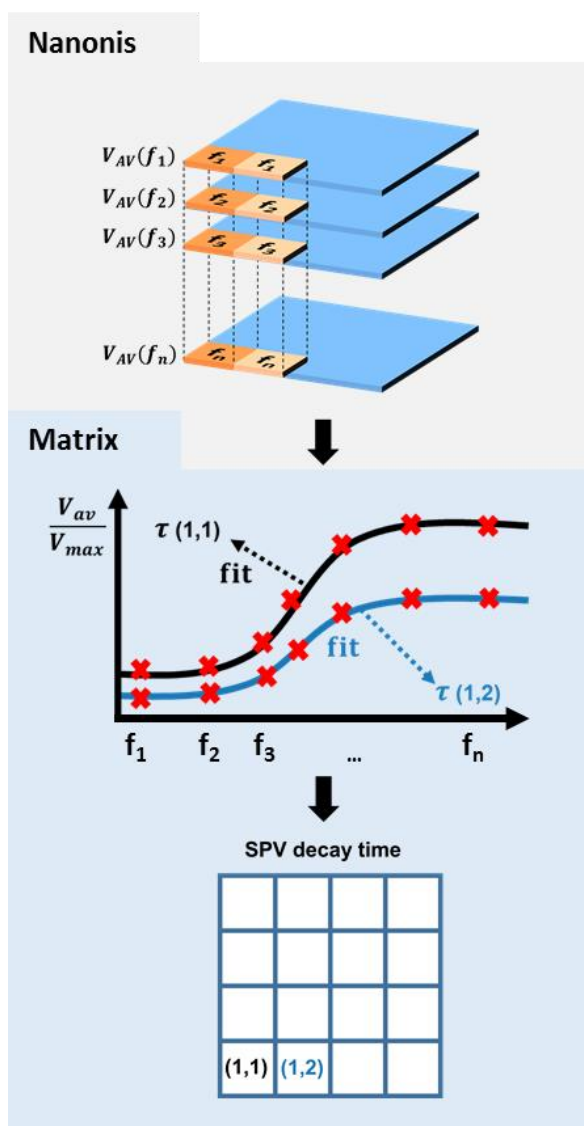


Figure 4.4– The spectroscopic approach is based on the acquisition of curves of the surface potential as a function of the illumination source modulation frequency on a 2-dimensional grid. When using the Nanonis SPM controller, the spectroscopic data is recorded as a stack of images. A post processing treatment is performed to reconstruct $V_{AV}(f)$ curves, and extract a time-constant on each pixel of the grid. When using the Matrix SPM controller, this step can be skipped.

4.2.1.1 Small grain polycrystalline silicon

As a first example of the implementation of FMI-KPFM, we mapped the spatial variations of the effective minority carrier lifetime in a small grain polycrystalline silicon thin

film grown on n-doped silicon. This sample was prepared by depositing polycrystalline silicon films by chemical vapour deposition onto an n-doped silicon substrate (phosphorus doping level in the 10^{15} cm^{-3} range), under $(\text{SiH}_4)/\text{H}_2$ flux at $800 \text{ }^\circ\text{C}$ and under a 20 Torr pressure. A post deposition annealing was performed under hydrogen flux to remove the native oxide. Additionally, to reduce the surface roughness (which originates from the variations in the grain crystallographic orientation), the films were polished before AFM/ KPFM characterizations by using chemical-mechanical planarization.

In this sample, FMI-KPFM was implemented using beam deflection non-contact AFM in frequency modulation mode under UHV. The topographic imaging was performed with frequency shifts (negative set-points) and vibration amplitudes of a few Hz and a few tens of nanometres, respectively. KPFM measurements have been performed in frequency modulation (FM) mode. Moreover, all data have been acquired with PtIr-coated silicon cantilevers (EFM, Nanosensors, resonance frequency in the 45–115 kHz range) annealed under vacuum to remove contaminants. Concerning the illumination source, a red laser (657 nm) from the Picoquant Company (Germany) was used in front side geometry (*i.e.*, sample directly illuminated by the laser). Here, the used optical power (2.24 mW/mm^2) is defined per unit of surface by taking into account the laser beam diameter. Besides, it is normalized in root mean square (RMS) units (*i.e.*, averaged power over one modulation cycle).

Upon FMI-KPFM single point measurements, a positive surface photovoltage was observed. Indeed, this positive surface photovoltage is consistent with the band alignment at the recessed Si/n-Si interface as depicted in Figure 4.5.

FMI-KPFM results over the sample are presented in Figure 4.6. Here, we note that, even after the surface polishing process, submicron sized domains can be easily identified in the AFM topographic images taken over the sample (Figures 4.6b,d). Over this sample, effective minority carrier lifetime values around few tens of μs were obtained upon the mathematical fit of the spectroscopy curves using Eq.4.1. A deeper analysis of the obtained images (Figures 4.6c,e) reveals the presence of dark patches of few tens of nanometres wide

which were found to be correlated with local contrasts in the damping images (Figure 4.6f), where the average effective carrier lifetime is significantly reduced.

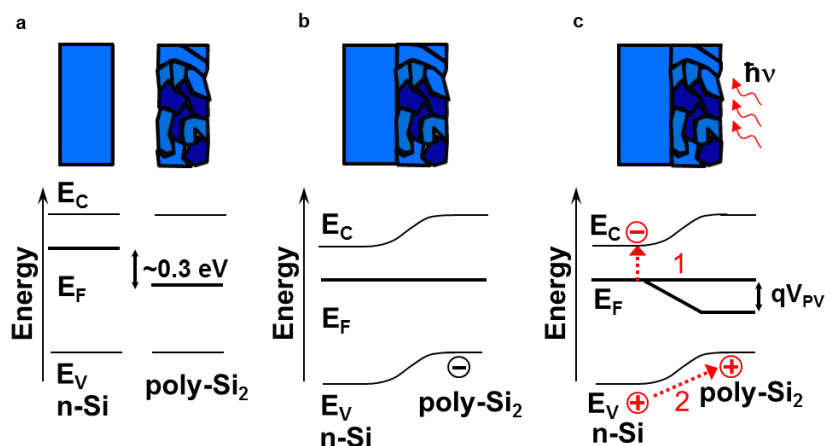


Figure 4.5– Schematic illustrations of the energy band diagrams for the n-doped silicon substrate (n-Si) and the poly-crystalline silicon thin film (poly-Si). **(a)** Hypothetic case without contact. The 0.3 eV shift between the Fermi levels is due to the doping (10^{15} cm⁻³) of the n-Si substrate. **(b)** Fermi level alignment and band bending under contact (dark state). **(c)** Under illumination, the holes accumulate in the poly-Si due to the internal electric field at the n-Si/poly-Si interface, this hole injection results in the tension identified as photovoltage V_{PV} . All panels were reproduced from Ref. [17].

The images taken at higher magnification display the same features than larger-scale images (Figures 4.6d,e) confirming that the observed contrasts have a physical origin. These observations are indeed consistent with an enhanced non-radiative Shockley–Read–Hall recombination due to surface states or recessed grain boundaries. Indeed, both effects are likely to occur in this sample because of the high density of grains with non-equivalent crystallographic orientations.

Additionally, the measured effective carrier lifetime values also suggest that non-radiative processes should be indeed the major pathway for the photo-carrier recombination in this sample.

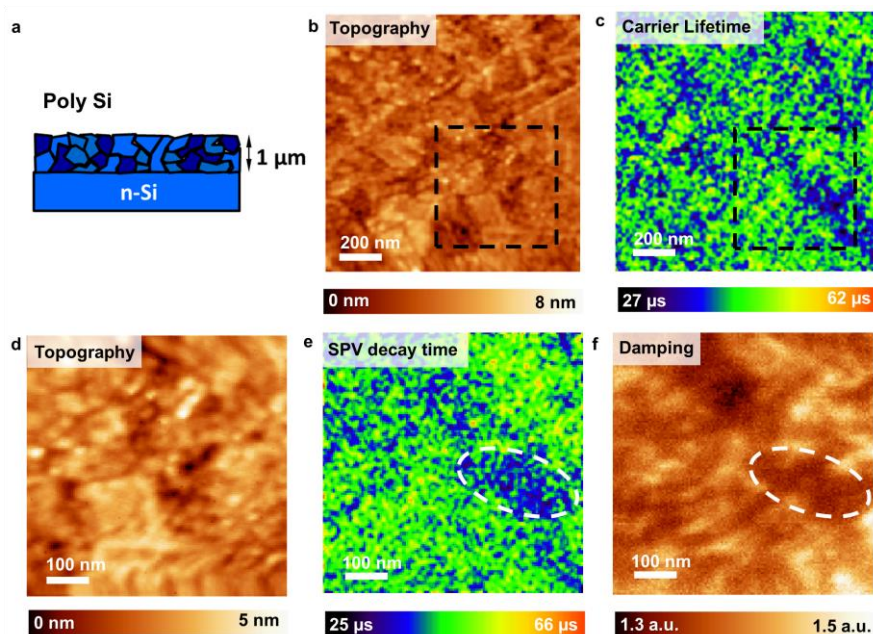


Figure 4.6– (a) Schematic structure of the poly-Si film grown by chemical vapour deposition on an n-doped silicon substrate. (b,c) Topographic and minority carrier lifetime images (150×150 pixels, 1500×1500 nm) acquired during the 2-dimensional spectroscopy under frequency-modulated illumination (655 nm, 20% duty, 2.24 mW/mm^2). (d–f) Topographic, SPV decay time, and dissipation images (128×128 pixels, 700×700 nm) acquired on the area highlighted by black dotted contours in b and c. White-dotted lines in e and f highlight correlations between local contrasts in the damping and SPV decay time images. All panels were reproduced from Ref. [17].

4.2.1.2 Silicon nanocrystal-based third generation solar cell

Having demonstrated a first implementation example of FMI-KPFM over a small grain polycrystalline silicon thin film, we now turn to a slightly more complex sample. In this section, we will investigate a silicon nanocrystal-based third generation solar cell as a second application example of the technique in the field of inorganic photovoltaics. A schematic structure of this sample is depicted in Figure 4.7a. A top view of the sample acquired by transmission electron microscopy (Figure 4.7b) shows the nanocrystals embedded in the SiO_2 matrix, the nanocrystals display difference sizes ranging from 3 to 10 nm and are

heterogeneously distributed. Moreover, nanocrystals with hydrogenated bonds have been used to reduce defects at the interface with the SiO₂ matrix.[20]

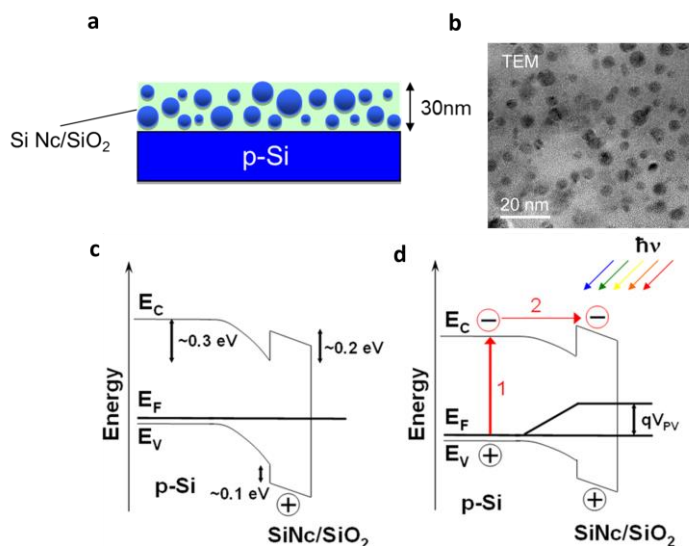


Figure 4.7– (a) Cross-sectional schematic of a sample with SiNC embedded in 30 nm of SiO₂. The layer of SiO₂ is deposited on the p-Si substrate. (b) Top view of the sample made using transmission electron microscopy. Schematic illustration of energy band diagrams of p-Si substrate and SiNC/SiO₂ layer in two cases: (c) layers are bounded and the internal electric field allows the Fermi levels alignment of the junction and (d) layers are bounded and under illumination. In this case, photo-generated electrons in the p-Si substrate are injected to the SiNC/SiO₂ layer, this injection gives origin to the potential identified as photo-voltage V_{PV} . All panels were reproduced from Ref.[21]

In this sample, a negative surface photo-voltage is observed. Indeed, under illumination, electron-hole pairs are photo-induced in the p-doped substrate. Subsequently, electrons are injected from the p-Si layer to the SiNc/SiO₂ matrix due to the band bending at the p-Si/SiNc/SiO₂ interface, resulting in a negative surface photo-voltage as depicted in Figures 4.7c-d.

Here, the FMI-KFPM measurements were carried out using a red (685 nm) LuxX (OmicronLaseraage GmbH) laser in front side geometry with an optical output power of 0.61 mW/mm² as the illumination source. During the 2-dimensional spectroscopy the illumination modulation frequencies were swept from 500 Hz to 120 kHz with a 50% duty.

Spectroscopic curves (Figure 4.8e) were fitted using Eq. 4.1, yielding effective minority carrier lifetimes of a few tens of microseconds. These results are consistent with the lifetime values previously measured on discrete locations of samples from the same series in “single-point” mode[9] and with photoluminescence measurements performed on similar SiNC/SiO₂ systems.[22] Moreover, the lifetime values indicate that non-radiative processes are the major pathway for the photo-carrier recombination. Theoretical calculations[23] have indeed shown that radiative recombination should occur on the ms time scale. Despite defects reduction by hydrogen passivation, dangling bonds[24] can still be present and act as local non-radiative recombination centres.

Now, the question that present itself is whether the 2-dimensional effective minority carrier lifetime map (Figure 4.8c) displays a contrasts that could be related to the sample morphology at the nanoscale. Unfortunately, the nature of the surface morphology does not allow identifying individual nanocrystals. Besides, neither the topographic nor the damping contrasts (Figure 4.8b) seem to display systematic correlations (nor anti-correlations) with the lifetime contrasts. In turn, it is clear that the lifetime image displays local contrasts which cannot be accounted by simple statistical fluctuations. This assumption is supported by the standard error (*i.e.*, standard deviation) of the mathematical fit performed over each spectroscopy curve. In fact, an image displaying this associated standard error value for each pixel of the effective minority carrier lifetime map is presented in Figure 4.8d.

The absence of systematic correlations between the effective carrier lifetime image and its associated error image strongly support the hypothesis that local contrasts present in the dynamical image must have a physical origin. In turn, these contrasts may be accounted by the existence of nanocrystals aggregates (or area displaying a higher density of nanocrystals), which would act as local recombination centres. The transmission electron microscopy image (Figure 4.7b) indeed revealed a non-uniform distribution of the nanocrystals within the silicon oxide matrix.

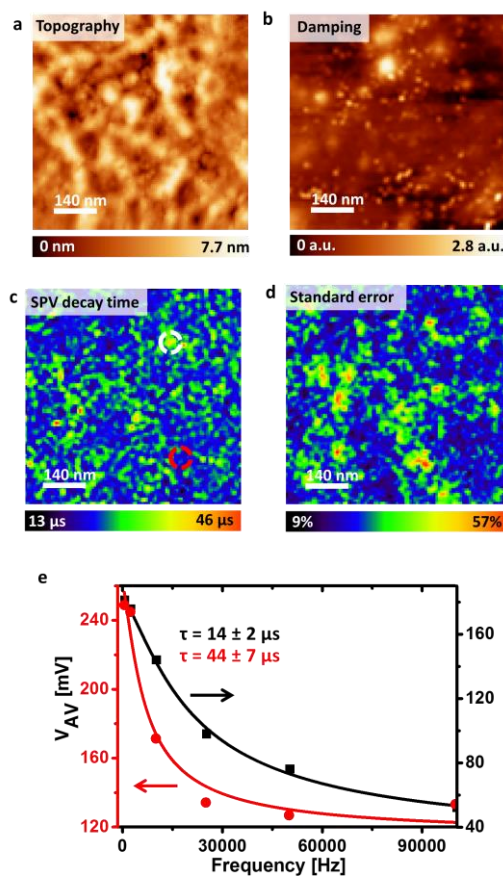


Figure 4.8– **(a)** Non-contact AFM topographic image (100×100 pixels, 700×700 nm) acquired during FMI-KPFM investigation (685 nm, 50% duty, 0.61 mW/mm²). **(b)** Damping image. **(c)** SPV decay time image. **(d)** Standard error of the SPV decay time image. **(e)** Spectroscopic curves showing the SPV evolution with respect to the illumination frequency modulation. Red and black curves were obtained over areas indicated in c as white and red dotted circles respectively. Panel a, and panels c-e were reproduced from Ref. [21]

Alternatively, surface contaminants could be invoked to account for the existence of localized recombination centres. However, this latter hypothesis seems unlikely, as the damping and lifetime contrasts are not clearly correlated nor anti-correlated.

4.2.2 Bulk heterojunction donor-acceptor organic photovoltaics

The study of the optoelectronic properties of organic photovoltaics (OPV) with KPFM can be traced back to the beginning of the twenty-first century. Around that time, a milestone in the field was reached thanks to the work of Shaheen and co-workers [25] who demonstrated that the D-A blend morphology plays a crucial role in the overall performance of OPV devices. In fact, the authors demonstrated that by implementing a much finer phase segregation between the donor and acceptor components, conversion efficiencies could be dramatically improved. This work was the predecessor of a series of investigations aiming to unveil the complex interplay between the D-A phase composition, interfaces morphology, photo carrier dynamics and transport. Actually, poly(2-methoxy-5-(3',7'-dimethyloctyloxy)-1,4-phenylenevinylene blended with methano-fullerene(6,6)-phenyl C₆₁-butyric acid methyl ester (MDMO-PPV-PCBM) has been used as a benchmark by several teams working in the field of KPFM measurements. Among these investigations we highlight the work of Chiesa et al.[26] who established the strength of KPFM to locally probe the photo-carrier generation in polymer solar cells.

KPFM is now a well-established technique which is often used to image the local SPV of bulk heterojunction (BHJ) D-A OPV samples.[27] This is done by performing KPFM investigations under dark conditions followed by under illumination measurements. Subtracting CPD images obtained under both conditions should yield the SPV image which in turn can be described as a kind of local mapping of the open circuit voltage.[28] As mentioned before, the SPV image owes part of its contrast to variations of the carrier dynamics at the local scale. However, this approach does not allow to separate the contributions of variations in the D-A gap from the contribution of charge carrier dynamics to the SPV contrasts. [28]

In that context, in the following, we will present our first attempts to use FMI-KPFM to address this issue at least to some extent. Actually, we will show how our technique can be used to map local non-geminate recombination rates in BHJ D-A organic photovoltaics. It is important to mention that results shown hereafter over OPV samples were obtained during the early stages of the technique's development, therefore results interpretation could be affected

by the presence of a few artefact sources. These possible sources of artefacts will be discussed in detail in the following chapter. Furthermore, in **Chapter 5** we will present a complementary set of results over OPV samples in which most sources of artefacts are accounted for.

Having said that, in the following we will investigate a BHJ OPV blend based on a fullerene derivative (IC₆₁BA) as the electron acceptor and a homemade (by INAC team) synthesized electron donor polymer (PDBS-BitQx).[29] This sample was selected as a first example of the implementation of FMI-KPFM on organic blends, as it features mesoscopic domains (Figure 4.9c) related to a compositional variation. Therefore, lifetime contrasts are highly likely to occur at the mesoscopic scale. Here, FMI-KPFM investigations were carried out in frequency modulation KPFM mode using a green (515 nm) LuxX (OmicronLasertechnik GmbH) laser in back side geometry (Figure 4.9a) with an optical output power of 0.32 mW/mm² as the illumination source. Moreover, during the 2-dimensional spectroscopy the illumination modulation frequencies were swept from 440 Hz to 10 kHz with a 20% modulation duty ratio. Spectroscopic curves were fitted using Eq. 4.1, yielding SPV decay times between few tens and few hundreds of microseconds.

FMI-KPFM results are presented in Figure 4.9. While, an overall negative shift of the surface potential of the sample is observed under illumination, consistent with the donor and acceptor energy level alignment with respect to the grounded substrate as depicted in Figure 4.9b, it is however interesting to observe that some regions of the sample exhibit a positive SPV behaviour (Figures 4.9d and 4.9e). In fact, the presence of a dual SPV behaviour could actually be considered as an intrinsic property of bare nanophase segregated organic blends, where both the electron donor or electron acceptor materials can form clusters near the surface which are embedded in a matrix of the opposite material, therefore revealing the presence of a different charge population, when under illumination.

In other words, even though a compositional gradient or non-inverted morphology is usually present, favouring the apparition of a single SPV polarity under illumination *i.e.*, a favourable concentration of the donor or the acceptor material at the surface[27], the presence

of clusters of the opposite material near the surface is very likely to be the reason behind the detection of a SPV whose polarity change from one region to the other over the sample.

Concerning the dynamic of this SPV, FMI-KPFM results show as expected a SPV decay time image (Figure 4.9f) displaying a contrast at a scale that matches that of the mesoscopic domains present in the topography.

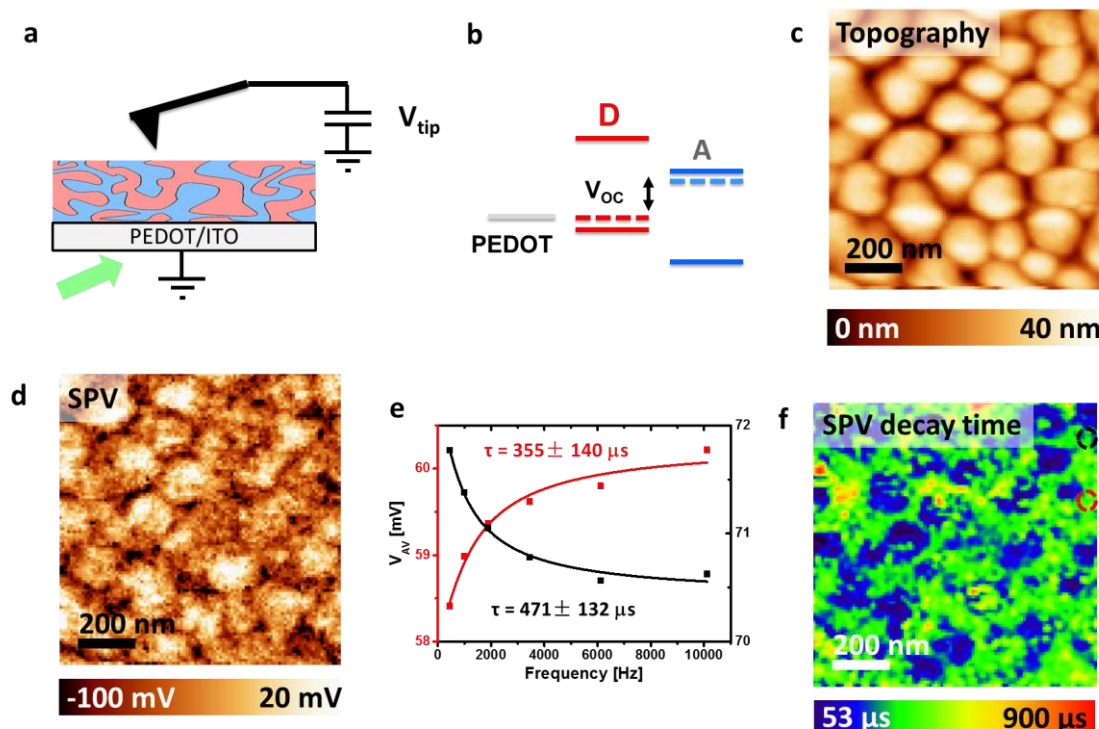


Figure 4.9– (a) FMI-KPFM investigations on back side geometry configuration. (b) Energy level alignment with respect to the grounded substrate. (c) Non-contact AFM topographic image (100×100 pixels, $1 \times 1 \mu\text{m}$) acquired during FMI-KPFM investigation (515 nm , 20% duty, 0.32 mW/mm^2). (d) SPV image displaying both a positive and a negative behaviour which appears to be position-dependent. (e) Spectroscopic curves showing the positive and negative SPV evolution with respect to the illumination modulation frequency. The black and the red curves indicate the mathematical fit adjustment over the data points indicated in f as black and red dotted circles respectively. (f) SPV decay time image displaying a contrast at a scale which matches that of c and d.

Now, to gain a deeper insight onto the sample structuration and the SPV dynamic at the nanoscale, we need to zoom-in. Indeed, in a second experiment, FMI-KPFM investigations were zoomed-in, and carried out in amplitude modulation KPFM mode with a 10% modulation duty ratio. All other parameters were kept the same. Results of this implementation are presented in Figure 4.10. Sample topography and damping images are shown in Figure 4.10a and Figure 4.10b respectively, while Figures 4.10c and 4.10d displays the SPV and the SPV decay time images correspondingly.

In this set of results the first thing we notice is that the SPV values exhibit a negative behaviour over all regions of the sample (Figures 4.10c and 4.10e), although this could be attributed to the fact that in amplitude modulation KPFM mode, the electrostatic force detection involves the whole tip and cantilever, consequently, the measured SP could be in fact the result of the averaging of different charges populations over an area of several tens of nanometres. This effect will be discussed in detail in **Chapter 5** when comparing the implementation of FMI-KPFM in both amplitude and frequency modulation modes.

For now, let us focus on the strong correlation between the damping and the SPV decay image, a correlation which sometimes can be extended to the topography image as well. Actually, from the damping image which is related to the chemical composition of the sample, it seems that mesoscopic features present in the topography image, possess in fact an internal nanoscale phase separation which can also be observed in the SPV decay image. Let us be cautious, while a one to one identification cannot be established, we do observe that the morphology and/or the chemical composition varies at the scale of few tens of nanometres over these domains which in some cases can also be observed as a contrast variation on the SPV decay image. A distinctive feature present on the SPV decay image, reflecting this change on the composition, can be found in the upper left region of this image. Indeed, in this region we observe a domain which is roughly divided in two zones with a marked SPV decay time contrast (Figure 4.10d). This contrast can also be found on the damping image (Figure 4.10b), suggesting that in fact the D-A mix ratio is not entirely homogenous over this domain. This reveals once more than the mixing rate or D-A phase separation, has a strong impact on photo-carrier dynamics (and on the SPV polarity as previously observed in Figure 4.9d)

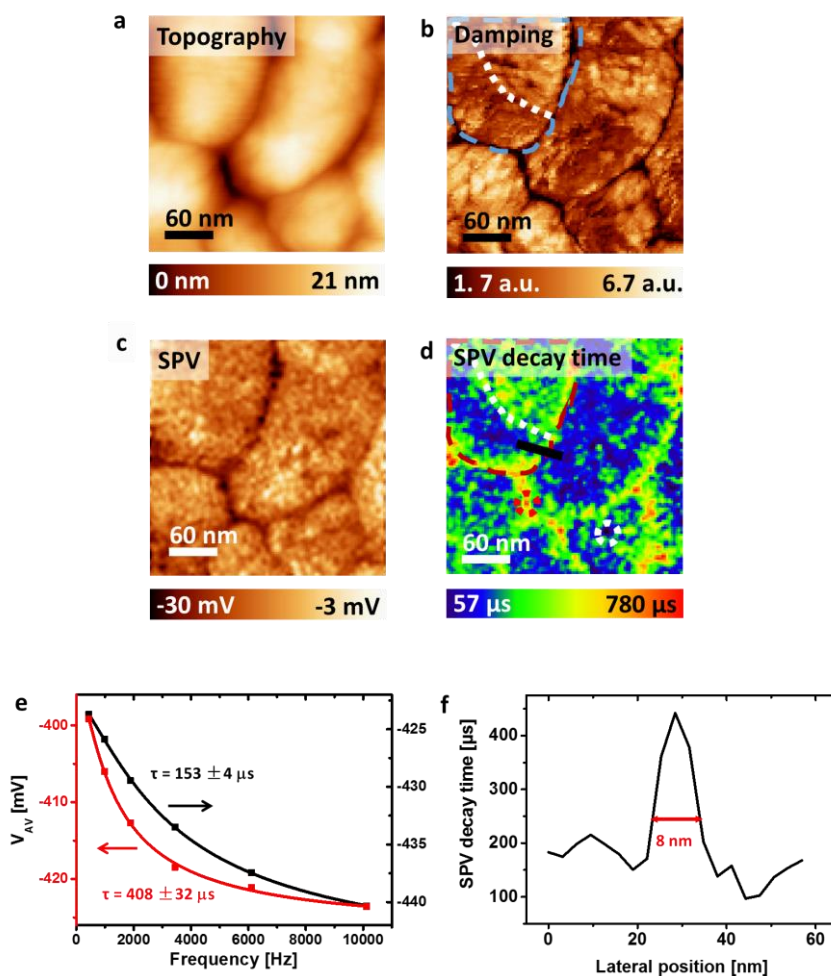


Figure 4.10– (a) Non-contact AFM topographic image (100×100 pixels, 300×300 nm) acquired during FMI-KPFM investigation (515 nm, 10% duty, 0.32 mW/mm²). (b,d) Damping and SPV decay time images respectively. In both images, dotted lines highlight a distinctive domain, roughly divided in two zones. In this domain it can be observed how the D-A phase separation impacts the photo-carrier dynamics. (c) SPV image displaying a negative behaviour (e) Spectroscopic curves showing the SPV evolution with respect to the illumination modulation frequency. Red and black data points were obtained over areas indicated in e as white and red dotted circles respectively. The black and the red curves indicate the mathematical fit adjustment over the data points. (f) Cross-section profile corresponding to the path highlighted by a black line in d.

Conversely, at the interface between these mesoscopic domains, the SPV decay time exhibit larger values, probably due to a lower D-A contact surface and/or due to a higher trap

density, hence lower recombination rates. While, the origin of the effective lifetime variations is unclear, this marked contrast at the interface between domains offer us the possibility to estimate the achievable FMI-KPFM lateral resolution as depicted in Figure 4.10f where a cross section profile over one of these interfaces regions on the SPV decay image reveals an achieved lateral resolution down to the sub-10 nm scale. This support the huge potential of our approach for local investigations on finely phase separated BHJ samples and other nanostructured and heterogeneous photoactive materials. Nevertheless, we highlight that this lateral resolution value should be considered an estimate, since actually, the precise quantification of FMI-KPFM lateral resolution is susceptible to be influenced by the mathematical fit accuracy of the spectroscopy curves as we saw before in the case of the silicon nanocrystal-based third generation solar cell. However, a weighted image of the SPV decay time taking into account the plausible lateral fluctuations due to the error margin of the mathematical fit (not shown) displays the same general contrast observed in Figure 4.9d.

Now, a deeper insight about the mechanisms behind the SPV decay time can be gained by analysing its evolution as a function of the intensity of the illumination source. Figure 4.11a shows a series of SPV decay images acquired over the same area of the sample for different light power conditions.

In Figure 4.11a it can be clearly observed that longer SPV decay times are displayed for images acquired at reduced illumination output powers. In fact, this is confirmed by Figure 4.11b where the average SPV decay time values measured over the white dotted circles present over the SPV decay time images as well as over the domains boundaries are plotted as a function of the illumination output power. Actually, this behaviour is consistent with carrier-concentration dependent non-geminate recombination processes, although we cannot exclude the existence of charge traps.[15, 30]

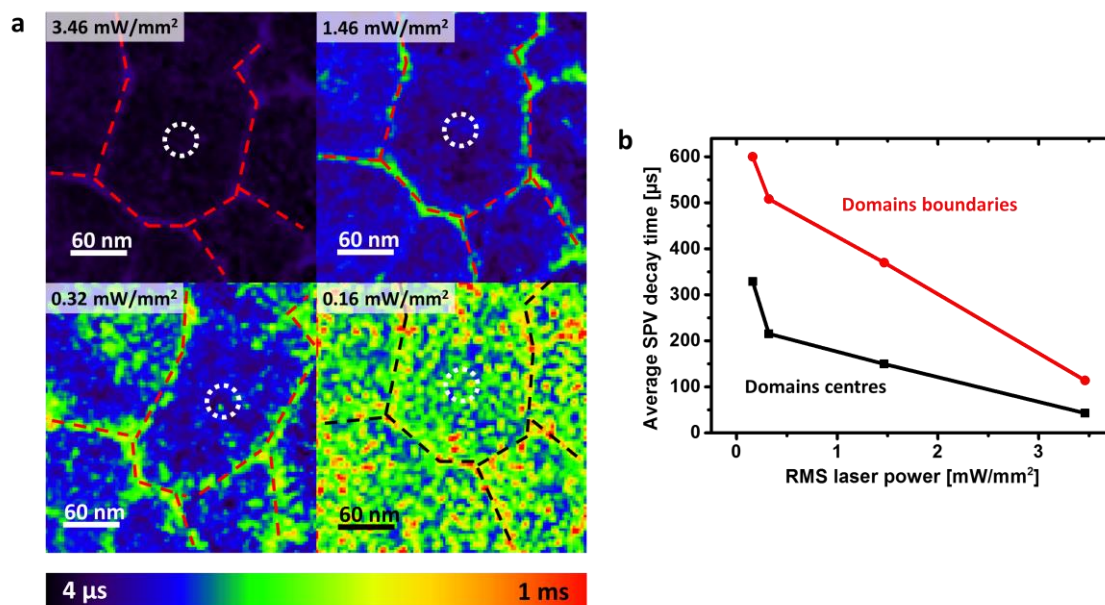


Figure 4.11– (a) SPV decay images acquired over the same area of the sample for different illumination intensities: from top to bottom and left to right: 3.46, 1.46, 0.32 and 0.16 mW/mm² respectively. Dashed lines over the images are eye guidelines indicating the same features over each image. (b) Average SPV decay time values measured over the white dotted circles present in a, and over the domains boundaries as depicted by the red dotted lines present in a as well, plotted as a function of the illumination output power.

Moreover, from Figure 4.11a, it can also be observed that images taken at reduced illumination output powers seems to be less resolved than those acquired at higher illumination intensities. This effect most likely reflects the impact of the fit accuracy on the global image contrast. Indeed, a quick comparison of the mathematical fit standard error for each of the images presented in Figure 4.11a (not shown), reveals a higher standard error of the mathematical fit for decreasing illumination output powers. This can be simply understood by considering the fact that spectroscopy curves acquired under higher optical powers display a larger SPV magnitude. This shows once again, that the SPV decay time image contrast (and by extent the lateral resolution) can be impacted by the accuracy of the post data acquisition numerical fit. This points out the crucial need to optimize the signal to noise ratio of the spectroscopic curves.

4.2.2.1 Pushing the illumination modulation frequency to the MHz regime

As a second application example of FMI-KPFM in the field of OPV, we now switch to a nanophase segregated BHJ solar cell based on a fullerene derivative (PC₇₁BM) as the electron acceptor and a homemade synthesized (by INAC team) wide bandgap polymer (PDBS-TQ) as the electron donor, yielding power conversion efficiencies over 5%. [29, 31] Here, we will explore what happens to the spectroscopy curves of the average potential when we push the illumination modulation frequency at values above 50 kHz. In fact, we note that to the best of our knowledge, prior to this work, all published photo-carrier dynamics investigations based on the use of KPFM under modulated illumination over BHJ D-A blends, were carried up to a modulation frequency of *ca.* 50 kHz. Up to that modulation frequency value, the average potential spectroscopy curve exhibit a monotonic dependence with respect to the modulation frequency of the illumination source. However, we will see that by further pushing the illumination modulation frequency, a non-monotonic behaviour of the average potential is revealed.

This non-monotonic behaviour can be observed in Figure 4.12. In this figure, we show the spectroscopy curve of the average potential as a function of the modulation frequency of the illumination source (PhoxXplus module from OmicronLaserae GmbH, rise and fall times <1.5 ns in digital modulation mode, 515 nm, 10% duty, 3.8 mW/ mm², large perturbation regime). Here, FMI-KPFM measurements were carried out using amplitude modulation KPFM in single point mode.

In this curve, we observe that when increasing the modulation frequency from 300 Hz to *ca.* 20 kHz, the average potential decreases toward more negative values, *i.e.*, the magnitude of the surface photo-voltage increases. Further increasing the frequency results in a photo-voltage diminution. However, surprisingly, the SPV does not vanish but increases again for frequencies higher than *ca.* 300 kHz. Our first interpretation of this phenomenon is that the measured average photo-potential shall originate from the contributions of (at least) two

different SPV components which are superposed and are characterized by strongly different dynamics.

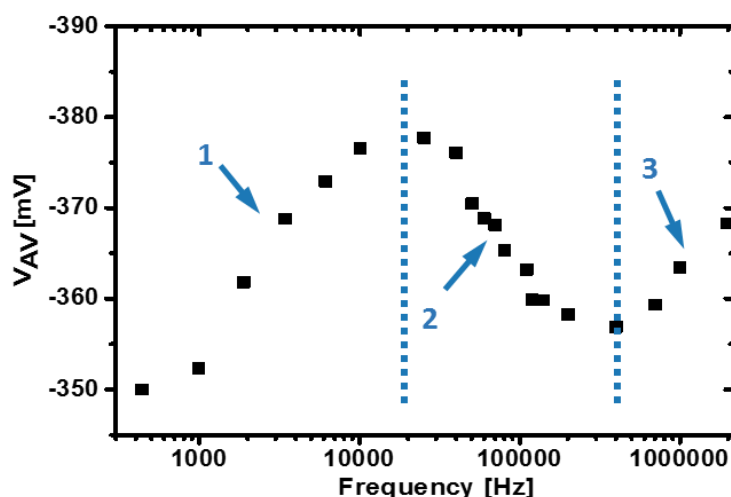


Figure 4.12– Spectroscopic curve of the average potential as a function of the modulation illumination frequency acquired over the nanophase segregated PDBS-TQ_x/PC₇₁BM blend. Blue dotted lines separated the three different regimes observed along the curve. These regimes reflect photo-carrier dynamics occurring simultaneously at different timescales.

Indeed, while in this first attempt to investigate the SPV behaviour at illumination modulation frequencies above 50 kHz, not all sources of artefacts were accounted for (see **Chapter 5** for the introduction of an improved FMI-KPFM protocol where most sources of artefacts are taken into account), and while it is true that alternative mathematical models can be proposed to describe the observed SPV non-monotonic behaviour, in all cases, the only reasonable way to explain this phenomenon, includes the presence of at least two different SPV components characterized by different dynamics. Furthermore, in the next chapter we will introduce additional evidence on the presence of these different SPV components and we will see that not only they can exhibit different dynamics, but they can also exhibit different polarities as well.

For now, in a first attempt to describe the SPV behaviour from Figure 4.12, a simplified mathematic model is proposed. Indeed, in a very naive approach, one could imagine the sum of the above mentioned average photo-potentials contributions, being represented by a dual set of independent parameters analogous to those previously introduced in Eq. 4.1.

For the development of this model, we will in a first step, no longer assume an “instantaneous” photo-charging, *i.e.*, we will consider a SPV built-up greater than zero ($\tau_b > 0$). Actually, $\tau_b > 0$ could indeed explain the second SPV regime as defined in Figure 4.12. In fact, for a given τ_b a certain light pulse duration is needed to attain the SPV saturation point. Moreover, as the illumination modulation frequency increases, and the light pulse duration is reduced, the instant SPV will eventually fail to reach its saturation point, thus decreasing the magnitude of the measured average SPV.

Taking into account the presence of $\tau_b > 0$ will result in Eq. 4.1 being partially modified as following:

$$\begin{aligned}
 V_{AV}(f) = & V_{Dark} + (V_{Light} - V_{Dark}) D \left(1 - e^{\frac{-D}{f\tau_b}} e^{\frac{-(1-D)}{f\tau_d}} \right) \\
 & + (V_{Light} - V_{Dark})(f\tau_d - f\tau_b) \left(1 - e^{\frac{-D}{f\tau_b}} \right) \left(1 - e^{\frac{-(1-D)}{f\tau_d}} \right)
 \end{aligned} \quad (4.2)$$

Eq. 4.2 defines the average photo-potential in the case of a single SPV component characterized by a built up and a decay time as depicted in Figure 4.13.

As mentioned, Eq. 4.2 can describe the first two regimes of the spectroscopic curve of the average potential presented in Figure 4.12. However it fails at describing the third regime present in the above presented curve.

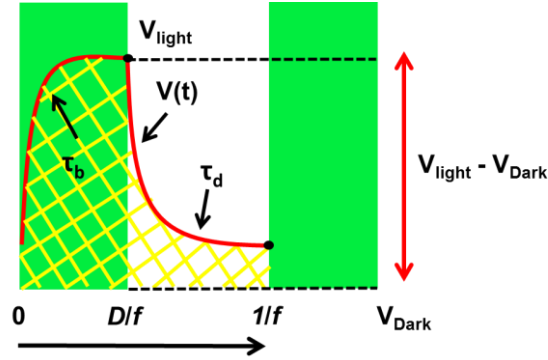


Figure 4.13– Case of a single SPV component characterized by a built up and a decay time

In order to account for this third regime, in a second step, we now introduce the concept of superposition to account for an average photo-potential that originates from the contributions of two different SPV components with strongly different dynamics. This results in an average photo-potential that can be described as:

$$\begin{aligned}
 V_{AV} = V_{Dark} + SPV_1 D \left(1 - e^{-\frac{-D}{f\tau_{b1}}} e^{-\frac{-(1-D)}{f\tau_{d1}}} \right) + SPV_1 (f\tau_{d1} - f\tau_{b1}) \left(1 - e^{-\frac{-D}{f\tau_{b1}}} \right) \left(1 - e^{-\frac{-(1-D)}{f\tau_{d1}}} \right) \\
 + SPV_2 D \left(1 - e^{-\frac{-D}{f\tau_{b2}}} e^{-\frac{-(1-D)}{f\tau_{d2}}} \right) + SPV_2 (f\tau_{d2} - f\tau_{b2}) \left(1 - e^{-\frac{-D}{f\tau_{b2}}} \right) \left(1 - e^{-\frac{-(1-D)}{f\tau_{d2}}} \right) \quad (4.3)
 \end{aligned}$$

where, $SPV_1 = V_{Light}^1 - V_{Dark}$, $SPV_2 = V_{Light}^2 - V_{Dark}$. Additionally, $\tau_{b1} \gg \tau_{b2}$ and $\tau_{d1} \gg \tau_{d2}$.

Eq. 4.3 defines the average photo-potential in the case of two different SPV components which are superposed and are characterized by strongly different dynamics as depicted in Figure 4.14.

However, we observe from Figure 4.12, that the average photo-voltage does not give any signs of decrease up to the upper modulation frequency allowed by the illumination chain. This can be interpreted as a light pulse duration (50 ns for a 2 MHz modulation frequency and a 10% duty cycle) which remains longer than the faster build-up time τ_{b2} . Therefore, the

second build-up time cannot be directly measured with our setup in its current form. This could explain the presence of three different regimes in the spectroscopy curve instead of four.

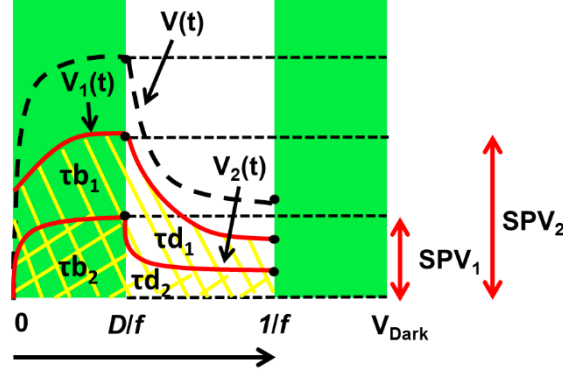


Figure 4.14– Case of two different SPV component characterized by different built up and a decay times

By extension, this also means that Eq. 4.3 can be simplified by making the approximation that $\tau_{b2} = 0$.

This will result in an average photo-potential that can be described in the following way:

$$V_{AV} = V_{Dark} + SPV_1 D \left(1 - e^{-\frac{-D}{f\tau_{b1}}} e^{-\frac{-(1-D)}{f\tau_{d1}}} \right) + SPV_1 (f\tau_{d1} - f\tau_{b1}) \left(1 - e^{-\frac{-D}{f\tau_{b1}}} \right) \left(1 - e^{-\frac{-(1-D)}{f\tau_{d1}}} \right) + SPV_2 D + SPV_2 (f\tau_{d2}) \left(1 - e^{-\frac{-(1-D)}{f\tau_{d2}}} \right) \quad (4.4)$$

Using Eq.4.4 we can now perform a mathematical fit to access the different dynamics of the spectroscopy curve presented in Figure 4.12. The result of this fit is shown in Figure 4.15.

While Eq. 4.4 constitutes a pragmatic solution to the challenge that represents FMI-KPFM data treatment in the case of a non-monotonic behaviour of the average potential, here, we raise awareness concerning the need to develop a more realistic and complete analytical model which should account for a series of photo-physical processes taken place in photo-active materials under modulated illumination, which in a first approach were excluded from

the above described model. In particular, Eq. 4.4 does not take into account the fact that depending on the imposed modulation frequency value, a quasi-steady state condition of the average potential is only reached after a certain number of excitation pulses.

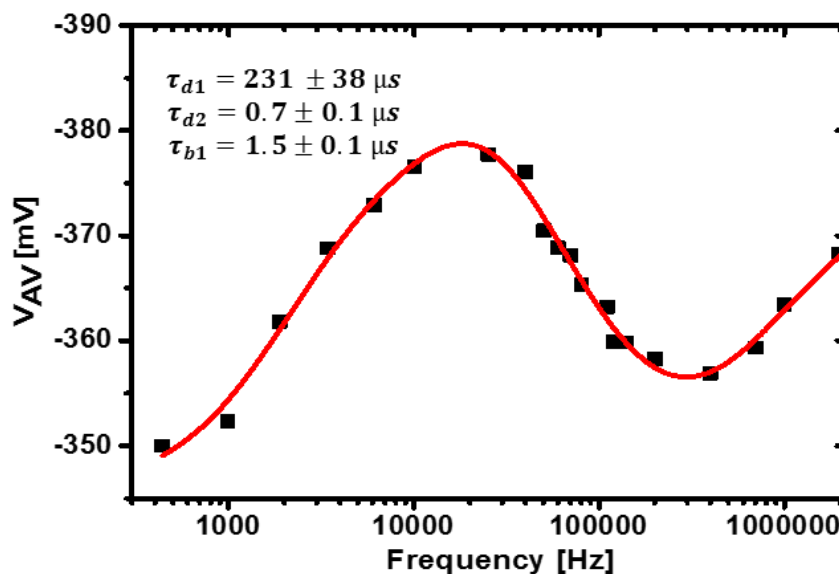


Figure 4.15– Spectroscopic curve of the average potential as a function of the modulation illumination frequency acquired over the nanophase segregated PDBS-TQx/PC₇₁BM blend. Red line correspond to the mathematical fit adjustment using Eq. 4.4.

Performing an analytical treatment of such phenomena was beyond the scope of this thesis, nevertheless an alternative numerical approach is proposed and demonstrated in **Chapter 6**. Indeed, in **Chapter 6** we will see how the behaviour of the spectroscopy curves of the average surface photo-voltage as a function of a frequency modulated excitation source in photovoltaic materials can be predicted using a numerical approach. This will enable in turn, the comparison between simulations and experimental results. This method represents an alternative way to determine the time constants values without the need to develop a complex analytical model.

In addition, so far we assumed that the superposed SPV contributions to the total average potential have same polarity, following previous studies including ours.[8-10, 17, 32]

However, as we will see in **Chapter 5**, in some BHJs samples, both positive and negative SPV behaviours can simultaneously coexist as a consequence of nanophase segregated clusters of different charge populations, suggesting that in fact FMI-KPFM data on BHJs can also be treated assuming superposed SPV contributions with inverted polarities.

Indeed, Eq. 4.4 should be understood as a simplified model, which here is implemented to perform the mathematical fit procedure required in FMI-KPFM, which in turn allow us to acquire several images of different photo-carrier dynamics occurring at different time scales within the sample. It is evident that time constant values calculated using Eq. 4.4 should be somewhat affected by approximations and simplifications of the model, therefore, caution should be taken when interpreting these values.

Having said that, we now turn to the results of FMI-KPFM implementation over the investigated sample, depicted in Figure 4.16.

In this sample we note that the dissipation image (Figure 4.16c) reveals that significant variations in the nanophase composition[33] occur at the scale of a few tens of nanometres.

Unambiguously, the dynamical images display heterogeneities at the same scale. This led us to conclude that both slow and fast SPV decay times are significantly impacted by morphological and/or compositional variations in this blend. However, we note that the dynamical contrasts does not display a systematic correlation (nor anti-correlation) with the dissipation ones. This observation suggests that while the damping contrasts originates only from variations in the tip-surface interaction, the dynamical ones may be influenced by contributions from the subsurface. The analysis of high-resolution images (not shown) demonstrates, however, that the dynamical SPV is not dominated by contributions from the bulk (otherwise local contrasts would be hardly resolved). In turn, these last data demonstrate the possibility to investigate the interplay between the nanostructure and the carrier dynamics down to the sub-10 nm scale.

Concerning the physical origin of these images, the question that presents itself is whether the fast and slow dynamics originate from different physical processes, or if one

measures only one phenomenon displaying different characteristic time scales. This could, for instance, be the case of a two trap population, the longer and faster decays being associated with the effect of deep and shallow traps, respectively.

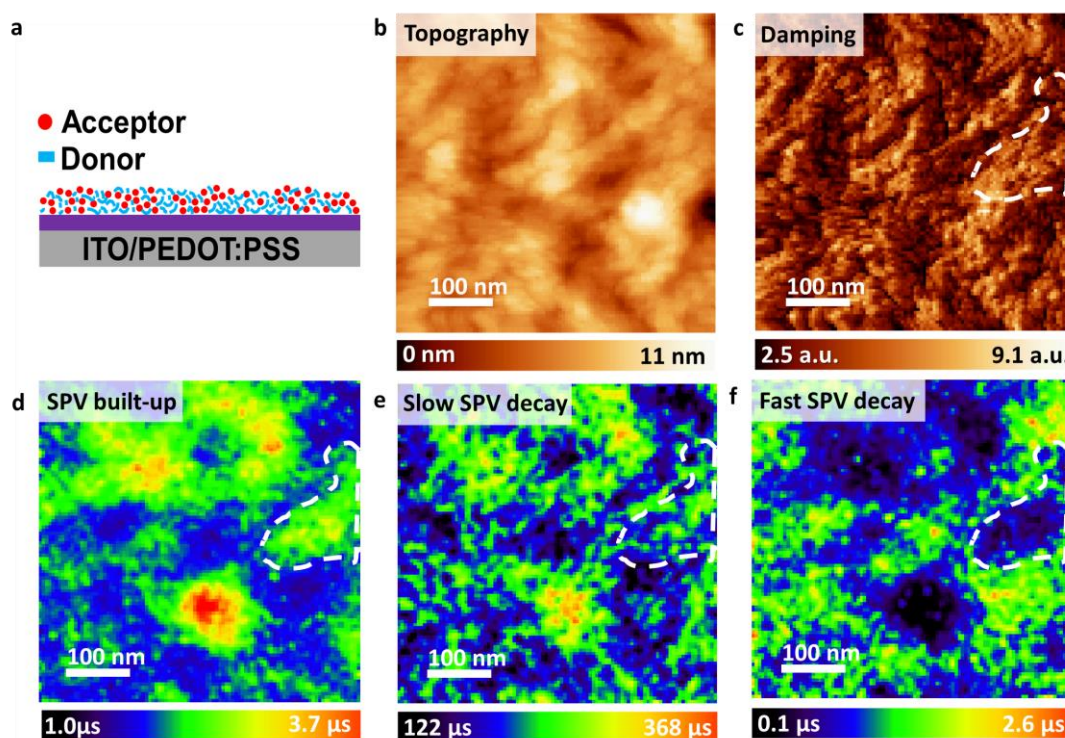


Figure 4.16– (a) Model proposed for the nanophase segregated PDDBS-TQ_x/PC₇₁BM blend morphology. (b) nc-AFM topographic image (100×100 pixels, 500×500 nm) acquired during the 2-dimensional spectroscopy under frequency-modulated illumination (515 nm, 10% duty, 3.8 mW/mm^2). (c) Dissipation image. (d–f) Images of (d) the “slow” build-up, (e) “slow” decay, and (f) “fast” decay time constants. All panels were reproduced from Ref. [17]

To answer this question, we will study the time constants evolution as a function of the intensity of the illumination source, just as we did in the case of the IC₆₁BA/ PDDBS-BitQ_x OPV blend. Figure 4.17a shows a series of spectroscopic curves acquired for different illumination conditions. The shape of these curves dramatically changes in the high frequency regime when decreasing the illumination intensity. The full set of fitted time constants is given in Figure 4.17b, which also shows that the fast decay time (τ_{d2}) constant is strongly reduced for

increasing optical powers, while the slow decay time (τ_{d1}) is quasi-independent of the illumination intensity. These behaviours are consistent and could be attributed to carrier-concentration dependent non-geminate recombination processes[15, 30] and trap-delayed mechanisms (with a recombination rate proportional to the trap density)[1, 30, 34] respectively.

We also note that the slow decay time (a few hundreds of microseconds) is similar to the lifetime of long-lived trap populations reported for other BHJ such as PBDTTPD:PCBM.[34] The fast decay times values (a few μ s for the maximum illumination intensity, *i.e.*, the maximum carrier density) seem also to agree relatively well with the results of macroscopic transient experiments on other blends.[18]

Moreover, concerning the origin of the built-up time, it could be tentatively attributed to the effective time needed to fill the traps responsible for the subsequent trap-delayed recombination mechanisms, however, more conclusive evidence is needed to validate this hypothesis since the relatively large τ_{b1} built-up times (few microseconds) observed in our experiments put some constraints on the physical nature of the trap states in our sample. However, we highlight that both the built-up and decay dynamics can strongly differ from one blend to the other depending of the relative strength of trapping effects[35] and can also change in time depending on the environmental conditions. This fact should be bear in mind when comparing our data with the results of former investigations carried out with macroscopic probes on other BHJs.

To sum it up, for the particular case of the PDDBS-TQx/PC₇₁BM sample[31], our first results suggest that the performance remain limited (with a maximum power conversion efficiency of ca. 5%) because of carrier trapping effects related to a non-optimized morphology.

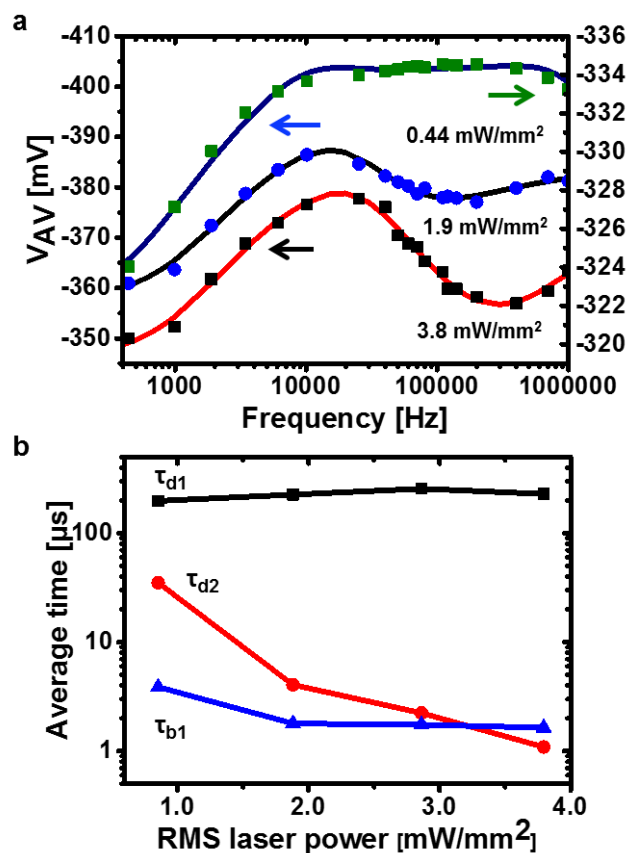


Figure 4.17– (a) Spectroscopic curves acquired for different illumination conditions on the nanophase segregated PDBS-TQx/PC₇₁BM blend. Black, blue, and green filled symbols represent the experimental data acquired at 3.8 mW/mm² (left Y scale), 1.9 mW/mm² (left Y scale), and 0.44 mW/mm² (right Y scale), respectively (all data recorded with a 10% duty). The red, black and dark-blue curves show the numerical fit for 3.8 mW/mm², 1.9 mW/mm² and 0.44 mW/mm² respectively. (b) Time constants as a function of the illumination intensity. All panels were adapted from Ref. [17]

4.2.3 Spectroscopic and time-resolved measurements over perovskite photovoltaics

As mentioned in **Chapter 2**, organic-inorganic hybrid perovskites have become a new stage for the improvement of state-of-the-art light harvesting devices.[36] This, due to an exceptional combination of properties such as direct band gap, high absorption coefficient and long effective carrier lifetimes among others. Indeed, during the past decade, photovoltaic solar

cells based on these materials have experience a skyrocketing increase on their energy conversion efficiencies, currently exceeding the 20% barrier.

A very important subject of research regarding perovskite photovoltaics, is the impact of grain boundaries on their internal electric field distribution and photo-carrier recombination mechanisms, especially in the case of polycrystalline thin films. Actually, this has been investigated using KPFM [37, 38], however, so far there is still a debate around whether the impact of the grain boundaries on the photo-carrier transport is beneficial or detrimental to the overall efficiency of the solar cell device. This uncertainty can be attributed to the contributions of ionic species to the surface potential contrasts.[37, 39-41] Actually, time-resolved measurements have given some insights pointing out to intra-grain ion migration mechanisms[40] as a phenomena which can significantly impact the surface potential measured by KPFM.

Nevertheless, despite an increasing amount of research, the understanding of the complex interplay that exists between the charge carrier populations, traps, and mobile ions remains uncomplete. Therefore, interpreting the surface potential and surface photo-voltage contrasts recorded by KPFM on polycrystalline lead halide perovskites thin films constitutes a difficult task.

In that context, perovskite single crystals [42, 43] represent an interesting alternative for basic research on hybrid perovskites. In fact, they can be used to probe the intrinsic material optoelectronic properties thanks to the absence of grain boundaries. Actually, performing KPFM measurements on single crystals may simplify the interpretation of the surface potential and surface photo-voltage data.

Another important subject of research involving these materials is the existence of a significant photostriction effect which can be roughly defined as the change of the internal strain of the material under illumination. In fact, this effect has been observed in MAPbI_3 single crystals by recording the height variations of an AFM tip as a function of the illumination state.[44, 45] This effect could potentially open the door to perovskite materials to a large range of applications such as the development of light-sensitive fast switching devices.

In the meantime, back to the field of photovoltaics, one of the main challenges that perovskite solar cells must still overcome in order to meet industrial production requirements, is to diminish the degradation of the material under operating conditions. Actually, as we will see in this section, the application of 2-dimensional FMI-KPFM investigations can be affected by this degradation effect. Indeed, performing these kind of investigations over perovskites can be quite challenging as the material tends to evolve during measurements.

In that context, here, in a first step, we will discuss the results of single point spectroscopy curves of the AFM tip height relative to the surface and of the surface potential during pulsed illumination sequences over a methylammonium lead tribromide single crystal ($\text{CH}_3\text{NH}_3\text{PbBr}_3$ also referred to as MAPbBr_3), since as mentioned before the study of this sample may allow the simplification of the SPV interpretation in terms of the intrinsic optoelectronic properties of the material. For this, we will look to reproduce experimental results previously reported by Almadori and co-workers.[45]

Furthermore, in a second step, we will study how this sample evolves with the illumination intensity/duration and we will demonstrate how FMI-KPFM can be applied over this sample without experiencing significant material degradation during measurements.

The sample (manufactured by D. Moerman – Mons University), was grown from N-dimethylformamide (DMF) solution at constant temperature. Basically, in this process $\text{CH}_3\text{NH}_3\text{Br}$ and PbBr_2 are used as precursors and are both soluble in DMF at room temperature. More information about the sample fabrication process can be found in Ref. [43].

As in the case of previous samples, the MAPbBr_3 single crystal was investigated under UHV conditions. In this case, the sample was fixed on a stainless steel sample-holder using an UHV-compatible electrically conductive silver epoxy bonding agent, dried at room temperature during a 24-hours period. Additionally, a cleavage with a scalpel was performed just before introducing the sample into the load-lock of the AFM system.

In a first step, the polarity and magnitude of the surface photovoltage under continuous illumination (*ca.* 20 mW/cm^2) was checked, as well as the AFM tip height relative to the surface

using single-pulse illumination sequences via a blue (405 nm) PhoxXplus (OmicronLaseraage GmbH) laser in front side geometry.

Figures 4.18a,b show the curves of the KPFM surface potential and of the tip height respectively.

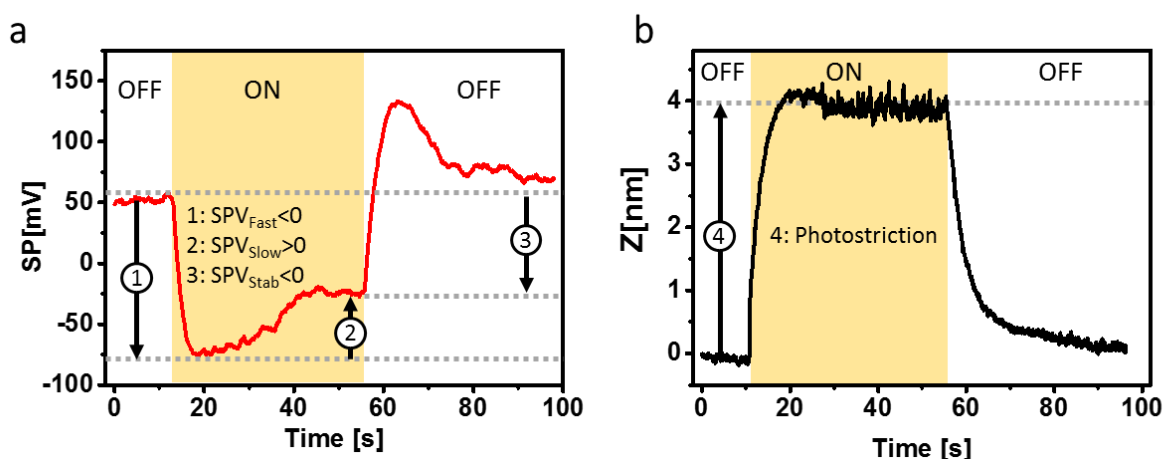


Figure 4.18– (a) Plot of the KPFM surface potential and (b) of the tip height change relative to its initial position as a function of time during a single illumination pulse. The arrows labelled 1, 2, 3 in (a) and 4 in (b) serve as eye guidelines, indicating the fast (1), slow (2) and stabilized (3) components of the surface photovoltage and the photostriction signal (4), respectively.

In Figure 4.18, we observe a fast SP response in the form of a negative photovoltage of *ca.* 130 mV upon sample illumination, followed by a slower progression and a subsequent stabilization of the SP signal under illumination at the timescale of a few tens of seconds. The surface photo-voltage at charge equilibrium which here is called SPV_{Stab} is therefore equal to the sum of a negative and a positive SPV term, referred hereafter as “fast” and “slow” SPV components, with regards to their different photo-response dynamics. Furthermore, after switching off the sample illumination, the SP displays a fast positive shift, exceeding in a first instance the original in-dark SP, followed by a slow relaxation towards the previously measured in-dark potential. These observations strongly agree with those previously reported by Almadori and co-workers over the same kind of sample. In turn, in his experiences, two successive single-pulse illumination sequences separated by a time-interval of a few tens of

seconds were applied, and dissimilar behaviours of the SP were reported for the first and second illumination pulses. Here, however, identical behaviours were observed for successive single-pulse illumination sequences separated by different time intervals ranging from a few seconds to a few minutes.

Concerning the tip height fast photo-response, it is strongly consistent with the photostriction effect reported by Almadori and co-workers. In fact, in their work, it was demonstrated that the surface photo-voltage and the observed AFM tip height variation does not arise from a cross talk between the Z and KPFM regulation loops. Indeed, by performing a series of test, they ruled out the existence of possible artefacts in AFM height investigations. Therefore, they attributed the measured change in the AFM tip height, to the photostriction response of the material, which was actually already been observed in MAPbI₃ single crystals.[44] Here, a very similar AFM tip height response is observed under similar illumination conditions. Additionally, investigations of this photostriction response as a function of the illumination output power (not shown), reveal an almost identical behaviour to the one previously reported by Almadori *et al.* It is therefore reasonable to attribute the observed tip height fast photo-response to the photostriction response of the material.

Regarding the physical origin of the different components of the observed surface photovoltage under continuous illumination, it is possible that the fast negative SPV response first observed just after illuminating the sample can be attributed to a downward band bending occurring at the surface of the MAPbBr₃ crystal [15] inducing an internal built-in electrical field which in turn induces a spatial separation of the photo-generated carriers of opposite signs in the space charge region.

At the same time, the slow SPV component strongly suggests that a charge redistribution occurs in the system within a few seconds, highly likely to arise from photo-induced ion-migration mechanisms.

Indeed, as previously mentioned, there is overwhelming evidence that at least to some extent, hybrid perovskites shall be understood as mixed electronic-ionic semiconductors.[46]

Actually, it is believed that in these materials ion migration occurs as a consequence of the existence of anion and cation vacancies.[47]

Finally, the return to the in-dark state is likely to occur via a two-steps process including first the photo-generated carriers and then the ionic species. Indeed, the observed SP overshoot present in Figure 4.18 suggest that most of the photo-carriers recombine quickly after the pulse extinction, leaving an excess of positive cations near the surface, at that moment, a reverse migration of the cations towards the bulk occurs at a slower time-scale. A scheme illustrating this process is reproduced from their work in Figure 4.19.

Further insight on the crystal photo-response can be gained by performing single-point FMI-KPFM investigations. In the following, spectroscopy investigations are carried out in frequency modulation KPFM mode using a blue (405 nm) PhoxXplus (OmicronLaserege GmbH) laser in front side geometry with an RMS optical output power of 2 mW/cm^2 as the illumination source. The illumination modulation frequencies were swept from 500 Hz to 2 MHz with a 10% duty.

Figure 4.20a shows the result of the implementation of single-point FMI-KPFM investigations. Here, it can be seen that the agreement between the fitting low based on Eq. 4.1 and the experimental points acquired on the MAPbBr_3 single crystal is excellent, suggesting that in this case, the SPV dynamics can be accurately accounted on the basis of a single time-constant decay. Moreover, Figure 4.20b shows that as expected, increasing the illumination power output, hence increasing the carrier density, leads to a decrease in the SPV decay time.

Actually, τ_d exhibits a linear drop as a function of the optical power when plotted in semi-logarithmic scale in the $5 \text{ mW/cm}^2 - 100 \text{ mW/cm}^2$ range. This observation strongly agrees with observations made by Almadori et al., and even though FMI-KPFM measurements were not performed in a non-perturbative regime, results here obtained also agree with previous results of macroscopic transient photovoltage measurements reported for $\text{MAPb}(\text{I}1-x,\text{Br}x)_3$ perovskite thin films.[48]

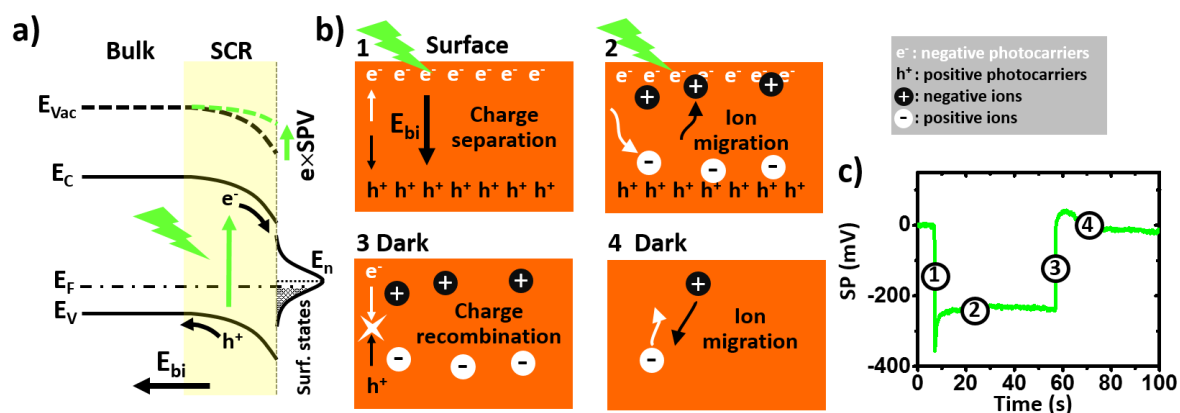


Figure 4.19– (a) Illustration of how charge transfer from surface states bends the energy bands of p-type MAPbBr₃. The resulting electric field separates the photo-carriers on both side of the space charge area. SCR: space charge region. E_F : Fermi level. E_n : surface states charge neutrality level. (b) Representation illustrating the photo-carrier generation and spatial separation by drift under the built-in electric field (step 1), the ion migration under illumination (step 2), the photo-carrier recombination (step 3) and the reverse ion migration in dark conditions (step 4). (c) Plot of the surface potential as a function of time during a typical illumination sequence. The timing of the 4 steps depicted in (b) and highlighted in (c) by numbered circles.

All panels were reproduced from Ref. [45]

As mentioned before, material degradation under operating conditions is currently one of the technical aspects which is holding back the industrial production of perovskite-based solar cells. In fact, these materials reveal a fast degradation and low stability mainly due to humidity, reaction with oxygen, illumination and heating. We observed this degradation effect multiple times while attempting to perform 2-dimensional FMI-KPFM measurements even under UHV conditions. In fact, first FMI-KPFM measurements attempts failed as the morphology of the sample dramatically changed when under illumination, even at low illumination intensities.

To demonstrate this, once again, we cleaved by means of a scalpel a MAPbBr₃ single crystal sample under ambient conditions. The sample was then loaded into the AFM system under UHV conditions to perform topography and surface potential measurements (spending as little time as possible in ambient conditions after the cleavage).

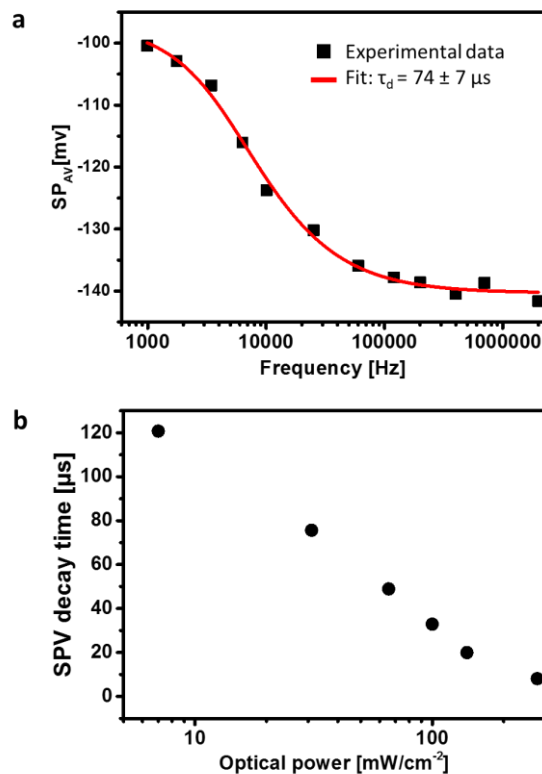


Figure 4.20– (a) Experimental points of the average surface potential as a function of the illumination modulation-frequency acquired at 405 nm with an optical peak power of 2 mW/cm^2 . The result of the numerical fit performed to extract the SPV decay time constant is displayed by a solid red line. (b) SPV decay time constant as a function of the optical power.

Figure 4.21 shows the morphology and surface potential measured over the same area of the sample. Here, we observe that the sample's morphology (and to some extent its surface potential) is already changing after just few seconds under low intensity illumination. Moreover, after few tens of minutes under illumination the sample surface completely changed and it becomes no longer possible to scan its surface due to the large topographic features which emerged.

To avoid sample evolution under illumination, and to be able to performed 2-dimensional FMI-KPFM investigations over the sample, we developed a sample preparation

protocol including the use of *in situ* cleaving facilities enabling to perform the mechanical sample cleavage under UHV inside the AFM preparation chamber.

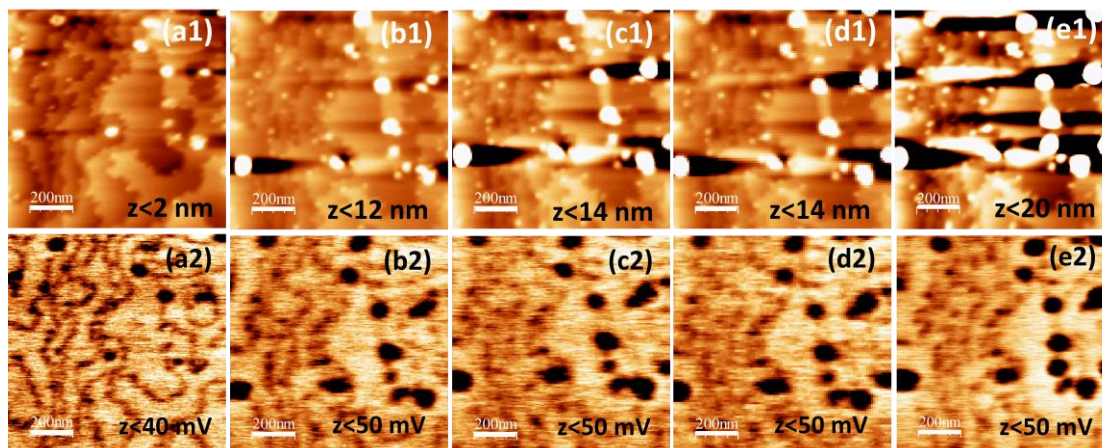


Figure 4.21—Topography (image index 1) and surface potential (image index 2) images: **(a)** before spot laser positioning (never exposed to light). **(b)** after spot laser positioning (sample illuminated during few seconds with $80 \mu\text{W}/\text{cm}^2$) **(c)** After 60 additional seconds under illumination at $34 \mu\text{W}/\text{cm}^2$ **(d)** After 300 additional seconds under illumination at $34 \mu\text{W}/\text{cm}^2$ **(e)** After *ca.* 5 hours more of modulated illumination at $72 \mu\text{W}/\text{cm}^2$.

Results shown in Figure 4.22 reveals that UHV cleavage is extremely effective at avoiding sample surface evolution even after an extended illumination exposure time (few days) and under a relatively high illumination output power ($2.8 \text{ mW}/\text{cm}^2$). Indeed, AFM topographic images of the sample cleaved under UHV conditions reveal very flat surfaces with visible atomic terraces.

At this point it is now possible to perform FMI-KPFM investigations over the sample. Here, similar to the case of previous single spectroscopy curves investigations, FMI-KPFM is implemented in frequency modulation KPFM mode using a blue (405 nm) PhoxPlus (OmicronLaseraGmbH) laser in front side geometry with an optical output power of $2.8 \text{ mW}/\text{cm}^2$ as the illumination source. Moreover, during the 2-dimensional spectroscopy the illumination modulation frequencies were swept from 990 Hz to 700 kHz

with a 30% duty ratio. Spectroscopic curves were fitted using Eq. 4.1, yielding SPV decay times of few hundreds of microseconds.

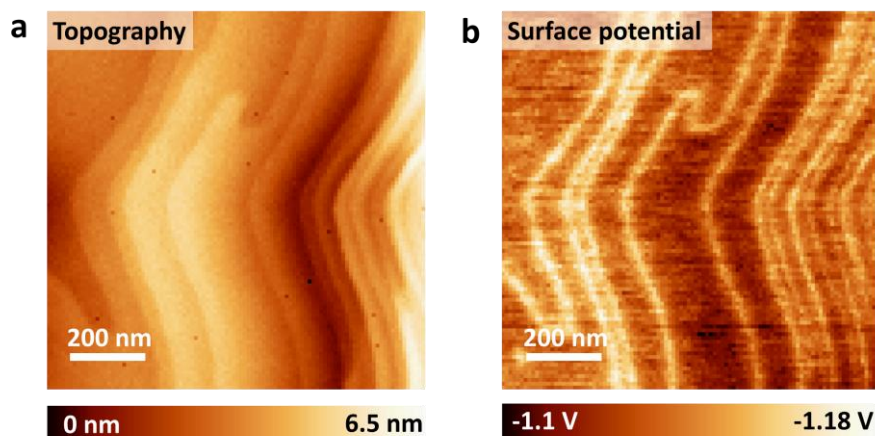


Figure 4.22– (a) Topography and (b) surface potential images of the UHV cleaved sample after several hours under illumination at 2.8 mW/cm².

FMI-KPFM results over the sample are presented in Figure 4.23. As expected, the SPV decay time image is rather homogeneous (we remind the reader that the sample in question is a single crystal). Even if over the SP images acquired at various illumination modulation frequencies a contrast is observed on the edges of the terraces, this does not seem to influence the dynamic SPV (SP at 700 kHz – SP at 990 Hz) nor the SPV decay time.

Images of the SPV decay time acquired over the same area of the sample at reduced illumination intensities (not shown) display the same homogeneous contrast with longer SPV decay time constants. Adding evidence to the conclusion that in MAPbBr₃ single crystals, both the dynamic SPV and the photo-carrier dynamics do not seem to vary at the scale of few hundred of nanometres despite the fact that a sharp contrast of the SP images can be observed over the edges of the atomic terraces visible on the topography image.

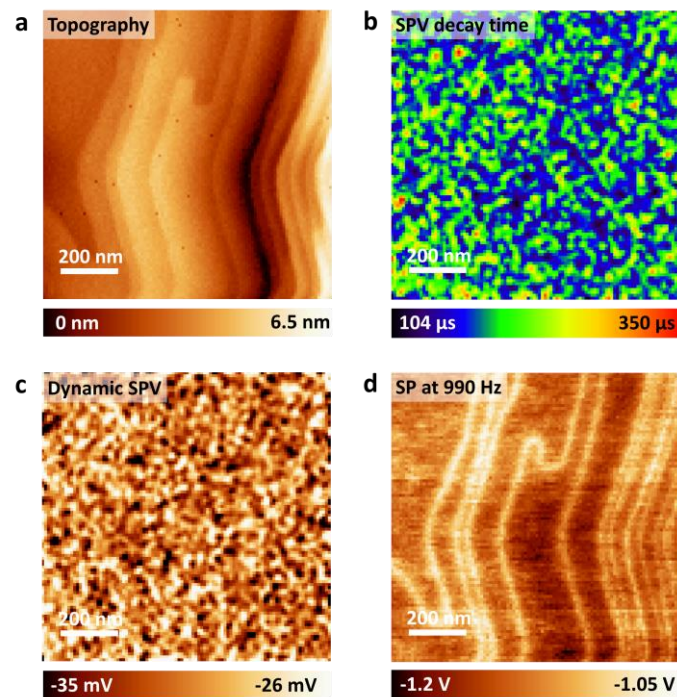


Figure 4.23– (a) Topography, (b) SPV decay time, (c) dynamic SPV and (d) SP at 990 Hz images of the UHV cleaved sample respectively.

Conclusion

In this chapter, detailed insights on FMI-KPFM dynamical SP imaging's operating principle, instrumentation, and data treatment were given. We demonstrated how this method can be applied to image the spatial variation of the SPV decay dynamics over a wide range of photovoltaic samples. The achieved lateral resolution enables investigations on optimized nanotechnology-based third-generation photovoltaics.

However, we must also highlight that there are still some open questions regarding the interpretation of FMI-KPFM results. Indeed, the mathematical model used in the data-fitting process is a particular subject of debate. In **Chapter 6**, we will approach this topic by proposing and demonstrating an alternative numerical approach which enables to predict the behaviour of spectroscopy curves of the average surface photovoltage as a function of the excitation source modulation frequency, enabling by this mean to compare simulations and experimental results.

Moreover, while the mathematical model plays a central role in data interpretation, there are some other plausible sources of artefacts which can lead to inaccuracies in the interpretation of results. In fact, it has been argued[49] that capacitance gradients effects present between tip and sample could influence the KPFM signal. Actually, it has been stated that the measured signal decay could be in fact the convolution of the CPD and capacitance gradient time responses. With this in mind, **Chapter 5** will cover this topic and will introduce how these polarization effects can be avoided/diminished and somewhat quantified.

References

1. McNeill, C.R., I. Hwang, and N.C. Greenham, *Photocurrent transients in all-polymer solar cells: Trapping and detrapping effects*. Journal of Applied Physics, 2009. **106**(2): p. 024507.
2. Hanfland, R., et al., *The physical meaning of charge extraction by linearly increasing voltage transients from organic solar cells*. Applied Physics Letters, 2013. **103**(6): p. 063904.
3. Ahrenkiel, R.K. and S. Johnston, *Contactless measurement of recombination lifetime in photovoltaic materials*. Solar Energy Materials and Solar Cells, 1998. **55**(1): p. 59-73.
4. Chen, J. and T. Sekiguchi, *Electron-Beam-Induced Current*, in *Compendium of Surface and Interface Analysis*, J. The Surface Science Society of, Editor. 2018, Springer Singapore: Singapore. p. 149-154.
5. Sinton, R.A. and A. Cuevas, *Contactless determination of current-voltage characteristics and minority-carrier lifetimes in semiconductors from quasi-steady-state photoconductance data*. Applied Physics Letters, 1996. **69**(17): p. 2510-2512.
6. Coffey, D.C., et al., *Mapping Local Photocurrents in Polymer/Fullerene Solar Cells with Photoconductive Atomic Force Microscopy*. Nano Letters, 2007. **7**(3): p. 738-744.
7. Coffey, D.C. and D.S. Ginger, *Time-resolved electrostatic force microscopy of polymer solar cells*. Nature Materials, 2006. **5**: p. 735.
8. Takihara, M., T. Takahashi, and T. Ujihara, *Minority carrier lifetime in polycrystalline silicon solar cells studied by photoassisted Kelvin probe force microscopy*. Applied Physics Letters, 2008. **93**(2): p. 021902.
9. Borowik Ł., L.H., Chevalier N., Mariolle D., Renault O., *Measuring the lifetime of silicon nanocrystal solar cell photo-carriers by using Kelvin probe force microscopy and x-ray photoelectron spectroscopy*. Nanotechnology, 2014. **25**(26): p. 265703.
10. Shao, G., et al., *Intensity-Modulated Scanning Kelvin Probe Microscopy for Probing Recombination in Organic Photovoltaics*. ACS Nano, 2014. **8**(10): p. 10799-10807.
11. Narchi, P., et al., *Nanoscale Investigation of Carrier Lifetime on the Cross Section of Epitaxial Silicon Solar Cells Using Kelvin Probe Force Microscopy*. IEEE Journal of Photovoltaics, 2016. **6**(6): p. 1576-1580.
12. Kronik, L. and Y. Shapira, *Surface photovoltage phenomena: theory, experiment, and applications*. Surface Science Reports, 1999. **37**(1): p. 1-206.
13. Tennyson, E.M., et al., *Nanoimaging of Open-Circuit Voltage in Photovoltaic Devices*. Advanced Energy Materials, 2015. **5**(23): p. 1501142.

14. Ellison, D.J., et al., *Determination of Quasi-Fermi Levels across Illuminated Organic Donor/Acceptor Heterojunctions by Kelvin Probe Force Microscopy*. Journal of the American Chemical Society, 2011. **133**(35): p. 13802-13805.
15. Cowan, S.R., A. Roy, and A.J. Heeger, *Recombination in polymer-fullerene bulk heterojunction solar cells*. Physical Review B, 2010. **82**(24): p. 245207.
16. Maurano, A., et al., *Recombination Dynamics as a Key Determinant of Open Circuit Voltage in Organic Bulk Heterojunction Solar Cells: A Comparison of Four Different Donor Polymers*. Advanced Materials, 2010. **22**(44): p. 4987-4992.
17. Fernández Garrillo, P.A., et al., *Photo-Carrier Multi-Dynamical Imaging at the Nanometer Scale in Organic and Inorganic Solar Cells*. ACS Applied Materials & Interfaces, 2016. **8**(45): p. 31460-31468.
18. Elliott, L.C.C., et al., *Probing Charge Recombination Dynamics in Organic Photovoltaic Devices under Open-Circuit Conditions*. Advanced Energy Materials, 2014. **4**(15): p. 1400356.
19. Li, G., et al., *Practical aspects of single-pass scan Kelvin probe force microscopy*. Review of Scientific Instruments, 2012. **83**(11): p. 113701.
20. Surana, K., et al., *Film-thickness-dependent conduction in ordered Si quantum dot arrays*. Nanotechnology, 2012. **23**(10): p. 105401.
21. Fernández Garrillo P. A., B.L., Caffy F., Demadrille R., Grévin B. *Imaging the Multi-Temporal Photo-Carrier Dynamics at the Nanometer Scale in Organic and Inorganic Solar Cells*. in *IEEE PVSC-44*. 2017. Washington D.C. - USA.
22. Dao, L.V., et al., *Time-resolved and time-integrated photoluminescence analysis of state filling and quantum confinement of silicon quantum dots*. Journal of Applied Physics, 2005. **97**(1): p. 013501.
23. Moskalenko, A.S., et al., *Single-particle states in spherical Si/SiO_2 quantum dots*. Physical Review B, 2007. **76**(8): p. 085427.
24. Cartier, E., J.H. Stathis, and D.A. Buchanan, *Passivation and depassivation of silicon dangling bonds at the Si/SiO₂ interface by atomic hydrogen*. Applied Physics Letters, 1993. **63**(11): p. 1510-1512.
25. Shaheen, S.E., et al., *2.5% efficient organic plastic solar cells*. Applied Physics Letters, 2001. **78**(6): p. 841-843.
26. Chiesa, M., et al., *Correlation between Surface Photovoltage and Blend Morphology in Polyfluorene-Based Photodiodes*. Nano Letters, 2005. **5**(4): p. 559-563.
27. Fuchs, F., et al., *High-Resolution Kelvin Probe Force Microscopy Imaging of Interface Dipoles and Photogenerated Charges in Organic Donor-Acceptor Photovoltaic Blends*. ACS Nano, 2016. **10**(1): p. 739-746.

28. B., G., *Kelvin Probe Force Microscopy characterization of organic and hybrid perovskite solar*, in *Kelvin Probe Force Microscopy - From Single Charge Detection to Device Characterization*, S.a.G. Sadewasser, Th. , Editor. 2018, Springer
29. Caffy, F., *Copolymères à grande largeur de bande interdite contenant des quinoxalines : nouveaux matériaux pour les cellules solaires organiques à hétérojonction*. 2016, Grenoble Alpes: Grenoble.
30. Heeger, A.J., *25th Anniversary Article: Bulk Heterojunction Solar Cells: Understanding the Mechanism of Operation*. *Advanced Materials*, 2014. **26**(1): p. 10-28.
31. Caffy, F., et al., *Synthesis, optoelectronic properties and photovoltaic performances of wide band-gap copolymers based on dibenzosilole and quinoxaline units, rivals to P3HT*. *Polymer Chemistry*, 2016. **7**(25): p. 4160-4175.
32. Cox, P.A., et al., *Imaging Charge Transfer State Excitations in Polymer/Fullerene Solar Cells with Time-Resolved Electrostatic Force Microscopy*. *The Journal of Physical Chemistry Letters*, 2015. **6**(15): p. 2852-2858.
33. García, R., R. Magerle, and R. Perez, *Nanoscale compositional mapping with gentle forces*. *Nature Materials*, 2007. **6**: p. 405.
34. Shuttle, C.G., et al., *Deep Energetic Trap States in Organic Photovoltaic Devices*. *Advanced Energy Materials*, 2012. **2**(1): p. 111-119.
35. Li, Z., et al., *Comparison of the Operation of Polymer/Fullerene, Polymer/Polymer, and Polymer/Nanocrystal Solar Cells: A Transient Photocurrent and Photovoltage Study*. *Advanced Functional Materials*, 2011. **21**(8): p. 1419-1431.
36. Chen, Q., et al., *Under the spotlight: The organic–inorganic hybrid halide perovskite for optoelectronic applications*. *Nano Today*, 2015. **10**(3): p. 355-396.
37. Yun, J.S., et al., *Benefit of Grain Boundaries in Organic–Inorganic Halide Planar Perovskite Solar Cells*. *The Journal of Physical Chemistry Letters*, 2015. **6**(5): p. 875-880.
38. Li, J.-J., et al., *Influence of N,N-Dimethylformamide Annealing on the Local Electrical Properties of Organometal Halide Perovskite Solar Cells: an Atomic Force Microscopy Investigation*. *ACS Applied Materials & Interfaces*, 2016. **8**(39): p. 26002-26007.
39. Bergmann, V.W., et al., *Local Time-Dependent Charging in a Perovskite Solar Cell*. *ACS Applied Materials & Interfaces*, 2016. **8**(30): p. 19402-19409.
40. Garrett, J.L., et al., *Real-Time Nanoscale Open-Circuit Voltage Dynamics of Perovskite Solar Cells*. *Nano Letters*, 2017. **17**(4): p. 2554-2560.
41. Yuan, Y., et al., *Anomalous photovoltaic effect in organic-inorganic hybrid perovskite solar cells*. *Science Advances*, 2017. **3**(3).
42. Shi, D., et al., *Low trap-state density and long carrier diffusion in organolead trihalide perovskite single crystals*. *Science*, 2015. **347**(6221): p. 519-522.

43. Saidaminov, M.I., et al., *High-quality bulk hybrid perovskite single crystals within minutes by inverse temperature crystallization*. Nature Communications, 2015. **6**: p. 7586.
44. Zhou, Y., et al., *Giant photostriction in organic–inorganic lead halide perovskites*. Nature Communications, 2016. **7**: p. 11193.
45. Almadori, Y., et al., *Multimodal noncontact atomic force microscopy and Kelvin probe force microscopy investigations of organolead tribromide perovskite single crystals*. Beilstein Journal of Nanotechnology, 2018. **9**: p. 1695-1704.
46. Chen, S., et al., *Mobile Ion Induced Slow Carrier Dynamics in Organic–Inorganic Perovskite $\text{CH}_3\text{NH}_3\text{PbBr}_3$* . ACS Applied Materials & Interfaces, 2016. **8**(8): p. 5351-5357.
47. Domanski, K., et al., *Migration of cations induces reversible performance losses over day/night cycling in perovskite solar cells*. Energy & Environmental Science, 2017. **10**(2): p. 604-613.
48. Kiermasch, D., et al., *Improved charge carrier lifetime in planar perovskite solar cells by bromine doping*. Scientific Reports, 2016. **6**: p. 39333.
49. Schumacher, Z., et al., *Measurement of Surface Photovoltage by Atomic Force Microscopy under Pulsed Illumination*. Physical Review Applied, 2016. **5**(4): p. 044018.

5 | Plausible sources of artefacts in frequency modulated illumination Kelvin probe force microscopy and how to avoid them

Content

5.1 Context.....	147
5.2 Capacitance artefacts	149
5.3 Comparing amplitude modulation and frequency modulation Kelvin probe force microscopy modes	156
5.4 Frequency mixing	157
5.5 Other sources of artefacts.....	159
5.6 An improved protocol for photo-carriers dynamics investigation.....	160
Conclusion	179
References.....	180

Ce chapitre présente les sources d'artefact de la technique introduite dans le chapitre précédant, comme les effets capacitifs et ceux induits par le mélange d'harmoniques. Un protocole de mesure amélioré est décrit, visant à diminuer ou annuler ces perturbations.

5.1 Context

In **Chapter 4** we introduced frequency modulated illumination Kelvin probe force microscopy (FMI-KPFM), a technique which enables to image the spatial variation of the surface photovoltage (SPV) dynamics over a wide range of photovoltaic samples with a sub-10 nm lateral resolution.[1-4] We saw how implementing FMI-KPFM can lead to a better

understanding of the complex interplay between the nanostructure, the photo-carrier transport, and recombination dynamics in organic[1, 2], inorganic[1, 3] and hybrid solar cells[5].

However, there are still some open questions regarding the interpretation of FMI-KPFM results, as well as the plausible presence of artefact sources which could lead to inaccuracies in the interpretation of results. In fact, the possible influence of capacitance gradients on the Kelvin probe force microscopy (KPFM) signal has been pointed as a potential source of artefacts in FMI-KPFM investigations.[6] Here, we will address this subject and we will discuss how these polarization effects can be quantified via the analysis of Kelvin probe force spectroscopy curves acquired under frequency modulated illumination.

In addition, we will shortly discuss another issue which has been recently demonstrated to be a source of artefacts in FMI-KPFM investigations; frequency mixing. [7] Actually, we will see that certain excitation modulation frequencies shall be eluded during the spectroscopy acquisition to avoid frequency mixing, an effect which can lead to falsified KPFM measurements.

Finally, an improved FMI-KPFM protocol developed to avoid/diminish the error associated with the mathematical fit procedure, as well as the most significant sources of artefacts, will be proposed and demonstrated. In this protocol, the contact potential difference (CPD) under continuous wave excitation and under dark conditions is registered prior to the average surface photo-voltage (SPV_{AV}) spectroscopy curve, over each point of a pre-defined grid area over the sample. This way, both the CPD in dark conditions and under continuous wave illumination are known values that can be fixed when performing the mathematical fit. Additionally, in this protocol the variation of the capacitance gradient under modulated illumination is registered separately, allowing to assess its influence on the KPFM signal as well as on the calculation of the photo-carrier dynamics.

5.2 Capacitance artefacts

As we saw in **Chapter 4**, FMI-KPFM relies on the measurement of an average surface photo-voltage as a function of the modulation frequency of an illumination source. This means that the accuracy of the SPV measurement determines both the achievable temporal and lateral resolution. However, a limiting factor of this approach is that SPV measurements based on KPFM are only sensitive to a change in the CPD. Yet, photo-carriers can also contribute to a change in the tip-sample capacitance as depicted in Figure 5.1.[8]

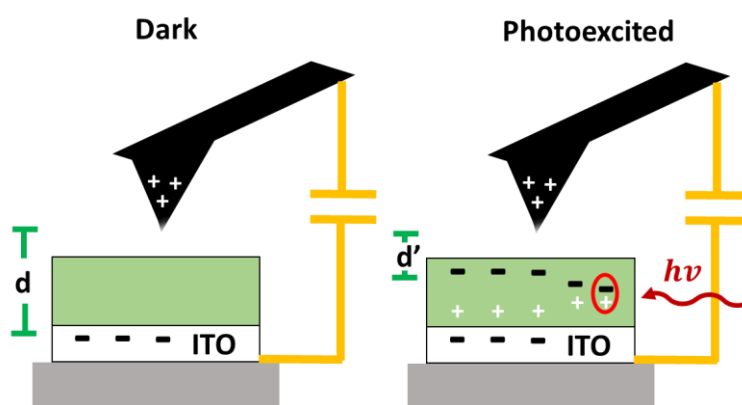


Figure 5.1– Scheme showing how photo-excited charges modify the effective distance between capacitor plates (d to d') therefore increasing the capacitive gradient measured by KPFM in the case of an OPV device.

Figure according to Ref. [8]

In [6], Schumacher and co-workers, demonstrated that a change in the capacitance gradient can lead to a potential systematic error in SPV measurements using established KPFM techniques. In fact, in their paper, it is argued that KPFM measurements carried out under modulated excitation over photovoltaic materials actually yields a V_{DC} signal weighted by the capacitance gradient variation, which depending on the KPFM implementation mode can be expressed as:

$$V_{DC} = \frac{(1 - D) \frac{dC}{dz} V_{CPD} + D \frac{dC^*}{dz} V_{CPD}^*}{(1 - D) \frac{dC}{dz} + D \frac{dC^*}{dz}} \quad (5.1)$$

for amplitude modulation (AM)-KPFM, where D is the modulation duty ratio, dC/dz and V_{CPD} are the capacitance gradient and CPD under dark conditions respectively and dC^*/dz and V_{CPD}^* are the capacitance gradient and CPD under continuous illumination respectively, and:

$$V_{DC} = \frac{(1 - D) \frac{d^2C}{dz^2} V_{CPD} + D \frac{d^2C^*}{dz^2} V_{CPD}^*}{(1 - D) \frac{d^2C}{dz^2} + D \frac{d^2C^*}{dz^2}} \quad (5.2)$$

for frequency modulation (FM)-KPFM, where d^2C/dz^2 and d^2C^*/dz^2 are the capacitance second derivative and the capacitance second derivative under continuous illumination respectively.

However, this change in the capacitance gradient can only be measured quantitatively if KPFM is performed in Kelvin probe force spectroscopy mode or if the electrostatic force spectral component F_{2w} signal is measured.[6] Here, in a first approach, we will assess this change by comparing images of the capacitance second derivative (Figure 5.2c) obtained via Kelvin probe force spectroscopy under various illumination modulation frequencies.

For this, the same nanophase segregated PDBS-TQx/PC₇₁BM blend previously introduced in **Chapter 4**, is investigated using Kelvin probe force spectroscopy under various modulated illumination conditions. In this mode, Kelvin parabolas are acquired over each point of a predefined grid area over the sample. As described in **Chapter 3**, this parabola reflects the behaviour of the frequency-shift (Δf) as a function of a static tip-sample bias (V_{DC}). By fitting this parabola with Eq. 3.35 (Figure 5.2b), it is possible to obtain not only the local CPD but also the local value of the capacitance second derivative (d^2C/dz^2). Then by changing the modulation frequency of the illumination source, we can access the variation of d^2C/dz^2 as a function of the illumination modulation frequency, allowing us to determine and somewhat quantify its influence on the measured KPFM signal obtained during FMI-KPFM investigations.

Figure 5.2a depicts a schematic illustration describing the general implementation of Kelvin probe force spectroscopy under frequency modulated illumination. It is worth

mentioning that using this mode, it is also possible to obtain CPD images as a function of the illumination modulation frequency (Figure 5.2d). However, at this stage, the interest on implementing Kelvin probe force spectroscopy under modulated illumination does not rely on mapping the photo-carrier dynamics. Instead, as mentioned above, here, Kelvin probe force spectroscopy under modulated illumination will be used to compare the different images of the capacitance gradient, obtained at different illumination modulation frequencies over the same region of the sample. This will allow us to evaluate the evolution that this capacitance gradient should experience during FMI-KPFM measurements and its influence on the KPFM signal.

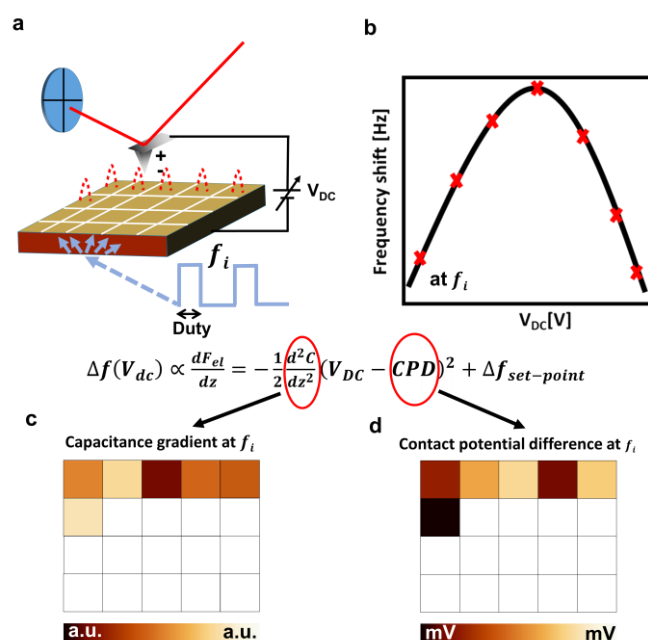


Figure 5.2– (a) Schematic illustration of Kelvin probe force spectroscopy under modulated illumination at f_i . Here, the frequency-shift is measured as a function of a static tip-sample bias which is swept from -1.5 V to 0.4 V. (b) The Kelvin parabola reflects the behaviour of the frequency-shift as a function of the static tip-sample bias. (c-d) Images of the capacitance gradient and the CPD respectively, obtained as a result of the mathematic fit performed using Eq. 3.35. By varying f_i different capacitance gradient and CPD images can be acquired, which in turn will allow us to assess the evolution of the capacitance gradient (and also the CPD) as a function of the illumination modulation frequency.

Figure 5.3a shows the capacitance gradient and CPD images acquired via Kelvin probe force spectroscopy under frequency modulated illumination (PhoxXplus module from

OmicronLasera GmbH, 515 nm, 10% duty, 3.8 mW/mm²) at 333 Hz, 10 kHz, 200 kHz and 2 MHz respectively. Figure 5.3b show the average Kelvin parabolas for the different illumination modulation frequencies, while Figure 5.3 show plot of the average values of the CPD and d^2C/dz^2 as a function of the illumination modulation frequency.

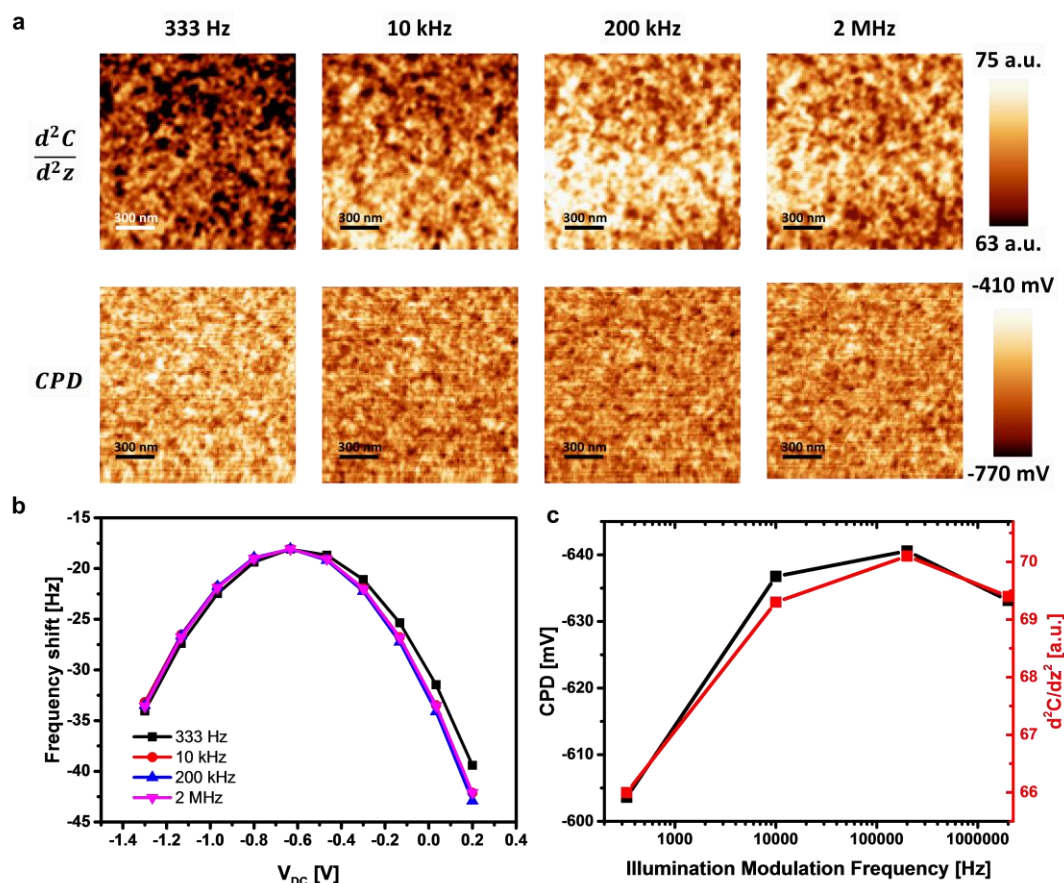


Figure 5.3– (a) Capacitance gradient and CPD images acquired via Kelvin probe force spectroscopy under frequency modulated illumination (515 nm PhoxXplus module) at 333 Hz, 10 kHz, 200 kHz and 2 MHz with a 10% duty and an illumination intensity of 3.8 mW/mm². (b) Average Kelvin parabolas for different illumination modulation frequencies. (c) Plot of the average values of the CPD (in black) and d^2C/dz^2 (in red) for the different illumination modulation frequencies.

Firstly, we turn to Figures 5.3a and 5.3c where we observe that indeed, a change of the capacitance gradient is observed under different illumination modulation frequencies, as

predicted by Schumacher and co-workers.[6] However, a closer look to Figure 5.3c shows that the magnitude of this capacitance gradient change is inferior to 7% of the entire signal.

Now, the question that presents itself is whether this small variation of the capacitance gradient during the FMI-KPFM spectroscopy can mislead the photo-carrier dynamics time constant calculation.

To answer this question, in the following we will implement a mathematical model to calculate a SPV decay time constant corrected from any influence caused by the varying capacitance. The development of this model can be found on the **appendix** of this thesis. In short, by taking into account the presence of a d^2C/dz^2 signal (displayed on red in Figure 5.3c) displaying a behaviour characterized by a decay time τ_d^* , a corrected SPV decay time can be re-calculated (Eq. 8.13). The mathematical fit performed over the d^2C/dz^2 signal for which Eq. 4.1 was also used, can be found on Figure 5.4a. Indeed, analogue to the case of τ_d, V_{Light} and V_{Dark} , using this model, it is possible to calculate a decay time τ_d^* along with the values of d^2C/dz^2 under continuous illumination (Γ_I) and in dark conditions (Γ_D), values which are then used to apply Eq. 8.13. Then, the influence of the capacitance effect over FMI-KPFM results can be established by comparing the corrected SPV decay time constant against the value obtained originally via one of the models described in Chapter 4, (in this case the model described by Eq. 4.1).

When performing this comparison (Figure 5.4b), we observe a similar adjustment of both models to the measured CPD data-points. Moreover, both τ_d and its corrected value seem to agree relatively well. This result can be interpreted as evidence suggesting that even if the presence of a varying capacitance gradient during KPFM investigations under frequency-modulated illumination has an influence over KPFM measurements, in this particular case, this influence does not seem to strongly affect the estimation of the SPV dynamics in FMI-KPFM investigations.

At this point, we highlight that measurements here presented over the nanophase segregated PDBS-TQx/PC₇₁BM blend were obtained after a 10-month time period following

measurements shown in the previous chapter. Therefore, it is very likely that the SPV response of the sample evolved, which explain the change in the SPV behaviour of the sample.

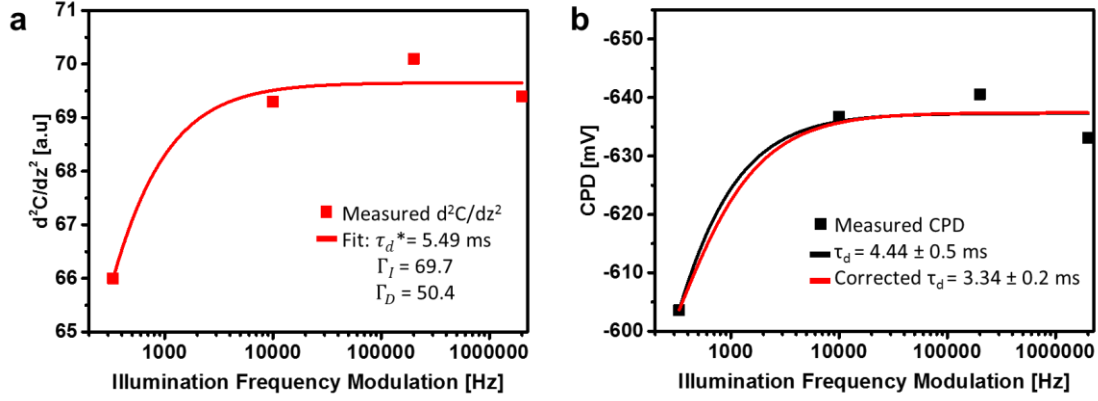


Figure 5.4– (a) Mathematical fit performed over the d^2C/dz^2 signal. (b) Adjustment of both models (Eq.4.1 and Eq. 8.13) to the measured CPD data-points. By taking into account the behaviour of d^2C/dz^2 as a function of the illumination modulation frequency, characterized by a decay time $\tau_d^* \approx 5.49$ ms, a corrected SPV decay time can be calculated.

Moreover, we highlight that results presented in Figure 5.4 were obtained using a modulation duty ratio of 10%, in this scenario, according to [6], V_{DC} shall correspond to:

$$V_{DC} = \frac{9 \frac{d^2C}{dz^2} V_{CPD} + \frac{d^2C^*}{dz^2} V_{CPD}^*}{9 \frac{d^2C}{dz^2} + \frac{d^2C^*}{dz^2}} \quad (5.3)$$

From Eq. 5.3 we can deduce that the influence of a changing capacitance gradient during frequency modulated illumination KPFM measurements, increases as the illumination modulation duty ratio approaches to 50%. Indeed, for a 10% modulation duty ratio, the average value of the capacitance gradient under frequency modulated illumination is dominated by the in-dark capacitance gradient value. This shows why it is convenient to use a small modulation duty ratio when performing FMI-KPFM measurements. Additionally, the use of a reduced modulation duty ratio in FMI-KPFM measurements allows to access a surface potential (SP) value closer to the value that should be measured in dark conditions (for the lowest illumination

modulation frequency). In general, this means that the magnitude of the SPV spectroscopy curve increases as the modulation duty ratio decreases. Therefore, the use of a reduced modulation duty ratio in FMI-KPFM investigations is not only advantageous to diminish capacitance-related artefacts, but is also useful to increase the average surface photo-voltage spectroscopy curve magnitude, which in turn increases the mathematical fit accuracy.

Another important aspect to keep in mind when performing FMI-KPFM measurements, is that capacitance-related artefacts such as the one described above, have a stronger influence over the KPFM signal when working in AM-KPFM mode. In fact, when performing FMI-KPFM investigations in AM-KPFM mode, the KPFM signal is more dependent on the capacitance change, as V_{DC} depends directly on the capacitance gradient rather than the capacitance second derivative as it is the case in FM-KPFM.

In addition to be more sensitive to light-induced capacitance changes, FMI-KPFM investigations performed in AM-KPFM mode can have a reduced lateral resolution compared to measurements performed in FM-mode.

In fact, as discussed in **Chapter 3**, in AM-KPFM, the detection of the electrostatic force component F_w involves the whole tip and cantilever. This can be especially critical, in the case of bare nanophase segregated organic blends and other bare samples where different charge populations can form nanophase segregated clusters. Over these samples, the measured SP can be the result of the averaging of these charges populations over an area of several tens of nanometres, therefore yielding a reduced SP absolute magnitude compared to what would be measured using FMI-KPFM in FM-KPFM mode, where the detection of the force gradient ($\partial F_w / \partial z$) is limited to the tip apex.

To better understand the differences between the implementation of FMI-KPFM measurements using AM- and FM-KPFM modes, in the following section we will compare FMI-KPFM results obtained over the IC₆₁BA-PDBS-BitQx blend previously investigated in **Chapter 4** under the same lightning conditions using both modes.

5.3 Comparing amplitude modulation and frequency modulation Kelvin probe force microscopy modes

In Figure 5.5, a comparison between the implementation of FMI-KPFM under same illumination conditions in both AM-KPFM and FM-KPFM modes over the IC₆₁BA-PDBS-BitQx blend previously introduced in **Chapter 4** is depicted.

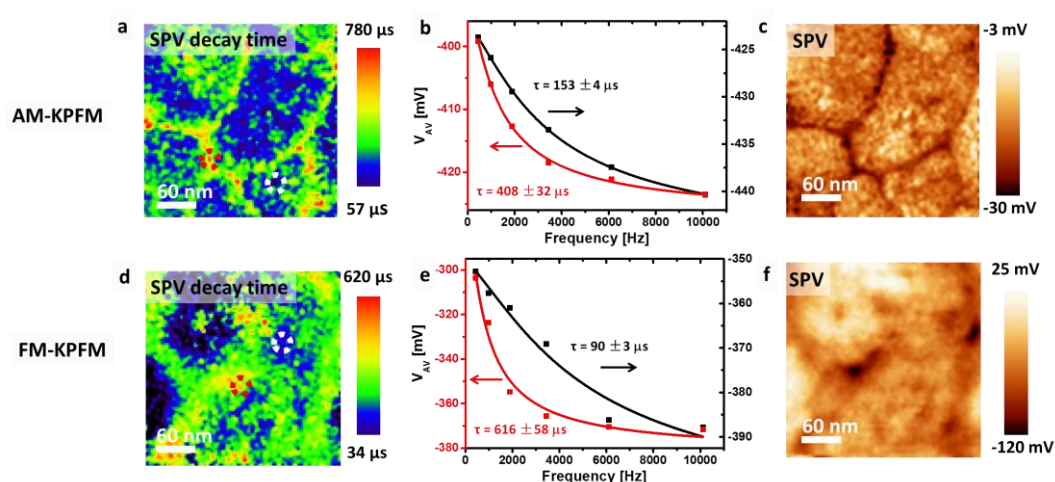


Figure 5.5– FMI-KPFM in AM-KPFM mode against FM-KPFM mode. **(a,d)** SPV decay time images acquired in AM-KPFM and FM-KPFM respectively. **(b,e)** Spectroscopic curves showing the SPV evolution with respect to the illumination modulation frequency obtained in KPFM-AM and FM modes respectively. Red and black data points were obtained over areas indicated in **(a)** and **(d)** as white and red dotted circles respectively. **(c,f)** SPV images acquired in AM-KPFM and FM-KPFM respectively. SPV images are the result of the subtraction of the SP images acquired at the lowest and highest illumination modulation frequency.

Although both set of images were not acquired over the exact same region of the sample, a rough comparison between both modes can be nonetheless established. In fact, the first thing we notice is that, as expected, the total variation of the average SP as a function of the illumination modulation frequency seems to be around 3 times larger when working in FM-KPFM mode as compared to measurements obtained in AM-KPFM mode. This can be observed from comparing Figure 5.5c and Figure 5.5f, as well as from comparing spectroscopy

curves shown in Figures 5.5b and 5.5e respectively. As already mentioned, this difference can be attributed to the fact that in AM-KPFM mode, the electrostatic force detection involves the whole tip and cantilever. Consequently, the measured SP is in fact the result of the averaging of different charges populations over an area of several tens of nanometres. However, this difference in the magnitude of variation between both set of SP data does not seem to affect the SPV decay time constant calculation (Figures 5.5a and 5.5d). Indeed, the photo-carrier dynamics time constants are dependent on the speed of the average surface potential variation as a function of the illumination modulation frequency and not on the magnitude of this variation.

In this particular example, due to the relatively strong surface photovoltage response of the sample under modulated illumination and therefore the good mathematical fit accuracy, the lateral resolution of the SPV decay time image obtained using AM-KPFM (Figure 5.5a) does not seem to be inferior to the one achieved in FM-KPFM mode (Figure 5.5d). However, in general, as a matter of caution, we recommend the implementation of FMI-KPFM investigations in FM-KPFM mode when dealing with bare nanophase segregated organic blends and other bare samples where nanophase segregated clusters of different charge populations are likely to be found, in order to maximize the magnitude of the SPV dynamics and consequently the mathematical fit accuracy which in turn benefits the lateral resolution.

5.4 Frequency mixing

An important aspect of FMI-KPFM implementation is the selection of the illumination modulation frequencies. For the correct acquisition of the spectroscopy curves, these frequencies shall be set evenly spaced along the x-axis of a semi-logarithmic chart. Moreover, usually between 7 and 30 frequencies are needed to properly follow the SPV photo-carrier dynamics behaviour.

Recently, it was unambiguously demonstrated that there is a possibility that for specific modulation frequencies, the excitation signal interferes in an unwanted way with the cantilever

oscillation or the ac-voltage that is applied for the detection of the CPD.[7] It goes without saying that such interference is expected to influence CPD measurements, leading to a falsification of KPFM results. In fact, using a combined simulation and experimental study, it was demonstrated that these modulation critical frequencies causing interference correspond to the fundamental cantilever eigenmode f_0 as well as the second cantilever eigenmode f_2 , and other related frequencies: [7]

$$\left(\frac{2}{m}\right) f_0 \quad (5.4)$$

$$\left(\frac{2}{m}\right) f_2 \quad (5.5)$$

where $m=1,3,5,7,\dots$

Additionally, it was proved that the smaller the factor m , the greater the frequency mixing effect on the KPFM signal.

This means that, in order to avoid frequency mixing artefacts in FMI-KPFM measurements, during the acquisition of CPD spectra, application of the modulation signal at the critical frequencies should be avoided.

Actually, the above described crosstalk or frequency mixing effect was sometimes observed during FMI-KPFM investigations performed during this thesis. In fact, this crosstalk phenomena was identified each time a dramatic decrease of the KPFM signal to noise ratio was observed under a single illumination modulation frequency. Whenever this effect was observed, the modulation frequency was consequently modified until the KPFM signal to noise ratio returned to its usual value.

However, thanks to the work of Sadewasser and co-workers, we now understand the origin of this frequency mixing and clear guidelines to avoid frequency mixing-related artefacts in time-resolved KPFM measurements have been given.

To sum up, the selection of the illumination modulation frequencies should be made in a way in which the data points of the CPD spectra are evenly distributed over the x-axis of a semi-logarithmic plot while at the same time avoiding critical frequencies defined by Eq. 5.4.

5.5 Other sources of artefacts

So far we have discussed the main sources of artefacts in FMI-KPFM investigations, however, there exist some other important aspects to bear in mind when implementing the technique that if not taken into account, could lead to unwanted effects during measurements that may perhaps falsify results.

FMI-KPFM relies on the measurement of the photovoltaic response of a sample under modulated illumination, this implies that only the sample should exhibit a photovoltaic behaviour. Indeed, FMI-KPFM measurements could be affected if the tip itself has a photovoltaic behaviour. That is why, it is recommended to check that the used tip is not contributing to the photovoltaic response of the sample when illuminated. This can be easily checked by illuminating a non-photovoltaic sample such as a metallic sample and observing the KPFM signal. This additional verification step could prove especially important when working with silicon tips. Nonetheless, we highlight that during measurements performed in this thesis, a photovoltaic response of the tip was never observed.

Another technical aspect concerning FMI-KPFM investigations that could eventually influence results is the fact that the laser used to illuminate the sample can sometimes reflect from the cantilever back side and the sample onto the position sensitive photodetector for the AFM detection, thereby leading to an artificial modification of the measured cantilever oscillation. However, this strongly depends on the specific setup used for the experiments. Indeed, a photodetector sensitive to visible light could be affected by this light reflections, however in our case, the photodetector of both of our systems are optimized for infrared light, diminishing the effect of possible reflections of the illumination laser which is usually either blue or green, with only some experiments carried out using a red laser.

5.6 An improved protocol for photo-carriers dynamics investigation

Having addressed the main sources of artefacts concerning FMI-KPFM investigations, in the following, an improved FMI-KPFM protocol is proposed and demonstrated over a BHJ OPV blend based on a fullerene derivative (PCBM₇₀) as the electron acceptor and a homemade synthesized (by INAC team) electron donor polymer (PTB₇), aiming to avoid/diminish the impact of the above mentioned artefact sources on photo-carrier dynamics measurements.

Figure 5.6 depicts this improved FMI-KPFM protocol. Actually, in this protocol, both the CPD under continuous wave excitation and the SPV_{AV} spectroscopy curve are simultaneously acquired at each point of the sample. In fact, by applying an illumination single pulse to the sample, prior to the acquisition of the SPV_{AV} spectroscopy curve, it becomes possible to measure values of both the CPD in dark conditions and under continuous wave illumination. This way, both the CPD in dark conditions and under continuous wave illumination are known values that can be fixed when performing the mathematical fit.

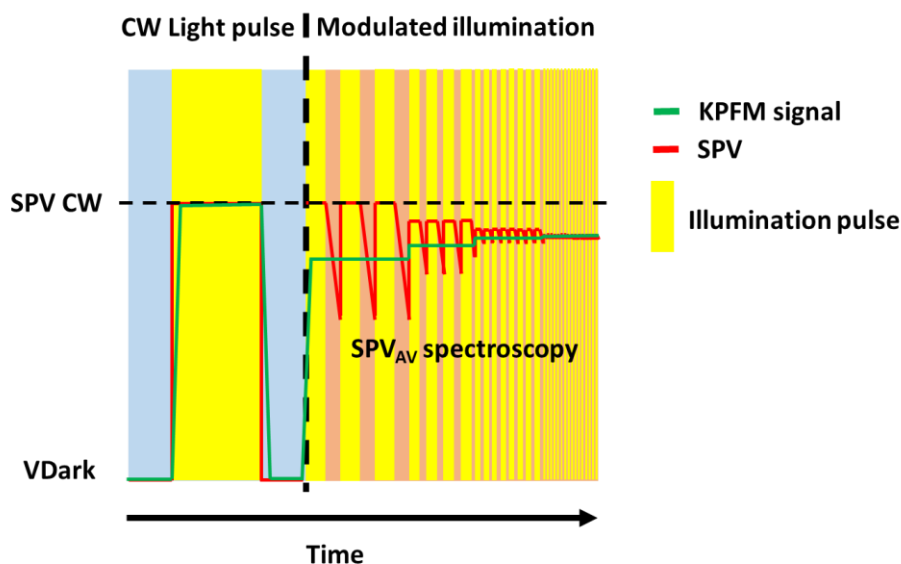


Figure 5.6– Improve FMI-KPFM protocol depiction.

Furthermore, under this protocol, the electrostatic force spectral component F_{2w} is separately registered via a lock-in amplifier, allowing access to the variation of the capacitance second derivative in FM-KPFM mode or the capacitance gradient in AM-KPFM as a function of the illumination modulation frequency. This, in turn will allow to assess its influence on the KPFM signal over each pixel of the SPV dynamic image(s). In fact, using this information along with the mathematical model implemented in Figure 5.4 and whose detailed development can be found in the **appendix** of this thesis, will allow us to calculate a SPV decay time image corrected from any influence of the varying capacitance.

Figures 5.7a and 5.7b show an example of results obtained when implementing this protocol in single-point mode over the sample. Here, the sample was optically excited using a green (515 nm) PhoxXplus module from OmicronLaseraage GmbH with a peak output power of 60 mW/cm^2 . Modulation frequencies were swept from few tens of Hz to 1 MHz with a 10% duty ratio. The continuous wave light pulse duration was nearly 1 second.

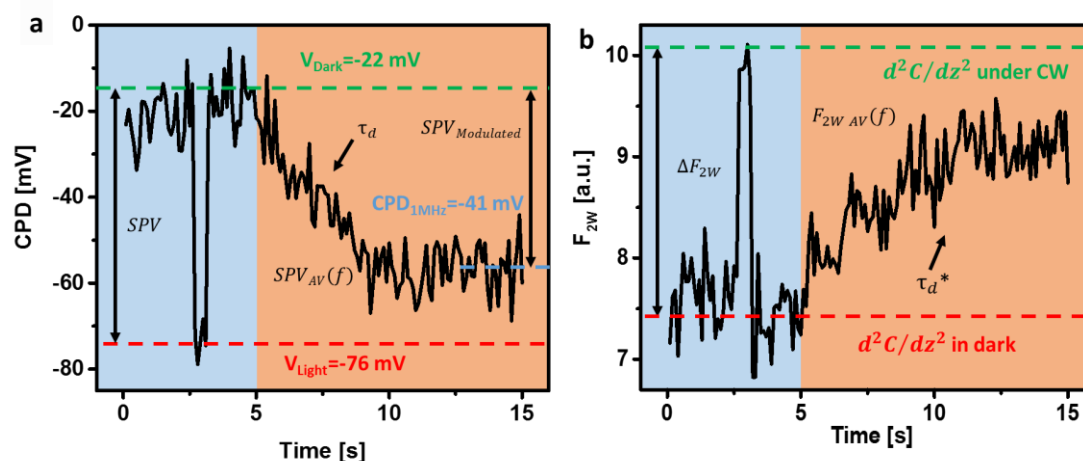


Figure 5.7– (a) CPD results from the implementation of the improved FMI-KPFM protocol. Here CPD under continuous wave excitation and under dark conditions are acquired along with the SPV_{AV} spectroscopy curve. V_{Dark} corresponds to the in-dark surface potential and V_{light} with the surface photo-voltage measured under continuous wave illumination. (b) Electrostatic force spectral component F_{2w} acquired at the same time as the CPD.

By recording the curve presented in Figure 5.7a over all pre-defined positions over the sample, it becomes possible to obtain two different SPV images, *i.e.*, one under continuous wave illumination (complete SPV) and another which comes from the subtraction between V_{Dark} and the CPD value registered at the highest illumination modulation frequency which will be called here “modulated” SPV. Moreover, a SPV decay time image can be obtained using an appropriated mathematical model such as the one described by Eq. 4.1 with the only difference that this time, both the CPD in dark conditions and under continuous wave illumination are known values and therefore can be fixed, increasing the overall fit adjustment to the curves.

Analogously, images of F_{2w} (also referred to as d^2C/dz^2) under illumination and in dark conditions can be obtained by recording the curve presented in Figure 5.7b in the same way as the CPD curves. Furthermore, this protocol enables to map the time constant (τ_d^*) associated to the d^2C/dz^2 variation as a function of the illumination modulation frequency. Using these images, we will ultimately apply the model implemented previously (Figure 5.4), and whose development can be found in the **appendix** of this thesis, to recalculate a new SPV decay time image corrected from capacitance-induced artefacts.

FMI-KPFM results obtained over the PCBM₇₀/PTB₇ blend via the above described protocol can be found in Figure 5.8, where the sample topography, both the complete and modulated SPV images, images of d^2C/dz^2 under continuous wave illumination and dark conditions along with both the SPV decay time (τ_d) and the d^2C/dz^2 decay time (τ_d^*) images are shown.

In figure 5.8a we observe a sample morphology with features in the range of few hundred of nanometres. While this can be interpreted as an indication pointing out that probably the sample phase-separation has not been optimized, it serves the experiment’s purpose in the sense that there is no need to achieve an exceptional lateral resolution to find a well-defined contrast in both SPV and the SPV decay time images.

Figures 5.8c and 5.8d display images of the SPV under continuous wave illumination and the “modulated” SPV respectively, the latter obtained upon the subtraction of the CPD image acquired at the highest illumination modulation frequency and the CPD image acquired

in dark conditions. Both SPV images present features of about the same size of those present in the topography image. In fact, correlations between both SPV images and the topography can easily be established, with valleys in Figure 5.8a corresponding to regions exhibiting a stronger SPV magnitude as can be observed in Figure 5.8b where the 4-dimensional image owes its contour to the topography image while the colour scale corresponds to that of Figure 5.8c.

It is also interesting to observe that both SPV images display the same contrast, although as anticipated by Figure 5.7a, the SPV under continuous wave illumination exhibit a higher magnitude compared to the “modulated” one. Figures 5.8e and 5.8f display images of d^2C/dz^2 under continuous wave illumination and in dark conditions respectively. Finally, Figures 5.8g and 5.8h show images of the SPV decay time (obtained by fitting spectroscopy curves with Eq. 4.1) and the d^2C/dz^2 decay time (τ_d^*). The latter will be used along with both d^2C/dz^2 images to recalculate a SPV decay time image corrected from capacitance-induced artefacts hereafter. As mentioned above, this correction is performed using the same model used to correct the SPV decay time in Figure 5.4.

Figure 5.9b shows the corrected SPV decay time image. When comparing this image against the original SPV decay time image, depicted again in Figure 5.9a (for comparison purposes), we notice that overall the contrast in both images remain the same. However, a change in the time constant magnitude is observed in some regions. A comparison between profile sections of both images is shown in Figure 5.9e.

Additionally, Figures 5.9c and 5.9d give detailed information on how the corrected SPV decay time image was calculated. Indeed, these figures detail the calculation process for the pixel 50*50 of Figures 5.9a and 5.9b. In fact, from the raw information obtained via the improved FMI-KPFM protocol (Figure 5.9c), values of V_{Dark} and V_{Light} are acquired along with values of Γ_D and Γ_L . Then a mathematical fit is performed over the portion of the d^2C/dz^2 signal which was acquired as a function of the illumination modulation frequency to obtain the value of τ_d^* . For this, we used an analogous version of Eq. 4.1 where V_{Dark} , V_{Light} and τ_d are replaced by Γ_D , Γ_L and τ_d^* respectively.

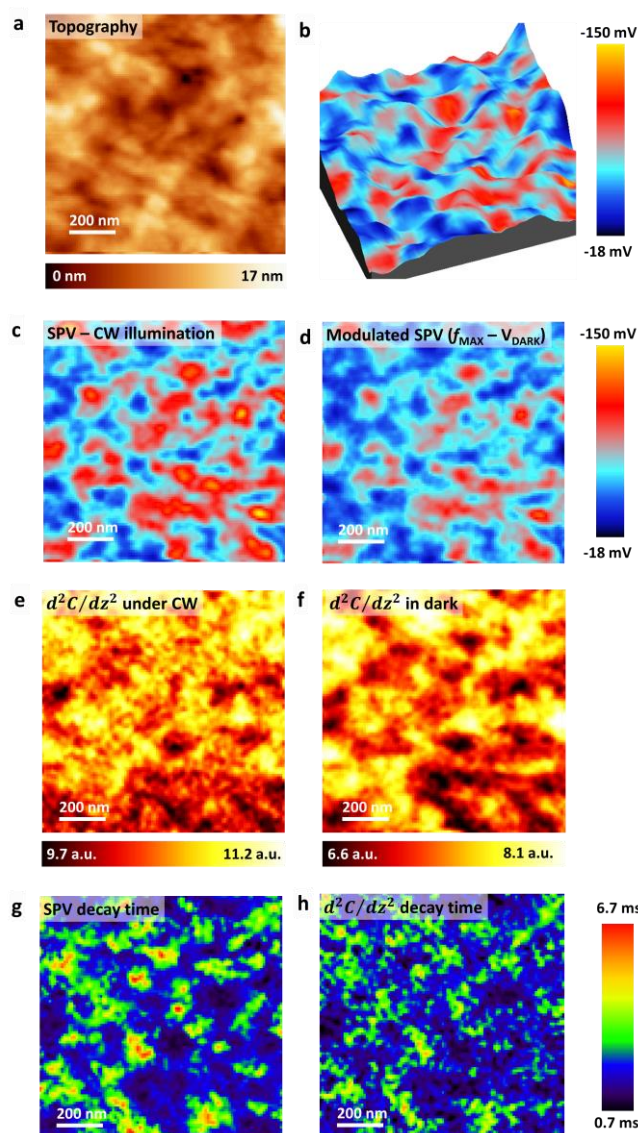


Figure 5.8– (a) PCBM₇₀/PTB₇ sample topography. (b) 4-dimensional image combining information from both the topography (contour) and the SPV under continuous wave illumination (colour scale) (c) SPV under continuous illumination image. (d) “Modulated” SPV. This image results from subtracting the CPD image acquired at the highest illumination intensity to the CPD image acquired in dark condition (V_{DARK}). (e) d^2C/dz^2 under continuous wave illumination. (f) d^2C/dz^2 in dark conditions. (g) SPV decay time (uncorrected from capacitance-induced artefacts). (h) d^2C/dz^2 decay time image.

Moreover, in this fit Γ_D and Γ_L are known values which are therefore fixed. In this case τ_d^* correspond to 0.68 ms as depicted in Figure 5.9c. Finally, using the know values of V_{Dark} ,

V_{Light} , Γ_D , Γ_L and τ_d^* , a corrected SPV decay time can be calculated using Eq. 8.13 as show in Figure 5.9d. Moreover, the adjustment of the mathematical fit over the CPD data points using Eq. 4.1 (in which V_{Dark} and V_{Light} were fixed as well) to calculate the non-corrected SPV decay time is also show in Figure 5.9d for comparison purposes. It is worth mentioning that the CPD data points show in Figure 5.9d were obtained by averaging the black curve depicted in Figure 5.9c for each discrete value of the illumination modulation frequency.

Furthermore, from Figure 5.9f we observe a comparison between the histogram of both SPV decay images. It is interesting to observe that the correction of the SPV decay time image leads to a SPV decay time values distribution which appears to be more symmetrical (resembling a Gaussian distribution). In any case, both SPV decay time images display an average value of the SPV decay time which is about the same.

At this point, something interesting to mention is that, while in Figure 5.9d we observe a rather good adjustment of both mathematical models (Eq. 4.1 and Eq. 8.13) to the measured data, the fit curves do not perfectly follow the data points over all frequency regimes. It would appear that the models used to fit the data, do not perfectly describe the physics behind the SPV behaviour. In fact, perhaps this mismatch between the data and the proposed models is due to the presence of multiple SPV dynamics. Actually, we already observed this discrepancy in Figure 5.6 where the SPV under modulated illumination displayed an inferior magnitude with respect to the SPV under continuous wave illumination. Therefore, in a further part of this chapter, we will propose a hypothesis to account for this behaviour. In short, the presence of a non-zero SPV built-up time, as well as the presence of different SPV contributions displaying inverted polarities will be pointed as the possible origin of the observed discrepancy.

Finally, to conclude this section, we will briefly comment on the differences between the acquisitions of the 2-dimensional frequency-spectroscopy data in closed loop mode, (*i.e.*, uninterrupted z-regulation), against open loop mode.

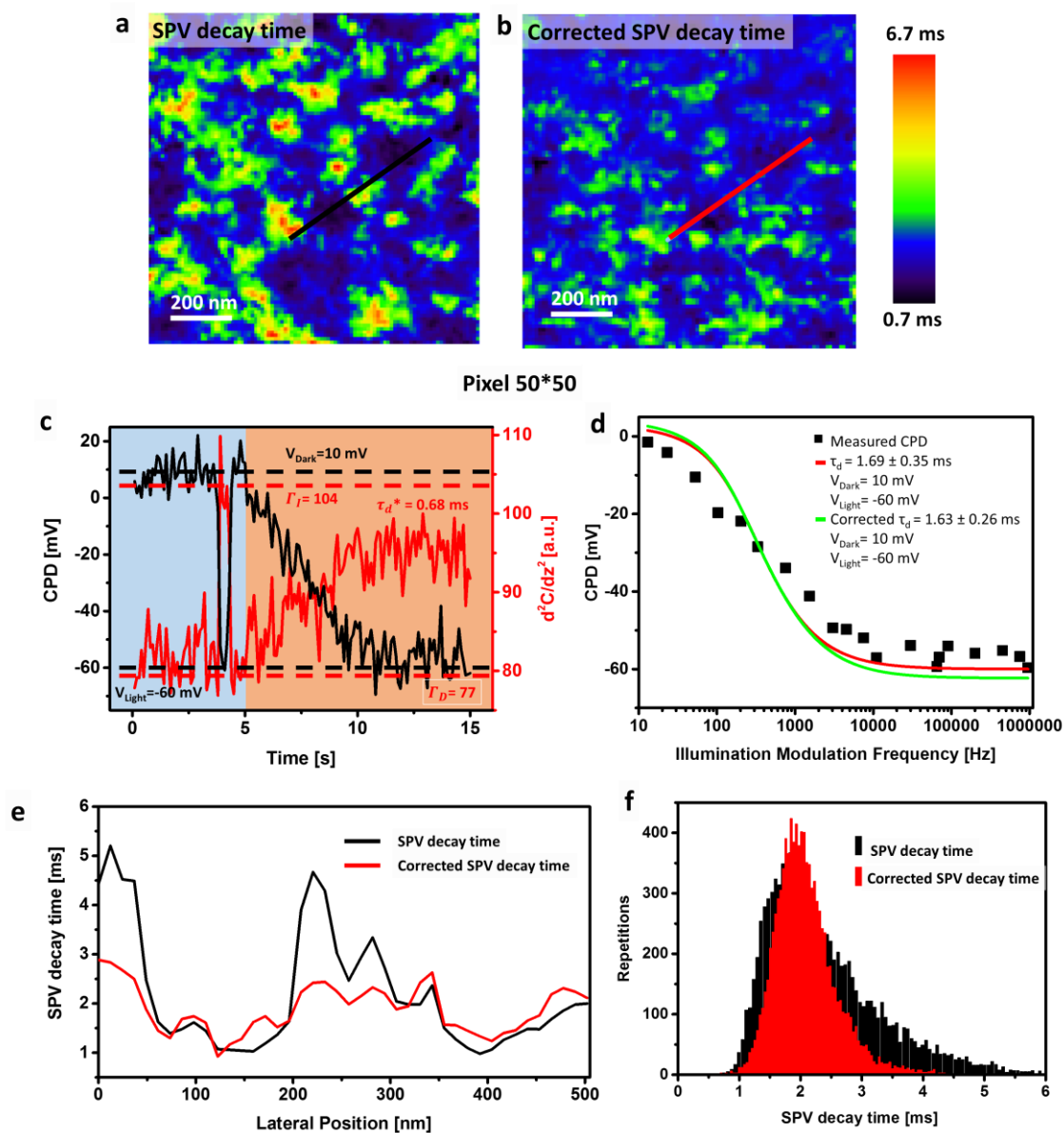


Figure 5.9– (a) SPV decay time image. (b) Corrected SPV decay image. (c) Raw information obtained via the improved FMI-KPFM protocol over pixel 50*50 of a and b. (d) CPD data and fit adjustment of models described by Eq. 4.1 (in red) and Eq. 8.13 (in green). (e) Profile section comparison of both SPV decay time images. (f) Histogram comparison between both the SPV decay time image (in black) and its corrected version (in red).

Actually, all 2-dimensional frequency-spectroscopy data presented so far have been acquired in close loop mode, this means that during the spectroscopy measurements, the feedback loop controlling the distance between the tip and the surface of the sample is activated. In this way, the distance between the tip and the sample is regulated to be constant during the duration of the experiment. However, by doing so, the z feed-back loop also regulates the F_{2w} signal. Actually, it can be demonstrated that, the z feed-back loop which is based on the control and regulation of the cantilever frequency shift, has an influence on the F_{2w} signal which is related to the capacitance gradient and sensitive to the tip-sample distance.

Figure 5.10 depicts two F_{2w} spectroscopy curves, acquired over the same PCBM₇₀/PTB₇ sample using the FMI-KPFM improved protocol under same experimental conditions in both open and close loop mode.

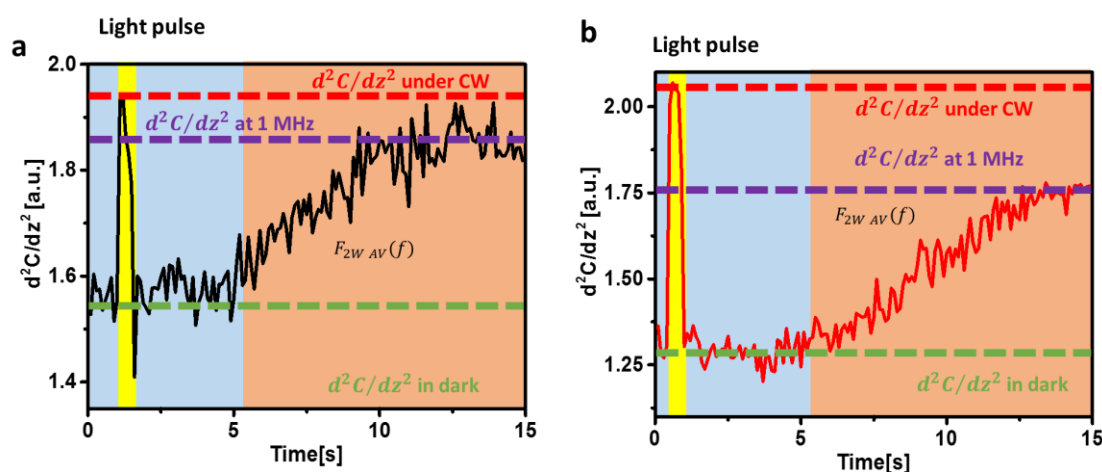


Figure 5.10– (a) Spectroscopy curve of F_{2w} obtained in close loop mode via FMI-KPFM in frequency modulation mode KPFM. (b) Spectroscopy curve of F_{2w} obtained in open loop mode via FMI-KPFM in frequency modulation mode KPFM.

From this Figure we observe that when working in open loop mode (Figure 5.10b), we obtain a spectroscopy curve with an improved signal-to-noise ratio compared to the one obtained in close loop mode (Figure 5.10a).

It goes without saying that this represents an advantage of spectroscopy data acquisition in open loop mode against close loop mode. However, the increase of the F_{2w} spectroscopy curve quality does not come without a price. In fact, there are several conditions that have to be fulfilled in order to carry trustworthy measurements in this mode, the most important one being the stability of the cantilever frequency shift during the spectroscopy. Indeed, if during the spectroscopy measurements the frequency shift of the cantilever is not reasonably stable, KPFM and topography results are likely to be influenced by artefacts. Moreover, in this mode, as the frequency shift of the cantilever can vary during the spectroscopy, an additional safety distance is needed between tip and sample (to minimize the risk of tip-sample crashing), preventing the acquisition of high resolution images. However, we stress that during this thesis, SPV decay time images (not shown) were acquired over the PCBM₇₀/PTB₇ sample using the improved FMI-KPFM protocol in both open and close loop mode, yielding almost identical results.

To sum up, the FMI-KPFM improved protocol offers several advantages over its predecessor. Indeed, by registering both the CPD under continuous wave illumination and in dark conditions prior to the spectroscopy, two different variable parameters (V_{LIGHT} and V_{DARK}) can be fixed in the mathematical model used to fit the CPD data and to calculate the SPV decay time. This, in turn increases the accuracy of the fit and therefore the accuracy of the time constant calculation. Moreover, by registering F_{2w} in the same way as the CPD signal, it becomes possible to obtain additional information from the sample, such as images of d^2C/dz^2 (or dC/dz in AM mode) under continuous wave illumination and in dark conditions, along with an image of the decay time constant associated with the capacitance change. Ultimately, this new information can be used to correct artefacts in the SPV decay time image caused by this capacitance change.

5.7 On the presence of surface photovoltage contributions displaying inverted polarities.

As previously discussed in **Chapter 4**, under illumination, some samples can exhibit both a positive and a negative SPV behaviour depending on the region over which measurements are taken. This is especially true in the case of bare donor-acceptor (D-A) OPV active layers, when even though a compositional gradient is usually present, favouring the apparition of a single SPV polarity under illumination, the presence of clusters of the opposite material near the surface exhibiting an inverted SPV polarity under illumination cannot be ruled out. In fact, as discussed in **Chapter 4**, the presence of these clusters is very likely to be the reason behind the detection of a SPV whose polarity changes from one region to the other over the sample.

In the following, to gain a deeper insight onto the presence of the described dual SPV behaviour, single-point FMI-KPFM measurements (improved protocol) were acquired over the PCBM₇₀/PTB₇ sample at two different illumination intensities.

Firstly, we observed that when shining the sample using a 15 mW/cm² illumination intensity, the magnitude of the SPV under continuous wave illumination is higher than when illuminating the sample at 300 mW/cm². Moreover, in both cases the photovoltaic response seems to be about the same under modulated illumination. This behaviour can be observed in detail in Figure 5.11.

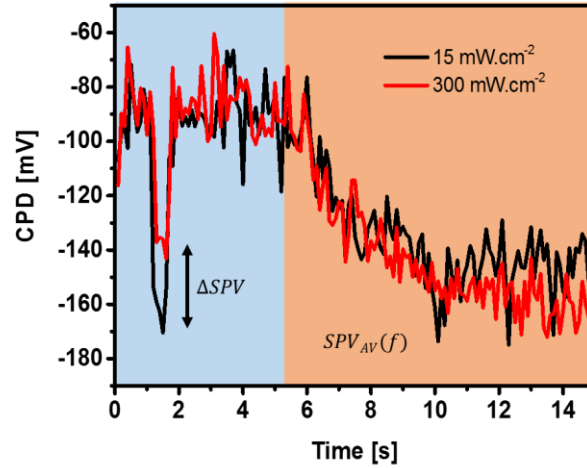


Figure 5.11– Single-points FMI-KPFM measurements taken under illumination intensities of *ca.* 15 mW/cm² and 300 mW/cm² over the same region of the sample.

For a clearer view of this behaviour, in Figure 5.12 we show the evolution of the SPV under continuous wave illumination measured over the same region of the sample (single-point measurements) as a function of the illumination intensity.

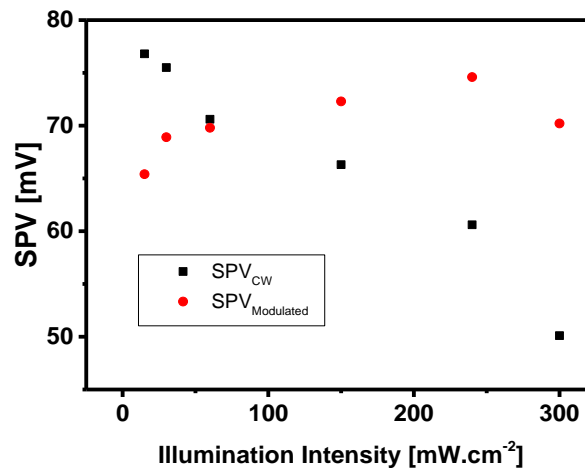


Figure 5.12– SPV under continuous wave illumination as a function of the illumination intensity.

In Figure 5.12 we observe that increasing the illumination intensity results in a decrease of the SPV under continuous wave illumination, on the other hand, the “modulated” SPV remains somewhat the same or varies very little regardless of the illumination intensity.

This behaviour can be interpreted as evidence suggesting the presence of inverted polarity SPV contributions. Basically, one could argue that given the morphology of the sample, the total SPV as measured under continuous wave illumination is in fact the superposition of different SPV contributions with different polarities and dynamics.

To better understand this, let us imagine two independent SPV contributions with inverted polarities that evolve differently with the illumination modulation frequency as depicted in Figure 5.13 by a numerical simulation (details on how to perform the presented numerical simulation can be found in **Chapter 6**).

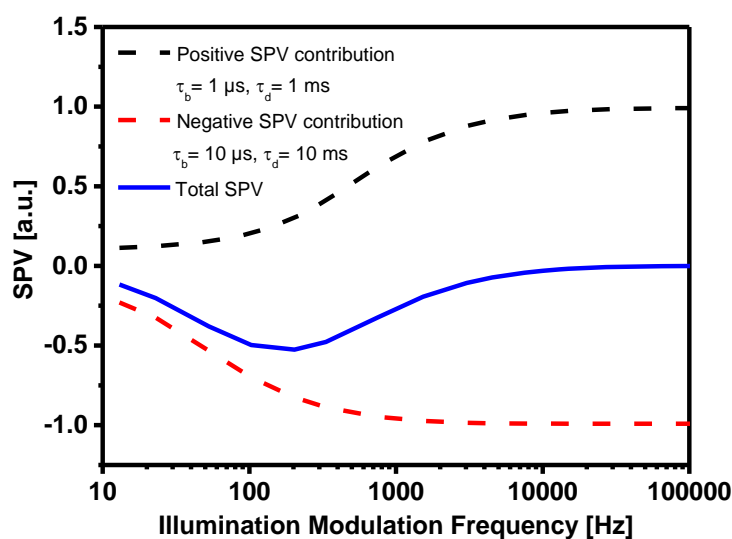


Figure 5.13– Numerical simulation showing two SPV contributions with inverted polarities and different dynamics, along with the resulting total SPV. Simulation parameters are indicated in the Figure. In both cases a 10% modulation duty ratio was assumed.

In Figure 5.13 we observed a simulated scenario in which at lower illumination modulation frequencies, the negative SPV contribution dominates and a negative total SPV is measured. However, as the illumination modulation increases, the positive SPV contribution start to develop, rendering more positive the magnitude of the total SPV.

Actually, while writing these lines, new evidence kindly provided by Dr. Benjamin Grévin, confirmed beyond any reasonable doubt, the presence of a SPV which is indeed the result of the superposition of at least two different SPV contributions exhibiting different polarities and dynamics.

Figure 5.14 shows FMI-KPFM results obtained by Dr. Grévin over the same PCBM₇₀/PTB₇ sample acquired under an illumination intensity of 1500 mW/cm².

Figure 5.14a show the SPV under continuous wave illumination as obtained from the spectroscopy curves analysis. In this image it is very interesting to observe both a negative and a positive SPV over the surface of the sample. Figure 5.14b shows more clearly this dual SPV behaviour. In this image the areas of the sample exhibiting a positive SPV are coloured in black and circled by green lines. Figure 5.14c depicts the “modulated” SPV image obtained upon subtracting the CPD image acquired at the highest illumination intensity to the CPD image acquired in dark condition (via the spectroscopy curve analysis). Here, we observe a negative SPV over the entire image. However, both Figures 5.14a and 5.14c exhibit a similar contrast. In fact, it seems that regions displaying a positive SPV in Figure 5.14a, display a weaker (although negative) SPV in Figure 5.14c. Similarly, when shining the sample at lower illumination intensities, we obtained an image of the SPV under continuous wave illumination (not show), exhibiting a weak negative SPV for regions previously exhibiting a positive SPV. Additionally, at this reduced illumination intensity, regions of the sample previously exhibiting a negative SPV, exhibit a stronger negative SPV.

To better understand this behaviour, it is necessary to take a look at the single-point spectroscopy curves depicted on Figures 5.14d and 5.14e.

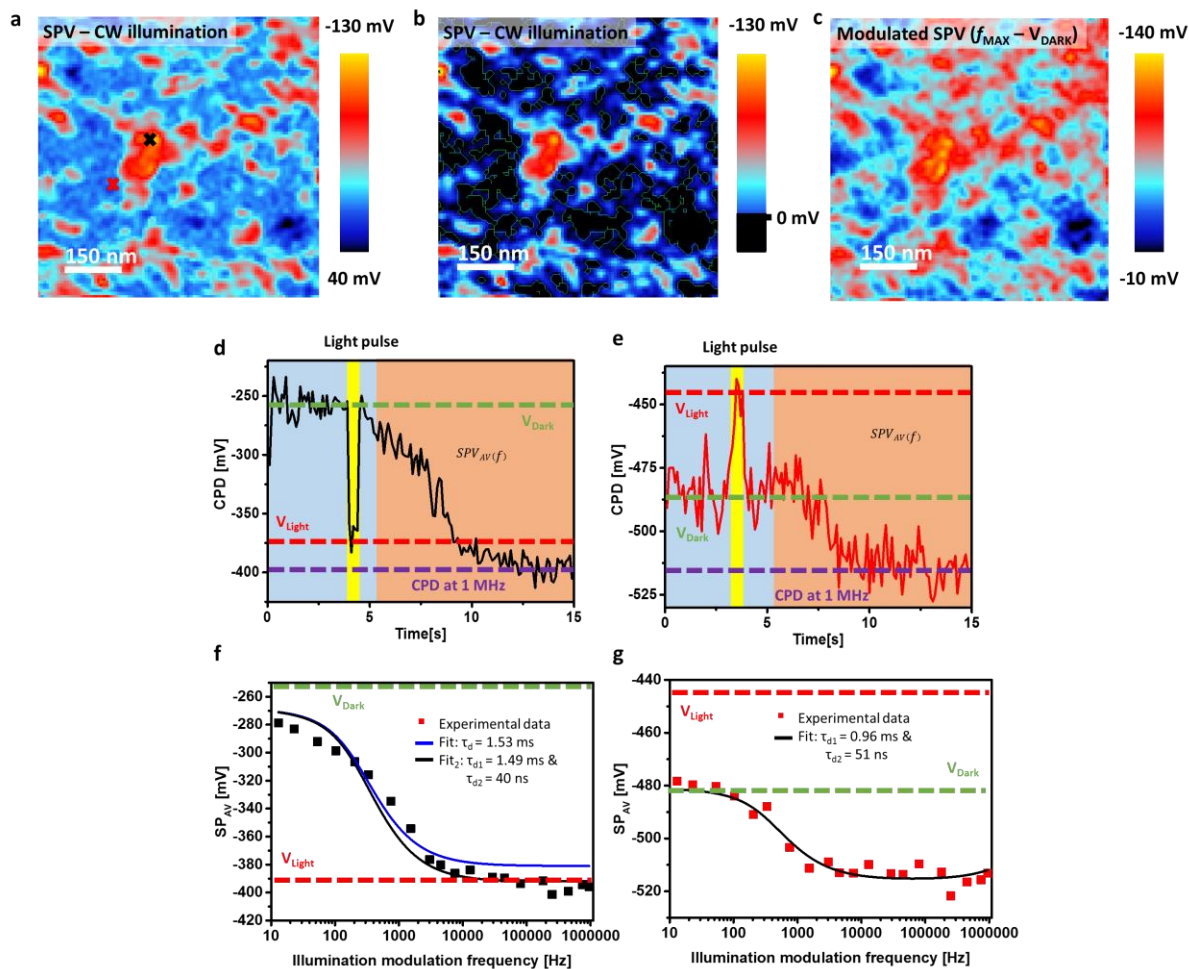


Figure 5.14– Unveiling the dual polarity SPV behavior: **(a)** Image of the SPV under continuous wave illumination obtained via FMI-KPFM. **(b)** Image of the SPV under continuous wave illumination highlighting the presence of both a positive and a negative SPV. **(c)** “Modulated” SPV image. **(d)** Spectroscopy curve acquired over the area of the sample indicated in **a** with a black cross. **(e)** Spectroscopy curve acquired over the area of the sample indicated in **a** with a red cross. In the Figure we observed an inversion of the SPV under continuous wave illumination with respect to the SPV measured under modulated illumination. **(f)** Different mathematical fits applied over the frequency-domain part of the signal previously presented in **d**. **(g)** Mathematical fit applied over the frequency-domain part of the signal previously presented in **e**.

These two single-point spectroscopy curves were obtained over regions indicated in Figure 5.14a by a black and a red cross respectively. In fact, from these curves, it would appear that depending on the region of the sample, the SPV under continuous wave illumination can

change its polarity with respect to the SPV under modulated illumination. This adds strong evidence suggesting the presence of different SPV contributions which evolve differently with the illumination modulation frequency as previously shown by the simulation on Figure 5.13.

From these curves one could predict that, if it was possible to further increase the illumination modulation frequency, the measured CPD would eventually match the one measured under continuous wave illumination. In fact, in both cases (Figures 5.14d and 5.14e), a positive SPV contribution would be expected to “kick in” at a certain frequency value, driving the value of the measured CPD towards the red dashed lines marking the CPD measured under continuous wave illumination.

At this point, we briefly make a pause on the discussion, to comment that during this thesis, SPV investigations at illumination modulation frequencies higher than 5 MHz were not possible due to set-up limitations. To the best of our knowledge, laser devices offering the possibility of being modulated in the MHz-GHz regime while offering the possibility to modify the modulation duty ratio without affecting the “squareness” of the modulated signal has not yet been fabricated. Nonetheless, an alternative approach to circumvent this issue might be the use of electrical signals to excite the sample instead of illumination pulses. This approach originally proposed by Narchi and co-workers has been already implemented over the cross section of an epitaxial silicon solar cell yielding promising results. [3, 9]

Coming back to the previous discussion, we can summarize that, in this sample, at high illumination intensities, the SPV can be characterized by at least two different SPV contributions exhibiting inverted polarities. In this case, the positive component appears to be several orders of magnitude faster than the negative one. This difference between dynamics can be understood intuitively by looking at Figures 5.14d and 5.14c. Nonetheless, another evidence on the presence of these two different dynamics can be observed on Figure 5.14f. In this Figure, the frequency-domain part of the spectroscopy curve presented in Figure 5.14d was plotted separately. Here, we observed that applying a mathematical fit taking into account a single SPV decay time, results in a non-optimized data adjustment. On the other hand, if we use an analytical model which describes two different time-constants, an improve adjustment

to the data is obtained. In a similar way, in Figure 5.14g we observe frequency-domain part of the spectroscopy curve presented in Figure 5.14e, the mathematical fit can only be applied using a model accounting for at least two different dynamics, otherwise the fit procedure fails at converging. From these observations, it would be fair to argue that the negative SPV contribution shall exhibit a SPV decay time around 1-1.5 ms, while the positive SPV contribution shall exhibit a decay time around 40-50 ns (for the applied illumination intensity, *ca.* 1500 mW/cm²).

Having discussed the implications of a SPV exhibiting a dual behaviour, we now take a moment to verify the self-consistency of the FMI-KPFM measurements in order to exclude the presence of artefacts misleading our conclusions. In this endeavour, images of the in-dark and under continuous wave illumination surface potential, as well as images of the in-dark and under continuous wave illumination d^2C/dz^2 , obtained via the improved FMI-KPFM protocol are compared to the same images acquired via standard KPFM investigations. Results are shown in Figure 5.15.

In Figure 5.15, we observe a full correspondence between images obtained via the improved FMI-KPFM protocol and standard KPFM investigations. These results imply that in this case, the improved FMI-KPFM protocol is not affected by additional sources of artefacts such as cantilever detuning during the illumination pulse even at the high illumination intensity used during the experiment.

Having checked FMI-KPFM results self-consistency, let us now take a look at the behaviour of d^2C/dz^2 during the spectroscopy (Figure 5.16). Here, contrary to the case of the SPV, its behaviour seems to be the same for all regions of the sample, exhibiting a similar trend with respect to the illumination modulation frequency. In fact, it seems that overall, spectroscopy curves of d^2C/dz^2 only experience a slight upwards and downwards shift from one region of the sample to the other.

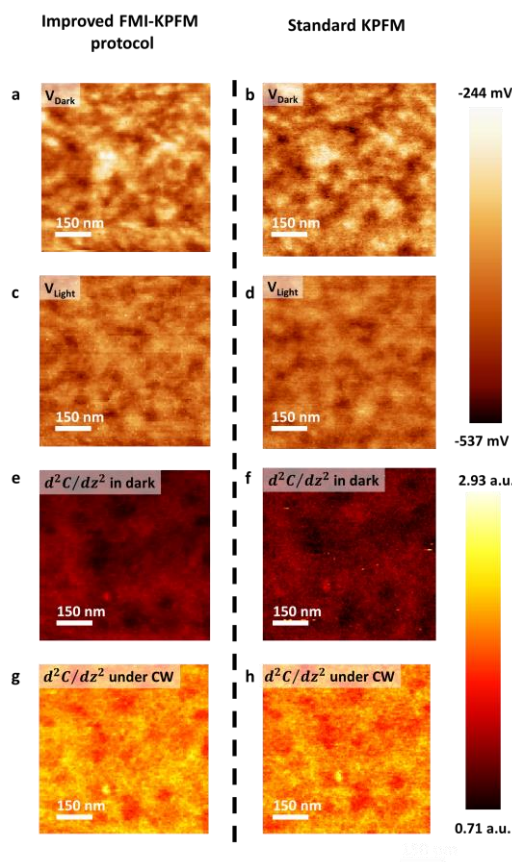


Figure 5.15– **(a,c,e,g)** Images of the in-dark and under continuous wave illumination surface potential, as well as images of the in-dark and under continuous wave illumination d^2C/dz^2 , obtained via the improved FMI-KPFM protocol respectively. **(b,d,f,h)** Images of the in-dark and under continuous wave illumination surface potential, as well as images of the in-dark and under continuous wave illumination d^2C/dz^2 , obtained via the standard KPFM investigations respectively. Data & processing courtesy of Dr. Benjamin Grévin.

Figure 5.16a shows an image of d^2C/dz^2 under continuous wave illumination obtained via the spectroscopy curves analysis. Analogously, Figure 5.16b shows an image of d^2C/dz^2 in dark conditions, again, obtained via the analysis of the spectroscopy curves acquired during the improved FMI-KPFM protocol implementation. Figures 5.15c and 5.15d show single-point spectroscopy curves of d^2C/dz^2 acquired at the same location as the single-point SPV spectroscopy curves presented in Figures 5.14d and 5.14e. From these curves we observed that

despite the fact that the SPV behaves very different in those locations, the behaviour of d^2C/dz^2 seems to be similar in both regions.

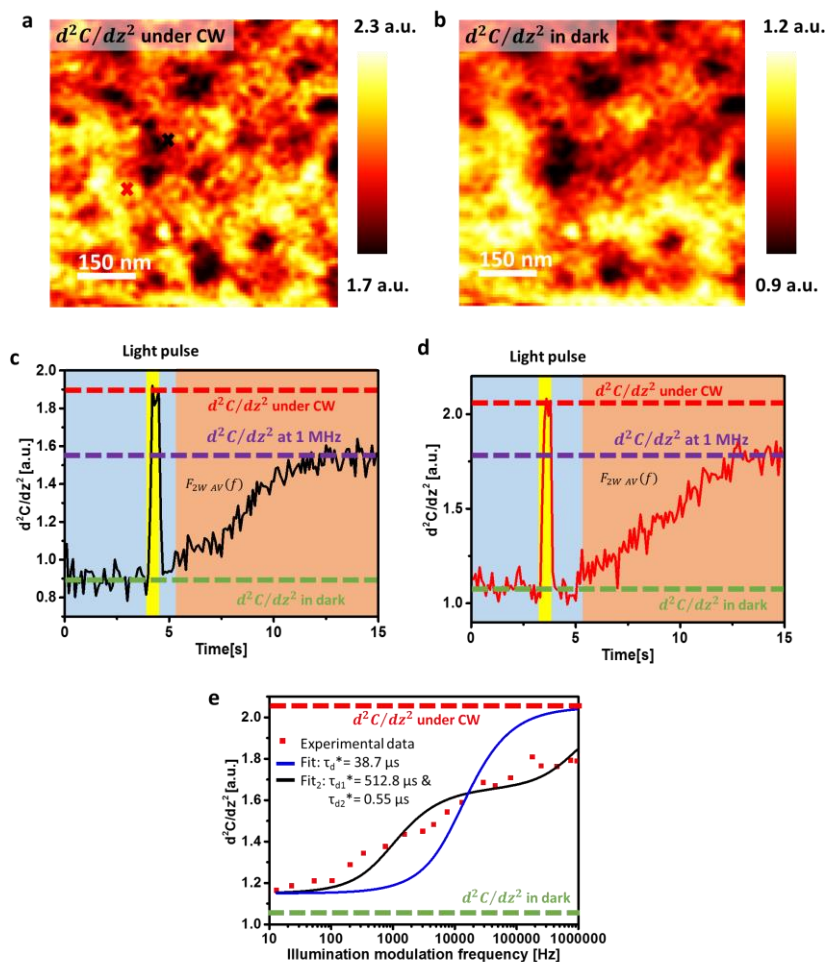


Figure 5.16– Image of d^2C/dz^2 under continuous wave illumination (a) and in dark conditions (b) obtained via the FMI-KPFM improved protocol.

However, when attempting to fit the frequency-domain data of the d^2C/dz^2 spectroscopy curve presented in Figure 5.16d to obtain τ_d^* (Figure 5.15e), we observed that similar to the case of the SPV, a mathematical model accounting for a single d^2C/dz^2 decay time, fails at describing the way the data evolves. To ensure a good fit adjustment, a model including the presence of two different dynamics was needed. The inconsistency between the

model accounting for a single decay time constant and the d^2C/dz^2 data, could be indeed the result of the presence of SPV contributions exhibiting different polarities, although this is not yet clear.

In any case, the presence of two decay constants in the d^2C/dz^2 signal (τ_{d1}^* and τ_{d2}^*), put some constraints to the analytical model previously used to account for capacitance artefacts on the calculation of the SPV dynamics. Actually, in this case, a new model would have to be developed to account for capacitance artefacts on the calculation of the SPV dynamics when the d^2C/dz^2 signal displays a non-monotonic behaviour. Such model could be obtained by developing the following expression:

$$V_{AV}KPFM = \frac{\int_0^{1/f} \Gamma(t)V(t)dt}{\int_0^{1/f} \Gamma(t)dt} \quad (5.6)$$

With $\Gamma(t) = \frac{dC}{dz}(t)$ in amplitude modulated KPFM and with $\Gamma(t) = \frac{d^2C}{d^2z}(t)$

However, such model risk of being complex and its implementation on the automatic fit procedure challenging. That is why, in the next chapter of this thesis we will take another approach by estimating the SPV dynamics based on numerical calculations rather than on mathematical fit procedures.

Conclusion

In this chapter, the discussion was focused on the presence of plausible sources of artefacts in FMI-KPFM measurements, such as capacitance and resonant-induced effects, and on how to avoid them.

We saw that capacitance gradients present between tip and sample, could in fact modify the KPFM signal under certain circumstances. We confirmed the presence of these effects by implementing Kelvin probe force spectroscopy measurements. Furthermore, in order to avoid having these unwanted effects, we gave guidelines and recommendations for the correct implementation of FMI-KPFM measurements such as working in FM-KPFM mode and using reduced modulation duty ratios.

During this chapter, we also compared the implementation of FMI-KPFM in AM and FM-KPFM modes. In fact, we saw that in general, we recommend the implementation of FMI-KPFM investigations in FM-KPFM mode when dealing with bare nanophase segregated organic blends and other bare samples where nanophase segregated clusters of different charge populations are likely to be found, due to the averaging of charge populations that we often found when working in AM-KPFM mode. Moreover, as mentioned above, in FM-KPFM mode, measurements were found to be less sensitive to capacitance-related artefacts.

We also discussed some other sources of plausible artefacts present in FMI-KPFM such as frequency mixing, photo-charges coming from the tip and the reflection of the illumination laser on the photodiode of the AFM system. In each case, guidelines were given to avoid/minimize these unwanted effects.

Finally, a new improved FMI-KPFM measurement protocol was introduced. This new protocol allowed us to counteract the majority of the discussed unwanted effects. Additionally, this new protocol allowed us to perform studies aimed at proving the presence of SPV contributions with inverted polarities on a BHJ OPV sample exhibiting a nanophase separation.

References

1. Fernández Garrillo, P.A., et al., *Photo-Carrier Multi-Dynamical Imaging at the Nanometer Scale in Organic and Inorganic Solar Cells*. ACS Applied Materials & Interfaces, 2016. **8**(45): p. 31460-31468.
2. Fernández Garrillo P. A., B.L., Caffy F., Demadrille R., Grévin B. *Imaging the Multi-Temporal Photo-Carrier Dynamics at the Nanometer Scale in Organic and Inorganic Solar Cells*. in *IEEE PVSC-44*. 2017. Washington D.C. - USA.
3. Fernández Garrillo, P.A., et al., *Comments on "Nanoscale Investigation of Carrier Lifetime on the Cross Section of Epitaxial Silicon Solar Cells Using Kelvin Probe Force Microscopy"*. IEEE Journal of Photovoltaics, 2018. **8**(2): p. 661-663.
4. Almadori, Y., N. Bendiab, and B. Grévin, *Multimodal Kelvin Probe Force Microscopy Investigations of a Photovoltaic WSe₂/MoS₂ Type-II Interface*. ACS Applied Materials & Interfaces, 2018. **10**(1): p. 1363-1373.
5. Almadori, Y., et al., *Multimodal noncontact atomic force microscopy and Kelvin probe force microscopy investigations of organolead tribromide perovskite single crystals*. Beilstein Journal of Nanotechnology, 2018. **9**: p. 1695-1704.
6. Schumacher, Z., et al., *Measurement of Surface Photovoltage by Atomic Force Microscopy under Pulsed Illumination*. Physical Review Applied, 2016. **5**(4): p. 044018.
7. Sadewasser, S., N. Nicoara, and S.D. Solares, *Artifacts in time-resolved Kelvin probe force microscopy*. Beilstein Journal of Nanotechnology, 2018. **9**: p. 1272-1281.
8. Coffey, D.C. and D.S. Ginger, *Time-resolved electrostatic force microscopy of polymer solar cells*. Nature Materials, 2006. **5**: p. 735.
9. Narchi, P., et al., *Nanoscale Investigation of Carrier Lifetime on the Cross Section of Epitaxial Silicon Solar Cells Using Kelvin Probe Force Microscopy*. IEEE Journal of Photovoltaics, 2016. **6**(6): p. 1576-1580.

6 | Towards the numerical analysis of spectroscopy curves

Content

6.1 Context.....	181
6.2 The need for numerical simulations.....	183
6.2.1 SPECTY.....	184
6.3 Numerical simulations on a silicon nanocrystal solar cell.....	187
6.4 Organic photovoltaics: Mathematical fit versus numerical analysis.	192
Conclusion	196
References.....	197

Dans ce chapitre, le traitement des données est présenté. Une attention particulière est accordée au développement d'une routine de simulation numérique automatique qui permet de prédire le comportement des photo-porteurs et de le comparer aux résultats expérimentaux, tout en apportant des informations complémentaires relatives à leurs processus dynamiques.

6.1 Context

In **Chapter 4** we saw that Kelvin probe force microscopy under frequency-modulated excitation has emerged as a useful technique for probing photo-carrier dynamics and gaining access to carrier lifetime at the nanoscale in a wide range of photovoltaic materials.[1-9] However, as already discussed, some aspects about the data interpretation of frequency modulated illumination Kelvin probe force microscopy (FMI-KPFM) and some other techniques based on the same approach are still the subject of debate. Indeed, in that regard,

special attention shall be given to the mathematical model used in the data-fitting process as it constitutes a determinant aspect in the time constants calculation. In particular, as previously mentioned, mathematical models used in the fit procedure that have been developed so far do not take into account the fact that depending on the imposed modulation frequency value, a quasi-steady state condition of the average potential is only reached after a certain number of excitation pulses. Moreover, analytical models taking into account the above described phenomenon, risk of being complex and their implementation on the fit procedure, challenging. Furthermore, such an ideal analytical model should also compensate for the capacitance-induced artefacts described in the previous chapter, rendering the model even more intricate. Additionally, even if such an intricate model is successfully implemented in the automatic fit procedure, we risk however of having a good curve adjustment to the data points at the expense of not obtaining meaningful time constant values. Indeed, during these thesis, we observed that the more complex the analytical model was, the higher the risk of having an interdependence between fit parameters, affecting the fidelity of the fit.

Therefore, in the following, we propose and demonstrate an automatic numerical simulation routine that enables to predict the behaviour of spectroscopy curves of the average surface photo-voltage as a function of a frequency modulated excitation source in photovoltaic materials, enabling the comparison of simulations and experimental results. In fact, by means of this comparison, it will be possible to adjust the simulated curves to match the experimental ones. Like this, the input parameters of the simulation should yield the time constants related to the experimental result, constituting an alternative method to determine the photo-carrier dynamics without the need of a complex analytical model.

In this chapter, we describe the general aspects of this simulation routine and compare it against experimental results previously obtained by Borowik *et al.*,[1] over the silicon nanocrystal solar cell previously investigated in **Chapter 4**, as well as against results obtained by intensity-modulated scanning Kelvin probe microscopy over the nano-phase segregated PDBSTQx/PC₇₁BM blend previously introduced in the same chapter. Moreover, we will show how this simulation routine can complement experimental results as additional information about the sample's photo-carriers dynamics can be gained via this numerical analysis

6.2 The need for numerical simulations

A common aspect among all KPFM frequency-modulated spectroscopy techniques is that in order to extract time constants associated to photo physical processes, a mathematical fit procedure is usually implemented. Indeed, all methods including a mathematical fitting procedure using equations related to the ones described in previous chapters have certain limitations. First, these equations only apply for specific cases of dynamical process of charge and a certain number of dynamical time constants (for example only one effective surface photovoltage (SPV) decay time, or two different SPV decay times and one SPV built-up time). This means that, in the case that there exist different dynamical processes from that described by these equations, a new equation must be developed. Secondly, in the case of equations with many fit parameters, it becomes easy to obtain a relatively good fit adjustment to data, however, constants found this way, risk of being an approximate, since one of the fit parameters can likely influence other fit parameter (dependency between fit parameters), meaning that several fit solutions are possible.

It is obvious that the mathematical model used in the fit procedure constitutes a determinant aspect in the time constants calculation, hence the need to define methods that could check the validity of the mathematical assumptions. This led us to develop a simulation routine that enables to predict the behaviour of spectroscopy curves of the average photovoltage as a function of a frequency modulated excitation source in photovoltaic materials.

In a previous work[1], our research group implemented a single exponential decay model to fit the spectroscopy curves acquired over a silicon nanocrystal solar cell. In the following, using a novel automated numerical analysis routine, we will verify the validity of the model by checking the self-consistency of the previously obtained results via the comparison of measured data, mathematical fit and simulations.

6.2.1 SPECTY

In a first approach, an exponential function can be used to describe the built-up and decay of the SPV in photoactive materials.[1-4, 8] Under this premise, we can model the SPV behaviour of a photovoltaic material under modulated excitation as a function of time for both the built-up and decay in the following way for the case of a single SPV built-up and decay time-constant (Eq. 6.1 and 6.2) and for a more general case with k or l number of build-up and decay time-constants (Eq. 6.3 and 6.4):

$$SPV_{Built-up} = 1 - e^{-\left(\frac{p+A}{\tau_b}\right)} \quad (6.1)$$

$$SPV_{Decay} = e^{-\left(\frac{i+B}{\tau_d}\right)} \quad (6.2)$$

$$SPV_{Built-up} = \sum_1^k \left(1 - e^{-\left(\frac{p+A}{\tau_{bk}}\right)^n} \right) \quad (6.3)$$

$$SPV_{Decay} = \sum_1^l \left(e^{-\left(\frac{i+B}{\tau_{dl}}\right)^n} \right) \quad (6.4)$$

Here, p is the time duration of the excitation pulse, i is the in-between-pulses time duration, both A and B are values that shift the $SPV_{Built-up}$ and SPV_{Decay} starting points, to ensure the SPV continuity between equations. Moreover, τ_b and τ_d are the SPV built-up and decay time constants respectively (more details about these parameters can be found on Figure 6.1). Finally, in the general form expression, n can have any value from 0 to 1, this parameter models the presence or absence of dispersive kinetics. In this form k and l are positive integer values that model the presence of multiple SPV dynamics.

The number of build-up and decay time-constants can be determined in advance from accessible literature by taking into account the type and proprieties of the material (doping level and type, defects concentration, gap, and so on). For instance, types of recombination mechanisms for silicon can be found in Ref. [10].

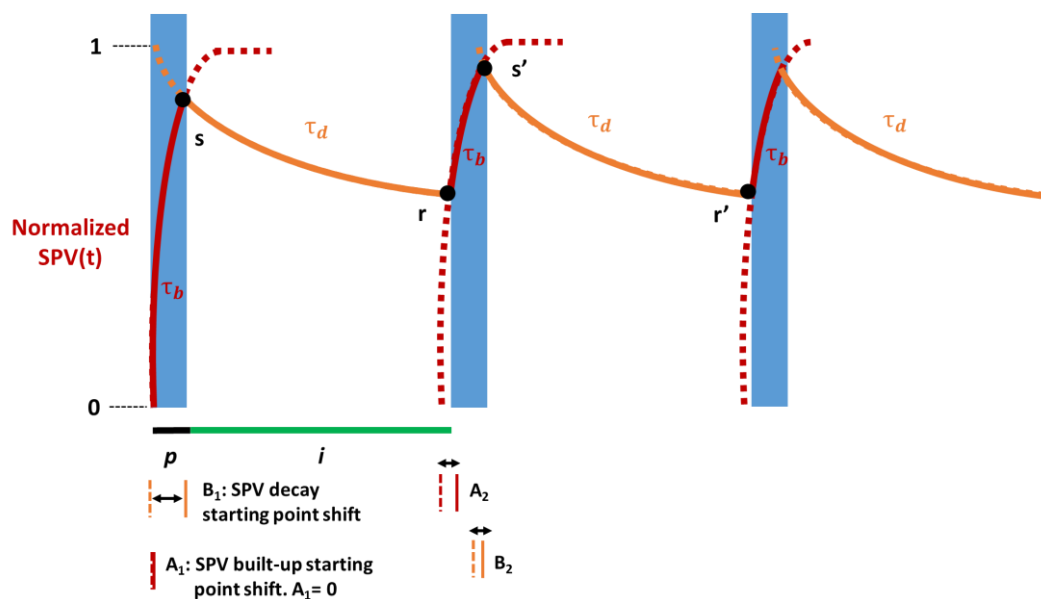


Figure 6.1– Physical description of simulation parameters.

Now, using Eq. 6.1 and Eq. 6.2 we can numerically model the normalized magnitude of the instant SPV as a function of time for different excitation modulation conditions (See Figure 6.2a). In other words, we can access the normalized magnitude of the instant SPV at any given point in time for any given modulation frequency. Depending on the imposed modulation frequency value, a quasi-steady state condition is reached after a certain number of excitation pulses, indicating that the equilibrium state of charges was reached. Once this condition is attained, we calculate the average value of the normalized SPV (*i.e.*, via integrals calculation). By performing this calculation at different modulation frequencies we can then plot the evolution of the normalized average surface photo-voltage magnitude as a function of the excitation modulation frequency as depicted in Figure 6.2b. A home-made software (SPECTY) implementing this routine was separately developed using the SCILAB open source coding tool and the batch processing options of OriginPro software (OriginLab Corp.) yielding same results.

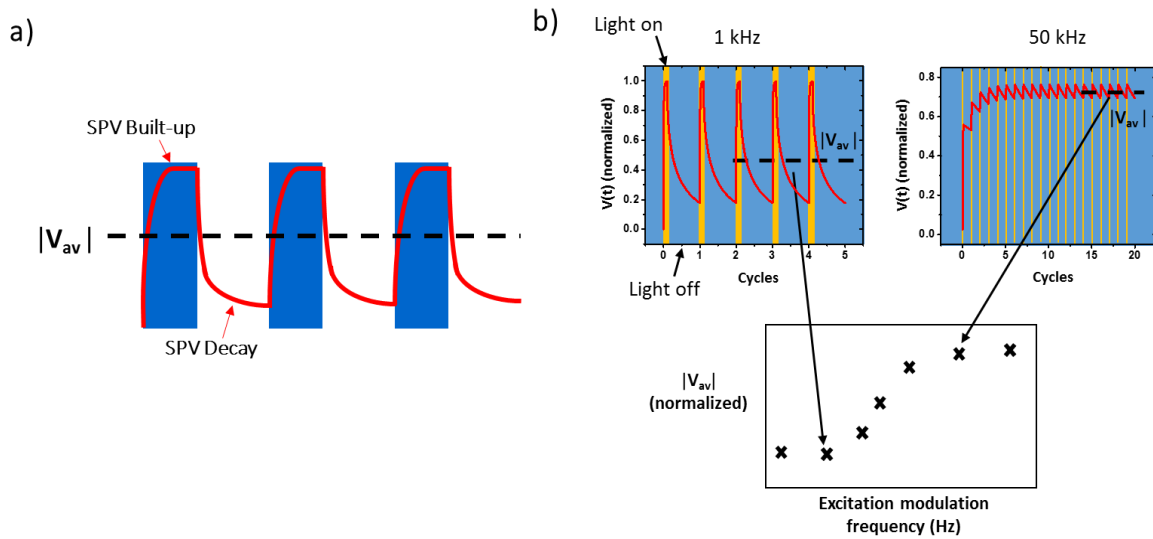


Figure 6.2– SPECTY working principle: **(a)** SPV built-up and decay are modelled using Eq. 6.1 and Eq. 6.2 respectively. **(b)** A quasi-steady state condition is reached after a certain number of excitation pulses. At this moment the average value of the normalized SPV is calculated. Performing this calculation at different modulation frequencies allows to plot the evolution of the normalized average surface photo-voltage magnitude as a function of the excitation modulation frequency. Reproduced from Ref. [11]

While both the syntax and the philosophy of the SCILAB open source coding tool and the batch processing options of OriginPro software are different, in both coding environments SPECTY is structured in a similar way. Figure 6.3 depicts the software flowchart detailing the algorithm used in the performed simulations. As depicted in this figure, upon the introduction of the simulation input parameters (SPV decay and built-up time constants along with the duty ratio and the frequency range), the software applies Eq. 6.1 or 6.3 to find the attained value of the surface photo-voltage just at the end of the illumination period (called “s” on Figures 6.1 and 6.3), then in a similar way, the software uses Eq. 6.2 or 6.4 to find the attained value of the surface photo-voltage after photo-carrier recombination occurred during the “in-dark” period (called “r” on Figures 6.1 and 6.3). To perform these calculations, the software needs to determine the values of both A and B for each illumination cycle. In the case of a single SPV built-up and decay time-constant (Eq. 6.1 and 6.2), $A = 0$ for the first illumination pulse, and $A = -Ln(1 - r)\tau_b$ for subsequent pulses, while $B = -Ln(s)\tau_d$. In the case of multiples SPV

built-up and decay time-constants (Eq. 6.3 and 6.4), $A = 0$ for the first illumination pulse, while the value of B and that of A for subsequent cycles can be found by numerical methods such as the least squares method.

This process is repeated until two consecutive “s” and “r” points have the same value which shall mean that the quasi-steady state condition was reached. Then, the average value of the last two pulses is calculated and storage in the form of a vector. At the end of the for loop, this vector is plotted yielding the spectroscopy curve $V_{AV}(f)$.

6.3 Numerical simulations on a silicon nanocrystal solar cell

Using SPECTY we can now verify the validity of the mathematical model used by Borowik *et al.*, where the minority carrier lifetime in a silicon nanocrystal solar cell was obtained by KPFM spectroscopy under frequency-modulated light illumination.[1] This can be done by fixing the SPV decay time in the numerical simulation to the value predicted by the mathematical fit used in that occasion and comparing the correspondence between the spectroscopy curve resulted from the mathematical fit and the data points obtained from the numerical simulation.

As discussed in a previous chapter, for the most part, FMI-KPFM and some other related techniques, do not take into account a SPV built-up time different from zero. This time, which as we already mentioned in previous chapter, is the time needed for the surface photovoltage to appear in the first place (as measured by KPFM) and is associated with the exciton generation, charge dissociation and charge transport along the material. Actually, in some cases, depending on the material and the excitation intensity, this time can be approximated to zero as the SPV built-up is usually much faster than the SPV decay. However, as we will see, taking into account a non-zero SPV built-up time can modify the interpretation of the spectroscopy curves, hence the estimation of the SPV time constants.

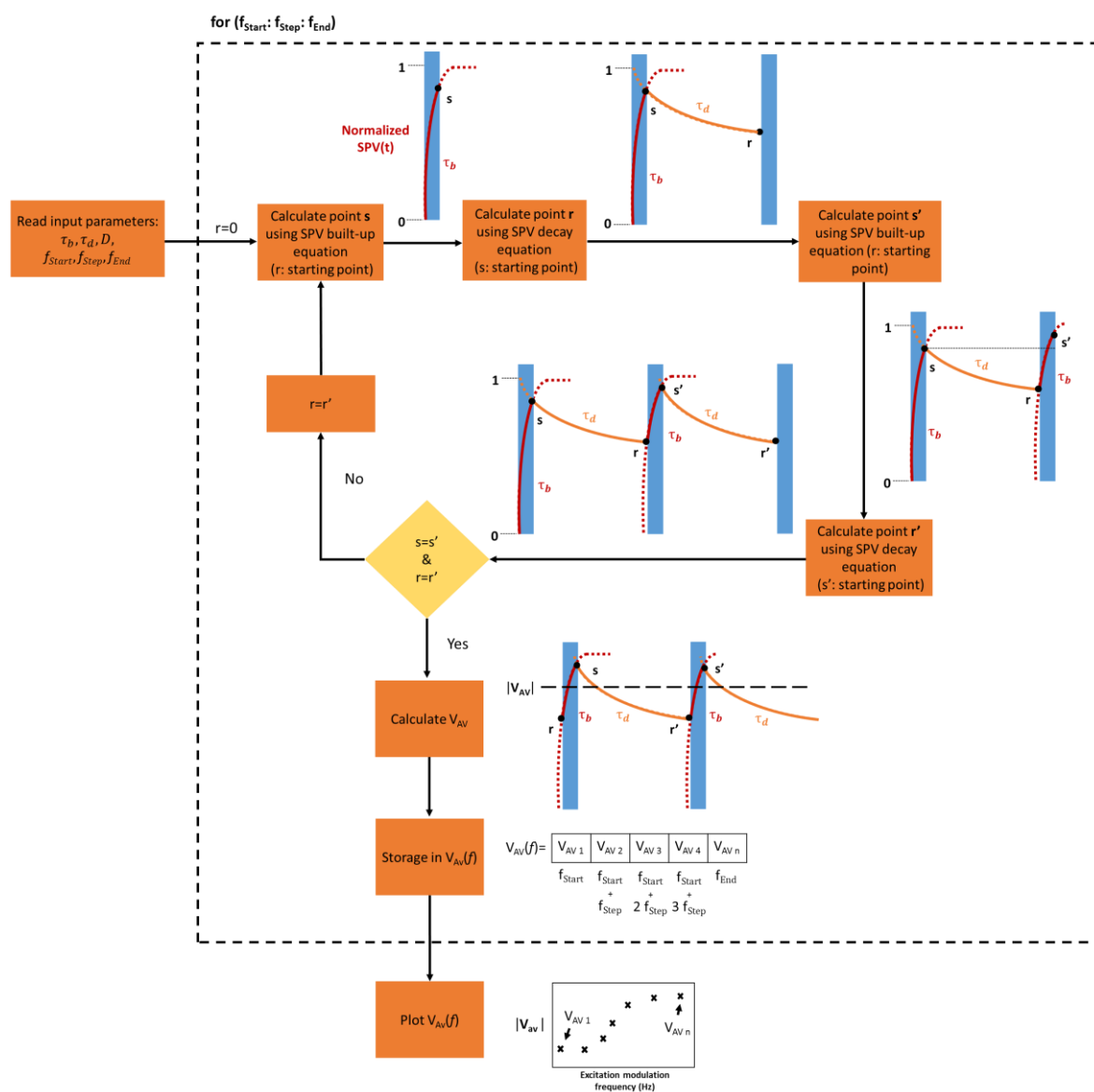


Figure 6.3– SPECTY's algorithm flowchart. Reproduced from Ref. [11]

Here, we highlight that the SPV built-up time can be physically interpreted in different ways depending on the sample and the photo-generation mechanism. In inorganic silicon samples for instance, this time constant can be attributed to the effective time needed for exciton generation, dissociation and carrier separation. On the other hand, in the case of some organic photovoltaic samples, the SPV built-up time can be attributed to the effective time

needed to fill lower energy states (traps). In a more general way it can be stated that the SPV built-up time is closely related to the carrier diffusion length within each particular material.

In [1], minority carrier lifetime values were calculated upon a mathematical fit procedure derived from previous publications[3] using the following expression:

$$\frac{\Delta V_{av}}{\Delta V_{max}} = D + \tau \cdot f \left(1 - e^{\left(\frac{D-1}{\tau f}\right)} \right) \quad (6.5)$$

Here, D is the modulation duty ratio, f is the modulation light frequency, $\Delta V_{av}/\Delta V_{max}$ is the ratio between the time-averaged surface potential and the saturated surface photo-voltage value and τ is the minority carrier lifetime.

Figure 6.4 depicts both the data points and the spectroscopy curve resulted from the mathematical fit from which the minority carrier lifetime was extracted in the silicon nanocrystal solar cell after H-passivation as presented in [1], as well as the simulated data-points. For the numerical simulation, τ_d was fixed at 70 μs (to match the value reported by Borowik and co-workers), and τ_b was fixed at 1 μs , but similar results were obtained using shorter values. On the other hand, the use of a $\tau_b > 1 \mu\text{s}$ yields simulated data-points which no longer follows the mathematical fit curve (green and gray squares in Figure 6.4). Both p and i were imposed to match the experimental parameters used in [1].

In Figure 6.4 we observe a full correspondence between the mathematical fit applied for the minority carrier lifetime extraction in the silicon nanocrystal solar cell after H-passivation and the numerical simulated data points ($\tau_b = 1 \mu\text{s}$), providing additional support for the KPFM frequency-modulated spectroscopy conceptual premise. Furthermore, this routine provides additional information about the SPV built-up time constant, as it shall be 1 μs at most so that the simulation agrees with measured data-points as shown in Figure 6.4, this information would not otherwise be accessible solely from the mathematical fit used in [1].

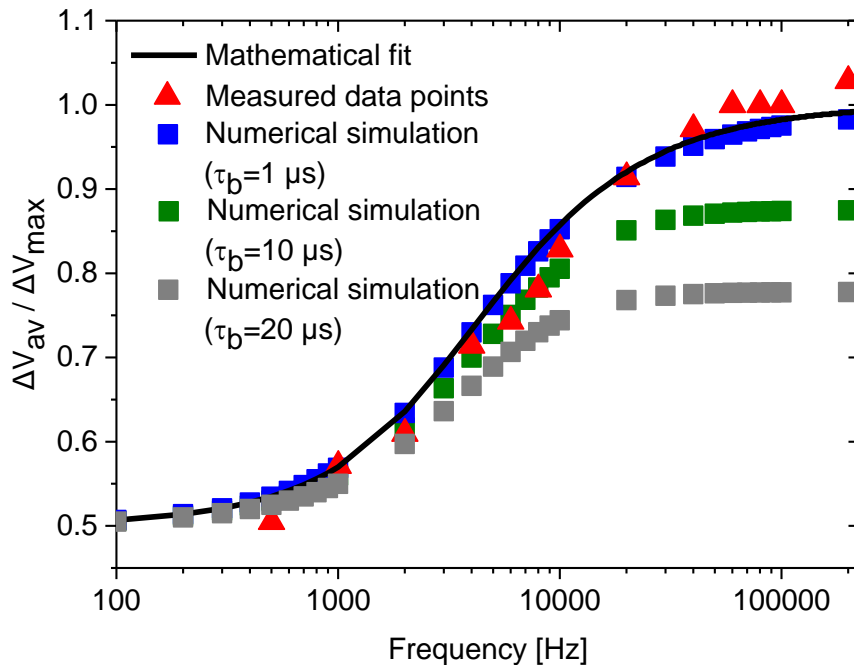


Figure 6.4– Comparison between spectroscopy curve obtained via the mathematical fit, measured data points and data points obtained by numerical simulations using $\tau_b = 1 \mu\text{s}$, $\tau_b = 10 \mu\text{s}$ and $\tau_b = 20 \mu\text{s}$ respectively. Data was extracted from Fig. 4 of [1]. Figure reproduced from Ref. [11]

Moreover, this time constant value strongly agrees with previous reports of the photo-generation and electro-hole pairs separation time scale for other silicon samples [9, 12, 13]

Additionally, SPECTY can provide graphic representations of how the SPV as a function of time evolves with the modulation frequency as show in Figure 6.5.

Information about the evolution of the SPV_{AV} as a function of the number of excitation cycles can also be accessed via the simulation routine as depicted in Figure 6.6. In fact, as above described, depending on the imposed modulation frequency value, a quasi-steady state condition is reached after a certain number of excitation pulses (charge equilibrium). In Figure 6.6 we note that as expected, the higher the modulation frequency is, the more illumination cycles are needed to attain the charge equilibrium state. Nonetheless, we stress

that even though more cycles are needed to attain this condition, in terms of time, it remains negligible compared to the KPFM integration time.

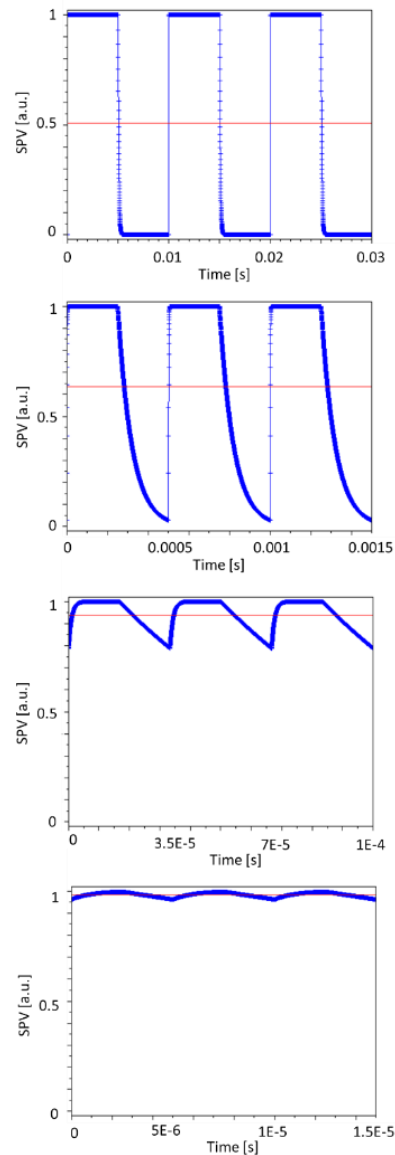


Figure 6.5– Simulated-SPV as a function of time for different excitation modulation frequencies, red line indicates average SPV value for each modulation condition. Modulation frequencies from top to bottom:

100 Hz, 2 kHz, 30 kHz, 200 kHz. Figure reproduced from Ref. [11]

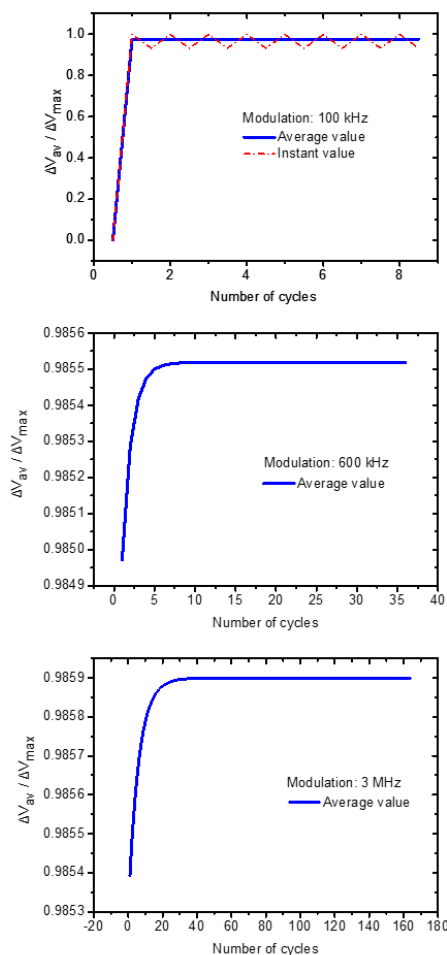


Figure 6.6– Simulated-SPV_{AV} as a function of the number of excitation cycles for different excitation modulation frequencies. From top to bottom: 100 kHz, 600 kHz and 3 MHz. Simulation at 100 kHz include the SPV instant value oscillation as depicted by the red dashed line. Graphs depicting results from simulations at 600 kHz and 3 MHz were zoomed-in so that the convergence process can be noticed.

Figure reproduced from Ref. [11]

6.4 Organic photovoltaics: Mathematical fit versus numerical analysis.

We now go back to the organic nano-phase segregated PDBSTQx/PC₇₁BM blend, previously investigated in **Chapter 4** and again in **Chapter 5**, over which we will apply the

improved FMI-KPFM protocol described in **Chapter 5** where the CPD under continuous wave excitation and the SPV_{AV} spectroscopy curve are simultaneously acquired. This way, both the CPD in dark conditions and under continuous wave illumination are known values that can be fixed when performing the mathematical fit. Here, the aim is to compare the results obtained via this improved protocol, against results obtained via the numerical analysis.

Figure 6.7 shows the obtained results, in this case, we used FMI-KPFM in frequency modulation mode. Here, the sample was optically excited using a green (515 nm) PhoxXplus module from OmicronLaserae GmbH with a peak output power of 50 mW/cm^2 . Modulation frequencies were swept from few tens of Hz to 10 kHz with a 10% duty ratio. At this point we highlight that measurements presented hereafter over the nanophase segregated PDBS-TQx/PC₇₁BM blend were obtained after an additional 10-month time period following measurements shown in the previous chapter. Once again, this means that its photo-physical properties most likely evolved even if the sample was stocked under UHV conditions. Therefore, comparisons regarding the photo-carriers dynamics cannot be easily established.

As it can be seen from Figure 6.7, the magnitude of the CPD measured under continuous wave illumination is higher than the average potential measured at the highest modulation frequency. In this scenario we propose that a non-zero SPV built-up time shall be accounted for.

In this endeavour, firstly the normalized SPV_{AV} spectroscopy curve is extracted as shown in Figure 6.8. As a second step, we fitted this SPV_{AV} spectroscopy curve using Eq. 4.1 and Eq. 4.2, as presented in **Chapter 4**, to estimate separately the SPV decay time constant (τ_d) and also τ_d together with a non-zero SPV built-up time constant (τ_b).[4]

Note that Eq. 4.1 does not take into account a non-zero SPV built-up time, as opposition to Eq. 4.2 which does indeed account for a non-zero SPV built-up. In both expressions, V_{Dark} and V_{light} are known values, therefore they can be fixed in the fit procedure.

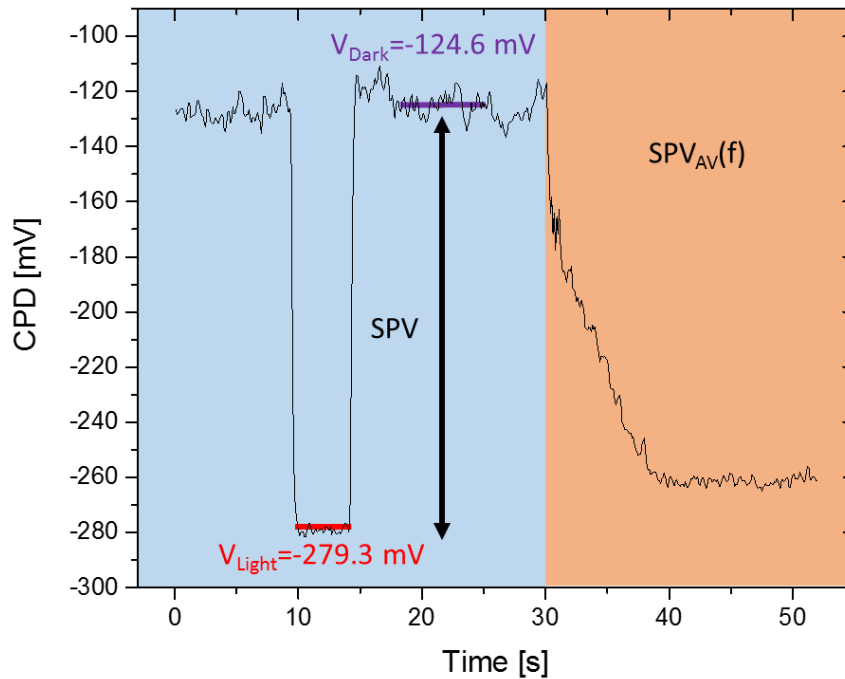


Figure 6.7– CPD data obtained from the implementation of the improved FMI-KPFM protocol where the CPD under continuous wave excitation and under dark conditions are acquired along with the SPV_{AV} spectroscopy curve. V_{Dark} corresponds to the in-dark surface potential and V_{light} with the surface photo-voltage measured under continuous wave illumination. Figure reproduced from Ref. [11]

In Figure 6.8, the result of the fit procedures is shown (red and green lines). Although a SPV decay time within the expected range is calculated in both fits (*ca.* 12 ms), the quality of the fits is not optimal (large deviation from data-points). In turn, if we use SPECTY to model the SPV_{AV} spectroscopy curve including the use of a non-zero SPV built-up time, the resulting curve (blue line) presents an improved adjustment to the data-points, suggesting that indeed, using SPECTY leads to a more accurate estimation of the SPV photo-carrier dynamics. Moreover, the slight differences between the simulated curve and the data points can be reasonably attributed to the influence of capacitance artefacts over the experimental data.

In this Figure, the blue line displays the best obtained result of the simulated average surface photo-voltage spectroscopy curve over the measured data-points using $\tau_d = 14.48 \text{ ms}$

and $\tau_b = 0.25$ ms. However, it is worth mentioning that while the simulated curve seems to better describe the data-set than the mathematical fit, all estimations yield similar SPV decay times.

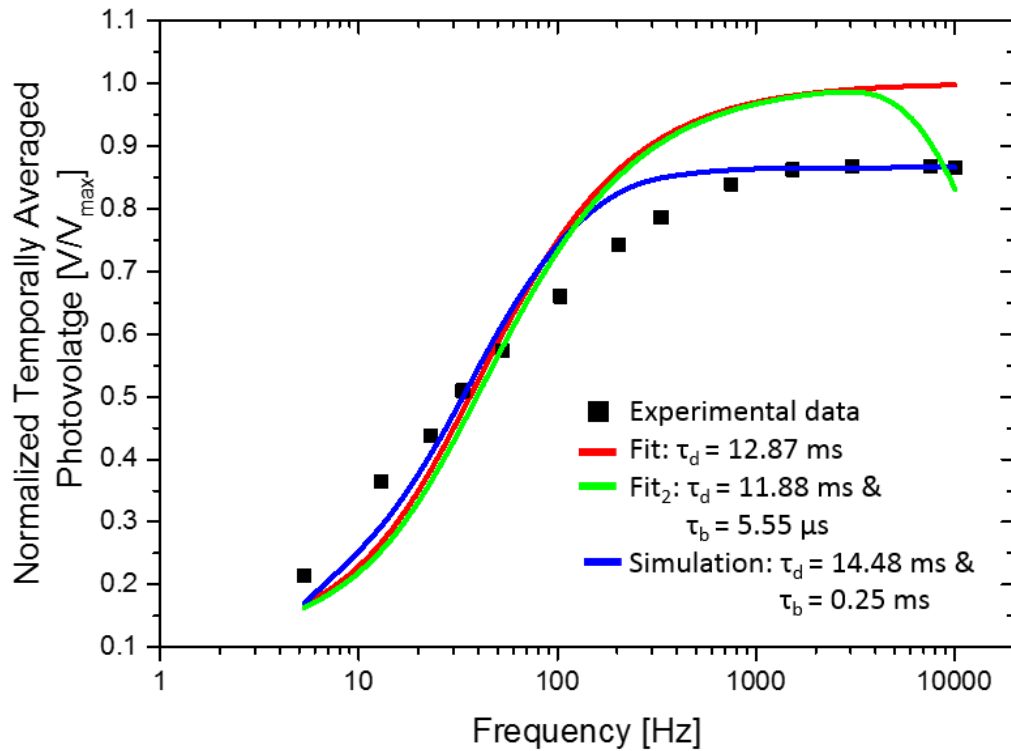


Figure 6.8– Comparison between curves: Mathematical fit (red and green lines) and simulated SPV_{AV} curve (blue line). The improved adjustment of the simulated SPV_{AV} curve compared to the mathematical fit is attributed to the inclusion of a non-zero SPV built-up time. Figure adapted from Ref. [11]

Conclusion

In this chapter, we proposed and demonstrated a novel automatic numerical simulation routine that enables the simulation of spectroscopy curves of the average surface photo-voltage as a function of a frequency modulated excitation source in photovoltaic materials provided that the time(s) constant(s) value(s) of the SPV dynamic(s) are specified as set-up parameters to the software.

We implemented this routine to check calculated time constant values associated to the minority carrier lifetime obtained with single-point FMI-KPFM on a silicon nanocrystal solar cell. Obtained results were not only confirmed by the numerical analysis, but additional information about the photo-carriers dynamics was found, which otherwise would not be accessible solely from the mathematical fit of the measured data.

We also implemented the numerical simulation routine to check results obtained over an organic photovoltaic blend via the improved FMI-KPFM protocol presented in **Chapter 5**. We saw that the simulated curve seems to better describe the data-set compared to the mathematical fit, however, all estimations yielded similar SPV decay times.

To sum it up, experiments and simulations here presented, seem to add evidence pointing out that in general, the use of SPECTY leads to a more accurate estimation of the SPV photo-carrier dynamics.

References

1. Borowik Ł., L.H., Chevalier N., Mariolle D., Renault O., *Measuring the lifetime of silicon nanocrystal solar cell photo-carriers by using Kelvin probe force microscopy and x-ray photoelectron spectroscopy*. Nanotechnology, 2014. **25**(26): p. 265703.
2. Shao, G., et al., *Intensity-Modulated Scanning Kelvin Probe Microscopy for Probing Recombination in Organic Photovoltaics*. ACS Nano, 2014. **8**(10): p. 10799-10807.
3. Takihara, M., T. Takahashi, and T. Ujihara, *Minority carrier lifetime in polycrystalline silicon solar cells studied by photoassisted Kelvin probe force microscopy*. Applied Physics Letters, 2008. **93**(2): p. 021902.
4. Fernández Garrillo, P.A., et al., *Photo-Carrier Multi-Dynamical Imaging at the Nanometer Scale in Organic and Inorganic Solar Cells*. ACS Applied Materials & Interfaces, 2016. **8**(45): p. 31460-31468.
5. Almadori, Y., N. Bendiab, and B. Grévin, *Multimodal Kelvin Probe Force Microscopy Investigations of a Photovoltaic WSe₂/MoS₂ Type-II Interface*. ACS Applied Materials & Interfaces, 2018. **10**(1): p. 1363-1373.
6. Coffey, D.C., et al., *Mapping Local Photocurrents in Polymer/Fullerene Solar Cells with Photoconductive Atomic Force Microscopy*. Nano Letters, 2007. **7**(3): p. 738-744.
7. Coffey, D.C. and D.S. Ginger, *Time-resolved electrostatic force microscopy of polymer solar cells*. Nature Materials, 2006. **5**: p. 735.
8. Narchi, P., et al., *Nanoscale Investigation of Carrier Lifetime on the Cross Section of Epitaxial Silicon Solar Cells Using Kelvin Probe Force Microscopy*. IEEE Journal of Photovoltaics, 2016. **6**(6): p. 1576-1580.
9. Fernández Garrillo, P.A., et al., *Comments on "Nanoscale Investigation of Carrier Lifetime on the Cross Section of Epitaxial Silicon Solar Cells Using Kelvin Probe Force Microscopy"*. IEEE Journal of Photovoltaics, 2018. **8**(2): p. 661-663.
10. Sinton, R.A. and R.M. Swanson, *Recombination in highly injected silicon*. IEEE Transactions on Electron Devices, 1987. **34**(6): p. 1380-1389.
11. Fernández Garrillo, P.A., B. Grévin, and Ł. Borowik, *Numerical analysis of single-point spectroscopy curves used in photo-carrier dynamics measurements by Kelvin probe force microscopy under frequency-modulated excitation*. Beilstein Journal of Nanotechnology, 2018. **9**: p. 1834-1843.
12. Sinton, R.A. and A. Cuevas, *Contactless determination of current-voltage characteristics and minority-carrier lifetimes in semiconductors from quasi-steady-state photoconductance data*. Applied Physics Letters, 1996. **69**(17): p. 2510-2512.
13. Vu, D.P. and J.C. Pfister, *Determination of minority-carrier generation lifetime in beam-recrystallized silicon-on-insulator structure by using a depletion-mode transistor*. Applied Physics Letters, 1985. **47**(9): p. 950-952.

7 | Conclusion

In the following, a concluding overview of results presented in this thesis will be given. Moreover, current research projects will be briefly discussed.

The first experimental results obtained during this thesis can be found in **Chapter 3**, where it was demonstrated how Kelvin probe force microscopy (KPFM) investigations can give access to the absolute work function (WF) value of a sample with a lateral resolution of few nanometres upon probe calibration. The results detailed in that part of the manuscript are of great interest since they concern the description, control and nano-characterization of electronics components and devices. Nonetheless, in the context of this thesis, WF measurements at the local scale are of especial interest due to its influence in the band line-up at the interface between organic materials and electrodes in photovoltaic devices. Moreover, these first set of results serve also to introduce the reader into the field of atomic force microscopy (AFM)-based physical measurements.

However, the main intention of this manuscript as we saw in **Chapters 4, 5 and 6**, is to serve as a guide for the implementation of frequency modulated illumination Kelvin probe force microscopy (FMI-KPFM) investigations over photovoltaic materials. In that context, the general objective of this thesis was to develop a new 2-dimensional spectroscopic imaging mode based on FMI-KPFM that could be used to investigate the complex relation between sample structuration and photo-carrier dynamics.

During this thesis, we successfully developed this technique and we show how it can be used to record simultaneously 2-dimensional images of the surface photo-voltage dynamics in photovoltaic materials with a sub-10 nm lateral resolution and with a temporal resolution which is only limited by the modulation illumination chain (with our current setup, time

constants of the order of few tens of nanoseconds were measured). Furthermore, while during this thesis, all measurements were carried out at room temperature, we anticipate that cryogenic experiments will help achieving further improvements in terms of lateral imaging resolution.

Moreover, we implemented this technique over a wide range of photovoltaic samples ranging from inorganic silicon-based solar cells to organic bulk-hetero junction solar cells and hybrid organic-inorganic perovskite solar cells. We show how this approach provided a way to quantify the impact of the morphology and nanostructure on the carrier mobility, trapping and recombination.

In addition to the development of this new technique, during this thesis we discussed its current limitations and some open questions regarding data interpretation. It was in **Chapter 5** where we pointed out these issues and gave detailed insights aiming at avoiding several plausible sources of measurement artefacts. For instance, we show how via the recording of the F_{2w} signal we were able to record capacitance gradient fluctuations, responsible of causing artefacts during FMI-KPFM investigations. Furthermore, we developed and implemented an improved FMI-KPFM protocol where capacitance-related artefacts are accounted for.

Nevertheless, some questions regarding the accuracy of the mathematical models used in the spectroscopy curve fit procedure still remain unclear. In particular, we raised awareness on the fact that models used in this thesis, as well as models used so far by other groups working on FMI-KPFM related techniques, do not take into account certain considerations required to accurately describe all the processes occurring in photovoltaic materials upon illumination. For instance, an ideal model should take into account the number of excitation pulses needed to reach the average potential quasi-steady state as well as to account for the plausible presence of surface photo-voltage contributions exhibiting different polarities.

In that context, we proposed an alternative approach, directed towards the development of a numerical tool allowing to simulate the behaviour of the average surface photo-voltage as a function of the modulation frequency of an excitation source signal in photovoltaic materials.

It was in **Chapter 6** where we introduced this tool which allowed us to compare simulated and experimental results. In fact, by adjusting the simulation parameters, we were able to reproduce spectroscopy curves that matched the experimental ones. In this way, the input parameters of the simulation yielded time constants related to the experiment, constituting an alternative method to determine the photo-carrier dynamics without the need of complex analytical models.

In that regard, there is one pending task should be addressed in the future, which is the adaptation of the numerical analysis of spectroscopy curves in an automated fashion so that images of the photo-carrier dynamics could be acquired automatically. Actually, our numerical tool allows the estimation of the photo-carrier dynamics manually. It is, the user has to adapt the input parameters in an iterative process until a good curve adjustment to the data points is obtained. Moreover, this process has to be repeated for all spectroscopy curves rendering the acquisition of images impractical. In the future, this process should be automated allowing to obtain photo-carrier dynamic images without the need of a mathematical fit procedure based on a particular model.

To sum up, FMI-KPFM constitutes an approach which provides a way to quantify the impact of the morphology and nanostructure on the carrier mobility, trapping and recombination. We believe that this approach will make an important contribution to the understanding of the complex interplay between the nanostructure, and the photo-carrier transport, trapping and recombination dynamics in organic, inorganic and hybrid solar cells.

Furthermore, we stress that the field of application of FMI-KPFM extends well beyond the case of energy materials. The ability to image the dynamics of surface photo-potentials is also a key in the field of opto-electronics, there is a huge potential for applications in the field of photo-transistors and photo-detectors. Indeed, besides addressing fundamental issues, photo-carrier dynamic measurements could allow better quantifying the impact of the elaboration process parameters on the optoelectronic properties of organic, inorganic and hybrid photoactive layers at the nanometre scale, thus targeting critical manufacturing processes.

Finally, while all presented FMI-KPFM investigations were performed using a single laser wavelength at the time, meaning that the photo-voltage dynamics information is only coming from a certain depth of the sample, in a next ambitious step, a 3-dimensional reconstruction of the photovoltage dynamics at the nanoscale could be accessed if FMI-KPFM measurements are implemented using different laser wavelengths (adapted to the light absorption of the sample) in a consecutive fashion.

Actually, while writing this manuscript, as a first step, and as part of a master internship subject, experiments involving the consecutive use of different laser wavelengths have already taken place. The goal of these experiments is to image the photo-carrier diffusion length over a wide range of photovoltaic samples. In short, this is done by measuring the photovoltaic response of the sample to various laser wavelengths. In this way, a well know mathematical model can be used to calculate the photo-carrier diffusion length of the material. Applying this protocol in a 2-dimensional FMI-KPFM fashion should allow to obtain nano-resolved images of this parameter. (Ph.D. thesis scheduled).

Moreover, besides the investigation of other samples using “conventional” FMI-KPFM, the development of other frequency-modulated illumination techniques for measuring photovoltaic dynamics is also a theme which is expected to be the subject of research. For example, one could imagine implementing conducting (c)-AFM, or even scanning tunnelling microscopy measurements under frequency modulated illumination. In that case, instead of measuring a contact potential difference (CPD), a small photo-current would be measured, the variation of this current as a function of the illumination modulation frequency should also give access to the photo-carrier dynamics of the material.

8 | Appendix

Content

8.1 Additional photo-carrier dynamic results over the cross section of epitaxial silicon solar cell.....	203
8.2 Correcting the fitting functions from the capacitance effects	207
References.....	213

8.1 Additional photo-carrier dynamic results over the cross section of epitaxial silicon solar cell

In [1], a technique to assess carrier lifetime at the nanoscale using Kelvin probe force microscopy (KPFM) combined with modulated frequency electrical bias excitation was demonstrated over the cross section of an epitaxial silicon solar cell. Using this technique, it was demonstrated that the surface potential behaviour of a nonintentional n-type defective layer at the interface between the c-Si wafer and the epitaxial layers behaves different at higher frequencies of bias excitation (1-5 MHz) than the rest of the epitaxial layer, implying different photo-carrier dynamics in this sample's interface region.

Here, we complement these results by adding the implementation of an automatic post-acquisition data processing where spectroscopy curves are generated (see Figure 8.1) from the data presented in Figure 6 of the above mentioned paper.[1]

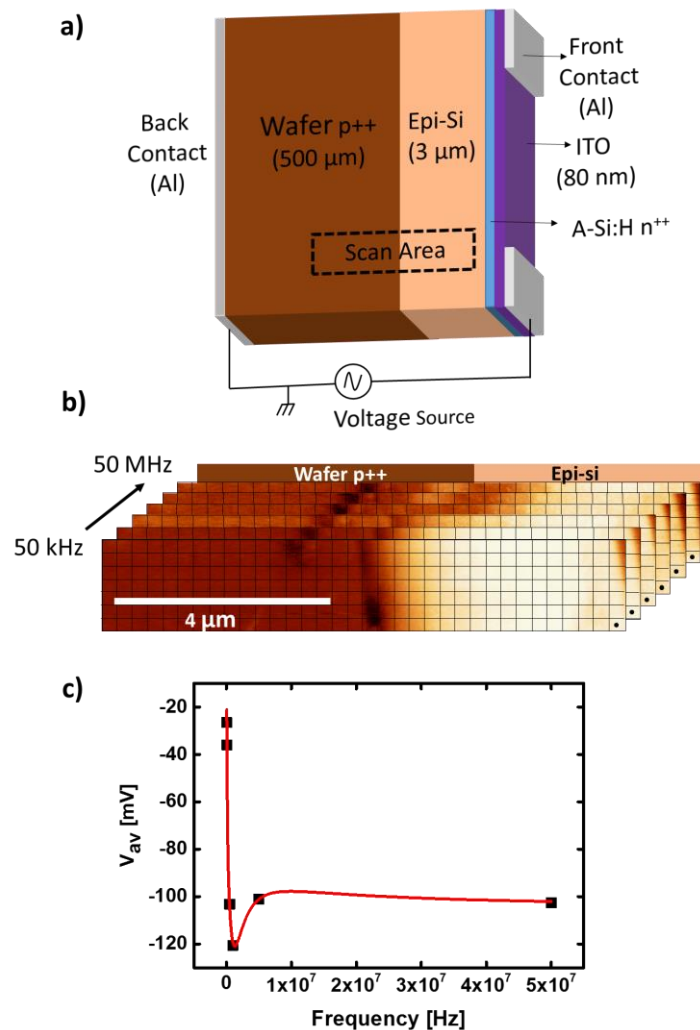


Figure 8.1– (a) Sample schematic. (b) Surface potential images associated with different frequencies of modulated electrical bias. The black dots on the right side corner represent the pixel of each image which value was used to generate the spectroscopy curve shown below. (c) Spectroscopy curve of V_{AV} as a function of the bias excitation modulation frequency generated by the post-acquisition data processing. The red line shows result of the mathematical fit performed using Eq. 4.4. Reproduced from Ref. [2]

The spectroscopy curves of V_{AV} a function of the frequency modulated bias (50 kHz, 100 kHz, 500 kHz, 1 MHz, 5 MHz and 50 MHz with 50% duty ratio), are then fitted using an automatic curve fit operation routine based on the least-square method, developed using the

SCILAB software. This routine allowed us to recalculate 2-dimensional dynamical images of each curve's characteristic time-constants (see Figure 8.2).

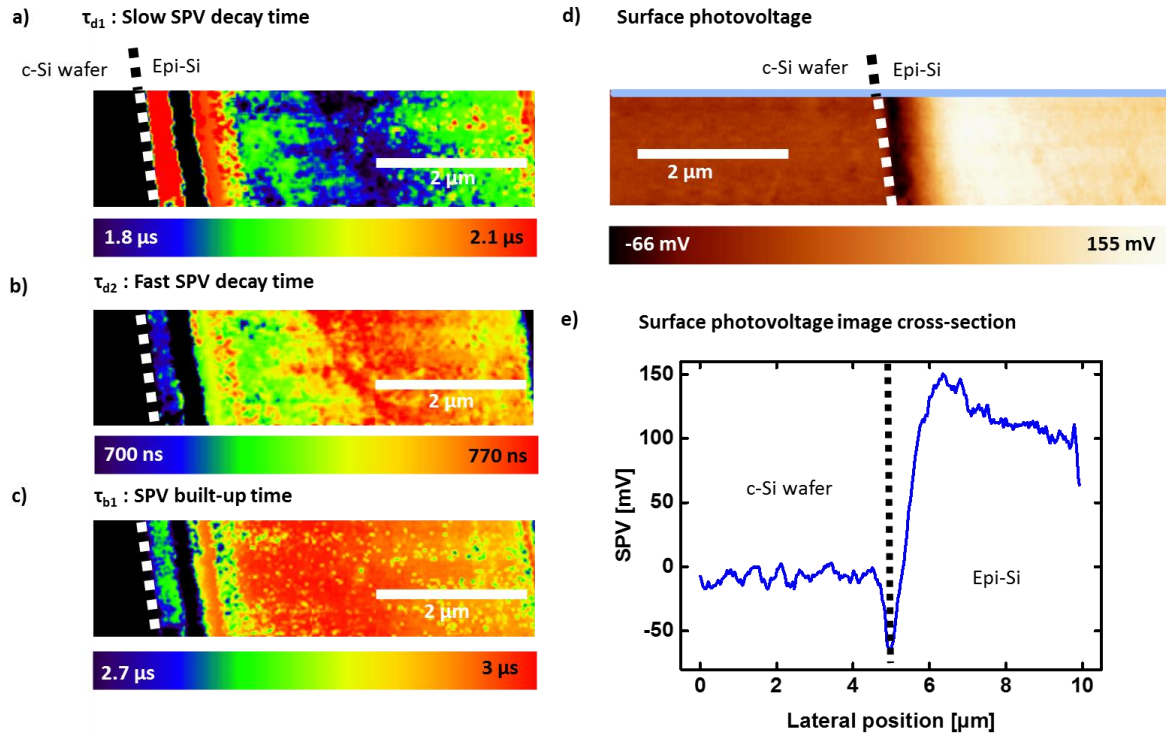


Figure 8.2– (a) Slow photovoltage decay image, attributed to trapping-detrapping effects. (b) “Fast” photovoltage decay time, attributed to the effective minority carrier lifetime of free carriers in the sample (c) Photovoltage built-up time, attributed to the effective time of exciton dissociation and carrier separation (d) Surface photovoltage image, obtained by subtracting the contact potential difference images acquired at the highest and the lowest excitation modulation frequency. It is important to mention that this photovoltage should be smaller in magnitude than the photovoltage that would be measured under continuous wave excitation (e) Cross section profile of (d) showing a negative surface photovoltage at the interface between the c-Si wafer and the epitaxial layer. Reproduced from Ref. [2]

The non-monotonic behaviour of the spectroscopy curve shown in Fig. 8.1c can be modelled in a phenomenological approach by considering the measured average surface photovoltage V_{AV} to be the superposition of at least two different surface photovoltage (SPV) contributions, each one with its own characteristic decay time constant.[3] This assumption is

consistent with the presence of two carrier recombination processes in the sample: i) an effective minority carrier lifetime and ii) a longer SPV decay time constant attributed to trapping de-trapping effect, common in crystalline silicon.[1, 4, 5] Then, the spectroscopy curves can be fitted using the mathematical expression derived in **Chapter 4** which models the behaviour of V_{AV} as a function of the excitation modulation frequency (Eq. 4.4).

Nonetheless, caution should be taken when implementing Eq. 4.4, since the above expression models the V_{AV} behaviour as a function of an excitation modulation frequency under quasi-steady state conditions. In other words, Eq. 4.4 requires that the equilibrium state of charges is reached, *i.e.*, the number of generated and recombined charges is equal for a given frequency. In this case, such condition is guarantee since images of the surface potential at different modulation frequencies were acquired individually, in contrast to a frequency spectroscopy sweep were the KPFM acquisition and its integration time become crucial parameters that should be set appropriately in order to fulfil Eq. 4.4 requirements.

Finally, Figures 8.2a, 8.2b and 8.2c depicts the recalculated 2-dimensional dynamical images obtained by implementing the described data treatment procedure. These images are in good agreement with results presented in [1] where carrier lifetimes were found to be in the 0.2 – 20 μ s range.

Figure 8.2b shows the distribution of carrier lifetimes over the sample, which we tentatively associate with non-radiative carrier recombination.[6] Moreover, in this image we observe that the contrast in the interface region between the c-Si wafer and the slightly n-doped epitaxial layer, strongly differs with the contrast observed in the rest of the of the sample's epitaxial layer, which agrees with one of the conclusion of [1] were is stated that this interface region is acting as a defective layer, hence shorter free carrier lifetimes are likely to be observed.

On the other hand, Figure 8.2a reflects longer carrier lifetime that we attributed to trapping–detrapping effects which are common in crystalline silicon[6] and were previously reported by Narchi et al.,[1]

Finally, Figure 8.2c depicts the SPV built-up time constant over the sample. In general, this image presents anti-correlated features when compared with Figure 8.2a. Considering the nature of the sample and its known properties, it is reasonable to state that this time constant is strongly associated with exciton dissociation process via generation centres and the subsequent carrier diffusion.[6]

Additionally, we present SPV image in Figure 8.2d and its cross-sectional profile in Figure 8.2e. As shown in Figure 8.2e, the cross-sectional profile shows a negative SPV at the interface between the c-Si wafer and the epitaxial layer. These data were obtained by subtracting the contact potential difference images acquired at the highest and the lowest excitation modulation frequency. As we explained earlier, this photovoltage should be smaller in magnitude than the photovoltage that would be measured under continuous wave excitation.

Summarizing, the results of this study confirm those previously reported by Narchi et al., [1] while adding substantially to their work by providing a way to generate 2-dimensional images of the photo-carrier dynamics in this sample, constituting an important tool to localize defective low-lifetimes layers and interfaces in photovoltaic materials with a nanometre resolution. Additionally, obtained results provide support for the conceptual premise that in the sample, the interface region between the c-Si wafer and the slightly n-doped epitaxial layer is acting as a defective layer.

8.2 Correcting the fitting functions from the capacitance effects

In the following we show how the functions used to fit the curves of the KPFM compensation potential as a function of the modulation frequency of the illumination source can be modified to take into account the capacitance effects.

First we use a simple exponential function with a characteristic time constant τ_d to describe the SPV decay dynamics between the light pulses. In a first step, for the sake of simplicity, we make the approximation that photo-potential built-ups instantaneously when the

light is turned on as depicted in Figure 8.3a (a similar correction procedure can be performed in the case of a non-instantaneous SPV built-up as shown hereafter).

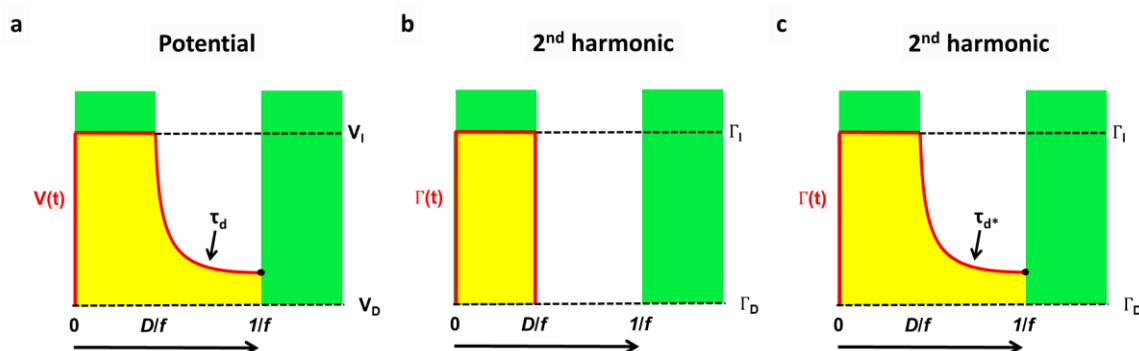


Figure 8.3– (a) Surface potential time-dependency under pulsed illumination in the case of an instantaneous photo-charging and a surface photovoltage decay with time constant τ_d . (b) Simplified time domain function used to take into account the effect of the capacitive contributions. (c) More complex function in which the 2nd harmonic signal displays its own decay time constant τ_d^* . In practice this function will be obtained by analysing the curves of the 2nd harmonic signal as a function of the modulation frequency.

The instantaneous potential over one modulation period can be described as:

$$0 \leq t \leq D/f \quad V(t) = V_I \quad (8.1)$$

$$D/f \leq t \leq 1/f \quad V(t) = V_D + (V_I - V_D)e^{-\frac{t-D/f}{\tau_d}} \quad (8.2)$$

Here, f and D represent the illumination modulation frequency and duty ratio, respectively. $V(t)$ is the instantaneous surface potential at a given time t . V_D is the in-dark surface potential, and V_I is the surface potential level under continuous illumination.

First, we calculate the average surface potential as a function of the modulation frequency. V_{AV} is calculated by integrating $V(t)$ over one period of the modulation signal $T = 1/f$:

$$V_{AV} = \frac{1}{T} \left(\int_0^{1/f} V(t) dt \right) \quad (8.3)$$

$$V_{AV} = \frac{1}{T} \left(\int_0^{D/f} V_I dt + \int_{D/f}^{1/f} V_D + (V_I - V_D) e^{-\frac{t-D/f}{\tau_d}} dt \right) \quad (8.4)$$

Solving the integrals yields:

$$V_{AV}(f) = DV_I + (1 - D)V_D + f\tau_d(V_I - V_D)e^{-\frac{1-D/f}{\tau_d}} \quad (8.5)$$

Using this function to fit the KPFM curves may result in some errors, because The KPFM loops yields a measurement of the average potential weighted by the capacitive gradient or the capacitive second derivative.

$$V_{AVKPFM} = \frac{\int_0^{1/f} \Gamma(t)V(t)dt}{\int_0^{1/f} \Gamma(t)dt} \quad (8.6)$$

With $\Gamma(t) = \frac{dC}{dz}(t)$ in amplitude modulated KPFM and with $\Gamma(t) = \frac{d^2C}{d^2z}(t)$ in frequency modulated KPFM, $\Gamma = 2^{\text{nd}}$ harmonic signal from the lock-in detection.

First, we make a simple calculation by weighting the instantaneous potential by using two different values for Γ over the dark and illuminated time-domains (Figure 8.3b).

$$0 \leq t \leq D/f \quad \Gamma(t) = \Gamma_I \quad (8.7)$$

$$D/f \leq t \leq 1/f \quad \Gamma(t) = \Gamma_D \quad (8.8)$$

$$V_{AVKPFM} = \left(\int_0^{D/f} \Gamma_I V_I dt + \int_{D/f}^{1/f} \Gamma_D \left(V_D + (V_I - V_D) e^{-\frac{t-D/f}{\tau_d}} \right) dt \right) / \left(\int_0^{D/f} \Gamma_I dt + \int_{D/f}^{1/f} \Gamma_D dt \right) \quad (8.9)$$

Solving the integrals yields:

$$V_{AVKPFM}(f) = \alpha V_I + \beta(1 - D)V_D + \gamma f\tau_d(V_I - V_D)e^{-\frac{1-D/f}{\tau_d}} \quad (8.10)$$

$$\text{With, } \alpha = \frac{\Gamma_I D}{D \Gamma_I + (1-D) \Gamma_D}, \beta = \frac{\Gamma_D (1-D)}{D \Gamma_I + (1-D) \Gamma_D} \text{ and } \gamma = \frac{\Gamma_D}{D \Gamma_I + (1-D) \Gamma_D}$$

In the case of a light-independent 2nd harmonic signal ($\Gamma_I = \Gamma_d$), one gets $\alpha = D$, $\beta = 1 - D$ and $\gamma = 1$.

Now, we consider that the 2nd harmonic signal displays a more complex behaviour, characterized by a decay time τ_d^* in the dark state (Figure 8.3c).

$$0 \leq t \leq D/f \quad \Gamma(t) = \Gamma_I \quad (8.11)$$

$$D/f \leq t \leq 1/f \quad \Gamma(t) = \Gamma_D + (\Gamma_I - \Gamma_D) e^{-\frac{t-D/f}{\tau_d^*}} \quad (8.12)$$

One can show by solving the integrals that:

$$V_{AV} KPFM(f) = \alpha V_I + \beta V_D + f(V_I - V_D) \left[\gamma \tau_d \left(1 - e^{-\frac{(1-D)}{f\tau_d}} \right) + \delta \frac{\tau_d \tau_d^*}{\tau_d + \tau_d^*} \left(1 - e^{-\frac{(1-D)(\tau_d + \tau_d^*)}{f\tau_d \tau_d^*}} \right) \right] \quad (8.13)$$

With:

$$\alpha = \frac{\Gamma_I D}{D \Gamma_I + (1-D) \Gamma_D + f \tau_d^* (\Gamma_I - \Gamma_D) \left(1 - e^{-\frac{(1-D)}{f\tau_d^*}} \right)} \quad (8.14)$$

$$\beta = \frac{(1-D) \Gamma_D + (\Gamma_I - \Gamma_D) \left(1 - e^{-\frac{(1-D)}{f\tau_d^*}} \right)}{D \Gamma_I + (1-D) \Gamma_D + f \tau_d^* (\Gamma_I - \Gamma_D) \left(1 - e^{-\frac{(1-D)}{f\tau_d^*}} \right)} \quad (8.15)$$

$$\gamma = \frac{\Gamma_D}{D \Gamma_I + (1-D) \Gamma_D + f \tau_d^* (\Gamma_I - \Gamma_D) \left(1 - e^{-\frac{(1-D)}{f\tau_d^*}} \right)} \quad (8.16)$$

$$\delta = \frac{\Gamma_I - \Gamma_D}{D \Gamma_I + (1-D) \Gamma_D + f \tau_d^* (\Gamma_I - \Gamma_D) \left(1 - e^{-\frac{(1-D)}{f\tau_d^*}} \right)} \quad (8.17)$$

Last, we consider the case of a non-instantaneous sample photo-charging under illumination (Figure 8.4).

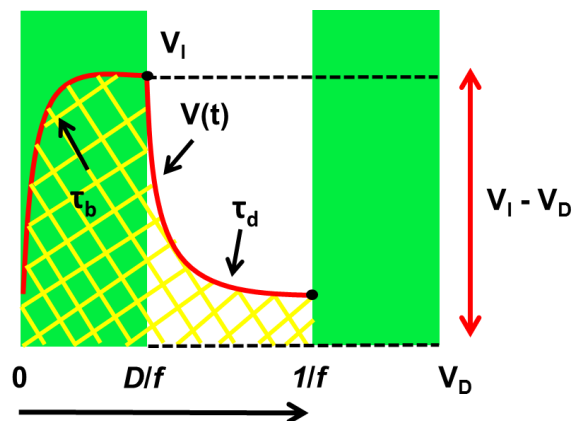


Figure 8.4– Case of a non-instantaneous sample photo-charging under illumination.

We describe the instantaneous surface photo-voltage $SPV(t) = V(t) - V_D$ by simple exponential functions with characteristic time constants τ_b and τ_d to describe the surface photo-voltage built-up τ_b and decay τ_d dynamics:

$$0 \leq t \leq D/f \quad SPV(t) = V(t) - V_D = K_1 \left(1 - e^{-\frac{t}{\tau_b}}\right) + K_2 \quad (8.18)$$

$$D/f \leq t \leq 1/f \quad SPV(t) = V(t) - V_D = K_3 \left(e^{-\frac{t-D/f}{\tau_d}}\right) \quad (8.19)$$

With: $K_1 \left(1 - e^{-\frac{D}{f\tau_b}}\right) + K_2 = K_3$, $K_3 = SPV_I \left(1 - e^{-\frac{D}{f\tau_b}}\right)$, $K_2 = K_3 e^{-\frac{1-D}{f\tau_d}}$, $SPV_I = V_I - V_D$

These time constants insure the continuity of the potential both for $t = 0 = 1/f$ and $t = D/f$.

The average surface potential V_{AV} calculated (detailed not shown) by integrating $V(t)$ over one period of the modulation signal $T = 1/f$ is:

$$V_{AV} = V_D + SPV_I D \left(1 - e^{-\frac{D}{f\tau_b}} e^{-\frac{(1-D)}{f\tau_d}} \right) + SPV_I (f\tau_d - f\tau_b) \left(1 - e^{-\frac{D}{f\tau_b}} \right) \left(1 - e^{-\frac{(1-D)}{f\tau_d}} \right) \quad (8.20)$$

Now we give the results of the calculation of the function that should be used to fit the average KPFM compensation loop by weighting the instantaneous potential by using two different values for Γ over the dark and illuminated time-domains.

$$0 \leq t \leq D/f \quad \Gamma(t) = \Gamma_I \quad (8.21)$$

$$D/f \leq t \leq 1/f \quad \Gamma(t) = \Gamma_D \quad (8.22)$$

$$V_{AV} = V_D + \alpha SPV_I D \left(1 - e^{-\frac{D}{f\tau_b}} e^{-\frac{(1-D)}{f\tau_d}} \right) + SPV_I (\beta f\tau_d - \alpha f\tau_b) \left(1 - e^{-\frac{D}{f\tau_b}} \right) \left(1 - e^{-\frac{(1-D)}{f\tau_d}} \right) \quad (8.20)$$

$$\text{With } \alpha = \frac{\Gamma_D}{D \Gamma_I + (1-D) \Gamma_D} \text{ and } \beta = \frac{\Gamma_I}{D \Gamma_I + (1-D) \Gamma_D}$$

The calculation can also be generalized (not shown here) by assuming the 2nd harmonic signal is characterized by its own build up and decay time constants in the dark and illuminated time domains.

References

1. Narchi, P., et al., *Nanoscale Investigation of Carrier Lifetime on the Cross Section of Epitaxial Silicon Solar Cells Using Kelvin Probe Force Microscopy*. IEEE Journal of Photovoltaics, 2016. **6**(6): p. 1576-1580.
2. Fernández Garrillo, P.A., et al., *Comments on "Nanoscale Investigation of Carrier Lifetime on the Cross Section of Epitaxial Silicon Solar Cells Using Kelvin Probe Force Microscopy"*. IEEE Journal of Photovoltaics, 2018. **8**(2): p. 661-663.
3. Fernández Garrillo P. A., B.L., Caffy F., Demadrille R., Grévin B. *Imaging the Multi-Temporal Photo-Carrier Dynamics at the Nanometer Scale in Organic and Inorganic Solar Cells*. in *IEEE PVSC-44*. 2017. Washington D.C. - USA.
4. Fernández Garrillo, P.A., et al., *Photo-Carrier Multi-Dynamical Imaging at the Nanometer Scale in Organic and Inorganic Solar Cells*. ACS Applied Materials & Interfaces, 2016. **8**(45): p. 31460-31468.
5. Cuevas, A. and D. Macdonald, *Measuring and interpreting the lifetime of silicon wafers*. Solar Energy, 2004. **76**(1): p. 255-262.
6. Schroder, D.K., *Carrier lifetimes in silicon*. IEEE Transactions on Electron Devices, 1997. **44**(1): p. 160-170.

Publications

The following publications resulted from the work of this thesis:

“Photo-Carrier Multi Dynamical Imaging at the Nanometer Scale in Organic and Inorganic Solar Cells” Pablo A. Fernández Garrillo, Łukasz Borowik, Florent Caffy, Renaud Demadrille, Benjamin Grévin. *ACS Applied Materials & Interfaces*, 8 (45), 31460–31468, **2016. ACS Editors' Choice**, featured in the French National Centre for Scientific Research (CNRS) website and LETI's 2017 scientific report, available online.

“Imaging the Multi-Temporal Photo-Carrier Dynamics at the Nanometer Scale in Organic and Inorganic Solar Cells” Pablo A. Fernández Garrillo, Łukasz Borowik, Florent Caffy, Renaud Demadrille, Benjamin Grévin. **2017 44th IEEE Photovoltaic Specialists Conference (PVSC2017)**.

“Comments on Nanoscale Investigation of Carrier Life time on the Cross Section of Epitaxial Silicon Solar Cells Using Kelvin Probe Force Microscopy” Pablo A. Fernández Garrillo, Paul Narchi, Pere Roca i Cabarrocas, Benjamin Grévin, Łukasz Borowik. *IEEE Journal of Photovoltaics*, 8(2), 661-663, **2018**.

“Calibrated Work Function Mapping by Kelvin Probe Force Microscopy” Pablo A. Fernández Garrillo, Benjamin Grévin, Nicolas Chevalier, Łukasz Borowik. *Review of Scientific Instruments*, 89(4), 043702, **2018. AIP Editors' Pick**.

“Numerical Analysis of Single-Point Spectroscopy Curves Used in Photo-Carrier Dynamics Measurements by Kelvin Probe Force Microscopy under Frequency Modulated Excitation” Pablo A. Fernández Garrillo, Benjamin Grévin, Łukasz Borowik. *Beilstein Journal of Nanotechnology*. 9, 1834-1843, **2018**.

Patent Application

Procède de Détermination de la Dynamique des Porteurs de Charge dans un Matériau Semi-Conducteur et Dispositif Associée. N° 1854973. Application date: 07/06/2018.

Inventors: Pablo Arturo Fernandez Garrillo, Łukasz Borowik, Benjamin Grévin. Submitted by CEA.

Conferences & Seminars

(First author contributions only)

Local Probing of the Photo-Carrier Lifetime by Kelvin Probe Force Microscopy on Third Generation Solar Cells. Pablo A. Fernandez Garrillo, Yann Almadori, Benjamin Grévin, David Moerman, Philippe Leclère, Łukasz Borowik. **MRS Fall Meeting. Boston (USA), November 2015.** (Oral presentation by Łukasz Borowik).

Imagerie de la Dynamique Multi-Temporelle des Photoporteurs à l'Échelle Nanométrique. Pablo A. Fernández Garrillo, Łukasz Borowik, Florent Caffy, Renaud Demadrille, Benjamin Grévin. **Forum des Microscopies à Sonde Locale. Juvignac (France), Mars 2017.** (Oral presentation by Pablo A. Fernández Garrillo).

Imaging the Multi-Temporal Photo-Carrier Dynamics at the Nanometer Scale in Organic Solar Cells. Pablo A. Fernández Garrillo, Łukasz Borowik, Florent Caffy, Renaud Demadrille, Benjamin Grévin. **E-MRS Spring Meeting. Strasbourg (France), May 2017.** (Oral presentation by Pablo A. Fernández Garrillo).

Imaging the Multi-Temporal Photo Carrier Dynamics at the Nanometer Scale in Organic and Inorganic Solar Cells. Pablo A. Fernández Garrillo, Łukasz Borowik, Florent Caffy, Renaud Demadrille, Benjamin Grévin. **IEEE PVSC44. Washington D.C. (USA), June 2017.** (Oral presentation by Pablo A. Fernández Garrillo).

Local probing of the photo-carrier lifetime dynamics by Kelvin probe force microscopy on third generation solar cells. Pablo A. Fernández Garrillo, Łukasz Borowik, Florent Caffy, Renaud Demadrille, Benjamin Grévin. **E-MRS Fall Meeting. Warsaw (Poland), September 2017.** (Oral presentation by Łukasz Borowik).

Photo-Carrier Multi-Dynamical Imaging at the Nanometer Scale in Organic and Inorganic Solar Cells. Pablo A. Fernández Garrillo, Łukasz Borowik, Florent Caffy, Renaud Demadrille, Benjamin Grévin. **Séminaire (Bruker) sur la caractérisation électrique à échelle nanométrique par Microscopie à Force Atomique. Grenoble (France), October 2017.** (Oral presentation by Pablo A. Fernández Garrillo).

Measuring Photo-Carrier Lifetime by KPFM under Frequency-Modulated Excitation: Simulations vs. Experimental Results. Pablo A. Fernández Garrillo, Benjamin Grévin, Łukasz Borowik. **EMRS Spring Meeting. Strasbourg (France), June 2018.** (Poster session by Pablo A. Fernández Garrillo).

Ultra-high vacuum investigations of methylammonium lead tribromide single crystals perovskites: sample stability and photo-carrier recombination. Pablo A. Fernandez Garrillo, Yann Almadori, Benjamin Grévin, David Moerman, Philippe Leclère, Łukasz Borowik. **MRS Fall Meeting. Boston (USA), November 2018.** (Poster session by Łukasz Borowik).

Acknowledgement

My time at CEA Grenoble was a truly enriching experience in both, professional and personal regards. During the last three years I had the opportunity to immerse myself in the fields of nanoscience and nanotechnology while strengthening my scientific knowledge in the dynamic field of photovoltaics. At the same time, I got to know excellent colleagues and friends who contributed directly or indirectly with the research I carried. Therefore I would like to thank all members of both INAC and LETI facilities for their support and their collegiality during the past three years. It has been a real pleasure to work in such a great environment and with such great colleges.

There are of course some members of both teams that I would like to thank in particular:

Firstly, my Ph.D. advisor Benjamin Grévin, to whom I will always be grateful for all the support and motivation that he gave me through these last three years. Never before I had encountered someone so passionate about research, fortunately his enthusiasm can be really contagious. His guidance and knowledge really helped me to shape my research and to improve my lab-skills, not to mention his help during this writing exercise. I will leave his laboratory with many nice memories and a few Jazz songs.

I would also like to thank my supervisor Łukasz Borowik, who was always there for me in case of need and who supported me since the beginning of my M.Sc. internship three and a half years ago. It was a real pleasure to share and work along with Łukasz during this time. His modesty, hard-work and management skills are for me the living example of what a researcher should be.

I would also like to thank Denis Mariolle for correcting the paragraphs written in French present in this thesis, as well as Nicolas Chevalier, Renaud Demadrille, Frédéric Chandezon,

Eric Sauvagnargues, Jean-Paul Barnes, Christophe Licitra, Anass Benayad, Eric De Vito, François Bertin, Olivier Renaud and Narciso Gambacorti for their kindness and enriching discussions, not to mention some collaborations.

This thesis would not be complete without thanking all the fellows Ph.D. students, interns and post-doc researchers that I had the pleasure to work with during these last years, specially Yann Almadori, Florent Caffy, Cyril Aumaitre, Jorge Morales, Munique Kazar, Maxime Godfroy, Isabelle Mouton, Maria Planells, Eric Langer, Maxime Gay, Valentin Aubriet, Maiglid Moreno, Lucas Bruas, Amal Ben Hadj, Olivier Bardagot, Jayanth Channagiri, Manon Berthault, Charlotte Zborowski, Sylvan Pouch, Mélanie David-Trabut, Tony Printemps, Arnaud Bordes, Luis Gomes, Riccardo Scarazzini, Robert Estivill, Viktoriia Gorbenko, Gael Goret, Djawhar Ferrah, Youcef Kerdja, Billal Allouche, Alam Figueroa and Natalia Turek.

Moreover, I would like to thank Thierry Mélin for his advice and assistance on multiple occasions.

Also, thanks to Christian Loppacher, Guillaume Schull, Pere Roca I Cabarrocas and Sascha Sadawasser who kindly accepted to participate in my Ph.D. thesis jury and reviewed this manuscript.

Thanks to Osyeiny Montero for her support.

Finally, I would like to thank all my family for their love and support, I own then everything. I would like to thank especially Luis David Garrillo, Susana Garrillo, Beatriz de Garrillo, Wintila Garrillo, Luis Guillermo Garrillo González, Luis Guillermo Garrillo Urdaneta, Gabriel Garrillo, Aura Garrillo, Ana de Garrillo, Abdenago Fernández and Emmanuel Fernández for all their love.